Two–Component Bose–Einstein Condensates: Equilibria and Dynamics at Zero Temperature and Beyond

Robert William Pattinson

Thesis submitted for the degree of
Doctor of Philosophy

School of Mathematics & Statistics
Newcastle University
Newcastle upon Tyne
United Kingdom

June 2014

To my parents, for their never ending love and support.

Acknowledgements

First of all, I would like to acknowledge my supervisors Nick Proukakis and Nick Parker for their guidance, enthusiasm and availability over the past few years, making my PhD interesting and enjoyable. My gratitude is extended to Danny McCarron, Simon Cornish, Tom Billam and Simon Gardiner for details regarding their experimental setup. Further to this, I would also like to acknowledge Gary Liu and Shih-Chuan Gou for collaborating with us in trying to model the experiment.

I want to thank the other postgraduates within the school for making my PhD a fun and enjoyable experience. In particular, I would like to mention Joy Allen, Matt Buckley, Donatello Gallucci, Fred Gent, Sarah Jowett, George Stagg, Nathan Barker, David Cushing, Tom Fisher, Holly Ainsworth, Jamie Owen, Nina Wilkinson, Kevin Wilson, Gavin Whitaker and Sam James for all the fun memories. I am grateful to all the other members of the Newcastle Superfluid group, namely Anthony Youd being my supervisor during my MMath project and for help with all things computing. I also want to mention friends from back home, Adrien de la Tour, Mathieu Yeme, Antoine Haettel, Caroline Manna, Camille Lapillonne, Yassin Belrhomari, Aude Guedeney, Ambroise Couissin, Elodie Marchat and Floriane Bonte, for always being around.

I want to say a huge thank you to my parents for encouraging me to always pursue my dreams and pointing me in the right direction. To my sister, Steph, for always being there. Finally, I want to thank Lucy Norris for her endless patience and love, and always suggesting takeaway pizza when it was called for!

Abstract

In this Thesis we study steady state solutions and dynamical evolutions of two–component atomic Bose–Einstein Condensates. We initially investigate the equilibrium properties of condensate mixtures in harmonic trapping potentials at zero temperature. Subsequently we simulate the coupled growth of these condensates by inclusion of damping terms. Finally, we investigate the evolution of coupled Bose gases via the so-called classical–field method.

A recent experiment [D. J. McCarron *et al.*, Phys. Rev. A, **84**, 011603(R) (2011)] achieved Bose–Einstein Condensation of a two–species ^{87}Rb–^{133}Cs phase segregated mixture in harmonic trapping potentials. Depending on relative atom numbers of the two species, three distinct regimes of density distributions were observed. For these experimental parameters, we investigate the corresponding time–independent ground state solutions through numerical simulations of the coupled Gross–Pitaevskii equations. By including experimentally relevant shifts between the traps, we observe a range of structures including 'ball and shell' formations and axially/radially separated states. These are found to be very sensitive to the trap shifts. For all three experimental regimes, our numerical simulations reveal good qualitative agreement.

The observed experimental profiles cannot be guaranteed to be fully equilibrated. This, coupled with the rapid sympathetic cooling of the experimental system, leads to a situation where growth may play a determining factor in the density structures formed. To investigate this further, we introduce phenomenological damping to describe the associated condensate growth/decay, revealing a range of transient structures. However, such a model always predicts the predominance of one condensate species over longer evolution times. Work undertaken by collaborators with the more elaborate Stochastic Projected Gross–Pitaevskii equations, which can describe condensate formation by coupling to a heat bath, predicts the spontaneous formation of dark–bright solitons. Motivated by this, we show how the presence of solitons can affect the condensate distribution, thus highlighting the overall dynamical role in the emerging patterns.

Finally, we use classical field methods to analyse the evolution of non trapped Bose gases from strongly nonequilibrium initial distributions. The contrast between miscible (overlapping) and immiscible (phase segregated) components gives rise to important distinctions for condensate fractions and the formation of domains and vortices. In addition, splitting the particles of a single component thermalised state into two components is investigated. We then study the effects of suddenly quenching the strength of the interspecies interactions. Under suitable conditions, this quench generates isotropic vortex tangles. While this tangle subsequently decays over time, we propose how a repeat sequence of quenches at regular intervals could be employed to drive the tangle, thereby potentially providing a novel route to the generation of quantum turbulence.

Contents

List of Figures

List of Tables

Part I

Introductory Material

Chapter 1

Introduction

The theoretical prediction of Bose-Einstein condensation dates back to the early 1920's when Planck's law for black–body radiation was re–derived by Satyendra Nath Bose from first principles [1] by assuming photons were identical and counting their distribution over energy states. Albert Einstein generalised these findings to massive particles, leading him to a theory for a gas of non–interacting atoms [2]: the Bose-Einstein distribution function was born. The distribution function for identical and indistinguishable particles at temperature T is given by

$$f(\epsilon_\nu) = \frac{1}{e^{(\epsilon_\nu - \mu)/kT} - 1} \tag{1.1}$$

where ϵ_ν denotes the energy of each single–particle quantum state labelled by ν, k is the Boltzmann constant and μ is the chemical potential of the system. The distribution gives the mean occupation number N_ν of the single–particle states, which is defined by

$$N_\nu = f(\epsilon_\nu)\, g_\nu = \frac{g_\nu}{e^{(\epsilon_\nu - \mu)/kT} - 1} \tag{1.2}$$

where g_ν is the degeneracy of the state ν. At low temperatures, these particles enter the same lowest energy quantum mechanical state; this is the Bose-Einstein condensate (BEC). In 1938, London suggested the connection between the then unexplained superfluidity of ^{4}He, by treating the strongly interacting liquid as a weakly interacting gas, and Bose-Einstein condensation of weakly interacting particles [3, 4].

A dilute weakly interacting atomic condensate was created for the first time in 1995 in ultracold gases of Rubidium ^{87}Rb [5], Sodium ^{23}Na [6], followed by Lithium ^{7}Li [7, 8] through the use of laser cooling methods. In these experiments the use of laser cooling alone was not sufficient in obtaining the low temperatures and high densities required for condensation and was therefore followed by evaporative cooling where the more energetic atoms are removed from the system thus allowing the remaining atoms to cool

through thermalising elastic binary collisions. This achievement was subsequently rewarded with Nobel Prizes in 1997 to Steven Chu, Claude Cohen–Tannoudji (theory) and William Phillips for laser cooling and trapping [9, 10, 11] and in 2001 to Carl Wieman, Eric Cornell and Wolfgang Ketterle for the achievement of BEC [12, 13].

1.1 Superfluid ^{4}He

Many of the properties of quantum fluids were established during the study of superfluid ^{4}He. The term superfluidity came into existence in 1938 when Kapitza [14] and Allen and Misener [15] measured the flow of viscosity of ^{4}He. It turned out that below the critical temperature 2.17K, ^{4}He becomes superfluid and has exceptional properties such as the ability to flow persistently around a loop due to the absence of viscosity. This also allows the liquid to flow through narrow channels. The idea of superfluidity only gained acceptance in 1941 with the introduction of the two-fluid model by Landau [16]. In this model, the superfluid component with no viscosity exists alongside the normal liquid; the relative ratio of their densities depending on temperature. At very low temperatures, the density of the superfluid component approaches the total density of the liquid while the density of the normal liquid vanishes. Due to the large interactions in the system, only about 10% of the particles are condensed i.e. in the lowest energy state. To achieve experimental realisation of BEC, a search for weakly interaction collisions between particles was required such that the system be easier to keep in gaseous form at very low temperatures. Close to the critical temperature, the situation is reversed: the density of the normal liquid approaches the density of the liquid while that of the superfluid tends to zero.

1.2 Bose–Einstein Condensation

In quantum mechanics, indistinguishable particles can be sorted into two classes depending on the value of their spin, originally interpreted as the rotation of a particle around some axis. There are fermions (half-integer spin) which follow Fermi-Dirac statistics and bosons (integer spin) which follow Bose–Einstein statistics (see Equation (1.1)). Due to the Pauli–exclusion principle, no more than one fermion can occupy a given quantum state. However, the number of bosons in the same state is unrestricted. Bosons are particles that exhibit symmetric states while fermions exhibit asymmetric ones. The two-particle wavefunctions are

$$\Psi = \frac{1}{\sqrt{2}} \left[\psi(x_1, E_a)\psi(x_2, E_b) + \psi(x_2, E_a)\psi(x_1, E_b)\right] \tag{1.3}$$

$$\Psi = \frac{1}{\sqrt{2}} \left[\psi(x_1, E_a)\psi(x_2, E_b) - \psi(x_2, E_a)\psi(x_1, E_b)\right] \tag{1.4}$$

for bosons and fermions respectively where the two particles are at positions x_1 and x_2 with energies E_a and E_b. If the particles have the same energy, i.e. $E_a = E_b$, the symmetric wavefunction becomes $\sqrt{2}\psi(x_1, E_a)\psi(x_2, E_a)$ showing that bosons can co-exist in the same state while the asymmetric wavefunction vanishes. The asymmetric wavefunction is null making it impossible for two fermions to occupy the same state. In fact, once a state is occupied by a boson, the probability of additional bosons scattering into the same state is increased.

The thermal de Broglie wavelength relates temperature to the mean interparticle spacing (see Figure 1.1), of order $n^{-1/3}$ where $n = N/V$ is the number density of a gas of N particles of volume V. The thermal de Broglie wavelength is given by

$$\lambda_T = \sqrt{\frac{2\pi\hbar^2}{mkT}} \tag{1.5}$$

where m is the atomic mass. We note that the wavelength is inversely proportional to the square root of the temperature T. At high temperatures, the interparticle spacing is much larger than the de Broglie wavelength ($n^{1/3} \gg \lambda_T$) such that classical particle like behaviour dominates, obeying the Boltzmann distribution. When the temperature is lowered, the wavelength increases and becomes comparable to the interparticle spacing ($n^{1/3} \approx \lambda_T$). The wave packets of the particles overlap and combine to form a giant matter wave, consistent with the system entering a quantum degenerate regime.

The criterion for Bose–Einstein condensation for a gas of identical particles in a three dimensional non–interacting uniform system is fulfilled when $n\lambda_T^3 \leq \zeta(3/2)$ [18] where $\zeta(3/2) \approx 2.612$ is the Riemann zeta function. Related to this condition, the expression for the critical temperature for which condensation occurs is

$$T_c = \frac{2\pi\hbar^2}{mk}\left(\frac{n}{\zeta\left(3/2\right)}\right)^{2/3}. \tag{1.6}$$

This critical temperature is the highest temperature at which the excited states become saturated and a anomalously large number of particles are forced into the lowest possible energy state (zero momentum). The collection of particles residing in the ground state is the BEC. The BEC transition is characterised in momentum space when a finite fraction of the particles occupy the zero momentum state and the occupancy of this momentum state is given by the well known result

$$N_0 = N\left[1 - \left(\frac{T}{T_c}\right)^{3/2}\right] \tag{1.7}$$

where N_0 is the number of particles in the condensate and N is the total number of particles in the system. A pure condensate ($N_0 = N$) results in the region near absolute

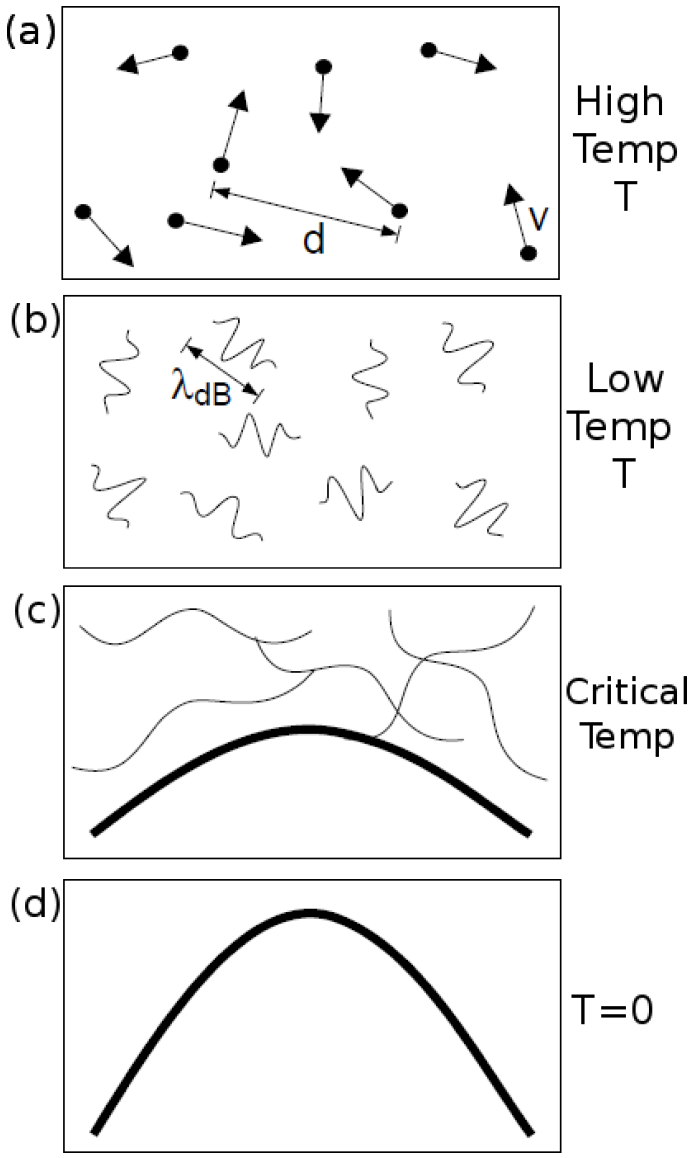

Figure 1.1: Criterion for Bose–Einstein condensation. (a) At high temperatures, the particles act like billiard balls in a weakly interacting gas where d is the interparticle spacing. (b) At low temperatures, the wavelength (λ_{dB}) properties of the particles start to emerge. (c) At the BEC transition temperature, the de Broglie wavelength becomes comparable to the distance between atoms and a Bose condensate forms. (d) When the temperature approaches absolute zero, all of the wavelengths overlap forming a pure BEC. Figure taken from Reference [17] with minor editing.

zero ($T = 0K$), although interactions also lead to quantum depletion.

In typical experiments, the gas is confined to a three–dimensional (3D) trapping potential which is harmonic

$$V(\mathbf{r}) = \frac{1}{2}m\left(\omega_x^2 x^2 + \omega_z^2 z^2 + \omega_z^2 z^2\right) \tag{1.8}$$

where ω_x, ω_y and ω_z are the harmonic oscillator frequencies in the x, y and z directions respectively. When the gas is in such a potential, the transition temperature in the abscence of interactions is given by

$$T_c = \frac{\hbar\bar{\omega}}{k}\left(\frac{N}{\zeta(3)}\right)^{1/3} \approx 0.94\hbar\bar{\omega}N^{1/3} \tag{1.9}$$

where $\bar{\omega} = (\omega_x\omega_y\omega_z)^{1/3}$ is the mean of the harmonic oscillator frequencies. In the next section, we outline the typical methods used for creating Bose–Einstein condensates experimentally, highlighting the use of harmonic trapping potentials and evaporative cooling in doing so.

From a theoretical point of view, the study of these dilute BECs is attractive due to the weak interactions leading to a mean–field macroscopic order parameter characterising, to first order, the wavefunction of the many–body system. A nonlinear Schrödinger type equation known as the Gross–Pitaevskii equation will be introduced in the next chapter which describes the macroscopic order parameter.

1.2.1 Experimental realisation

In order to avoid a gas turning to solid at ultra–low temperatures, a gas can become long lived at these temperatures by making it extremely dilute. The densities required are around 10^{13} – 10^{15} particles per cm^3, much lower than commonly experienced (around 10^{19} particles per cm^3). Using these densities in the expression for the critical temperature for condensation (1.6) predicts temperatures of under 10^{-6}K. At such very low temperatures, scattering only occurs in the s-wave scattering channel (corresponding to the angular momentum $l = 0$) with the high energy scattering channels (p–wave, d–wave...) suppressed. The strength of scattering is determined by a characteristic parameter, a_s, known as the s–wave scattering length. Diluteness in a three dimensional system is given by

$$a_s^3 n \ll 1. \tag{1.10}$$

The very low temperatures required in order to form a BEC were impossible prior to the development of laser cooling and magnetic and optical trapping of atoms in the 1980's for which the 1997 Nobel Prize was awarded to Steven Chu, Claude Cohen Tannoudji and

William Phillips. It was first believed that spin–polarised hydrogen atoms would make the ideal candidate for BEC due to the weak interactions between atoms and prediction to remain in gaseous form right down to absolute zero [19]. The work in attempting to achieve BEC with this species proved instrumental in developing evaporative cooling, an important technique used in the final steps during the creation of any BEC. Mainly for the reasons which made spin–polarised hydrogen a good candidate for condensation, it was not possible to create BEC at this time. Reducing the temperature enough to realise BEC at experimentally workable densities with small scattering lengths was extremely difficult. Several experiments were then initiated with heavier alkali metals. They turned out to be more suitable for the realisation of BEC due to their weak s–wave scattering and due to the presence of only one outer–electron in the s–orbital, which makes them ideal for laser cooling and magnetic trapping.

It was not until 1995, some 70 years after BEC was first predicted, that the first experimental observation of a pure BEC was seen in a cloud of rubidium (^{87}Rb) atoms by a team of scientists at JILA at the University of Colorado led by Professors Carl Wieman and Eric Cornell [5]. This was soon followed with BEC realisation in sodium ^{23}Na by the group of W. Ketterle at the Massachusetts Institute of Technology (MIT) [6] and also in ^{7}Li by the group of R. G. Hulet [7, 8] at Rice University. The Nobel Prize was later awarded to Carl Wieman, Eric Cornell and Wolfgang Ketterle in 2001 for

the achievement of Bose-Einstein condensation in dilute gases of alkali atoms, and for early fundamental studies of the properties of the condensates [20].

However it was not until 1998 that experimental realisation of BEC in spin–polarised hydrogen atoms was achieved by the group of T. J. Greytak and D. Kleppner at MIT [21] due to complications, such as a tendency of the atoms to spin flip and form molecules.

In typical experiments, around 10^9 atoms are cooled to velocities corresponding to temperatures around 1K through a Zeeman slower: the atoms are slowed with laser beams in the opposite direction to the flow of the atoms. The atoms are slowed by the radiative force produced by the absorption of photons.

The vapour is then loaded into a Magneto–Optical Trap (MOT) and Doppler cooling is employed to cool the atoms further (μK temperatures) with the use of counter propagating lasers placed in each perpendicular direction: front and back, left and right, up and down. Here, if we take the laser to be 'red' detuned, i.e. the frequency is less than the atomic resonant frequency, then the atoms travelling in the opposite direction to a laser beam will lose momentum equal to that of the photon by absorbing the photon. The atom, now in an excited state, will spontaneously emit the photon in a random direction, increasing the atom's momentum in that given direction. However, this leads to a net decrease of momentum along the axis of the laser. This overall process of absorption/emission cools

the gas in all directions due to the six counter–propagating laser beams. Known as the Doppler limit, there is a lower attainable bound on the temperature of the gas through the use of MOTs; this occurs when heating created by the momentum gain through the emission of photons equals that of the cooling from photon absorption.

Through use of a technique known as Sisyphus cooling, it is possible to lower the temperature to a limit known as the recoil limit (1μK). As the atoms climb up the polarisation gradient, created by the counter–propagating orthogonally–polarised laser beams, they gain potential energy while losing kinetic energy. Once the atoms have reached the top of this potential gradient, they are optically pumped into a state with lower potential energy where the climb up the potential starts over. Each time the process is repeated, the atoms lose kinetic energy, lowering the temperature of the system.

The low temperatures achieved thus far with laser cooling are not enough to achieve Bose–Einstein condensation with typical densities, which are low in order to avoid loses due to three–body collisions. Often, the final step in the process is to use evaporative cooling to reduce the temperature of the system further. In this case, the walls of the trapping potential are lowered slowly enough so that high energy atoms escape from the trap and the remaining atoms re–thermalise to a new lower temperature. This essentially truncates the tails of the thermal distribution. Experimentally, by flipping the higher energy atoms they are no longer held by the trap and are expelled. To form a condensate, this process must be done slowly so that the density remains high enough to form a condensate without losing too many atoms from the trap. This process is continued until temperatures reach the order of nano–Kelvin: that is low enough for condensation, with Bose–Einstein condensates, in general, forming for temperatures $< 10^{-6}$K at densities 10^{-13}cm^{-3}.

In addition to the first experiments with ^{87}Rb [5], ^{23}Na [6] and ^{7}Li [7, 8] mentioned above, to date BEC has been achieved in many other atomic species such as ^{85}Rb [22], ^{41}K [23], ^{4}He [24], ^{174}Yb [25], ^{133}Cs [26], ^{52}Cr [27], ^{84}Sr [28, 29], ^{86}Sr [30], ^{88}Sr [31], ^{40}Ca [32], ^{164}Dy [33]. Figure 1.2 shows the velocity–distribution of a gas of expanding rubidium atoms illustrating the discovery of BEC [20].

A period of rapid growth in ultra–cold atomic physics followed the first experimental realisations of BEC. Due to this unprecedented experimental control, trapped quantum gases provide the means to study many–body quantum physics. The weak interactions between the atoms make experimental realisations a useful test–bed for direct comparison between quantum theory and experiment.

Experimental advances have led to exotic trapping potentials allowing for a wealth of geometries to be created with BECs. Firstly, by increasing the trap frequency in one direction, it is possible to create a disk shaped condensate which is effectively 2D. The dynamics are frozen out in one direction once the temperature and chemical potential are

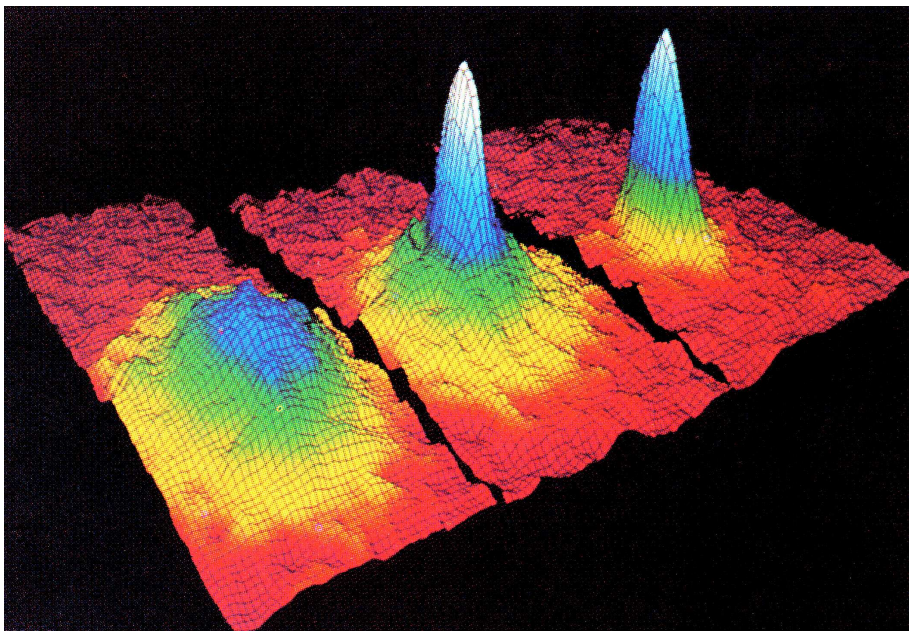

Figure 1.2: Velocity-distribution of a gas of expanding rubidium atoms at three different temperatures ($T > T_c$, $T \approx T_c$ and $T < T_c$), confirming the discovery of BEC. The figure shows three–dimensional snapshots. From left to right the atoms condense from less dense red, yellow and green areas to very dense blue and white areas. Figure from Reference [20].

small relative to the energy of the trap in this direction. For example, such a geometry is useful in the context of studying quantum vortices, tiny whirlpools which are supported in BECs. These will stay relatively straight in this 2D trap and is therefore regularly used in vortex dynamics experiments [34, 35]. By increasing the trap frequency in a second direction (quasi–1D trap), the system becomes effectively 1D as all but one direction has its dynamics frozen. In sufficiently elongated geometries, microscopic excitations known as solitons are stable. As solitons are of relevance to this thesis, these are introduced in more detail later on. Other realisable trapping geometries are ring (toroidal) traps where persistent flow in a BEC has been observed [36, 37, 38, 39, 40], optical lattices [36, 41, 42] which are potential candidates for quantum computing [43] and are used to probe the superfluid to Mott insulator transition [44], double–well geometries [45] in order to study Josephson oscillations [46] and more recently uniform potentials [47] in order to ease the difference between experimental realisation and "conventional" study of spatially uniform many–body systems.

In this thesis, the study of two interacting BECs is performed in great detail. These systems will now be introduced through an overview of important previous work that has been done both theoretically and experimentally.

1.2.2 Theoretical Modelling

At temperatures very close to absolute zero such that $T \ll T_c$ a nonlinear Schrödinger–type equation, known as the Gross–Pitaevskii equation (reviewed in the following Chapter), is a very good description of BEC stationary solutions and dynamics such as dynamics under expansion, shape oscillations, sound, interface effects (see [48] for review), dark solitary waves [49, 50, 51, 52], bright solitary waves [53, 54, 55, 56, 57, 58] and vortices [59, 60, 61].

Many theoretical approaches exist for finite temperature modelling where the condensate mode coexists with occupied excited modes, known as the thermal cloud. The thermal cloud should be taken into consideration as should its interactions with the condensate. The models typically employed to describe such systems can be split into two main categories, depending on whether the thermal cloud is considered as static or dynamical (in different levels of approximation). In the following Chapter, a number of the theories used to describe the condensate, the thermal cloud and interactions between these are reviewed.

1.3 Condensate Mixtures

1.3.1 Experimental Studies

Experimental and theoretical work has advanced greatly since the first experimental realisation of a two–component BEC, or mixture, with two different hyperfine spin states of ^{87}Rb [62]. These first overlapping condensates were created through sympathetic cooling of one hyperfine state in contact with the other evaporatively cooled state. Mixtures have been produced using two different hyperfine spin states of a single isotope [62, 63, 64, 65, 66, 67, 68, 69, 70, 71, 72], different isotopes of the same atomic species [73] and different atomic species [74, 75, 76, 77]. A key feature of these systems is that they exhibit miscible and immiscible behaviour depending on the strength of the inter–species interactions. Miscibility, where the interactions favour an overlap between the two species, has been observed [73, 76] as well as immiscibility, where repulsion between the species favours their spatial separation [63, 70, 73, 77].

1.3.2 Theoretical Studies

Stationary Solutions

Since the first experimental realisation of a two–component BEC, many static and dynamical properties have been studied numerically and analytically in harmonic trapping potentials. Ground state density profiles, where the obtained results correspond to the lowest energy for the system, were first investigated by Ho and Shenoy in 1996 [78] (This was done in the context of the Thomas–Fermi (TF) approximation, which gives an approximate analytical description of a condensate in a harmonic trap and shall be reviewed

in the following Chapter). Due to the co–centred traps considered, a range of symmetric miscible and immiscible structures were accessed by varying interaction strengths and particle numbers. These results were confirmed when two hyperfine states of the same atom (equal masses) were considered [79] and for different atomic species (nonequal masses) [80]. The latter case was also the first to consider non co–centred trapping potentials and the arising asymmetric ground state structures. All possible classes of stationary solutions have been found within the Thomas–Fermi approximation in idealised one–dimensional systems [81]. In addition, in one dimension (1D), coexisting or segregated phases with strong interactions were exhibited depending on parameters [82]. The boundary between inter-penetrating BECs has been studied in great detail [83]. Metastable states, which do *not* correspond to the lowest energy for the system, have been obtained numerically [84]. Under external perturbation, there can be a macroscopic transition from metastable states to the true ground state in symmetric trapping potentials. When immiscible condensates are considered (phase–separated regime), studies on binary BECs revealed two distinct steady state solutions [85]. The first, for weakly segregated condensates where each density profile does not take on the symmetric profile of the trap due to surface tension however the sum of both profiles do. The second, for strongly segregated condensates where the total density profile takes a different symmetry than that of the trap. Using Monte–Carlo simulations, Reference [86] found additional steady state solutions with broken symmetry. The transition from symmetric to asymmetric ground states has been investigated [87, 88, 89]. Spontaneous symmetry breaking has been observed where one species has attractive self–interactions [90]. In addition, the ground state geometry can undergo a smooth transition from planar to ellipsoidal to cylindrical geometry for phase separated condensates [91]. Finally, the ground states for rotating two–component BECs have been classified [92, 93].

Experimentally obtained steady state solutions can be skewed by gravity when considering different atomic species due to one component being affected more than the other. This gravitational sag has been included in a few models. Ground state density profiles in time averaged orbiting potentials, where gravity separates the centres of the two species, have been numerically calculated [94, 95]. By tilting the eigenaxes of the trapping potential, non–trivial gravitational sag is included and symmetric and asymmetric ground state density profiles emerge [96].

Stability

The range for stability in a two–component system was first predicted for a sodium–rubidium mixture in a harmonic trap [97]. By finding the symmetric steady–state solutions with different parameter regimes, the stability of these solutions has been investigated when disturbed by an external force [98]. Similarly to a one species condensate, when

attractive interactions are present, a system collapse has been observed [99, 100]. With rotational symmetry, the Rayleigh–Taylor instability at the interface of the condensates breaks the symmetry of the condensate interface when interaction strengths or harmonic trap frequency is changed [101].

Dynamics at $T = 0$

Many dynamical features of condensate mixtures have been looked at theoretically. Modulation instability is a phenomenon in which weak spatial perturbations grow exponentially into a train of localised waves and have been simulated for two colliding BECs [102, 103] or by transferring half of the particles in a single species condensate into a different hyperfine state [104, 105] following the experimental procedure at MIT [72]. Modulation instabilities have also been studied in 1D [106] and quasi–1D [107] geometries. Dark–bright solitons [108] have been studied in binary mixtures where the second component fills in the gap left by the phase slip: these dynamical features are of relevance to this thesis and shall be introduced in more detail later on. Vortices have also been extensively studied in multicomponent condensates [67, 109, 110, 111, 112, 113, 114, 115, 116, 117, 118].

Finite Temperature Models

In 1998, finite temperature theory where interactions with non–condensed atoms are considered (see [119] for review) was applied to two–component condensates when Hartree–Fock models involving the collision of one condensate and one thermal atom were simulated numerically [120, 121, 122, 123]. The steady states obtained can admit both symmetric and asymmetric solutions. This was later expanded to the so–called Popov approximation [124], allowing for studies at high temperatures [125]. Asymmetric density profiles have been studied from Monte–Carlo simulations at low–temperatures [126]. Investigation into the stability conditions for thermodynamic states were conducted [127]. Finally, modulation instabilities with the inclusion of an additional growth term have been studied [128].

Non–Harmonic Trapping Potentials

Other trapping potentials have been considered with condensate mixtures. BECs in a double well magnetic trap have been used to study the tunnelling between each well [129]. Two–component systems have also been examined in optical lattices [130], where the potential has spatially periodic wells, and more recently in ring potentials where the fragility of the system was found to depend on the speed of persistent currents [131].

Other Quantum Gas Mixtures

Spinor condensates, which have at least three components with internal spin degrees of freedom, are also generating much current interest (see [132] for a review).

Other varieties of ultracold atomic mixtures have been seen. These include Bose–Fermi mixtures (studied experimentally [133, 134, 135, 136, 137] and theoretically [138, 139, 140, 141, 142, 143, 144, 145, 146, 147]).

1.4 Macroscopic Excitations — Solitons

There has been great interest in nonlinear properties of BECs [148] since their first experimental realisation. These include the manifestation of solitons in one and multiple component systems, for which we will now give a detailed introduction.

1.4.1 Dark Solitons

A dark soliton is a stationary or propagating localised excitation which features a phase slip in the ambient density and forms a density dip [149] (see Figure 1.3). Dark solitons are supported for repulsive interactions [150]. First created in 1987 in nonlinear optics [151], dark solitary waves have been created in atomic BECs in a controlled manner [49, 51, 152, 153, 154, 155] or through dynamical processes [156, 157, 158, 159] and are a topic of intense research [160].

In [49, 51, 152, 153, 154, 155], phase imprinting was used by implementing a homogeneous potential, generated by a far detuned laser beam, which is applied to half of the condensate for a given time such that the wave function acquires an additional phase factor. Changes to the density cause no significant perturbation leading to the formation of a dark soliton [49, 152, 153]. Through use of this method, collisions of counter–propagating dark solitons in atomic BECs were investigated verifying the concept of non-destructive transmission, in agreement with numerical simulations [155]. In another experiment, a pair of matter wave dark solitons was generated by merging two condensates initially prepared in a double well potential [154]. Finally, dark solitons have been generated through two–component BECs where the soliton exists in one component and is initially filled with the second component. The second component is then selectively removed [51].

Various techniques have been used to create dark solitons through dynamical processes. Firstly, via a slow light technique, a disk shaped region of atoms was suddenly removed from the condensate generating counter propagating dark solitons [156]. In Reference [157] dark solitons emerged when a barrier, formed by a beam, swept through the condensate at intermediate speeds. For slow speeds, the fluid flow was steady while at fast speeds soliton formation ceased and the absence of excitations was surprisingly once again observed.

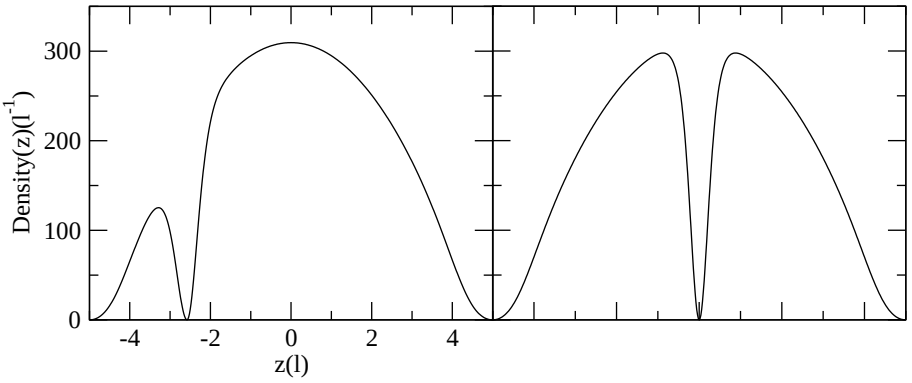

Figure 1.3: Densities of condensate containing a single dark soliton with π phase slip at $z(l) = 3.5$ (left) and $z(l) = 0.0$ (right) in 1D harmonic trapping potential.

For two of these experiments, the dark solitary wave decayed into vortex rings due to their inherent instability to transverse excitations [51, 156].

1.4.2 Dark–Bright Solitons

Existing only in binary mixtures of BECs with strong repulsive interspecies interactions such that the condensates are immiscible, the bright soliton exists here due to the coupling with the dark soliton: the density dip left by the dark soliton in one component is filled in with the bright soliton in the other component (see Figure 1.4). These macroscopic excitations have recently been achieved experimentally using two different hyperfine states of ^{87}Rb through counter flowing BECs [161, 162, 163] or a phase imprinting method [164].

Dark–bright solitons have also been studied analytically and numerically at zero–temperature [106, 108, 165, 166, 167, 168, 169, 170, 171, 172, 173, 174, 175, 176]. Recently, work has been done on the non–ideal case of finite temperature for solitons in mixtures [177].

1.5 Quantum Turbulence

Turbulence is a complex dynamical process that has been studied in many fields for centuries. While eddies form the base for turbulence in a classical fluid, quantised vortices are the topological defects appearing in BECs. Quantisation of circulation means that the rotational motion is constrained to discrete vortices that all have the same core size. See References [178, 179] for recent reviews on quantum turbulence in both superfluids and atomic BECs. Relevant to this Thesis, here we introduce some of the recent developments on quantum turbulence in two component systems. Quantum turbulence in binary mixtures was first generated numerically through couterflow instabilities [180], the

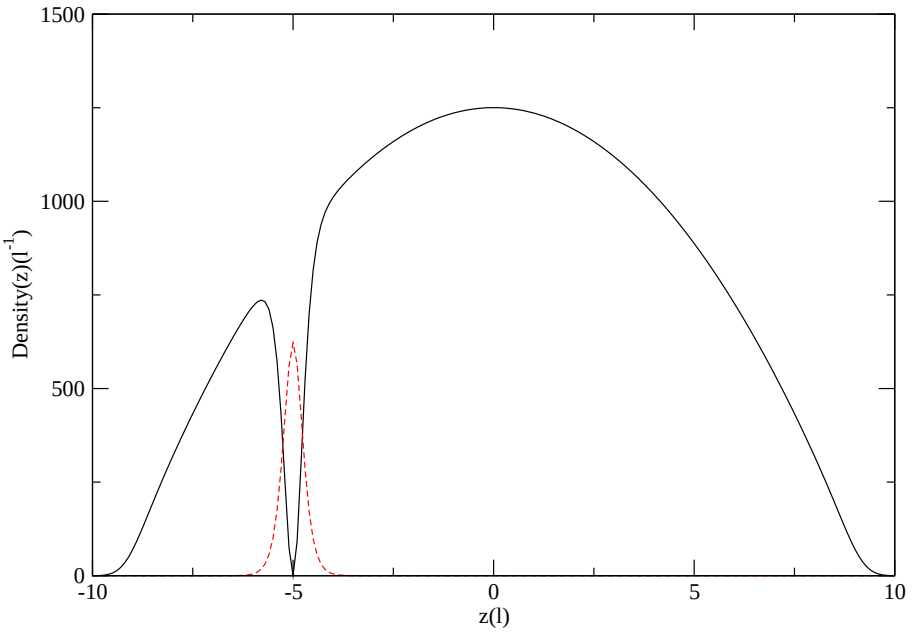

Figure 1.4: Densities of condensates containing a single dark–bright soliton with π phase slip in first component at $z(l) = 5.0$ in 1D harmonic trapping potential. Solid black curve — component 1; Dashed red curve — component 2.

two miscible BECs were counter propagated and quantised vortices are nucleated. Reference [181] generated quantum turbulence through the Rayleigh–Taylor instability in immiscible condensates in harmonic trapping potentials. Other work has been carried out for spinor condensates [182, 183, 184].

1.6 Thesis Outline

We wish to give a brief outline of this Thesis and highlight collaborative work, also noted in relevant chapters. Divided into three main parts, the first part of this Thesis introduces the notions used to generate results in Parts II and III.

Part I – Introduction to Bose Gases

We begin, in Chapter 2, by providing the theoretical concepts required in order to understand numerical models used in this thesis. We start, from the second order Hamiltonian, by reviewing the Gross–Pitaevskii equation (GPE), a Schrödinger like equation widely used in describing condensates at zero temperature. The GPE is then generalised into coupled equations, one for each component considered in a mixture, where an additional term is present taking into account interspecies interactions. Finally, we introduce different theories used in describing condensate interaction with the thermal cloud, which can

play an important role in analysing experimental results.

Part II – Bose–Einstein Condensate Mixtures in Harmonic Trapping Potentials

After showing our numerical procedure matches previously obtained numerical ground state solutions of the coupled Gross–Pitaevskii equations [80], in Chapter 3 we qualitatively reproduce the density profiles observed in a recent ^{87}Rb–^{133}Cs experiment [77]. To achieve these results we take into account asymmetries in the harmonic trapping potentials via additional linear potentials before imaginary time propagation (see Appendix B). The work presented in this Chapter is an expansion of previously published work:

- *Equilibrium solutions for immiscible two-species Bose-Einstein condensates in perturbed harmonic traps*,
  R. W. Pattinson, T. P. Billam, S. A. Gardiner, D. J. McCarron, H. W. Cho, S. L. Cornish, N. G. Parker, and N. P. Proukakis,
  Phys. Rev. A 87, 013625 (2013).

In Chapter 4, we expand on our studies investigated in Chapter 3 on condensate mixtures to include growth dynamics while using the same experimental parameters. We briefly discuss results obtained by our collaborators I. K. Liu *et al.* (Department of Physics, National Changhua University of Education, Changhua 50058, Taiwan) with the coupled Stochastic Projected Gross–Pitaevskii equations to motivate our work on dark–bright solitons in mixtures when condensate growth is considered. The work presented in this Chapter is partially an expansion of previously submitted work:

- *A Phenomenological Model of the Growth of Two–Species Atomic Bose–Einstein Condensates*,
  R. W. Pattinson, N. G. Parker, and N. P. Proukakis,
  J. Phys.: Conf. Ser. 497 012029 (2014).

with results also to appear in a report comparing the simple dissipative model to the more accurate coupled Stochastic Projected Gross–Pitaevskii equations modelled by our collaborators.

Part III – Classical Field Methods for Non Trapped Bose Gases

In Chapter 5 we switch gears slightly and focus on non trapped gases via the classical fields method. We outline the numerical procedure for solving a system with highly nonequilibrium initial conditions. Firstly, the evolution of a single component system is examined. Similar simulations with two components, either coexisting in the same spatial domain or phase segregated, are then studied. These two components are either both nonequilibrated or obtained by splitting the particles of a thermally equilibrated single component state.

We then investigate the effects of suddenly quenching the intercomponent interactions. This work was undertaken thanks to the help of A. J. Youd.
In Chapter 6 we briefly review the main findings of this Thesis and discuss opportunities for follow on work.

Chapter 2

Theoretical Framework

At zero–temperature, where the lowest energy level is macroscopically occupied and when the gas is dilute enough such that particle interactions are weak, a common model to describe Bose–Einstein condensates is a nonlinear Schödinger equation (NLSE) known as the Gross–Pitaevskii equation (GPE). In order to describe condensate mixtures, this model can be trivially generalised to two coupled Gross–Pitaevskii equations (CGPEs). The GPE model has proven to be a good description for many static and dynamical properties both for single condensate systems [18] and for condensate mixtures [164], even though thermal contributions and quantum fluctuations are not taken into account. The CGPEs form the basis for the numerical results presented in Part II of this thesis. In this chapter, we introduce the GPE and its solutions followed by a 'generalisation' of these for the CGPE.

To improve on the theoretical description, finite temperature effects can be added using a range of different models. Such models are reviewed in the latter part of this Chapter, with some emphasis on classical field methods which are then used in Part III of this Thesis to simulate non trapped homogeneous finite temperature condensate mixtures.

2.1 Gross–Pitaevskii Equation: Origin and Explanation

A system formed from N interacting bosons can be described by an N–body wavefunction $\Psi\left(\mathbf{r}_1,..,\mathbf{r}_N,t\right)$ where $\mathbf{r}_i$ is the position of atom i. This wavefunction obeys the well known Schrödinger equation

$$i\hbar\frac{\partial\Psi}{\partial t}=\left[-\frac{\hbar^2}{2m}\left(\nabla_1^2+\nabla_2^2+...+\nabla_N^2\right)+V\left(x_1,x_2,...,x_N\right)\right]\Psi. \tag{2.1}$$

where ∇_i is the derivative with respect to $\mathbf{r}_i$. For a system of many particles, it is impractical to find a direct solution for the many–body wavefunction. The N–body wavefunction is reduced into a more manageable form through use of a map into an occupation num-

ber basis set. The system Hamiltonian can be written in terms of Bose field operators $\hat{\Psi}(\mathbf{r},t)$ $\left(\hat{\Psi}^{\dagger}(\mathbf{r},t)\right)$ for annihilation (creation) of a particle at position $\mathbf{r}$ and time t as

$$\begin{aligned}\hat{\mathrm{H}} = &\int \mathrm{d}\mathbf{r}\hat{\Psi}^{\dagger}(\mathbf{r},t)\left[-\frac{\hbar^2}{2m}\nabla^2 + V_{ext}(\mathbf{r},t)\right]\hat{\Psi}(\mathbf{r},t) \\ &+ \frac{1}{2}\int\int \mathrm{d}\mathbf{r}\mathrm{d}\mathbf{r}'\hat{\Psi}^{\dagger}(\mathbf{r},t)\,\hat{\Psi}^{\dagger}(\mathbf{r}',t)\,V(\mathbf{r}-\mathbf{r}')\,\hat{\Psi}(\mathbf{r}',t)\,\hat{\Psi}(\mathbf{r},t)\end{aligned} \tag{2.2}$$

where $V(\mathbf{r}-\mathbf{r}')$ is the two–body interatomic potential and $V_{ext}(\mathbf{r},t)$ the external potential. The Bose field operators obey the following commutation relations

$$\begin{aligned}&\left[\hat{\Psi}(\mathbf{r},t),\hat{\Psi}^{\dagger}(\mathbf{r}',t)\right] = \delta(\mathbf{r}-\mathbf{r}'), \\ &\left[\hat{\Psi}^{\dagger}(\mathbf{r},t),\hat{\Psi}^{\dagger}(\mathbf{r}',t)\right] = \left[\hat{\Psi}(\mathbf{r},t),\hat{\Psi}(\mathbf{r}',t)\right] = 0.\end{aligned} \tag{2.3}$$

In a sufficiently dilute gas, the interatomic potential can be approximated by an effective contact potential due to low–energy, s–wave collisions such that [119]

$$V(\mathbf{r}-\mathbf{r}') = g\delta(\mathbf{r}-\mathbf{r}'), \tag{2.4}$$

and the effective interaction strength is defined by

$$g = \frac{4\pi\hbar^2 a}{m}, \tag{2.5}$$

where a is the s–wave scattering length. It is important to note that for $g > 0$ the effective interactions are repulsive while for $g < 0$ interactions are effectively attractive. The second quantised Hamiltonian (2.2) evolves according to the Heisenberg equation of motion

$$\mathrm{i}\hbar\frac{\partial\hat{\Psi}(\mathbf{r},t)}{\partial t} = \left[\hat{\Psi}(\mathbf{r},t),\hat{H}\right]. \tag{2.6}$$

Thus, by substituting (2.2) into (2.6), we obtain

$$\mathrm{i}\hbar\frac{\partial\hat{\Psi}(\mathbf{r},t)}{\partial t} = \left[-\frac{\hbar^2}{2m}\nabla^2 + V_{ext}(\mathbf{r},t)\right]\hat{\Psi}(\mathbf{r},t) + g\hat{\Psi}^{\dagger}(\mathbf{r},t)\,\hat{\Psi}(\mathbf{r},t)\,\hat{\Psi}(\mathbf{r},t). \tag{2.7}$$

We can separate the Bose field operator into two parts via

$$\hat{\Psi}(\mathbf{r},t) = \hat{\phi}(\mathbf{r},t) + \hat{\psi}(\mathbf{r},t), \tag{2.8}$$

where $\hat{\phi}(\mathbf{r},t)$ and $\hat{\psi}(\mathbf{r},t)$ correspond to a field operator for the condensate and the non–condensate respectively. Under the symmetry breaking assumption, the operator $\hat{\phi}(\mathbf{r},t)$ is replaced by $\phi(\mathbf{r},t)$, known as the condensate wavefunction, whereby all field operator

dependence is in $\hat{\psi}(\mathbf{r},t)$. This leads to the total number of condensed atoms not being conserved. However, it can be assumed that the addition or removal of an atom does not affect the state of the system, $N \pm 1 \simeq N$ for a condensate containing a large number of atoms. We are, in essence, decomposing the bosonic field operator in terms of a macroscopically populated mean field term defined as the ensemble average $\phi(\mathbf{r},t) = \langle\hat{\Psi}(\mathbf{r},t)\rangle$ and a fluctuation term $\hat{\psi}(\mathbf{r},t)$. We can approximate the atom density into two contributions $n(\mathbf{r},t) = \langle\hat{\Psi}^{\dagger}(\mathbf{r},t)\,\hat{\Psi}(\mathbf{r},t)\rangle = n_c(\mathbf{r},t) + n_t(\mathbf{r},t)$ through use of Equation (2.8). These are a condensate density $n_c(\mathbf{r},t) = |\phi(\mathbf{r},t)|^2$ and a non–condensate density $n_t(\mathbf{r},t) = \langle\hat{\psi}^{\dagger}(\mathbf{r},t)\,\hat{\psi}(\mathbf{r},t)\rangle$. It is thus common to identify $n_t(\mathbf{r},t)$ as the density of the thermal atoms and $\hat{\psi}(\mathbf{r},t)$ as the operator for the thermal cloud.

In the limit of zero–temperature, we assume the thermal depletion of the system is negligible. In addition, in weakly interacting systems ($a \ll \lambda_{\mathrm{dB}}$) quantum fluctuations may not play a large role and we can therefore neglect thermal contributions such that $\hat{\psi}(\mathbf{r},t) = 0$. Hence we set $\hat{\Psi}(\mathbf{r},t) = \phi(\mathbf{r},t)$. The Heisenberg equation of motion (2.7) reduces to

$$\mathrm{i}\hbar\frac{\partial\phi(\mathbf{r},t)}{\partial t} = \left[-\frac{\hbar^2}{2m}\nabla^2 + V_{ext}(\mathbf{r},t) + g\,|\phi(\mathbf{r},t)|^2\right]\phi(\mathbf{r},t)\,. \tag{2.9}$$

This is the Gross–Pitaevskii Equation (GPE). Introduced independently by Gross [185, 186, 187] and Pitaevskii [188, 189] in the early 1960's to study vortex lines in an imperfect Bose gas, the GPE [48] is of the form of a time–dependent Schrödinger equation with the addition of a nonlinear term $g\,|\phi(\mathbf{r},t)|^2\,\phi(\mathbf{r},t)$ arising from atomic interactions. The wavefunction is normalised to the total number of particles

$$N = \int |\phi|^2\,\mathrm{d}\mathbf{r}. \tag{2.10}$$

For $T \ll T_c$ where T_c is the critical temperature for condensation, the GPE is a good description of many features of BEC dynamics such as dynamics under expansion, shape oscillations, sound, interface effects (see [48] for review), dark solitary waves [49, 50, 51, 52], bright solitary waves [53, 54, 55, 56, 57, 58] and vortices [59, 60, 61].

2.2 Time–Independent Solutions

Stationary states can be found by eliminating the time dependence in the GPE through the substitution

$$\phi(\mathbf{r},t) = \phi_0(\mathbf{r})\,e^{-\mathrm{i}\mu t/\hbar}, \tag{2.11}$$

where μ is the chemical potential of the system, characterising the energy required to remove an atom from the system. From Equation (2.9), the resulting time–independent

equation is

$$\mu\phi_0(\mathbf{r}) = \left[-\frac{\hbar^2}{2m}\nabla^2 + V_{ext}(\mathbf{r}) + g\left|\phi_0(\mathbf{r})\right|^2\right]\phi_0(\mathbf{r}). \tag{2.12}$$

This can also be found by minimising, at fixed μ, the quantity $E-\mu N$ [18] where E is the energy functional of the system

$$E(\phi) = \int \mathrm{d}\mathbf{r}\left[\frac{\hbar^2}{2m}\left|\nabla\phi(\mathbf{r})\right|^2 + V_{ext}(\mathbf{r})\left|\phi(\mathbf{r})\right|^2 + \frac{1}{2}g\left|\phi(\mathbf{r})\right|^4\right], \tag{2.13}$$

and N the fixed total number of particles

$$N = \int \mathrm{d}\mathbf{r}\left|\phi(\mathbf{r})\right|^2. \tag{2.14}$$

2.3 Ground State Solutions in Harmonic Traps

In Figure 2.1, we show the time–independent solutions for attractive, repulsive and non interacting condensates in a harmonic trapping potential in three dimensions. In the case of a non–interacting condensate ($g = 0$), the ground state has a Gaussian density profile. For an anisotropic trapping potential (nonequal trapping frequencies) the ground state wavefunction is [18]

$$\phi_0(\mathbf{r}) = \frac{\sqrt{N}}{\pi^{3/4}\left(l_x l_y l_z\right)^{1/2}} e^{-x^2/2l_x^2} e^{-y^2/2l_y^2} e^{-z^2/2l_z^2}, \tag{2.15}$$

where the widths l_i $(i = x, y, z)$ of the wavefunction in each direction are given by

$$l_i = \sqrt{\frac{\hbar}{m\omega_i}}. \tag{2.16}$$

For effectively attractive interactions ($g < 0$), the ground state solution is narrower and taller in comparison to the Gaussian solution for an ideal Bose gas. For repulsive interactions ($g > 0$), the ground state density profile has an increased width and lower maximum, approaching the form of an inverse parabola. Here, we introduce the interaction parameter

$$\chi = \frac{Na_s}{l}, \tag{2.17}$$

where l is the harmonic oscillator length in an isotropic system ($l = l_x = l_y = l_z$). χ is a measure of the effects of the interactions on the system. For small $\chi(\ll 1)$, we are in the weakly interacting regime, close to the ideal Bose gas limit $\chi = 0$. When $\chi \gg 1$, we are in the strongly interacting regime. In this latter regime, the Thomas–Fermi (TF) limit is a well known approximation for the ground state of the system and shall be introduced in

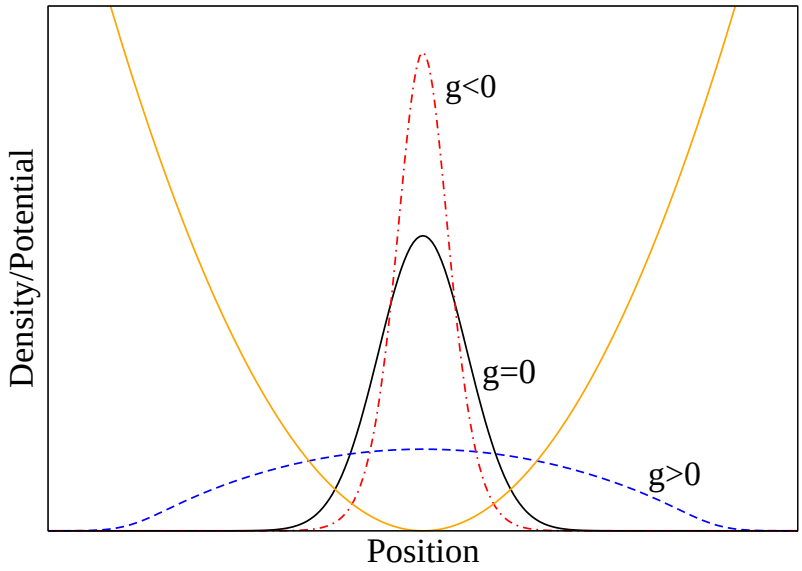

Figure 2.1: Schematic of ground state density profiles with repulsive interactions (blue, dash), non–interacting (black, solid), and attractive interactions (red, dash–dot) of the GPE for a harmonic potential (orange). The wavefunctions are normalised to the same number of atoms i.e. equal in all three cases.

the following subsection.

2.3.1 Thomas–Fermi Limit

In a harmonic trapping potential, the simplest solution to Equation (2.12) is obtained by ignoring the kinetic energy term. This is a good approximation everywhere except the trap edges provided we are in the limit of large N with large repulsive interactions ($g > 0$) such that the $g\left|\phi\left(\mathbf{r}\right)\right|^2\phi\left(\mathbf{r}\right)$ term dominates [190] and $\chi \gg 1$. In this limit, the ground state solution is approximated by

$$\phi\left(\mathbf{r}\right) = \begin{cases} \sqrt{\mu - V_{ext}\left(\mathbf{r}\right)/g}, & \text{if } \mu \geq V_{ext}\left(\mathbf{r}\right) \\ 0, & \text{otherwise} \end{cases} \tag{2.18}$$

which is known as the Thomas–Fermi (TF) solution for a condensate in a harmonic trapping potential

$$V_{ext}\left(\mathbf{r}\right) = \frac{1}{2}m\left(\omega_x^2x^2 + \omega_y^2y^2 + \omega_z^2z^2\right), \tag{2.19}$$

where $\omega_x, \omega_y, \omega_z$ are the trapping frequencies. The TF radius is given by

$$R_i = \sqrt{\frac{2\mu}{m\omega_i^2}},\ i = x, y, z \tag{2.20}$$

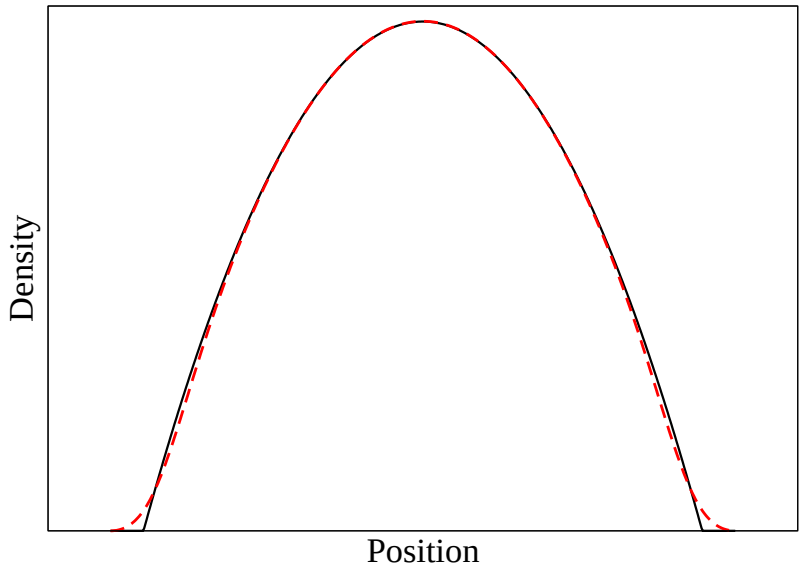

Figure 2.2: Schematic of Thomas–Fermi approximation (black, solid) and the ground state density profile obtained numerically (red, dashed).

which characterises the spatial extent of the condensate. In this regime, the condensate density distribution takes the shape of an inverted parabola but the approximation fails close to the condensate edge $r \simeq R_i$ where it abruptly vanishes rather than diminishing gradually in comparison to the exact numerical solution (shown in Figure 2.2). This is due to the kinetic energy contribution being significant at the condensate edge. As χ increases, this discrepancy at the edge decreases.

2.4 Solutions in a Homogeneous System

For a homogeneous condensate ($V_{ext} = 0$), the time–independent GPE becomes

$$-\frac{\hbar^2}{2m}\nabla^2\phi\left(\mathbf{r}\right) + g\left|\phi\left(\mathbf{r}\right)\right|^2\phi\left(\mathbf{r}\right) = \mu\phi\left(\mathbf{r}\right). \tag{2.21}$$

Initially we assume that (over the biggest spatial extent) the effect of the kinetic energy contribution $\nabla^2\phi\left(\mathbf{r}\right)$ can be neglected to first approximation due to the behaviour of the fluid being dominated by interactions. If $g > 0$, this becomes

$$g\left|\phi\left(\mathbf{r}\right)\right|^2\phi\left(\mathbf{r}\right) = \mu\phi\left(\mathbf{r}\right) \rightarrow g\left|\phi\left(\mathbf{r}\right)\right|^2 = \mu. \tag{2.22}$$

Remembering that the condensate density is given by $n_c = \left|\phi\left(\mathbf{r}\right)\right|^2$, we find

$$n_c = \frac{\mu}{g} = \text{constant}. \tag{2.23}$$

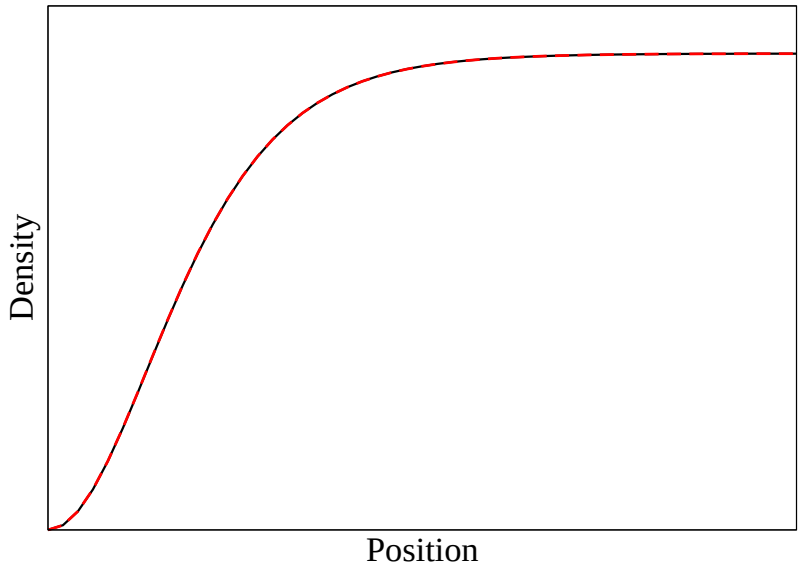

Figure 2.3: Healing at hard wall given by Equation (2.26) (black, solid) and the ground state density profile obtained numerically (red, dashed).

The characteristic lengthscale ξ corresponds to the spatial region needed by the condensate to reach its equilibrium far from perturbations and is obtained by balancing the kinetic energy term and the interaction term in Equation (2.21). We replace $\nabla^2\phi(\mathbf{r})$ by $2\phi(\mathbf{r})/\xi^2$ where the spatial scale of variations is denoted by ξ, obtaining

$$\frac{\hbar^2}{m}\frac{1}{\xi^2} = g\left|\phi(\mathbf{r})\right|^2 = gn_c(\mathbf{r}). \tag{2.24}$$

Hence the healing length, for repulsive interaction ($g > 0$), is given by

$$\xi = \frac{\hbar}{\sqrt{mgn_c}}. \tag{2.25}$$

In the presence of a hard–wall boundary, the fluid density is pinned to zero. Taking the boundary at $x = 0$, the solution in the x–direction is given by

$$\phi(x) = \sqrt{n_c}\tanh\left(\frac{x}{\xi}\right). \tag{2.26}$$

In Figure 2.3, we show the healing at a hard wall given by the solution (2.26) and compare to the exact solution obtained numerically. These match up perfectly.

In the case of the non–interacting ($g = 0$) ideal Bose gas, the GPE reduces to the Schrödinger equation. However for attractive interactions ($g < 0$), the condensate is no longer stable in a homogeneous system.

2.5 Hydrodynamic Equations

The wavefunction of the system $\phi(\mathbf{r},t)$ is a complex function and can be expanded in terms of amplitude $\sqrt{n_c}$ and phase $\theta(\mathbf{r},t)$ variables through the Madelung transformation [191]

$$\phi(\mathbf{r},t) = \sqrt{n_c(\mathbf{r},t)}e^{\mathrm{i}\theta(\mathbf{r},t)}, \tag{2.27}$$

where $n_c(\mathbf{r},t) = |\phi(\mathbf{r},t)|^2$ represents the density of the system. By plugging this into the GPE (2.9), it can be shown that the imaginary terms lead to a conservation of mass equation

$$\frac{\partial n_c}{\partial t} + \nabla \cdot (n_c \mathbf{v}) = 0 \tag{2.28}$$

where the superfluid velocity is defined by its phase

$$\mathbf{v} = \frac{\hbar}{m}\nabla\theta. \tag{2.29}$$

Similarly, equating the real terms with this substitution gives Euler's equation

$$\left(\frac{\partial}{\partial t} + \mathbf{v}.\nabla\right)\mathbf{v} = -\frac{1}{n_c}\nabla P + \mathbf{F}, \tag{2.30}$$

with the addition of a quantum pressure term [192]

$$P = \frac{1}{2}gn_c^2 - \frac{1}{4}n_c\nabla^2(\ln n_c). \tag{2.31}$$

The force term $\mathbf{F} = -\nabla V$ arises in the case of trapped gases from the harmonic confining potential.

2.6 Quantisation of Circulation

The Madelung transformation defines the superfluid velocity as the gradient of the phase (see Equation (2.29)). Circulation is defined by

$$\kappa = \oint \mathbf{v} \cdot \mathrm{d}\mathbf{r}. \tag{2.32}$$

Using Equation (2.29) we can write

$$\kappa = \frac{\hbar}{m}\Delta\theta \tag{2.33}$$

where $\Delta\theta$ is the change of phase around a vortex. In order for the wavefunction to remain single valued the change of phase around a vortex must be an integer multiple of 2π. The

circulation must be in integer value of $2\pi\hbar/m$

$$\kappa = l\frac{2\pi\hbar}{m} \tag{2.34}$$

where $l = 0, \pm1, \pm2$,... When the phase winds round in an anticlockwise direction, the vortex is negatively charged while when it winds in a clockwise direction, it is positively charged. Onsager [193] was the first to propose a description for quantisation of circulation. Feynman independently proposed quantised vortex lines [194].

2.7 Harmonic Oscillator Units

For a harmonic trapping potential (2.19), the most commonly used scalings to make the GPE (2.9) dimensionless are harmonic oscillator units. Length is expressed in units of the non–interacting harmonic oscillator length $l = \sqrt{\hbar/m\bar{\omega}}$, energy in terms of harmonic oscillator energy $\hbar\bar{\omega}$ and time in terms of $\bar{\omega}^{-1}$ where $\bar{\omega} = (\omega_x\omega_y\omega_z)^{1/3}$, such that

$$\tilde{t} = t\bar{\omega},\ \tilde{x} = \frac{x}{l},\ \tilde{y} = \frac{y}{l},\ \tilde{z} = \frac{z}{l} \text{ and } \tilde{E} = \frac{E}{\hbar\bar{\omega}}, \tag{2.35}$$

where the tilde denotes the dimensionless quantity. In order to conserve the number of particles in the system, we require

$$N = \int |\phi|^2 \,\mathrm{d}\mathbf{r} = \int |\phi|^2 \, l^3 \mathrm{d}\tilde{\mathbf{r}} == \int \left|\tilde{\phi}\right|^2 \mathrm{d}\tilde{\mathbf{r}}. \tag{2.36}$$

Hence

$$\tilde{\phi}\left(\tilde{\mathbf{r}}, t\right) = \phi\left(\mathbf{r}, t\right) l^{3/2}. \tag{2.37}$$

The GPE becomes

$$\mathrm{i}\frac{\partial\tilde{\phi}\left(\tilde{\mathbf{r}}, \tilde{t}\right)}{\partial\tilde{t}} = \left[-\frac{1}{2}\tilde{\nabla}^2 + \tilde{V}_{ext}\left(\tilde{\mathbf{r}}\right) + \tilde{g}\left|\tilde{\phi}\left(\tilde{\mathbf{r}}, \tilde{t}\right)\right|^2\right]\tilde{\phi}\left(\tilde{\mathbf{r}}, \tilde{t}\right), \tag{2.38}$$

where

$$\tilde{V}_{ext}\left(\tilde{\mathbf{r}}\right) = \frac{1}{2\bar{\omega}^2}\left(\omega_x^2\tilde{x}^2 + \omega_y^2\tilde{y}^2 + \omega_z^2\tilde{z}^2\right) \text{ and } \tilde{g} = \frac{g}{\hbar\bar{\omega}l^3}. \tag{2.39}$$

Similarly, the energy of the system is now given by

$$\tilde{E} = \int \mathrm{d}\tilde{\mathbf{r}}\left[\frac{1}{2}\left|\tilde{\nabla}\tilde{\phi}\left(\tilde{\mathbf{r}}, \tilde{t}\right)\right|^2 + \tilde{V}_{ext}\left(\tilde{\mathbf{r}}\right)\left|\tilde{\phi}\left(\tilde{\mathbf{r}}, \tilde{t}\right)\right|^2 + \frac{1}{2}\tilde{g}\left|\tilde{\phi}\left(\tilde{\mathbf{r}}, \tilde{t}\right)\right|^4\right], \tag{2.40}$$

and the chemical potential, in the time–independent case, is

$$\tilde{\mu} = \frac{\mu}{\hbar\bar{\omega}}. \tag{2.41}$$

We use this form of the GPE in Chapters 3 and 4 which consider condensate mixtures in harmonic trapping potentials (although we then drop the tilde for simplicity).

2.8 Natural Units

In a homogeneous system, the natural unit of length to use in non–dimensionalising the GPE (2.9) is the healing length ξ. Energy E is rescaled in terms of the chemical potential μ and speed v is expressed in units of the speed of sound $c = \sqrt{gn_c/m}$ [160] such that

$$\tilde{x} = \frac{x}{\xi},\ \tilde{y} = \frac{y}{\xi},\ \tilde{z} = \frac{z}{\xi},\ \tilde{E} = \frac{E}{\mu} \text{ and } \tilde{v} = \frac{v}{c}, \tag{2.42}$$

where the tilde once again denotes the dimensionless quantity. The wavefunction density is expressed in units of the homogeneous density n_c and becomes

$$\tilde{\phi} = \frac{\phi}{\sqrt{n_c}}. \tag{2.43}$$

From these rescalings, it follows that time $\tilde{t}$ and frequency $\tilde{\omega}$ are given by

$$\tilde{t} = \frac{tc}{\xi} \text{ and } \tilde{\omega} = \frac{\omega\xi}{c}. \tag{2.44}$$

The GPE (2.9) reduces to the dimensionless form

$$\mathrm{i}\frac{\partial\tilde{\phi}}{\partial t} = \left[-\frac{1}{2}\nabla^2 + \tilde{V}_{ext}\left(\mathbf{r}\right) + \left|\tilde{\phi}\right|^2\right]\tilde{\phi}, \tag{2.45}$$

where $\tilde{V}_{ext}(\mathbf{r}) = 0$ in a homogeneous system but is included here for completeness. The energy functional is now given by

$$\tilde{E} = \int \mathrm{d}\mathbf{r}\left[\frac{1}{2}\left|\nabla\tilde{\phi}\left(\mathbf{r},t\right)\right|^2 + \tilde{V}_{ext}\left(\mathbf{r}\right)\left|\tilde{\phi}\left(\mathbf{r},t\right)\right|^2 + \frac{1}{2}\left|\tilde{\phi}\left(\mathbf{r},t\right)\right|^4\right]. \tag{2.46}$$

We use this form of the GPE in Chapter 5 where condensates are considered in periodic boxes.

2.9 Reduced Dimensionality

In a quasi–1D system in a harmonic trapping potential (assuming $\omega_x = \omega_y$ and $\omega_\perp \ll \omega_z$), the radial component tends towards the harmonic oscillator ground state. The reduced dimensionality equations are derived by decoupling the wave function into the product of a time–dependent axial component and a time–independent radial component. Therefore,

Atom	$m(10^{-27})$kg	$a_s(a_0)$
^{4}He	6.64	302 [195]
^{23}Na	38.18	62 [196]
^{41}K	68.06	78 [197]
^{87}Rb	144.42	100 [198]
^{133}Cs	220.78	280 [199]

Table 2.1: Table of mass m and s–wave scattering lengths a_s for the most common atomic species that have been condensed.

we take

$$\phi\left(\mathbf{r},t\right)=\tilde{\phi}\left(z,t\right)\phi_{\perp}\left(x,y\right), \tag{2.47}$$

where

$$\phi_{\perp}\left(x,y\right)=\sqrt{\frac{m\omega_{\perp}}{\hbar\pi}}e^{-m\omega_{\perp}x^{2}/2\hbar}e^{-m\omega_{\perp}y^{2}/2\hbar}. \tag{2.48}$$

The prefactor is obtained from the normalisation condition $\int \mathrm{d}x\mathrm{d}y\left|\phi_{\perp}\left(x,y\right)\right|^{2}=1$. These approximations give rise to the following 1D GPE

$$\mathrm{i}\hbar\frac{\partial\tilde{\phi}\left(z,t\right)}{\partial t}=-\frac{\hbar^{2}}{2m}\frac{\partial^{2}\tilde{\phi}}{\partial z^{2}}+\left[V\left(z\right)+U\left|\tilde{\phi}\right|^{2}+\hbar\omega_{\perp}\right]\tilde{\phi} \tag{2.49}$$

where $U=g/2\pi l_{\perp}^{2}$, $V\left(z\right)=\int \mathrm{d}x\mathrm{d}yV_{ext}\left(\mathbf{r}\right)$ and, $l_{\perp}=\sqrt{\hbar/m\omega_{\perp}}$ is the transverse harmonic oscillator length [200]. Substituting this approximation into the equation for the system energy (2.13) and integrating out the dependence on x and y gives

$$E_{z}\left(t\right)=\int \mathrm{d}z\left[\frac{\hbar^{2}}{2m}\left|\frac{\partial\tilde{\phi}\left(z,t\right)}{\partial z}\right|^{2}+\hbar\omega_{\perp}\left|\tilde{\phi}\left(z,t\right)\right|^{2}+V\left(z\right)\left|\tilde{\phi}\left(z,t\right)\right|^{2}+\frac{g}{4\pi l_{\perp}^{2}}\left|\tilde{\phi}\left(z,t\right)\right|^{4}\right]. \tag{2.50}$$

For the time–independent case, the 1D chemical potential absorbs the additional $\hbar\omega_{\perp}$ term such that a new chemical potential

$$\mu_{1D}=\mu-\hbar\omega_{\perp} \tag{2.51}$$

can be defined.

2.10 Two–Component Condensates

In this section, we generalise part of the theory introduced in the current chapter for a two–species BEC. In the time–dependent coupled Gross–Pitaevskii equations (CGPE), each equation describes one condensate similar to the GPE with the addition of a new nonlinear

interaction term in both equations in order to include the interspecies interactions. These are given by

$$\begin{aligned} \mathrm{i}\hbar\frac{\partial\phi_1(\mathbf{r},t)}{\partial t} &= \left[-\frac{\hbar^2}{2m_1}\nabla^2 + V_1 + g_{11}\left|\phi_1(\mathbf{r},t)\right|^2 + g_{12}\left|\phi_2(\mathbf{r},t)\right|^2\right]\phi_1(\mathbf{r},t), \\ \mathrm{i}\hbar\frac{\partial\phi_2(\mathbf{r},t)}{\partial t} &= \left[-\frac{\hbar^2}{2m_2}\nabla^2 + V_2 + g_{22}\left|\phi_2(\mathbf{r},t)\right|^2 + g_{12}\left|\phi_1(\mathbf{r},t)\right|^2\right]\phi_2(\mathbf{r},t), \end{aligned} \tag{2.52}$$

where the subscripts $1, 2$ denote the different condensate components and

$$g_{ii} = \frac{4\pi\hbar^2 a_{ii}}{2m_i} \text{ for } i = 1,2 \text{ and } g_{12}\,(=g_{21}) = \frac{2\pi\hbar^2\left(m_1+m_2\right)a_{12}}{m_1 m_2}, \tag{2.53}$$

are the *intra*–species and *inter*–species interaction strengths respectively. The full derivation for these equations is given in Appendix A. The time–independent equations are obtained by using the substitution $\phi_i(\mathbf{r},t) = \phi_{0i}(\mathbf{r})\,e^{-\mathrm{i}\mu_i t/\hbar}$ for each wavefunction in Equation (2.52) and give

$$\begin{aligned} \mu_1\phi_{01}(\mathbf{r}) &= \left[-\frac{\hbar^2}{2m_1}\nabla^2 + V_1(\mathbf{r}) + g_{11}\left|\phi_{01}(\mathbf{r})\right|^2 + g_{12}\left|\phi_{02}(\mathbf{r})\right|^2\right]\phi_{01}(\mathbf{r}), \\ \mu_2\phi_{02}(\mathbf{r}) &= \left[-\frac{\hbar^2}{2m_2}\nabla^2 + V_2(\mathbf{r}) + g_{22}\left|\phi_{02}(\mathbf{r})\right|^2 + g_{12}\left|\phi_{01}(\mathbf{r})\right|^2\right]\phi_{02}(\mathbf{r}). \end{aligned} \tag{2.54}$$

The energy of the system is given by

$$\begin{aligned} E(\phi_1,\phi_2) = &\int \mathrm{d}\mathbf{r}\left[\frac{\hbar^2}{2m_1}\left|\nabla\phi_1(\mathbf{r})\right|^2 + V_1(\mathbf{r})\left|\phi_1(\mathbf{r})\right|^2 + \frac{1}{2}g_{11}\left|\phi_1(\mathbf{r})\right|^4\right] \\ &+ \int \mathrm{d}\mathbf{r}\left[\frac{\hbar^2}{2m_2}\left|\nabla\phi_2(\mathbf{r})\right|^2 + V_2(\mathbf{r})\left|\phi_2(\mathbf{r})\right|^2 + \frac{1}{2}g_{22}\left|\phi_2(\mathbf{r})\right|^4\right] \\ &+ \int \mathrm{d}\mathbf{r}\left[g_{12}\left|\phi_1(\mathbf{r})\right|^2\left|\phi_2(\mathbf{r})\right|^2\right], \end{aligned} \tag{2.55}$$

and N_1 and N_2, the condensate atom numbers in each species, are respectively given by

$$N_i = \int \mathrm{d}\mathbf{r}\left|\phi_i(\mathbf{r})\right|^2. \tag{2.56}$$

The CGPEs can be written in dimensionless form and in reduced dimensions in the same fashion as shown for single species condensates through Equations (2.35) and (2.47).

2.10.1 Overlapping and Segregated Phases

In this Section, we derive the immiscibility criterion following the analysis of [85]. For simplicity, we consider a homogeneous system where $V_1(\mathbf{r}) = V_2(\mathbf{r}) = 0$ with hard wall

barriers and neglect the kinetic energy terms in Equations (2.54), giving

$$\begin{aligned} g_{11}\left|\phi_1\right|^2 + g_{12}\left|\phi_2\right|^2 &= \mu_1, \\ g_{22}\left|\phi_2\right|^2 + g_{12}\left|\phi_1\right|^2 &= \mu_2. \end{aligned} \tag{2.57}$$

If the condensates overlap the densities $\rho_i = |\phi_i|^2$ can be written as $\rho_i = N_i/V$ where V is the volume. Equations (2.57) become $g_{11}\rho_1 + g_{12}\rho_2 = \mu_1$, $g_{22}\rho_2 + g_{12}\rho_1 = \mu_2$ and the corresponding total energy is given by

$$E_{ov} = \frac{1}{2}\left[g_{11}\frac{N_1^2}{V} + g_{22}\frac{N_2^2}{V} + 2g_{12}\frac{N_1 N_2}{V}\right]. \tag{2.58}$$

For small g_{12}, excitations are stable and any perturbation will increase the system energy by a small amount. Hence in this regime, this is the ground state of the system. However, if g_{12} is large, this is no longer true. We shall show that phase segregated states have a lower total energy.

Consider phase segregated condensates where the two condensates occupy different positions in space. We ignore any energy from the thickness of the interface between the two condensates. Let V_i be the volume occupied by condensate i. The densities are now given by $\rho_i = N_i/V_i$. Equations (2.57) are now $g_{ii}\rho_i = \mu_i$ and the total energy is

$$E_{seg} = \frac{1}{2}\left[g_{11}\frac{N_1^2}{V_1} + g_{22}\frac{N_2^2}{V_2}\right]. \tag{2.59}$$

We minimise E_{seg} with respect to V_1 and V_2 to give $g_{11}N_1^2/V_1^2 = g_{22}N_2^2/V_2^2$. Using $V = V_1 + V_2$, we obtain an expression for the volume occupied by each of the condensates in terms of the total volume

$$\begin{aligned} V_1 &= \frac{V}{1 + \sqrt{g_{22}/g_{11}}\,(N_2/N_1)}, \\ V_2 &= \frac{V}{1 + \sqrt{g_{11}/g_{22}}\,(N_1/N_2)}. \end{aligned} \tag{2.60}$$

The condensate densities are then written as

$$\begin{aligned} \rho_1 &= \left(1 + \sqrt{\frac{g_{22}}{g_{11}}}\frac{N_2}{N_1}\right)\frac{N_1}{V}, \\ \rho_2 &= \left(1 + \sqrt{\frac{g_{11}}{g_{22}}}\frac{N_1}{N_2}\right)\frac{N_2}{V}. \end{aligned} \tag{2.61}$$

The total energy can now be written as

$$E_{seg} = \frac{1}{2}\left[g_{11}\frac{N_1^2}{V} + g_{22}\frac{N_2^2}{V} + 2\sqrt{g_{11}g_{22}}\frac{N_1 N_2}{V}\right]. \tag{2.62}$$

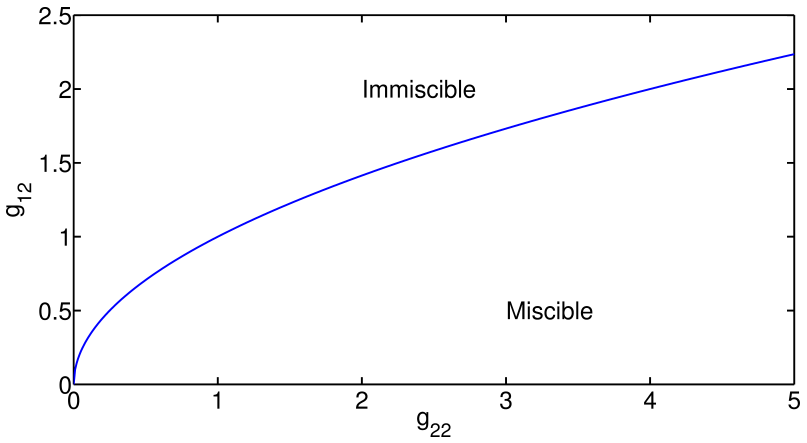

Figure 2.4: Boundary between miscibility and immiscibility for $g_{11} = 1$.

The difference in energies between the overlapping and segregated states is

$$\Delta E = E_{ov} - E_{seg} = (g_{12} - \sqrt{g_{11}g_{22}})\,\frac{N_1 N_2}{V}. \tag{2.63}$$

Thus, for large enough *inter*–species interactions

$$g_{12} > \sqrt{g_{11}g_{22}} \tag{2.64}$$

the energy for the phase segregated state is lower and the system favours this layout. This result is independent of the particle numbers and condensate size. This results has also been found using stability analysis [18, 97].

We thus take the critical value of the interspecies interaction strength to be

$$g_{12}^c = |\sqrt{g_{11}g_{22}}|\,. \tag{2.65}$$

For $g_{12} < -g_{12}^c$, the condensates collapse due to the attractive interactions between each species overwhelming the repulsive interactions within each species. For $g_{12} > g_{12}^c$, the mutual repulsion between the condensates dominates, forcing phase segregation between them such that the condensates no longer overlap (immiscible). For $-g_{12}^c < g_{12} < g_{12}^c$, the repulsion between particles of the same species dominates and the condensates overlap (miscible). We note here, summing the density profiles of each component of a two–species system in harmonic trapping potentials leads to an inverse parabola for the overall density profile. Figure 2.4 shows the miscible and immiscible regions when $g_{11} = 1$. Typical values for interspecies scattering are given in Table 2.2.

Atoms	$a_s(a_0)$	Immiscibility Criteria
^{23}Na–^{87}Rb	73 [201]	$a_s > 78a_0$
^{41}K–^{87}Rb	650 [197]	$a_s > 88a_0$
^{87}Rb–^{133}Cs	206 [202]	$a_s > 167a_0$

Table 2.2: Table of s–wave interspecies scattering lengths a_s and immiscibility criteria for interactions between different possible atomic species.

2.10.2 Thomas–Fermi Approximation in Two–Species System

Similarly to Section 2.3.1, we consider a two–species system in harmonic trapping potentials and ignoring the kinetic energy term. In the limit of large N_1 and N_2 with large repulsive self–interactions ($g_{11} > 0, g_{22} > 0$), the ground state solutions are approximated by

$$\begin{aligned} \phi_1(\mathbf{r}) &= \sqrt{\frac{g_{22}\left[\mu_1 - V_1(\mathbf{r}) - g_{12}\left(\mu_2 + V_2(\mathbf{r})\right)\right]}{g_{11}g_{22} - g_{12}^2}}, \\ \phi_2(\mathbf{r}) &= \sqrt{\frac{g_{11}\left[\mu_2 - V_2(\mathbf{r}) - g_{12}\left(\mu_1 + V_1(\mathbf{r})\right)\right]}{g_{11}g_{22} - g_{12}^2}}. \end{aligned} \tag{2.66}$$

if $g_{ii}\left[\mu_j - V_j(\mathbf{r}) - g_{12}\left(\mu_i + V_i(\mathbf{r})\right)\right]/(g_{11}g_{22} - g_{12}^2) > 0$ or 0 otherwise. For large g_{12}, the results given by the TF approximation for a two–species condensate become unsatisfactory in comparison to exact numerical results [80].

2.10.3 One–Dimensional Dark–Bright Solitons

Immiscible condensate mixtures can support nonlinear structures in the form of dark–bright solitons. These are characterised by a gap in the density of the dark component with a phase slip across its centre while the bright component occupies the space left due to the required immiscibility between the two condensates. On a homogeneous background ($V_i = 0$) with $g_{ij} = 1$, the 1D dark–bright soliton solution for the dark soliton in component one and the bright soliton in component two is given by [108]

$$\begin{aligned} \psi_1 &= \mathrm{i}\sqrt{\mu_1}\sin(\alpha) + \sqrt{\mu_1}\cos(\alpha)\tanh\{\kappa\left[z - q(t)\right]\} \\ \psi_2 &= \sqrt{\frac{N_2\kappa}{2}}\exp(\mathrm{i}\Omega_2 t)\exp\left(\mathrm{i}z\kappa\tan(\alpha)\right)\operatorname{sech}\{\kappa\left[z - q(t)\right]\} \end{aligned} \tag{2.67}$$

where the soliton inverse length is $\kappa = \sqrt{\mu_1\cos^2(\alpha) + (N_2/4)^2} - N_2/4$, the bright component frequency shift $\Omega_2 = \kappa^2(1 - \tan^2(\alpha)/2) + \mu_1 - \mu_2$, the soliton position is $q(t) = q(0) + t\kappa\tan(\alpha)$ and α the velocity–angle.

In the remainder of this section, we present numerical results of the CGPE with one

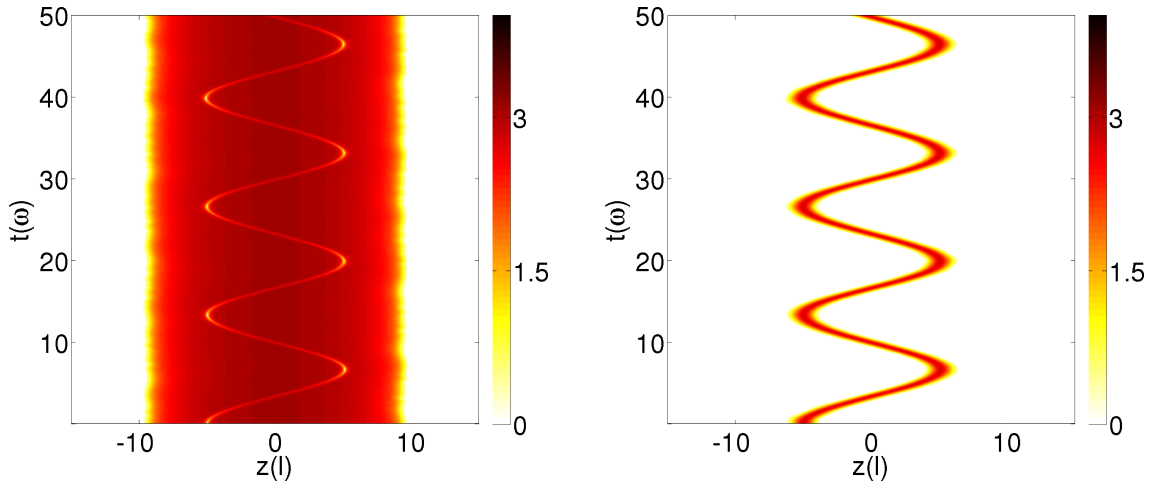

Figure 2.5: Time evolution of a dark–bright soliton with initial phase slip at $z(l) = -5$ with $N_1 = 15000$ and $N_2 = 400$. Left — dark component; right — bright component.

or two appropriately imprinted dark–bright solitons. For simplicity, we initially consider a 1D system with harmonic trapping potentials where $\omega_1 = \omega_2$, $m_1 = m_2$ and repulsive interaction strengths such that the immiscibility criteria is satisfied, i.e. $g_{12}^2 > g_{11}g_{22}$. Figure 2.5 shows the dynamical evolution over time of a dark–bright soliton initially chosen to be off–centre. Similarly to a system with no bright component, the soliton oscillates backwards and forwards in the harmonic trap with no dissipation while the bright component follows the trajectory of this dark soliton. The amplitude is determined by the distance from the centre of the trapping potential and the frequency of these oscillations by the particle numbers [162]. If the soliton was initially positioned at the centre of the trap $z = 0$, no oscillations would occur. The width of the dark soliton varies depending on the number of bright particles in the system: if these increase, the width of the dark soliton also increases as shown in Figure 2.6. The oscillation frequency of the dark–bright soliton does not depend on the number of particles in the bright component. It is solely dependent on the initial location of the phase slip. The height of the bright soliton is determined by the location i.e. depth, of the dark soliton due to our numerical imprinting: the closer it is located to the trap centre, the more the height of the bright component increases, thus reducing its width (see Figure 2.7).

Interactions between two dark–bright solitons, first investigated in Reference [108], have also been of recent interest. An example of such collisions is shown in Figure 2.8. The initially static soliton at the centre of the trap $z(l) = 0$ is distorted by the quicker moving soliton initially at $z(l) = 5$. This forces the central soliton to start oscillating with increasing amplitude over time. The particle number in each bright component remains constant, i.e. there is no exchange of particles between the solitons.

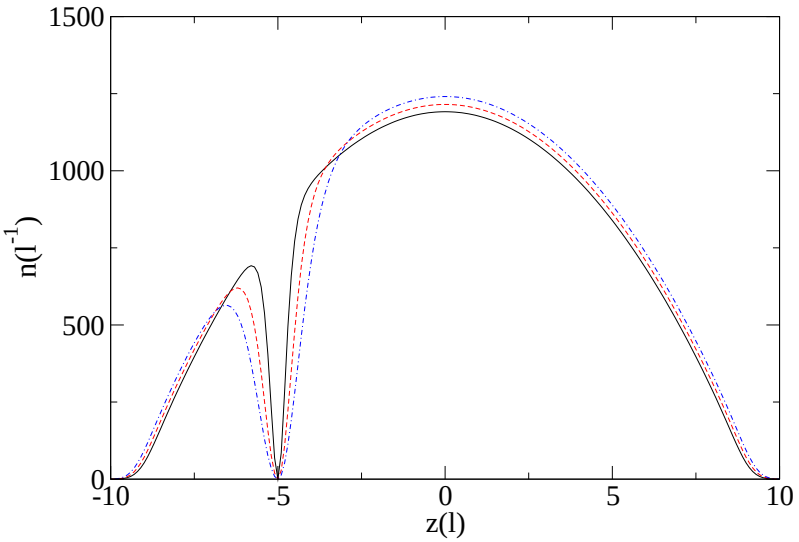

Figure 2.6: Density profiles of dark component with dark–bright solitons at $z(l) = -5$ with $N_1 = 15000$. (Solid) black curve — $N_2 = 400$; (dashed) red curve — $N_2 = 1000$; (dot–dashed) blue curve — $N_2 = 1600$.

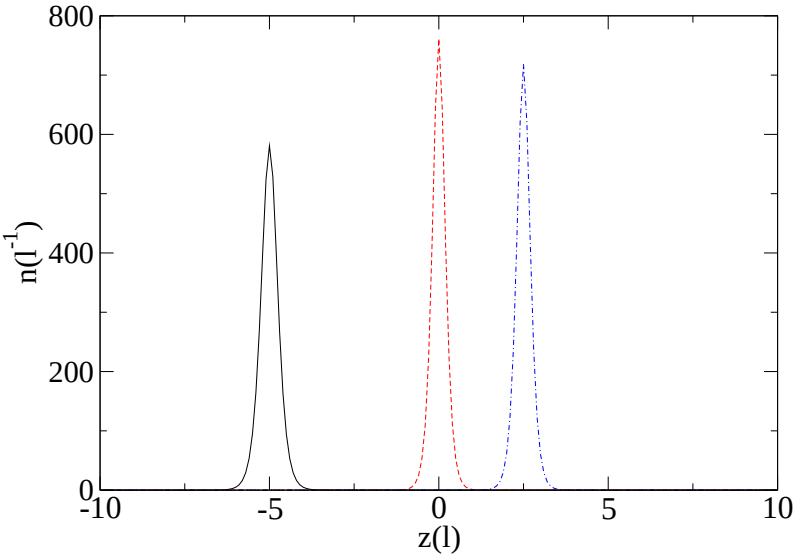

Figure 2.7: Density profiles of bright component with dark–bright solitons with $N_1 = 15000$ and $N_2 = 400$. (Solid) black curve — phase slip at $z(l) = -5$; (dashed) red curve — phase slip at $z(l) = 0$; (dot–dashed) blue curve — phase slip at $z(l) = 2.5$.

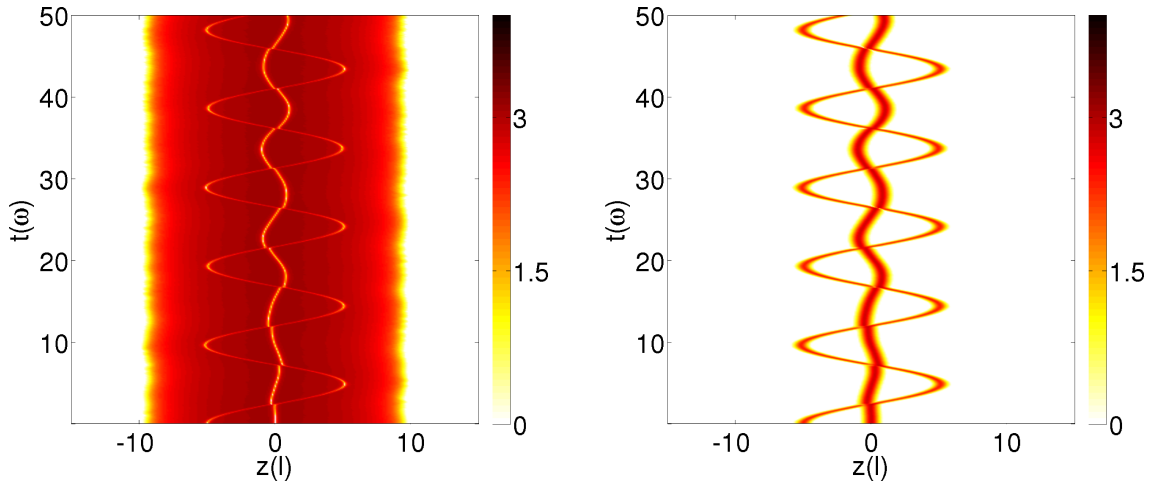

Figure 2.8: Time evolution of dark–bright soliton with initial phase slip at $z = -5$ and $z = 0$ with $N_1 = 15000$ and $N_2 = 400$. Left — dark component; right — bright component.

2.11 Finite Temperature Approaches

At temperatures lower than the critical temperature for condensation ($T \leq T_c$) and above absolute zero there will be macroscopic occupation of the condensate mode but also of many of the low–energy excited modes. In fact, even at $T \geq T_c$, when the condensate is not present many of these excited modes will be highly occupied. In this section we review a number of the theories used to describe the condensate, the thermal cloud and interactions between these. While some of these theories are used directly in obtaining results presented in this Thesis, a broader range of theories are reviewed for context. Namely in Subsection 2.11.4, a GPE with phenomenological damping is shown to arise from a number of finite temperature approaches.

2.11.1 Static Thermal Cloud Models

The generalisation made to the GPE in coupling the condensate dynamics to the thermal cloud shall now be described. Following this, a quantum–Boltzmann equation (QBE) shall be introduced for the evolution of the thermal cloud. We once again use the substitution (2.8) in Equation (2.7). Taking an average gives

$$i\hbar\frac{\partial\phi\left(\mathbf{r},t\right)}{\partial t} = \left[-\frac{\hbar^2}{2m}\nabla^2 + V_{ext}\left(\mathbf{r}\right)\right]\phi\left(\mathbf{r},t\right) + g\langle\hat{\Psi}^{\dagger}\left(\mathbf{r},t\right)\hat{\Psi}\left(\mathbf{r},t\right)\hat{\Psi}\left(\mathbf{r},t\right)\rangle, \tag{2.68}$$

where, due to symmetry breaking, terms including the average of only one non–condensate operator are considered to be zero i.e. $\langle\hat{\psi}^{\dagger}\rangle = \langle\hat{\psi}\rangle = 0$. Expanding the final term gives

$$\langle\hat{\Psi}^{\dagger}\hat{\Psi}\hat{\Psi}\rangle = n_c\phi + m\phi^{\star} + 2n_t\phi + \langle\hat{\psi}^{\dagger}\hat{\psi}\hat{\psi}\rangle, \tag{2.69}$$

where $n_c(\mathbf{r},t) = |\phi(\mathbf{r},t)|^2$ is the condensate density, $n_t(\mathbf{r},t) = \langle\hat{\psi}^\dagger(\mathbf{r},t)\,\hat{\psi}(\mathbf{r},t)\rangle$ is the non–condensate density and $m(\mathbf{r},t) = \langle\hat{\psi}(\mathbf{r},t)\,\hat{\psi}(\mathbf{r},t)\rangle$ is the anomalous average which has an unequal number of annihilation and creation operators. The equation of motion for the condensate thus becomes

$$\begin{aligned} i\hbar\frac{\partial\phi(\mathbf{r},t)}{\partial t} = &\left[-\frac{\hbar^2}{2m}\nabla^2 + V_{ext}(\mathbf{r}) + g\left(n_c(\mathbf{r},t) + 2n_t(\mathbf{r},t)\right)\right]\phi(\mathbf{r},t) \\ &+ gm(\mathbf{r},t)\,\phi^\star(\mathbf{r},t) + g\langle\hat{\psi}^\dagger(\mathbf{r},t)\,\hat{\psi}(\mathbf{r},t)\,\hat{\psi}(\mathbf{r},t)\rangle. \end{aligned} \tag{2.70}$$

If all the particles are in the condensate ($n_t, m, \langle\hat{\psi}^\dagger\hat{\psi}\hat{\psi}\rangle \to 0$), we recover the GPE.

The Hartree–Fock Limit

In the Hartree–Fock (HF) limit, the anomalous average and triplet term $\langle\hat{\psi}^\dagger(\mathbf{r},t)\,\hat{\psi}(\mathbf{r},t)\,\hat{\psi}(\mathbf{r},t)\rangle$ are neglected, retaining only terms with one creation and one annihilation term. In this limit the time–independent generalised GPE becomes

$$\left[-\frac{\hbar^2}{2m}\nabla^2 + V_{ext}(\mathbf{r}) + gn_{c0} + 2gn_{t0}\right]\phi_0 = \mu\phi_0 \tag{2.71}$$

where the subscript 0 denotes a static value. The additional term n_{t0} is the equilibrium thermal cloud. Conventionally, the excitation spectrum can be described semiclassically using the momentum $\mathbf{p}$ and the local energy $\tilde{\epsilon}$ of the thermal atoms as given by the HF energies of the form

$$\tilde{\epsilon}(\mathbf{r},\mathbf{p}) = \frac{|\mathbf{p}|^2}{m} + V_{ext}(\mathbf{r}) + 2g\left[n_{c0}(\mathbf{r}) + n_{t0}(\mathbf{r})\right]. \tag{2.72}$$

The Hartree–Fock–Bogoliubov Limit

The Hartree–Fock–Bogoliubov (HFB) limit is a generalisation of the HF limit which includes all creation and annihilation quadratic terms i.e. the anomalous average and its conjugate. However, this approximation has a fundamental limitation: prohibited for the symmetry breaking theory, the homogeneous spectrum of elementary excitations does not vanish in the limit of zero–momentum but rather leaves a gap.

The HF and HFB limits form a good basis for finite temperature theory, however they neglect important information about particle collisions between condensate and thermal cloud, mainly due to neglecting the triplet term $\langle\psi^\dagger(\mathbf{r},t)\,\psi(\mathbf{r},t)\,\psi(\mathbf{r},t)\rangle$. A higher order theory is required to account for these collisions.

2.11.2 Zaremba–Nikuni–Griffin (ZNG) model

In the ZNG approach, the anomalous average is neglected and the product of the three non–condensate terms is found to be imaginary constituting a growth/decay term in a generalised GPE [203, 204, 205]

$$i\hbar\frac{\partial\phi\left(\mathbf{r},t\right)}{\partial t}=\left[-\frac{\hbar^{2}}{2m}\nabla^{2}+V\left(\mathbf{r}\right)+g\left(\left|\phi\left(\mathbf{r},t\right)\right|^{2}+2n_{t}\left(\mathbf{r},t\right)\right)-iR\left(\mathbf{r},t\right)\right]\phi\left(\mathbf{r},t\right), \tag{2.73}$$

where $iR\left(\mathbf{r},t\right)$ describes the exchange of particles between the condensate and the thermal cloud

$$R\left(\mathbf{r},t\right)=\frac{\hbar}{2\left|\phi\left(\mathbf{r},t\right)\right|^{2}}\int\frac{\mathrm{d}\mathbf{p}}{\left(2\pi\hbar\right)^{3}}C_{12}\left[f\left(\mathbf{p},\mathbf{r},t\right),\phi\right]. \tag{2.74}$$

The expression for the collisional integral between the condensate and the thermal cloud $C_{12}[f,\phi]$ will be given at a later point in this section.

The Wigner distribution function $f\left(\mathbf{p},\mathbf{r},t\right)$ is the phase space distribution function for an atom of momentum $\mathbf{p}$, at location $\mathbf{r}$ and at time t and describes the non–condensate particles by the relation $n_{t}\left(\mathbf{r},t\right)=\int\frac{\mathrm{d}\mathbf{p}}{\left(2\pi\hbar\right)^{3}}f\left(\mathbf{p},\mathbf{r},t\right)$.

Now that collisional particle exchange has been introduced into the condensate evolution, the corresponding evolution for the thermal cloud is required in order to form a closed system of equations which maintain total atom number. The formulation of Zaremba, Nikuni and Griffin [206, 207, 208] is based on a Boltzmann–like equation for the dynamics of the thermal cloud

$$\frac{\partial f}{\partial t}+\frac{\mathbf{p}}{m}\cdot\nabla_{\mathbf{r}}f-\left(\nabla_{\mathbf{r}}U_{\mathrm{eff}}\right)\cdot\left(\nabla_{\mathbf{p}}f\right)=C_{12}\left[f,\phi\right]+C_{22}\left[f\right], \tag{2.75}$$

where $\nabla_{\mathbf{r}}$ and $\nabla_{\mathbf{p}}$ are the gradients in position and momentum respectively. Firstly, $C_{12}[f,\phi]$ describes the transfer of a particles from condensate to the thermal cloud and vice–versa, defined as [203]

$$\begin{aligned}C_{12}\left[f,\phi\right]=&\frac{4\pi}{\hbar}g^{2}\left|\phi\right|^{2}\int\frac{\mathrm{d}\mathbf{p}_{2}}{\left(2\pi\hbar\right)^{3}}\int\frac{\mathrm{d}\mathbf{p}_{3}}{\left(2\pi\hbar\right)^{3}}\int\frac{\mathrm{d}\mathbf{p}_{4}}{\left(2\pi\hbar\right)^{3}}\\&\times\left(2\pi\hbar\right)^{3}\delta\left(m\mathbf{v}_{c}+\mathbf{p}_{2}-\mathbf{p}_{3}-\mathbf{p}_{4}\right)\delta\left(\epsilon_{c}+\tilde{\epsilon}_{2}-\tilde{\epsilon}_{3}-\tilde{\epsilon}_{4}\right)\\&\times\left(2\pi\hbar\right)^{3}\left[\delta\left(\mathbf{p}-\mathbf{p}_{2}\right)-\delta\left(\mathbf{p}-\mathbf{p}_{3}\right)-\delta\left(\mathbf{p}-\mathbf{p}_{4}\right)\right]\\&\times\left[\left(f_{2}+1\right)f_{3}f_{4}-f_{2}\left(f_{3}+1\right)\left(f_{4}+1\right)\right],\end{aligned} \tag{2.76}$$

where $f_{i}=f\left(\mathbf{p}_{i},\mathbf{r},t\right)$ and $\tilde{\epsilon}_{i}=\left|\mathbf{p}_{i}\right|^{2}/m+V_{ext}\left(\mathbf{r}\right)+2g\left[\left|\phi\left(\mathbf{r}_{i},t\right)\right|^{2}+n_{t}\left(\mathbf{r}_{i},t\right)\right]$ is the Hartree–Fock energy of the thermal atoms. $C_{22}[f]$ describes collisions between two particles in the

thermal cloud

$$\begin{aligned} C_{22}[f] =& \frac{4\pi}{\hbar} g^2 \int \frac{\mathrm{d}\mathbf{p}_2}{(2\pi\hbar)^3} \int \frac{\mathrm{d}\mathbf{p}_3}{(2\pi\hbar)^3} \int \frac{\mathrm{d}\mathbf{p}_4}{(2\pi\hbar)^3} \\ & \times (2\pi\hbar)^3 \delta(\mathbf{p} + \mathbf{p}_2 - \mathbf{p}_3 - \mathbf{p}_4) \delta(\tilde{\epsilon} + \tilde{\epsilon}_2 - \tilde{\epsilon}_3 - \tilde{\epsilon}_4) \\ & \times [(f+1)(f_2+1) f_3 f_4 - f f_2 (f_3+1)(f_4+1)]. \end{aligned} \tag{2.77}$$

The δ–function in Equations (2.76) and (2.77) represent the conservation of energy and momentum during these scattering processes. The function f_i is the statistical factor for a particle to be destroyed in state i and $(f_i + 1)$ for the creation in state i. Equations (2.73) and (2.75) represent a closed system which self–consistently solve for the condensate in the presence of a fully dynamical thermal cloud and are conventionally referred to as the ZNG equations.

However this scheme is based on symmetry–breaking. Condensate formation from zero initial seed can not be reproduced as the existence of a small condensate is assumed. In addition, important fluctuations present near the initial region are not accounted for. To model these aspects, the addition of stochastic effects into the system evolution is required.

2.11.3 Stochastic (Projected) Gross–Pitaevskii Equation (S(P)GPE)

First derived by Stoof [209, 210], the SGPE describes the 'coherent' region of low-lying modes which encompasses the condensate and other highly-degenerate modes, with such modes assumed to be in contact with the 'incoherent' region of higher lying modes, which is assumed to be in thermal equilibrium.

Within this approximation, the evolution of the coherent region is given by the SGPE [209, 211, 212]

$$\begin{aligned} i\hbar \frac{\partial \phi(\mathbf{r},t)}{\partial t} &= [1 - iR(\mathbf{r},t)] \left(-\frac{\hbar^2}{2m}\nabla^2 + V(\mathbf{r}) + g|\phi(\mathbf{r},t)| - \mu \right) \phi(\mathbf{r},t) + \eta(\mathbf{r},t) \\ &\approx [1 - i\gamma(\mathbf{r},t)] \left(-\frac{\hbar^2}{2m}\nabla^2 + V(\mathbf{r}) + g|\phi(\mathbf{r},t)| - \mu \right) \phi(\mathbf{r},t) + \eta(\mathbf{r},t) \end{aligned} \tag{2.78}$$

where the noise term $\langle \eta^\star(\mathbf{r},t)\, \eta(\mathbf{r}',t') \rangle = 2\gamma(\mathbf{r},t)\, k_B T \hbar \delta(\mathbf{r} - \mathbf{r}') \mathrm{d}t$ can provide a seed for condensate growth and $\gamma(\mathbf{r},t) = i(\beta/4)\hbar\Sigma^K(\mathbf{r},t)$. Within this scheme, the strength of the interactions between the coherent and incoherent regions is thus defined by the Keldysh self–energy

$$\begin{aligned} \hbar\Sigma^K(\mathbf{r},t) =& -4\pi i g^2 \int \frac{\mathrm{d}\mathbf{p}_2}{(2\pi\hbar)^3} \int \frac{\mathrm{d}\mathbf{p}_3}{(2\pi\hbar)^3} \int \frac{\mathrm{d}\mathbf{p}_4}{(2\pi\hbar)^3} \\ & \times (2\pi\hbar)^3 \delta(\mathbf{p}_2 - \mathbf{p}_3 - \mathbf{p}_4) \delta(\epsilon_c + \tilde{\epsilon}_2 - \tilde{\epsilon}_3 - \tilde{\epsilon}_4) \\ & \times [f_2(f_3+1)(f_4+1) + (f_2+1) f_3 f_4]. \end{aligned} \tag{2.79}$$

The $iR(\mathbf{r},t)$ source term in this approach is similar to that in Equation (2.73) where it describes the transfer of particles between the coherent and incoherent region and is given by

$$\begin{aligned} R(\mathbf{r},t) =& 2\pi g^2 \int \frac{\mathrm{d}\mathbf{p}_2}{(2\pi\hbar)^3} \int \frac{\mathrm{d}\mathbf{p}_3}{(2\pi\hbar)^3} \int \frac{\mathrm{d}\mathbf{p}_4}{(2\pi\hbar)^3} \\ & \times (2\pi\hbar)^3 \delta(\mathbf{p}_2 - \mathbf{p}_3 - \mathbf{p}_4) \delta(\epsilon_c + \tilde{\epsilon}_2 - \tilde{\epsilon}_3 - \tilde{\epsilon}_4) \\ & \times [f_2(f_3+1)(f_4+1) - (f_2+1) f_3 f_4]. \end{aligned} \tag{2.80}$$

The thermal energies are now defined as $\tilde{\epsilon}_i = |\mathbf{p}_i|^2/2m + V_{ext} + 2g\langle|\phi(\mathbf{r},t)|^2\rangle$ and f_i once again represents the Wigner functions for the thermal cloud. It is possible to approximate the source term iR (2.80) in term of the Keldysh self–energy

$$iR(\mathbf{r},t) \approx -\frac{\beta}{4}\hbar\Sigma^k(\mathbf{r},t)\left[-\frac{\hbar^2}{2m}\nabla^2 + V_{ext} + g|\phi|^2 - \mu\right]. \tag{2.81}$$

This defines a fluctuation–dissipation relation for this system.

Stochastic Projected Gross–Pitaevskii Equation (SPGPE)

A similar model, which includes the presence of a projector $\mathcal{P}$, has been derived by Davis, Gardiner and co–workers [213, 214]. The SPGPE is given by

$$i\hbar\frac{\partial\phi(\mathbf{r},t)}{\partial t} = \mathcal{P}\left[(1 - i\gamma(\mathbf{r},t))\left(-\frac{\hbar^2}{2m}\nabla^2 + V(\mathbf{r}) + g|\phi(\mathbf{r},t)| - \mu\right)\phi(\mathbf{r},t)\right] + \mathcal{P}[\eta(\mathbf{r},t)]. \tag{2.82}$$

Once again the approach is applicable for high temperatures where all coherent region modes are highly occupied in the energy cutoff. Without a projector, the numerical grid imposes an implicit cutoff relative to the chosen grid spacing. The projector imposes an explicit energy cutoff in order to restrict the coherent region to highly populated modes. The addition of the explicit projector ensures superior numerical accuracy and a more rigorous means of ensuring validity. The coupled SPGPEs(CSPGPEs) were used by our collaborators I. K. Liu and S. C. Gou to investigate the formation of condensate mixtures. These results are discussed in Chapter 4 in relation to work we have undertaken.

In the following Section the damped GPE(DGPE), used to obtain results presented in this Thesis, is introduced. The DGPE is a particular sub–equation of the S(P)GPE (and of ZNG).

2.11.4 The Damped Gross–Pitaevskii Equation (DGPE)

By neglecting the noise term η in Equation (2.78), the condensate evolution can be cast in the form

$$\mathrm{i}\hbar\frac{\partial\phi\left(\mathbf{r},t\right)}{\partial t}=\left(1-\mathrm{i}\gamma\right)\left[-\frac{\hbar^{2}}{2m}\nabla^{2}+V_{ext}\left(\mathbf{r},t\right)+g\left|\phi\left(\mathbf{r},t\right)\right|^{2}\right]\phi\left(\mathbf{r},t\right). \tag{2.83}$$

where γ denotes the growth rate of the system depending in general on position and time. First implemented to trapped Bose gases to discuss damping of excitations [215], the addition of a phenomenological coefficient γ into the GPE was originally suggested by Pitaevskii [216, 217]. In this approach, γ is taken to be constant and is chosen such that it agrees qualitatively with experiments, although the values used have no microscopic justification. Reference [218] used $\gamma\approx 4\alpha m a_{s}^{2}kT/\pi\hbar^{2}$ and chose $\alpha\approx 3$ to fit most growth experiments.

This dissipative equation has been used in numerous contexts, including the studies of vortex lattice growth [219, 220], dark soliton decay [221] and as a route to turbulence [222].

The DGPE (2.83) can be seen to arise as a special case of above theoretical models in a number of different ways. For example, we can neglect the explicit projector in addition to the noise term η in the SPGPE (2.82). Similar approximations can be made to the ZNG formalism. The DGPE can also be obtained from the GPE (2.9) by setting $t\rightarrow\left(1-\mathrm{i}\gamma\right)t$.

The coupled DGPEs(CDGPEs) are of relevance to the Thesis and are used to obtain the numerical results in Chapter 4. In the following Section, we introduce classical field methods where the dynamical evolution of ϕ is modelled with the GPE but now describes a set of modes rather than a wavefunction.

2.11.5 Classical Field Methods

In classical field methods, more commonly referred to as C–field methods, the GPE is used for modelling all coherent modes (low–lying modes) of a finite temperature system (reviewed in [223]). A common misconception is that the GPE can only simulate condensates at absolute zero. These C–field methods consist of treating the low energy modes as a classical object. To consider the evolution of this system, it is necessary to start with strongly nonequilibrium initial conditions

$$\phi\left(\mathbf{r},t=0\right)=\sum_{k}^{k_{max}}a_{k}\exp\left(i\mathbf{k}\cdot\mathbf{r}\right) \tag{2.84}$$

where the phases of the complex amplitudes a_k are distributed randomly [224]. This initial condition ensures that there is a high number of highly populated modes with momentum less than a particular value k_{max} and ϕ describes a set of modes rather than the condensate

wavefunction. We stress here that the standard GPE for an interacting condensate can be recovered by starting with 100% occupation of the zero momentum $k = 0$ mode and keeping only this mode in the model. We note that the condensate occupation is equal to $n_0 = |a_0|^2$. Numerical simulations begin far from equilibrium (2.84) and are evolved over a time period until equilibrium appears to have been reached. The dynamics conserve the total particle number, N, and kinetic energy, E_{kin},

$$N = V \int n_k\,(t)\,\mathrm{d}k, \tag{2.85}$$

$$E_{kin} = V \int k^2 n_k(t)\mathrm{d}k, \tag{2.86}$$

where V is the volume of the system.

The momentum cut-off used can be imposed through a projector, such as in the projected GPE (PGPE) and neglect any coupling between the coherent region to the effective heat bath [225]. The PGPE was shown to describe the correct thermal behaviour of a Bose gas as long as all relevant modes are highly occupied [226]. Although the projector is recommended in harmonic trapping potentials in order to explicitly impose a energy cutoff, a cutoff arises naturally in numerical simulations due to the discretisation of the GPE equation and is not typically included in this model where periodic boxes are used. Large numerical simulations of the GPE with strongly nonequilibrium initial state was first used [224] to clarify and confirm the theoretical evolution of the system suggested in [227, 228, 229]. Reference [224] also presented the first quasicondensate evolution of vortices in numerical simulations. Quasicondensates are phase–fluctuating condensates in which density fluctuations are largely suppressed [230]. Other finite temperature models (ZNG, S(P)GPE...) can also be used to describe quasicondensates.

In c–field simulations, the condensate fraction (condensate number over total particle number) tends to increase and finally converge over time [231, 232]. The temperature of the system is not set directly but can be subsequently extracted through the condensate fraction [233]. The evolution dynamics of vortex rings was considered in the context of this classical fields approximation and it showed that the collisions with noncondensed particles reduce the radius of a vortex ring until it completely disappears [233].

The evolution of two Bose gases has been considered starting from a strongly nonequilibrium initial states [234]. In comparison to the case of no interaction between particles of different gases, weak repulsive interactions (miscible) between both gases would increase the condensate fraction for one gas and decrease for the other as they equilibrate to the same temperature.

C–field methods are used to investigate non trapped systems and is used in Chapter 5 of this Thesis.

In this Chapter, while stressing the importance of finite temperature effects, we introduced theoretical approaches for describing BECs. Using the CGPEs, our initial focus in Part II is to investigate steady state solutions of condensate mixtures at zero–temperature in harmonic trapping potentials. We then include the growth term which leads to new interesting dynamics. Part III focusses on C–field methods in two component quasicondensates.

Part II

Bose–Einstein Condensate Mixtures in Harmonic Trapping Potentials

Chapter 3

Steady State Solutions of Trapped Two–Species Bose–Einstein Condensates

In this Chapter, we study the equilibrium density structures that arise in a two-species condensate under harmonic trapping.

As a first test of our numerical code, we reproduce the three–dimensional (3D) ^{23}Na–^{87}Rb results from Reference [80]. This also shows how varying the number of particles and the interspecies interaction strengths gives different ground state solutions. We then demonstrate the extreme sensitivity of the equilibrium density profiles on the initial conditions used, in the context of a one–dimensional (1D) mixture. The main focus of the Chapter is to investigate the extent to which the CGPEs reproduce experimental findings of Reference [77] in a ^{87}Rb–^{133}Cs two-species condensate, with and without an asymmetrically perturbed potential between the two species (imposed via the addition of linear potentials). We show that these results qualitatively reproduce the density profiles observed experimentally.

3.1 Reproducing the Results of H. Pu *et al.* [Phys. Rev. Lett., 80, 1130 (1998)].

The first steady state solutions for mixtures of different atomic species were obtained numerically in 1998 by Pu *et al* [80] who considered a mixture of ^{23}Na and ^{87}Rb. In this section we shall numerically reproduce these ground state density profiles by using the TF approximation as initial condition for imaginary time propagation. Imaginary time is implemented by making the substitution $\mathrm{d}t \to -\mathrm{i}\mathrm{d}\tau$ and the wavefunction decays towards the ground state of the system (see Appendix B). Similarly to Reference [80],

we use the CGPEs written in terms of harmonic oscillator units. However we note here a discrepancy in the dimensionless units used: an additional factor of $1/\sqrt{2}$ is present in the scalings for length such that $l_{(1)Pu} = \sqrt{\hbar/2m\bar{\omega}}$ in Reference [80] in comparison to our units presented in Section 2.7. For an exact comparison between the results of Reference [80] and our numerical simulations, it is necessary to multiply our grid axes by $1/\sqrt{2}$ thus giving, for example in the x direction, $\tilde{x} = x/\sqrt{2}l = x/l_{Pu}$. Similar conversions are required in the y and z directions. In addition, our condensate wavefunctions must be rescaled by a factor of $\sqrt{2}^{3/2}$ such that $\tilde{\phi}_i(\mathbf{r},t) = \phi_i(\mathbf{r},t)\, l_{(1)}^{3/2}\sqrt{2}^{3/2} = \phi_i(\mathbf{r},t)\, l_{(1)Pu}^{3/2}$. In our calculations, we take Rb as species 1 and Na as species 2. We have spherically symmetric traps, as defined by Equation (1.8), where $\omega_{(1)\perp} = \omega_{(1)z} = 2\pi \times 160$Hz and $\omega_{(2)\perp} = \omega_{(2)z} = 2\pi \times 310$Hz. The scattering length is taken to be $a_{11} = 6$nm for Rb and $a_{22} = 3$nm for Na. The strength of the interactions in out harmonic oscillator units are given by $g_{ii} = 4\pi\hbar a_{ii}/m_1\omega_{(1)\perp}l_1^3$ $(i = 1, 2)$ and $g_{12} = 2\pi\hbar a_{12}(m_1 + m_2)/m_1 m_2 \omega_{(1)\perp} l_1^3$. Our numerical simulations were carried out with 64^3 grid points with spatial discretisation $\Delta = 0.3125$ in all three directions.

Figure 3.1 shows our numerically obtained steady state solutions with these parameters and $g_{12} > 0$. These are in excellent qualitative and quantitative agreement with Figure 1 from Reference [80]. Figures 3.1(a) correspond to weak interspecies interactions $g_{12}^2 < g_{11}g_{22}$. The widths of both condensate density profiles are wider and have lower peaks in comparison to the situation when no interspecies interactions are present, i.e. $g_{12} = 0$ (Figure 3.1(c)). Considering large interspecies interactions $g_{12}^2 > g_{11}g_{22}$ (Figure 3.1(b)), Na occupies the outer regions of the trapping potential (peak density no longer in the centre) forming a shell around the central Rb. The additional confinement from the outer Na particles squeezes the Rb cloud in the trap centre and increases its peak density value. The larger the number of Na condensate atoms is (Figure 3.1(b)(iii)), the more apparent this phenomena becomes. Similarly, for large Rb atoms in the system, the Na condensate is pushed further away from the trap centre (Figure 3.1(b)(i)).

We also considered negative (attractive) interspecies interactions $g_{12} < 0$ in Figure 3.2. We found that the system would numerically collapse if the amplitude of these interactions were large enough to satisfy the criterion $g_{12}^2 > g_{11}g_{22}$. Therefore we only show the results for weak attractive interactions $g_{12}^2 < g_{11}g_{22}$. In this case, both species want to occupy the same space: the centre of the trapping potential. In comparison to the scenario of no interspecies interactions (Figure 3.1(c)), the condensates are compressed in the trap centre giving density profiles with smaller widths and higher peaks.

In this section, we have shown how changes in the condensate atom numbers and interspecies interactions play a role on the condensate density profiles and a rich number of steady state solutions are obtained. In addition, our results match both qualitatively and quantitatively those seen in Reference [80] proving that our numerical code gives

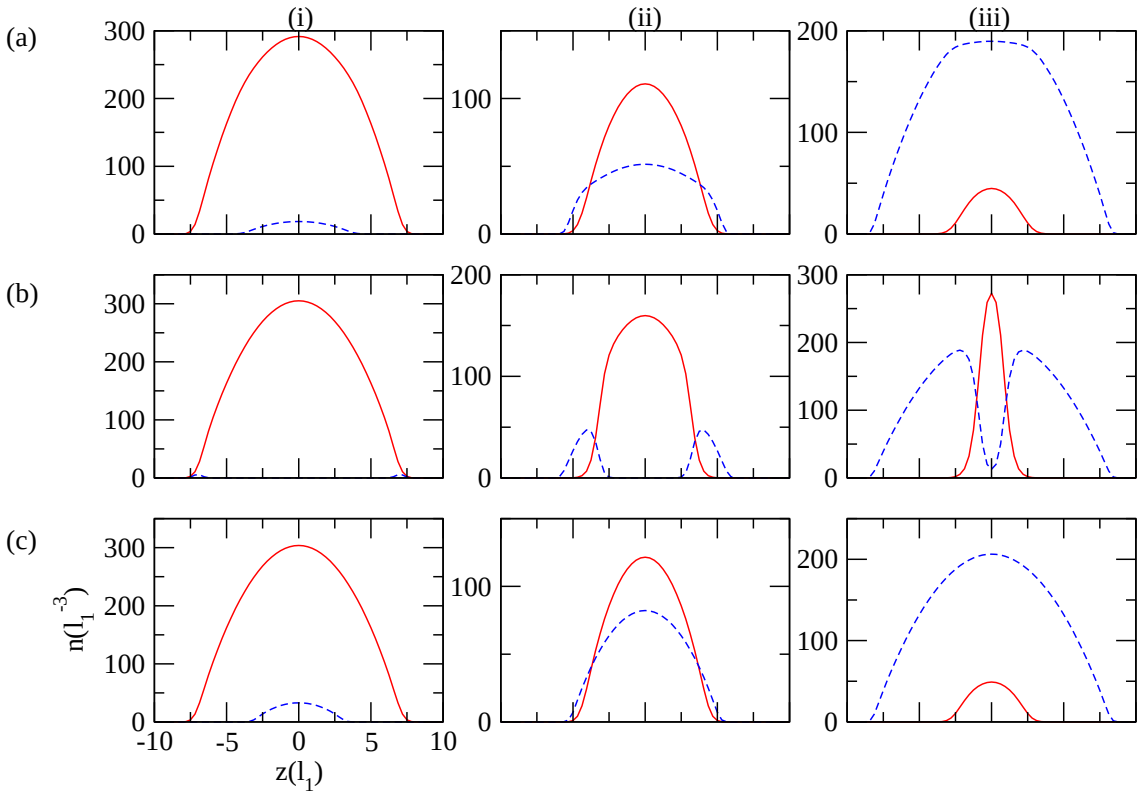

Figure 3.1: Ground state density profiles with $a_{11} = 6$nm ($g_{11} = 0.45$), $a_{22} = 3$nm ($g_{22} = 0.059$) and (a) weak interspecies interactions $a_{12} = 1.8$nm ($g_{12} = 0.085$ and $g_{12}^2 < g_{11}g_{22}$ – miscible), (b) strong interspecies interactions $a_{12} = 3.6$nm ($g_{12} = 0.17$ and $g_{12}^2 > g_{11}g_{22}$ – immiscible) or (c) no interspecies interactions $a_{12} = 0$ ($g_{12} = 0$ and $g_{12}^2 < g_{11}g_{22}$ – miscible). In each of these cases, three sets of atom numbers are considered: (i) $N_1 = 2 \times 10^5$, $N_2 = 2 \times 10^3$; (ii) $N_1 = N_2 = 2 \times 10^4$; (iii) $N_1 = 2 \times 10^3$, $N_2 = 2 \times 10^5$. Red (solid) — Rb (species 1), Blue (dashed) — Na (species 2).

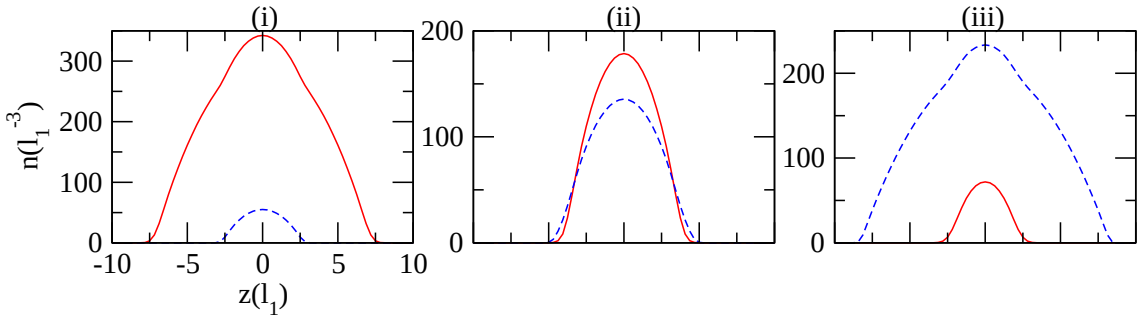

Figure 3.2: Ground state density profiles with $a_{11} = 6$nm ($g_{11} = 0.45$), $a_{22} = 3$nm ($g_{22} = 0.059$) and negative interspecies interactions $a_{12} = -1.8$nm ($g_{12} = -0.085$ and $g_{12}^2 < g_{11}g_{22}$ – miscible). Three sets of atom numbers are considered: (i) $N_1 = 2 \times 10^5$, $N_2 = 2 \times 10^3$; (ii) $N_1 = N_2 = 2 \times 10^4$; (iii) $N_1 = 2 \times 10^3$, $N_2 = 2 \times 10^5$. Red (solid) — Rb (species 1), Blue (dashed) — Na (species 2).

accurate results. In the next section, we shall talk about how the ground state density profiles change depending on the initial conditions used in imaginary time propagation.

3.2 Sensitivity to Parameters

Instabilities often arise when solving equations numerically. Here, we show how these can arise during convergence of the CGPE (i.e. during imaginary time propagation) for various initial conditions. For simplicity we focus on a 1D two-species system. Similarly to Section 2.9 for a one component system, the relation between the 1D and 3D mean-field CGPEs are given by $U_{ii} = g_{ii}/2\pi l_{i\perp}^2$, $U_{12} = g_{12}/\pi\left(l_{1\perp}^2 + l_{2\perp}^2\right)$, $\mu_{i(1D)} = \mu_i - \hbar\omega_{i(x,y)}$ and $l_{i\perp} = \sqrt{\hbar/m_i\omega_{i(x,y)}}$ is the transverse harmonic oscillator length. Similarly to [235] where solutions within the TF approximation were considered, we use simple parameters for immiscible condensates of equal condensate particle numbers $N = N_1 = N_2$, equal trap frequencies $\omega_1 = \omega_2$, equal masses $m_1 = m_2$ and immiscible condensates with interactions $U_{22} = 1.01U_{11}$, $U_{12} = 1.52U_{11}$.

We perform imaginary time propagation of the CGPEs subject to three different initial conditions. Convergence is decided when the fractional difference in energy between consecutive time steps is lower than 10^{-9}. In dimensionless form, we take as the initial state either of the following cases:

(i) the Gaussian ground state harmonic oscillator solution for each species $\phi_i = e^{-\omega_i z^2/2\zeta^2}$ (in first instance we take $\zeta = 1$)

(ii) a Thomas-Fermi (TF) initial state for each species $\phi_i = \sqrt{(\mu_i - V(z))/g_{ii}}$ when $\mu_i \leq V_i(z)$ or 0 otherwise

(iii) a homogeneous initial state (uniform density) $\phi_i = \sqrt{N_i}/L$ where L is the length of our numerical grid.

Each initial condition is suitably normalised to the desired N.

In Figure 3.3, we compare the steady state density profiles that emerge through each of these initial conditions. The first row, Figure 3.3 (a), corresponds to the parameters $U_{11} = 6\left(\hbar\bar{\omega}l^3 2\pi l_\perp\right)$ and $N = 150$. The oscillator length l is given by $\sqrt{\hbar/m_1\omega_1}$. The Gaussian initial condition gives rise to a steady state which features many corrugations in the density profile obtained. The TF initial state gives rise to a central cloud of species 1 surrounded by species 2. This is consistent with previously obtained solutions [235]. For the homogeneous initial state, we obtain a steady state which is similar to the TF result but features additional small clouds of species 1 at the periphery.

The fractional difference in energies for each of these systems, given in Table 3.1, shows that in all cases considered the ground states given by the TF initial conditions have the

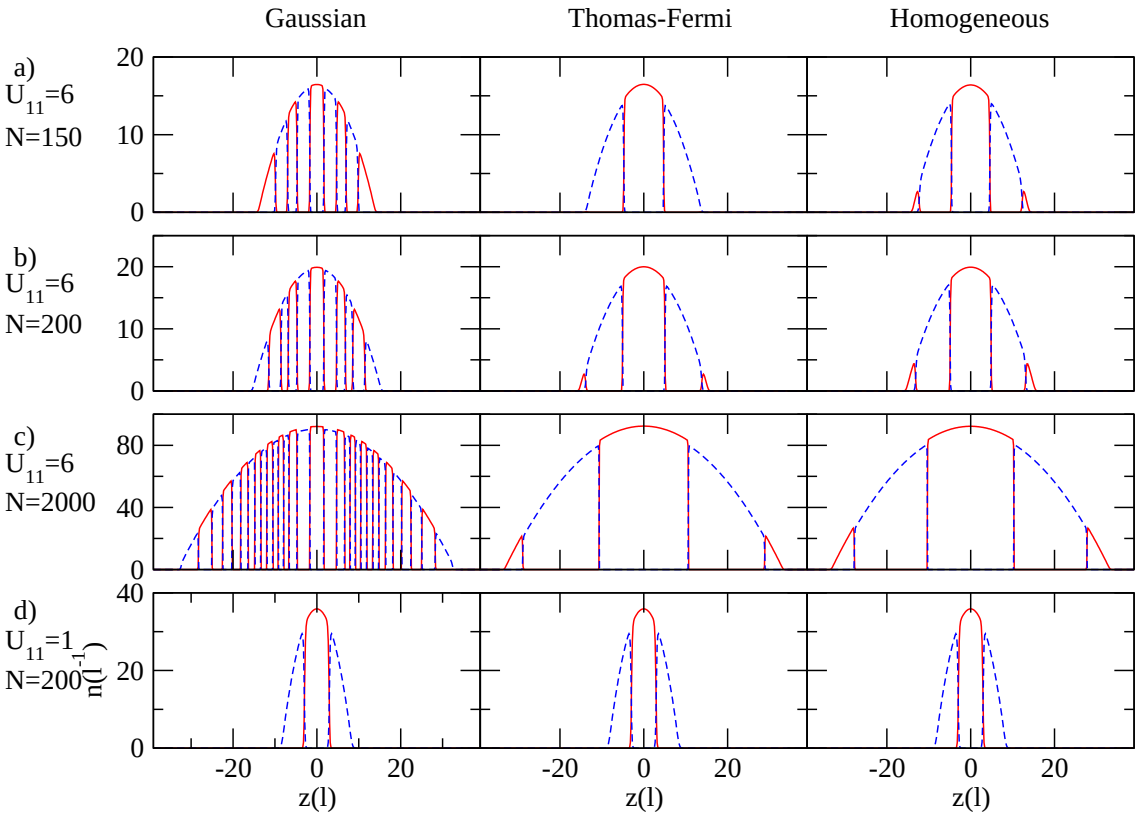

Figure 3.3: Ground state density profiles, with $N = N_1 = N_2$, $\omega_1 = \omega_2$, $m_1 = m_2$ and $U_{22} = 1.01U_{11}$, $U_{12} = 1.52U_{11}$, such that the immiscibility criterion is satisfied. Columns correspond to Gaussian, TF and homogeneous initial conditions for imaginary time propagation. (a) $U_{11} = 6\left(\hbar\bar{\omega}l^3 2\pi l_\perp\right)$, $N = 150$. (b) $U_{11} = 6\left(\hbar\bar{\omega}l^3 2\pi l_\perp\right)$, $N = 200$. (c) $U_{11} = 6\left(\hbar\bar{\omega}l^3 2\pi l_\perp\right)$, $N = 2000$. (d) $U_{11} = 1\left(\hbar\bar{\omega}l^3 2\pi l_\perp\right)$, $N = 200$. Solid blue curve – species 1; Dashed red curve – species 2.

smallest energies followed by the homogeneous initial condition and finally the Gaussian. We thus identify the state derived from the TF initial condition to be the ground state of the system. The difference in energies, however, is small and typically less than 2%. The additional corrugations arising from the Gaussian and homogeneous initial conditions are attributed to a modulational instability of the condensates early in the imaginary-time propagation. This leads to the formation of density corrugations in the system. Imaginary time propagation then converges to one of several metastable states with these corrugated forms.

For a slightly increased atom number, N, Figure 3.3 (b), we find that the TF-based solution becomes closer to the homogeneous-based solution, both featuring small clouds of species 1 at the periphery. The Gaussian-based solution is essentially unchanged. For a significantly larger atom number, Figure 3.3 (c), all profiles become wider due to the increased repulsion in the system. The TF and homogeneous-based solutions maintain the same structural form as above, albeit broader. However, the Gaussian-based solution

	E($\hbar\omega$)		
	Gaussian	Thomas–Fermi	Homogeneous
$U_{11} = 6$, $N = 150$	59.57	58.68	58.73
$U_{11} = 6$, $N = 200$	72.11	71.04	71.08
$U_{11} = 6$, $N = 2000$	331.24	328.15	328.28
$U_{11} = 1$, $N = 200$	72.44	71.21	71.27

Table 3.1: Table of energy $E(\hbar\omega)$ corresponding to plots in Figure 3.3.

features a much greater number of density corrugations. Finally, in Figure 3.3 (d), we plot the results for when the interaction strengths between atoms are reduced compared to Figure 3.3 (b). In this regime of weak interactions, all three initial conditions lead to the same solution in which a cloud of species 1 is surrounded by species 2.

The Gaussian-based solution features the greatest sensitivity. In order to parametrise these effects further we introduce the number of interfaces as a measure of the number of corrugations in the system. Above, we employed the ground harmonic oscillator solution corresponding to the Gaussian width $\zeta = 1$. Here we will vary ζ to assess its role on the steady state solution obtained. In Figure 3.4(a) we plot the number of interfaces in the steady state solution as a function of ζ. As ζ is increased (the Gaussian initial state becomes wider), the number of interfaces decreases exponentially until the minimum is reached, matching the number of interfaces in the ground state (which corresponds to the TF and homogeneous-based solutions in Figure 3.3(c)). In Figure 3.4(b) and (c), we show the initial conditions and ground state density profiles for two cases: (i) $\zeta = 1$ and (ii) $\zeta = 10$ respectively. These results show firstly that a range of metastable states are possible in the system, characterised by an increased number of density corrugations over the ground state. Secondly, the results suggest that the size of the initial trial solution relative to the ground state is key to determining which state is obtained via imaginary time propagation.

The overall density profiles have the same inverted parabola profile independent of the number of corrugations. This is due to the condensates being normalised to the same number of particles irrespective of the initial condition i.e. the area under the curves are the same. The examples we have chosen here are believed to greatly enhance the sensitivity due to our oversimplified choice of $N_1 = N_2 = N$. In general, namely in 3D, the solutions obtained are also sensitive to the initial conditions, although they were considerably less sensitive than in 1D.

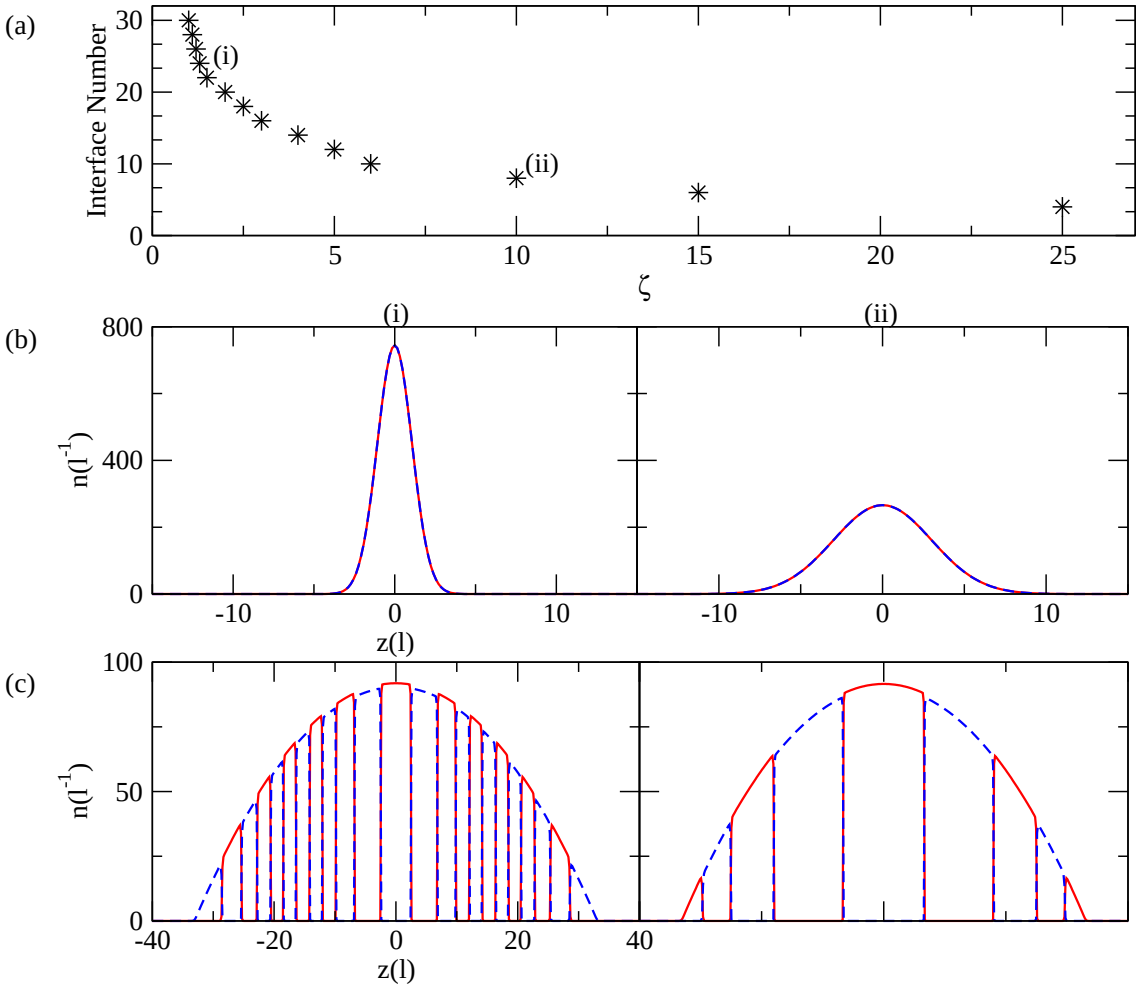

Figure 3.4: Same parameters (ω_i, m_i, U_{22} and U_{12}) as in Figure 3.3 (c) with $N = 2000$, $U_{11} = 6\left(\hbar\bar{\omega}l^3 2\pi l_\perp\right)$. (a) Number of interfaces between species plotted against the width of the Gaussian trial solution ζ. (b) Numerical initial conditions for points (i)($\zeta = 1$) and (ii)($\zeta = 10$) respectively. (c) Ground state density profiles for points (i) and (ii) respectively. Solid blue curve – species 1; Dashed red curve – species 2.

3.3 Matching the Experimental Results of D. J. McCarron *et al.* [Phys. Rev. A, 84, 011603(R) (2011)].

A recent two-species experiment with ^{87}Rb–^{133}Cs condensate mixtures [77] revealed distinct regimes of density distributions, depending on the relative numbers of ^{87}Rb and ^{133}Cs atoms as shown in Figure 3.5. This experiment exploits efficient sympathetic cooling of ^{133}Cs via elastic collisions with evaporatively cooled ^{87}Rb atoms, initially in a magnetic quadrupole trap and subsequently in a levitated crossed dipole trap [236]. The large interspecies background scattering length of $a_{12} \simeq 650\ a_0$ enables efficient sympathetic cooling but also gives rise to large inelastic three body losses [237]. This presents an obstacle to condensation at high densities which is overcome by fast evaporative cooling; this is achieved by reducing the dipole trap beam powers followed by tilting the trap using an applied magnetic field gradient. Dual species condensates are produced in the same trapping potential containing up to $\sim 2 \times 10^4$ atoms of each species. The optical dipole trap exerts harmonic trapping on the condensates.

As shown in Figure 3.5 (a)–(b) the two-species BEC always forms one of three structures correlated to the atom number present in each condensate. Typical axial density profiles from each region (after time of flight expansion) are shown in Figure 3.5 (b). For Regions I and III, one of two possible loosely symmetric cases is obtained: the Rb sits in the centre for Region I while the Rb is spatially split by the Cs in Region III. In Region II, the condensates adopt asymmetric density profiles, sitting side-by-side along the weaker axial direction of the trap. A dramatic spatial separation reveals this mixture to be immiscible as repulsive interspecies interactions dominate intraspecies interactions at the magnetic bias field of 22.4 G used in the experiment. As we will see, these experimental profiles do *not* match the cylindrically-symmetric equilibrium solutions (presented in Figure 3.5(c)).

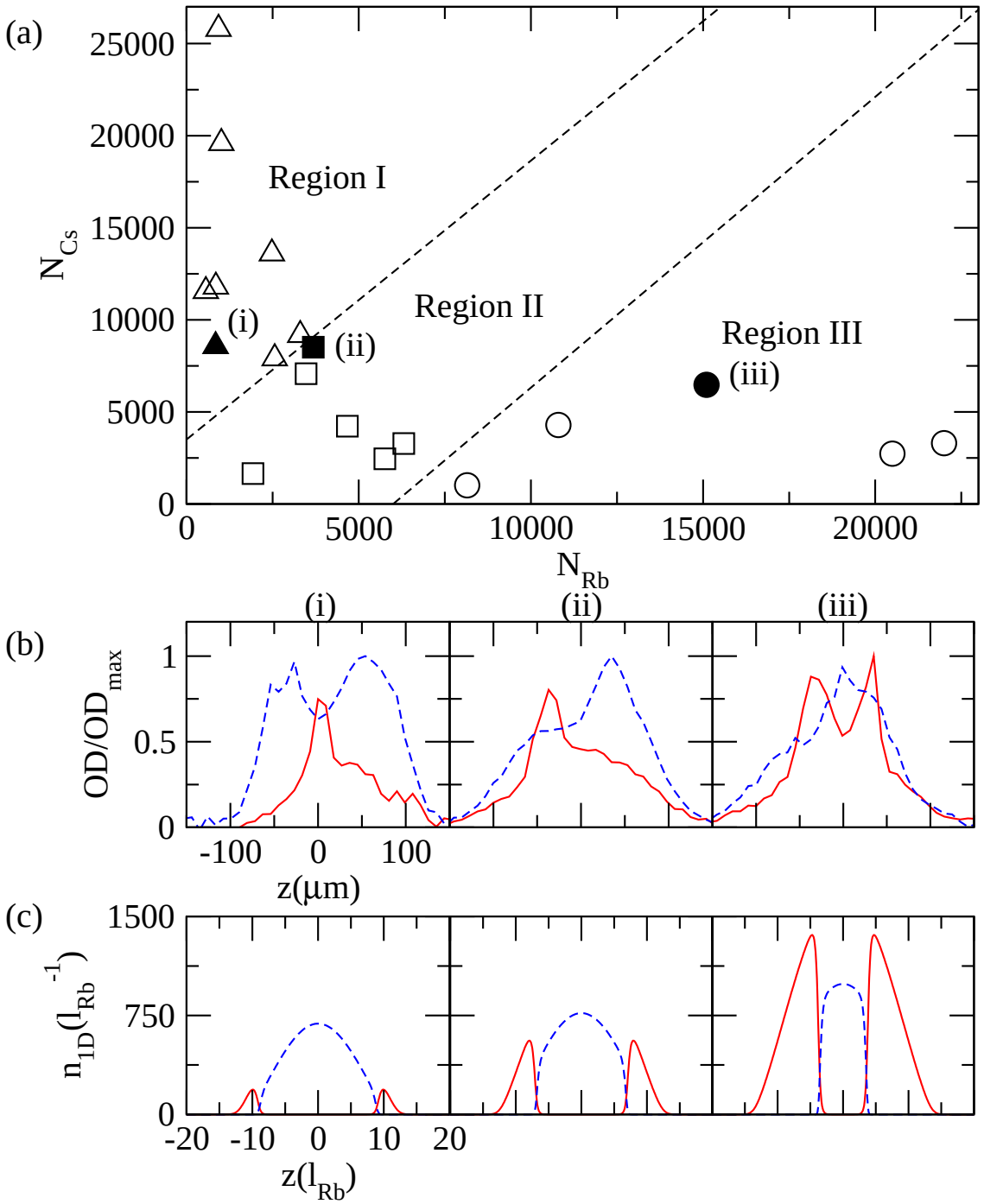

Figure 3.5: (a) Experimental data for a quantum degenerate ^{87}Rb–^{133}Cs mixture (reproduced from data in [D. J. McCarron *et al.*, Phys. Rev. A, **84**, 011603(R) (2011)]). Depending on atom numbers, three distinct structures are observed represented here through triangles, squares and circles (Regions I, II and III). (b) Experimental integrated axial density profiles corresponding to the filled symbols in (a), observed after time-of-flight expansion [H. W. Cho *et al.*, The European Physical Journal D, **65**, 125 (2011)] and rescaled to the optical depth (OD) maximum. (c) Numerically calculated cylindrically symmetric ground state density profiles corresponding to the atom numbers for each of the filled points in (a) and the experimental density profiles shown in (b). (Solid) red curve — Rb; (dashed) blue curve — Cs.

3.3.1 System Parameters and Test Cases

Following the experiment of Reference [77] we consider a ^{87}Rb–^{133}Cs BEC mixture. The trap frequencies are taken to be $\omega_{x(\mathrm{Rb})} = \omega_{y(\mathrm{Rb})} = 2\pi \times 32.2$ Hz, $\omega_{x(\mathrm{Cs})} = \omega_{y(\mathrm{Cs})} = 2\pi \times 40.2$ Hz in the transverse directions and $\omega_{z(\mathrm{Rb})} = 2\pi \times 3.89$ Hz, $\omega_{z(\mathrm{Cs})} = 2\pi \times 4.55$ Hz in the axial direction. The intraspecies and interspecies scattering lengths are taken to be $a_{\mathrm{Rb}} = 100\ a_0$ [198], $a_{\mathrm{Cs}} = 280\ a_0$ [199] and $a_{\mathrm{RbCs}} = 650\ a_0$ [202]. These interaction strengths satisfy the immiscibility criterion $g^2_{\mathrm{RbCs}} > g_{\mathrm{Rb}} g_{\mathrm{Cs}}$ and we expect phase separated condensates.

Throughout the work on this two–species mixture, we adopt harmonic oscillator units where time, length and energy are expressed in units of $1/\bar{\omega}_{\mathrm{Rb}} = 10$ ms, $l_{\mathrm{Rb}} = \sqrt{\hbar/m_{\mathrm{Rb}}\bar{\omega}_{\mathrm{Rb}}} \simeq 0.54\ \mu$m and $\hbar\bar{\omega}_{\mathrm{Rb}}$, respectively. The numerical methods used in obtaining the ground state density profiles in this section are the same as described previously in Section 3.1.

The experiment of Reference [77] observed three regimes of density structure, depending on the atom number in each species. These three regimes correspond to the triangles (Region I), squares (Region II) and circles (Region III) in Figure 3.5 (a). We focus on one representative set of atom numbers from each structural regime:

(i) $N_{\mathrm{Rb}} = 840$ and $N_{\mathrm{Cs}} = 8570$

(ii) $N_{\mathrm{Rb}} = 3680$ and $N_{\mathrm{Cs}} = 8510$

(iii) $N_{\mathrm{Rb}} = 15100$ and $N_{\mathrm{Cs}} = 6470$

These particular test cases are indicated by the three filled symbols in Figure 3.5 (a) and correspond to the experimental images presented in Figure 3.5 (b). We denote ^{87}Rb as species 1 and ^{133}Cs as species 2. In our numerical simulations, the spatial discretisation is set to $\Delta = 0.2$ in all three directions.

3.3.2 Symmetric Trapping Potentials

Here, we consider the two-species condensates to be confined by co-centred harmonic traps and use centred initial conditions i.e. the trapping potentials for both species are centred relative to each other and are perfectly harmonic. We thus anticipate symmetric density profiles in all directions to emerge in our numerical mean–field simulations. Figure 3.5 (c) shows the corresponding numerically–obtained integrated axial density ground states profiles. Our obtained states are all symmetric in space and phase-separated, as expected. For all three cases considered we observe the same qualitative structure in that the Cs cloud resides at the trap centre, with the Rb cloud surrounding it. This is the so-called 'ball-and-shell' formation [80]. As we move from Region I to Region III, the qualitative structure does not change; only the relative amplitude of the condensates and location

of condensate interfaces (change from Rb to Cs or vice-versa) change as N_{Rb} increases and N_{Cs} decreases. Note that the observed preference in our numerical results for Cs to be centrally positioned is consistent in our previous Rb–Na theoretical studies where the tendency is for the component with the higher atomic mass to reside centrally (see Figure 3.1). This dynamical system has a substantial total parameter space, with even a restriction to cylindrical symmetry leaving eight dimensionless parameters that can in principle be independently varied (see Appendix A.1 for dimensional analysis done by S. A. Gardiner, Durham University). Many of these parameters will, in practice, be fixed in any given experimental configuration. Hence, for example, in the experimental configuration described in Reference [77], it is not possible for the distributions of Rb and Cs to be simply exchanged by changing the particle numbers (the most easily accessible handle to change the systems location in parameter space). This means, for example that the disagreement of Figures 3.5(b)(i) and 3.5(c)(i) is unlikely to be due to incorrect atom counting.

Our results (Figure 3.5 (c)) agree qualitatively with the experimental observations (Figure 3.5 (b)) only for Region III: both the experiment and our numerical results (Figure 3.5 (b) (iii) and (c) (iii)) show Cs to be in a central position, but not those obtained for the other Regions. The experimental images include the presence of a broad thermal cloud, which is often large, and have undergone time-of-flight expansion, and so our comparison of density profiles is limited to the qualitative structural form only. For Region I, the location of the condensates is reversed: experimentally Rb occupies the centre of the trap while numerically it is Cs. In the case of Region II, a symmetric steady state solution emerged as was expected while experimentally the condensates sit side by side in an asymmetric disposition in the z direction. This suggests that a form of asymmetry enters the experimental set up. Theoretically, it has been shown that the symmetry in a two species system can be broken in many different ways to give rise to two separated side–by–side condensates [71, 91, 94, 235].

In the following Section, we shall discuss small shifts that are present between the trapping potentials of the two species which introduce asymmetry into the system. We will then start to investigate whether the introduction of these shifts and asymmetries may dictate the density structures that form and may enable us to reconcile the differences with the experimental results in Regions I and II.

3.3.3 Experimental Asymmetries

In the experiment of Reference [77] a magnetic tilt is applied to the otherwise harmonic potential to enhance evaporative cooling. This tilt is applied in one of the transverse directions, and results in a shift in relative trap centres by up to 3 microns. Additionally, the small difference in magnetic moment–to–mass ratio for each species, coupled with

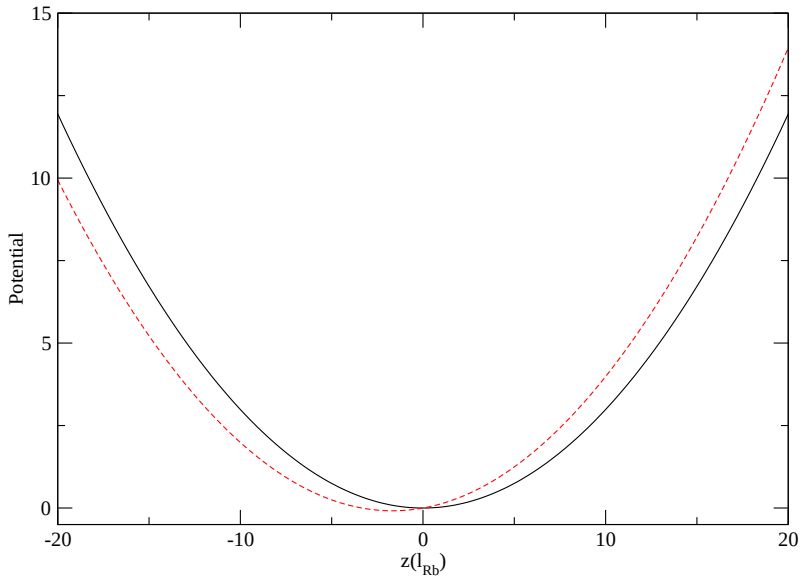

Figure 3.6: Experimental harmonic oscillator trapping potentials in axial direction with no offset $\alpha_z = \alpha_x = 0$ (black – solid) and offset in axial direction $\alpha_z = 0.1(\hbar\bar{\omega}_{\mathrm{Rb}}/l_{\mathrm{Rb}})$, $\alpha_x = 0$ (red – dashed).

minute unavoidable misalignments of the dipole trap beams with respect to the magnetic potential, may result in offsets between the trap centres of up to 2 μm in all directions. Further trap effects, such as differential gravitational sag, are also present. The combined result is that the potentials experienced by the two species have a slight offset in space. To incorporate the presence of such shifts in our simulations we add linear potentials in the axial and *one* transverse direction to species 1 (Rb) such that its trapping potential takes on the modified form

$$V_1 = \frac{1}{2}m_1\left(\omega_{x(1)}^2x^2 + \omega_{y(1)}^2y^2 + \omega_{z(1)}^2z^2\right) + \alpha_x x + \alpha_z z. \tag{3.1}$$

The gradients for the linear potentials are given by α_x and α_z in the transverse and axial directions respectively. In Figure 3.6, we compare symmetric $\alpha_z = 0$ and asymmetric $\alpha_z \neq 0$ harmonic trapping potentials. In changing the value of α_z to be non–zero, the trap minima moves in the axial direction in addition to being lowered. The distance between the trap minima of Rb and Cs is given by

$$\delta_z = \frac{\alpha_z}{m_1\omega_{z(1)}^2} \text{ and } \delta_x = \frac{\alpha_x}{m_1\omega_{x(1)}^2} \tag{3.2}$$

in the axial and transverse directions respectively. Our initial analysis in the previous section focused on symmetric ground state density profiles, obtained in the limit $\alpha_x = \alpha_z = 0$, for which the traps of each species are co-centred.

3.3.4 Role of Shifted Trapping Potentials

Axial Linear Potential

We start by looking at how the addition of a linear potential in the axial direction influences the ground state solutions. Results presented here are based on a linear potential of gradient $\alpha_z = 0.02$ ($\hbar\bar{\omega}_{\rm Rb}/l_{\rm Rb}$). This corresponds to an axial shift of $\delta_z = 0.9$ μm in the trap centres, which is well within the experimental bounds detailed in Section 3.3.3. The value of the linear potential gradient employed here, and the value of the transverse linear potential employed in the next section, are chosen such that their combined result, presented in Section 3.3.4, gives the best agreement to experiments that mean field theory can yield, while remaining within the bounds of the experimental uncertainties.

The numerically–obtained ground state solutions are presented in Figure 3.7 as both integrated (a) axial density profiles and (b) 2D density profiles. First consider the profile for Region III (Figure 3.7(iii)). The same structure remains from the symmetric system, i.e. central Cs surrounded by Rb, albeit now skewed slightly due to the linear potential. The profile for Region II (Figure 3.7(ii)) now jumps to an asymmetric side-by-side state, in qualitative agreement with the experimental profile for this region (Figure 3.5(b)(ii)). For Region I (Figure 3.7(i)) the density profile also becomes asymmetric under the axial linear potential, and as such it remains inconsistent with the corresponding experimental observation (Figure 3.5(b)(i)).

Increasing the linear potential past a critical value of $\alpha_z \simeq 0.1$ ($\hbar\bar{\omega}_{\rm Rb}/l_{\rm Rb}$) gives axially asymmetric density profiles for all three regimes while decreasing the gradient below another critical value of $\alpha_z \simeq 0.01$ ($\hbar\bar{\omega}_{\rm Rb}/l_{\rm Rb}$) leads to the ball–in–shell structure for all three cases, i.e. central Cs surrounded by Rb.

Transverse Linear Potential

Next we look at the influence of a additional linear potential in *one* transverse direction, taken to be the x direction (no axial linear potential is applied here). We focus on a gradient of $\alpha_x = 1.5$ ($\hbar\bar{\omega}_{\rm Rb}/l_{\rm Rb}$) which corresponds to an axial shift of $\delta_x = 1.0$ μm in the trap centres. This is comfortably within the experimental bounds detailed in Section 3.3.3. Figure 3.8 shows the corresponding integrated ground state density profiles.

The integrated axial density profiles for Region III (Figure 3.8(a)(iii)) is again a qualitative match to that obtained experimentally. However, the actual 3D structure is now such that the Rb cloud lies offset transversely to the central Cs cloud, curving around it in the positive x half-plane, as visible in the corresponding integrated 2D density plot (Figure 3.8(b)(iii)). This is a subtly different structure to that observed in the previous sections where the Rb cloud was split either side of the Cs cloud. The 1D density profile for Region II (Figure 3.8(a)(ii)) shows similar results to the symmetric case where the Cs sits

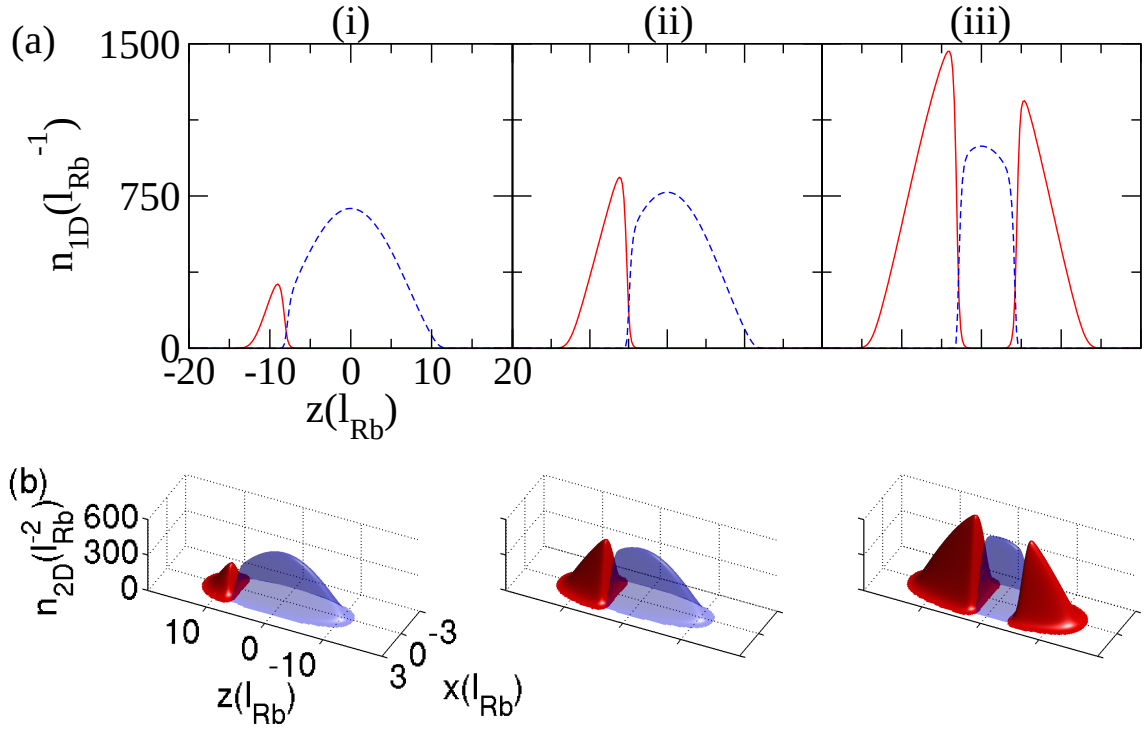

Figure 3.7: Ground states under a linear axial potential $\alpha_z = 0.02$ ($\hbar\bar{\omega}_{\rm Rb}/l_{\rm Rb}$). (a) Integrated axial density profiles and (b) 2D density profiles, for the three cases corresponding to the filled symbols in Figure 3.5 (a). (Solid) red curve — Rb; (dashed) blue curve — Cs.

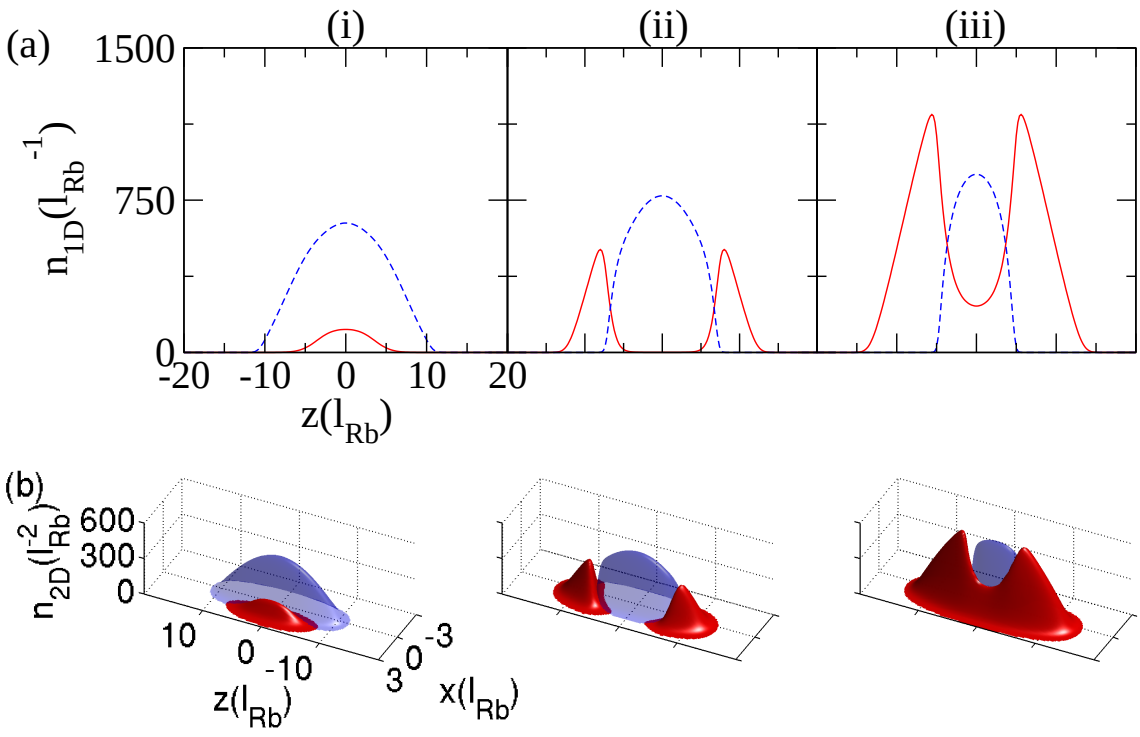

Figure 3.8: Ground states under a linear transverse potential $\alpha_x = 1.5$ ($\hbar\bar{\omega}_{\rm Rb}/l_{\rm Rb}$). Integrated (a) axial density profiles and (b) 2D density profiles, for the three cases corresponding to the filled symbols in Figure 3.5 (a). (Solid) red curve — Rb; (dashed) blue curve — Cs.

in the centre with Rb split axially into two distinct regions and thus not consistent with the corresponding experimental profile. As visible in the 2D density plot (Figure 3.8(b)(ii)), the outer Rb clouds become skewed towards the positive x direction, but not sufficiently to become linked to one side of the Cs cloud forming one Rb cloud. Importantly, for Region I, the integrated axial density profile (Figure 3.8(a)(i)) has undergone a marked change, with both condensates apparently overlapping. This does not contradict the presence of phase separation; as seen in the corresponding 2D density profiles (Figure 3.8(b)(i)), the condensates phase separate transversely due to the transverse linear potential. Although this result is still different from the corresponding experimental profile (Figure 3.5(b)(i)), it is somewhat closer in that the Rb becomes positioned in the centre in the axial direction.

Increasing the linear potential past a critical value of $\alpha_x \simeq 3$ ($\hbar\bar{\omega}_{\rm Rb}/l_{\rm Rb}$) gives transverse asymmetric density profiles for all three regimes while decreasing the gradient to values below approximately $\alpha_x \simeq 0.4$ ($\hbar\bar{\omega}_{\rm Rb}/l_{\rm Rb}$) gives rise to a split in the Rb to surround the Cs positioned in the centre.

So far we have presented numerical results for symmetric trapping potentials and linear potentials in either the axial direction or a transverse direction. Results obtained for Region III qualitatively match those obtained experimentally. For Region II, we obtain

a reasonable match through use of an additional axial linear potential. Through use of an additional transverse linear potential we have captured some, but not all, of the features from Region I. We will next explore the extent to which a combination of both axial and transverse shifts, as likely to be relevant experimentally, enables a closer match to the experimental profiles.

Combined Result: Axial and Transverse Linear Potential

We consider the three representative points in Section 3.3.1, one for each region, in turn starting with Region I.

Region I: A summary of how different gradients of linear potentials in the axial and transverse directions affect the ground state density profiles for Region I is shown in Figure 3.9. We distinguish three distinct structures: a three peak profile in which the Cs remains in the centre while the Rb is split axially into two distinct regions, an axially side–by–side structure, or a transversely side–by–side structure. Starting from the symmetric three peaked distribution (bottom left in Figure 3.9), we see that a small increase in α_z gives rise to axially side-by-side density profiles: for a weak axial linear potential $\alpha_z = 0.01$ $(\hbar\bar{\omega}_{\mathrm{Rb}}/l_{\mathrm{Rb}})$, the ground state has switched to the axially side–by–side formation. On the other hand, α_x needs to be increased more drastically to observe the switch of the ground state to a transversely side–by–side formation. This is due to competing effect of the condensate repulsion and the strong transverse trapping. When combining linear potentials in both axial and transverse directions, we see that for small $\alpha_z < 0.04$ $(\hbar\bar{\omega}_{\mathrm{Rb}}/l_{\mathrm{Rb}})$ the condensates favour a transverse side–by–side formation while this becomes an axial side–by–side formation for larger values. For $\alpha_z = 0.04$ $(\hbar\bar{\omega}_{\mathrm{Rb}}/l_{\mathrm{Rb}})$ and $\alpha_x = 2.25$ $(\hbar\bar{\omega}_{\mathrm{Rb}}/l_{\mathrm{Rb}})$, we see a combination of these side–by–side structures in that the Rb cloud lies diagonally to the side of the Cs cloud. For intermediate values of α_x and α_z, e.g. $\alpha_x = 0.4$ $(\hbar\bar{\omega}_{\mathrm{Rb}}/l_{\mathrm{Rb}})$ and $\alpha_z = 0.01$ $(\hbar\bar{\omega}_{\mathrm{Rb}}/l_{\mathrm{Rb}})$, we see a transversely side–by–side formation in which the Rb is particularly narrow and highly peaked, and the Cs features a small central density dip.

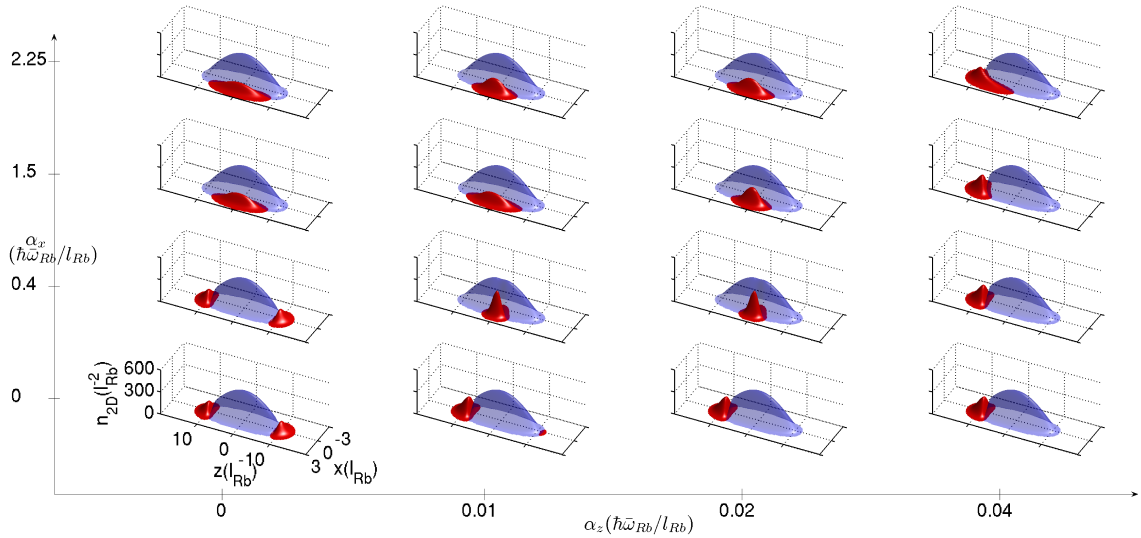

Figure 3.9: Integrated 2D density profiles of the ground state as a function of the linear potential gradient in the axial (horizontal) and one transverse (vertical) direction applied to species 1(Rb). Atom numbers correspond to point (i) in Figure 3.5 (a). Red (black) — Rb; Blue (grey) — Cs.

Region II: Now, we will consider the test case for Region II and a summary of how different gradients of linear potentials affect the ground state density profiles for Region II is shown in Figure 3.10. We once again distinguish three different density profiles, similar to Region I with the now larger number of Cs condensate atom numbers having an impact on the gradient of additional linear potential required to go from a symmetric to asymmetric ground state density profile. When α_x is increased, the two peaks of Rb move around the central Cs in the transverse direction until they join and form a single condensate cloud such as for $\alpha_x = 2.25$ $(\hbar\bar{\omega}_{\mathrm{Rb}}/l_{\mathrm{Rb}})$. On the other hand, when α_z is non–zero, asymmetric axial density profiles are observed firstly in the three peak formation where one Rb peak is higher than the other. Further increasing the gradient in the axial direction leads to a axially asymmetric side–by–side formation as seen experimentally. When combining linear potentials in both the axial and transverse directions, the condensates prefer a three peak density profile for small $\alpha_x < 2.25$ $(\hbar\bar{\omega}_{\mathrm{Rb}}/l_{\mathrm{Rb}})$ and $\alpha_z < 0.02$ $(\hbar\bar{\omega}_{\mathrm{Rb}}/l_{\mathrm{Rb}})$. This changes to an axially asymmetric side–by–side formation for larger $\alpha_z > 0.01$ $(\hbar\bar{\omega}_{\mathrm{Rb}}/l_{\mathrm{Rb}})$. Finally, the Rb cloud lies diagonally to the side of the central Cs condensate for large $\alpha_x > 1.5$ $(\hbar\bar{\omega}_{\mathrm{Rb}}/l_{\mathrm{Rb}})$.

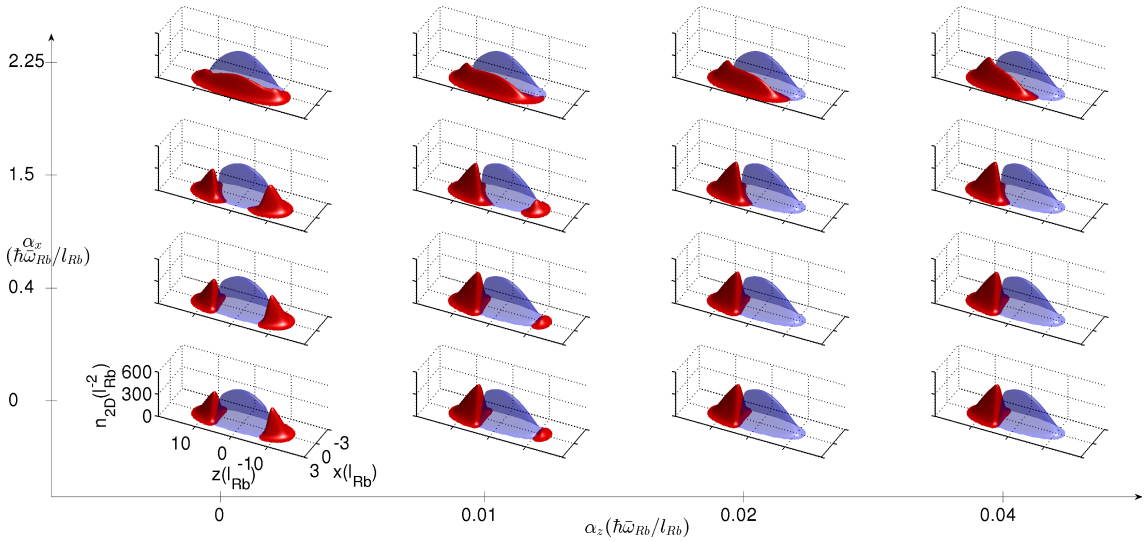

Figure 3.10: Integrated 2D density profiles of the ground state as a function of the linear potential gradient in the axial (horizontal) and one transverse (vertical) direction applied to species 1(Rb). Atom numbers correspond to point (ii) in Figure 3.5 (a). Red (black) — Rb; Blue (grey) — Cs.

Region III: Finally, we consider the test case for Region III and a summary of how different gradients of linear potentials affect the ground state density profiles for Region III is shown in Figure 3.11. It is clear from the obtained ground state density profiles, all the experimentally relevant linear potentials lead to a three peak regime apart from $\alpha_x > 1.5$ $(\hbar\bar{\omega}_{\mathrm{Rb}}/l_{\mathrm{Rb}})$ where we find a transversely asymmetric densities. No axially asymmetric profiles are observed for these linear potentials but can be observed by increasing α_z further. This region is the more robust of the three considered in terms of experimentally relevant gradients for the additional linear potentials due to the large N_{Rb} particle number.

We will see next that these profiles now give good qualitative agreement with the experimental observed condensates for all regions.

Matching of Experimental Profiles: Best Results of Mean Field Theory

We now combine our previous analyses to demonstrate the extent to which addition of linear potentials in both the axial and one transverse direction matches the experimental profiles for all three regimes for a given set of linear potentials. From Figure 3.9, we can see that we require $\alpha_z = 0.01$ $(\hbar\bar{\omega}_{\mathrm{Rb}}/l_{\mathrm{Rb}})$ or 0.02 $(\hbar\bar{\omega}_{\mathrm{Rb}}/l_{\mathrm{Rb}})$ and $\alpha_x = 0.4$, 1.5 or 2.25 $(\hbar\bar{\omega}_{\mathrm{Rb}}/l_{\mathrm{Rb}})$ to match the results for Region I. After a similar analysis for Region II and Region III from Figures 3.10 and 3.11, the experimentally relevant gradients of the linear potentials required to match all three simultaneously are $\alpha_z = 0.02$ $(\hbar\bar{\omega}_{\mathrm{Rb}}/l_{\mathrm{Rb}})$ and $\alpha_x = 1.5$ $(\hbar\bar{\omega}_{\mathrm{Rb}}/l_{\mathrm{Rb}})$ (hence justifying the use of those values in previous Sections). These linear potentials correspond to a displacement in the trap minima of $\delta_z = 0.9$ μm and $\delta_x = 1.0$ μm, both of which are well within experimental bounds detailed in Section 3.3.3.

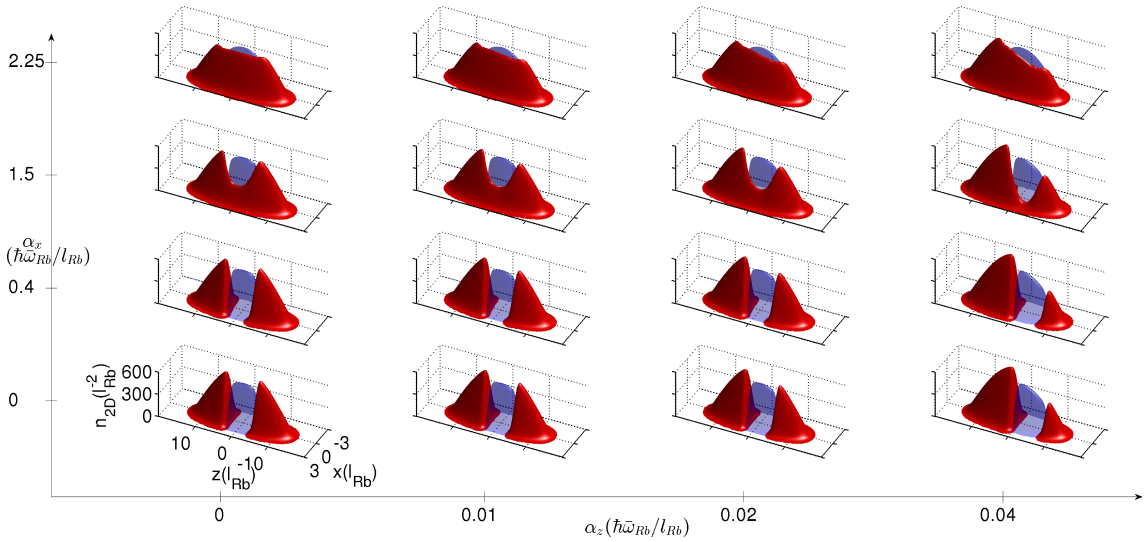

Figure 3.11: Integrated 2D density profiles of the ground state as a function of the linear potential gradient in the axial (horizontal) and one transverse (vertical) direction applied to species 1(Rb). Atom numbers correspond to point (iii) in Figure 3.5 (a). Red (black) — Rb; Blue (grey) — Cs.

The numerical results for these gradients are shown in Figure 3.12 as both integrated axial density profiles (Figure 3.12(a)) and 3D isosurface plots of density (Figure 3.12(b)). Our ground state results are now in very good qualitative agreement with the experimental profiles (Figure 3.5(b)) in all three regimes. For Region III, the ground state has the Rb cloud divided into two parts positioned either side of the central Cs cloud. For Region II, we obtain the side–by–side formation in which the Cs cloud sits to the right of Rb cloud. For Region I, the ground state features the Rb cloud to be centrally located in the axial direction, but shifted transversely, while the Cs has a small density dip at the centre.

The central density dip in the Cs profile for Region I is more pronounced in the experimental observations, e.g. Figure 3.5(b)(i), than in our above results. An inherent feature of solving the CGPEs for an immiscible two-species BEC is a sensitivity to the initial trial wavefunction. All of our results presented so far have been based on TF initial trial wavefunctions (for the quoted condensate atom numbers for each species), as described in Section 2.10. By their nature, the TF profiles tend to be broadly distributed in space, and this tends to favour a more broad distribution of condensates in the final static solution obtained. We find that employing an initial distribution for the Rb cloud which is tightly localised at the origin yields static solutions which feature a localised Rb cloud and a slightly more prominent density dip in the adjacent Cs cloud, in closer agreement with the experimental profiles for Region I. These numerical results are presented in a Section 3.3.5.

We have also looked at introducing axial asymmetry (without permanent trap shifts) through shifts in our numerical initial conditions. Specifically, the TF initial conditions

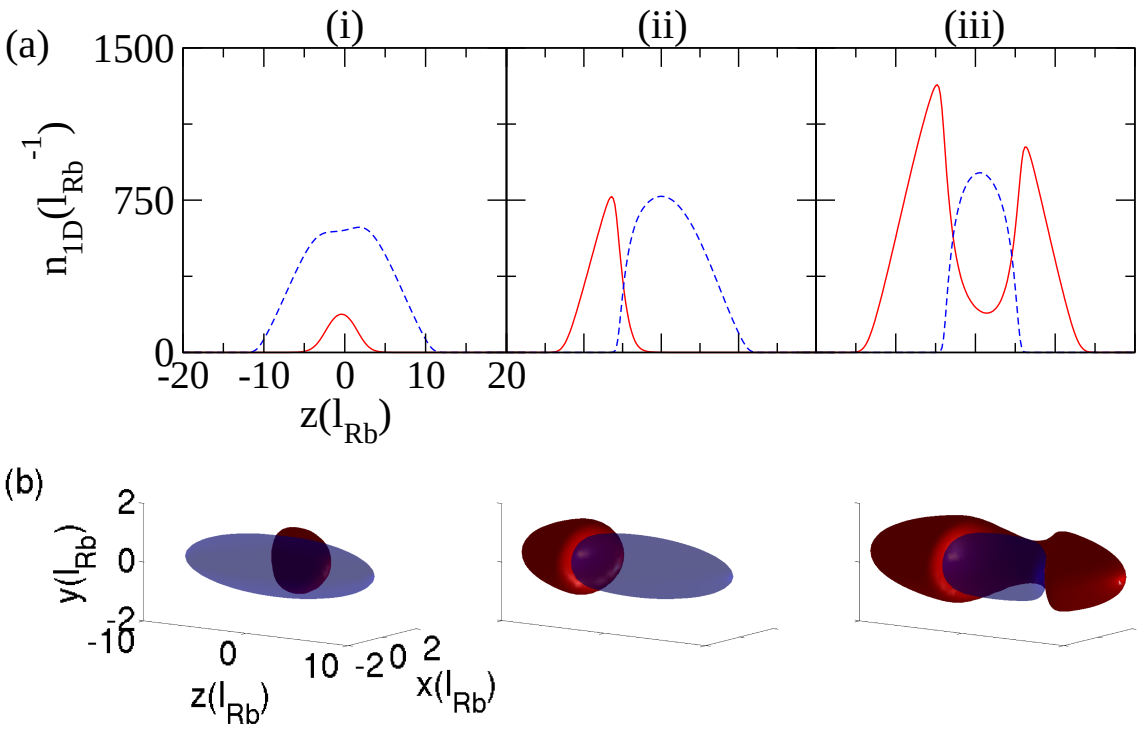

Figure 3.12: Ground states under an axial linear potential $\alpha_z = 0.02$ ($\hbar\bar{\omega}_{\rm Rb}/l_{\rm Rb}$) and a transverse linear potential $\alpha_x = 1.5$ ($\hbar\bar{\omega}_{\rm Rb}/l_{\rm Rb}$). (a) 1D density profiles and (b) 3D isosurface plots, each corresponding to the filled symbols in Figure 3.5 (a). (Solid) red curve — Rb; (dashed) blue curve — Cs.

for each species are initially offset along the z–axis. Similarly to the use of the linear potential, this initial offset could be tailored to reproduce the experimental results to a similar degree of accuracy. The asymmetries introduced via additional linear potentials are likely to represent a better physical representation of the shifts present in the experimental setup.

3.3.5 Changing Initial Conditions

Consider the test case in Region I and fully symmetric trapping ($\alpha_x = \alpha_z = 0$). Using TF profiles as initial states we obtained the integrated axial density profile shown in Figure 3.5(c)(i) in which the Rb sits either side of the central Cs cloud. By beginning instead with a very narrow Gaussian profile for the Rb while retaining the TF profile for Cs (assuming essentially here that the Cs condensate grew first) we can obtain a metastable solution whose integrated axial profile features the Rb sitting in at the trap centre and a small density dip in the ambient Cs cloud, in qualitative agreement with the corresponding experimental profile (see Figure 3.13). These solutions have higher energy than that of the solutions observed in Figure 3.5 (c) (i) and so therefore are not the 'true'

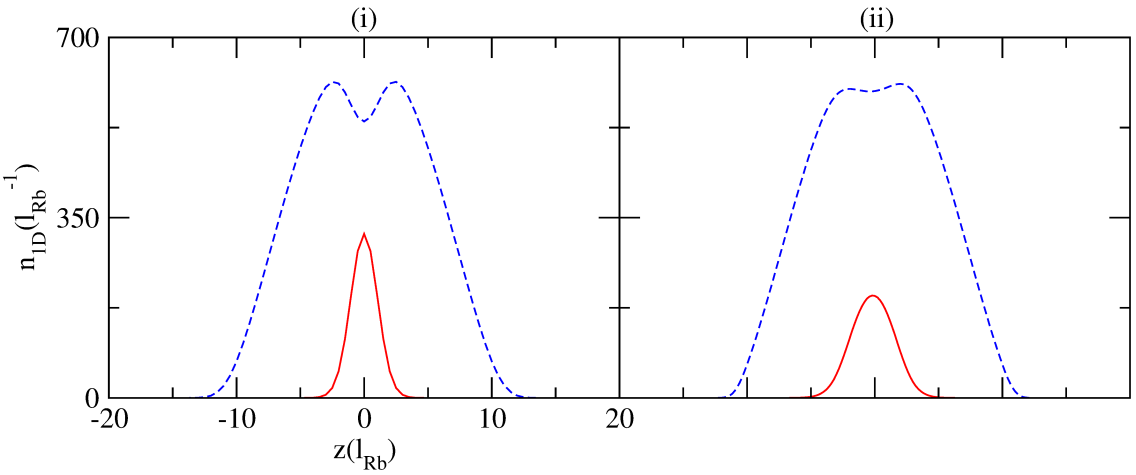

Figure 3.13: 1D ground states of Region I under an axial linear potential $\alpha_z = 0.02$ ($\hbar\bar{\omega}_{\mathrm{Rb}}/l_{\mathrm{Rb}}$) and a transverse linear potential $\alpha_x = 1.5$ ($\hbar\bar{\omega}_{\mathrm{Rb}}/l_{\mathrm{Rb}}$). Initial TF profile for Cs and (i) initial narrow Gaussian for Rb, or (ii) initial TF profile for Rb. (Solid) red curve — Rb; (dashed) blue curve — Cs.

ground states. However, in the presence of trap shifts (α_x, $\alpha_z \neq 0$), we essentially regain the true solution presented previously, i.e. the effect of the initial numerical state becomes washed out. Given that we achieve essentially no improvement in our final comparison to the experimental profiles by changing the initial states, we do not present any further results on this.

Time of flight expansion of the static solutions following the sudden removal of all trapping potentials has also been modelled numerically for this two–species system by Tom Billam (Jack Dodd Centre for Quantum Technology, Department of Physics, University of Otago, Dunedin, 9016, New Zealand). This expansion is performed experimentally prior to imaging. The analysis of these results showed that expansion does not affect the structures formed. The overall phase separation features appeared to be captured very well under the assumption made here that the profiles observed in the experiments are the true equilibrium profiles and that these profiles are dominated by their respective condensate component, with thermal clouds simply modifying these profiles by the addition of characteristic thermal tails.

3.4 Chapter Summary

In this Chapter, we have numerically simulated the ground state density profiles of two–species BECs starting with a Na–Rb mixture studied in [80] and found matching results. We then looked into an idealised 1D case with different initial conditions for the method of steepest descent to find that the width of this initial state determined which final ground state profile was obtained. In 1D, the steady state solutions are extremely sensitive to the

initial conditions. Finally we qualitatively reproduced the three density profiles observed in recent experimental results [77] with the simplest mean–field CGPEs where additional linear potentials were included with the harmonic trapping potentials to account for small asymmetries present in the experimental setup.

The density distributions are mainly determined by the underlying condensates as their interactions are dominant over those of the respective thermal atoms, and so the condensate features determine the relative picture. Advancing our studies into steady state solutions with thermal clouds such as in Hartree–Fock (previously investigated in [120, 121, 122, 123] for two–components) is not likely to introduce any major novel features but simply to extend the agreement of the observed profiles to the region of the thermal tails.

Thus, rather than undertaking such a study, in the following Chapter we chose to look into the dynamical structures that can arise by including the thermal cloud into our simulations. This was partly motived by the realisation that the rapid sympathetic cooling of this experimental system may lead to a situation where growth plays a determining factor in the final density structures formed.

Chapter 4

Growth Dynamics in Trapped Condensate Mixtures

In this Chapter, we explore the dynamics of growth in condensate mixtures using the same experimental parameters as in Chapter 3. Starting with a short introduction to the numerical methods used for solving the Coupled DGPEs (CDGPEs) where the damping terms γ_i determine the rate of growth/decay of the system, we present a number of results from numerical simulations. Following this, we briefly present the dynamical results of condensate growth obtained with the SPGPEs performed through a collaboration with I. K. Liu and S. C. Gou (Department of Physics, National Changhua University of Education, Changhua 50058, Taiwan). The latter acts as motivation for our subsequent work on the dynamics of dark–bright solitons in the framework of the CDGPEs also presented in this Chapter.

4.1 Numerical Procedure

To simulate growth in a one component condensate, we begin our dynamical simulation with an initial steady state solution obtained through imaginary time propagation with low particle numbers N and chemical potential μ. Using the DGPE (2.83), the chemical potential is suddenly increased from the initial $\mu = \mu_0$ at $t = 0$, such that $\mu \geq \mu_0$ for $t > 0$. Since μ parametrises the number of atoms in the system, this increase in μ drives the growth of the condensate. At the same instant, the growth rate γ is set to be non–zero. The growth saturates when the total energy of the system converges to a final value. In Figure 4.1, a typical example of condensate particle growth (a) and integrated density profiles (b) for a single species condensate are shown. As the system evolves over time, the number of particles increases until it reaches an upper bound controlled by the new chemical potential. Simultaneously, the peak density value and condensate width increase

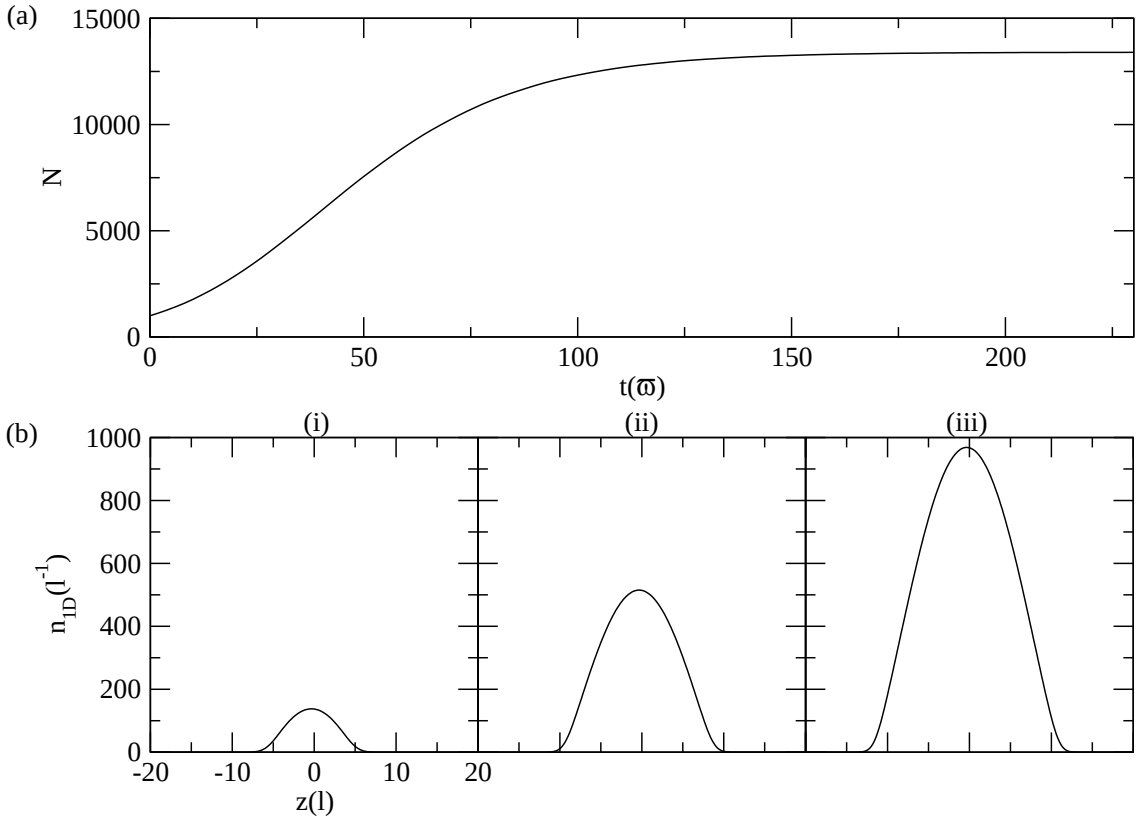

Figure 4.1: (a) Typical condensate particle growth curve against time for a single species condensate using DGPE with initial atom number $N = 2000$ and $\gamma = 0.01$. (b) Integrated, in x and y density, profiles at (i) $t = 0$, (ii) $t = 50$ and (iii) $t = 200(\bar{\omega})$.

in accordance with the number of particles.

4.2 Growth In Binary Condensates

To obtain the coupled DGPEs (CDGPEs), we use the substitution $t \to (1 - \mathrm{i}\gamma_i)\, t$ in each of Equations (2.52), introducing phenomenological dissipation which implies that particle numbers are no longer necessarily conserved. Here, γ_i determines the growth/decay rate of each species of the system. As first mentioned in Section 2.11.4 for a one species condensate, these growth rates may be estimated by fitting to experimental growth data. The following CDGPEs are thus obtained

$$\begin{aligned} \mathrm{i}\hbar\frac{\partial\phi_1}{\partial t} &= (1-\mathrm{i}\gamma_1)\left(-\frac{\hbar^2}{2m_1}\nabla^2 + V_1 + g_{11}\left|\phi_1\right|^2 + g_{12}\left|\phi_2\right|^2 - \mu_1\right)\phi_1 \\ \mathrm{i}\hbar\frac{\partial\phi_2}{\partial t} &= (1-\mathrm{i}\gamma_2)\left(-\frac{\hbar^2}{2m_2}\nabla^2 + V_2 + g_{22}\left|\phi_2\right|^2 + g_{12}\left|\phi_1\right|^2 - \mu_2\right)\phi_2. \end{aligned} \tag{4.1}$$

A similar numerical procedure to the one component system in Section 4.1 is used to simulate growth in the two component system. To achieve this, we choose to suddenly change the chemical potentials of each species; however, we note that the chemical potentials μ_1 and μ_2 are not independent of each other in the coupled equations due to the additional nonlinear term describing interspecies interactions.

We now present numerical results of the CDGPEs (4.1) with parameters from Reference [77] as used previously in this Thesis; for simplicity and we take $\gamma_1 = \gamma_2$. Growth data was not taken during those experimental realisations [238] and in fact the observed profiles cannot therefore be guaranteed to be fully equilibrated. The aim of this Chapter is to investigate whether starting with some initial density profiles in each of the three different experimental regions (see Figure 3.5), it is possible to observe evolution sequences in which the particle number growth curves pass from one region to another, demonstrating a change in the density profiles. In all of the results presented here, the trap asymmetries used for the best match between mean–field theory and experiments in Section 3.3.3 are considered ($\delta_z = 0.9\mu$m, $\delta_x = 1.0\mu$m).

4.2.1 Typical Growth Simulation

In Figure 4.2 (a) and (b), we show a typical evolution of the condensate particle numbers in each species and the combined total particles against time based on our dissipative model (Equations (4.1)). Here, we start with a large number of atoms for Cs in comparison to Rb. $N_{\rm Cs}$ decreases until it vanishes from the system while the growth of $N_{\rm Rb}$ continues until a maximum is reached. The total number decreases drastically at the start but then grows again slowly over time. This suggests that for an equal damping rate $\gamma_1 = \gamma_2$ a low number of Cs atoms is required before Rb can start to grow at a quicker pace. We also present four corresponding density profiles at $t = 0, 16, 40$ and $80(\bar{\omega})$. The initial density distribution is a symmetric density distribution where the Rb and Cs BECs sit side by side in a transverse direction. As the condensate particle numbers evolve over time, the condensate clouds become asymmetric until a side–by–side formation in the axial direction emerges. Finally, a one species condensate forms for long times as no Cs particles remain in the condensate (for the parameters chosen here).

4.2.2 Growth Trajectories Through $N_{\rm Cs}$–$N_{\rm Rb}$ Plane

Figure 4.3 shows the trajectories of multiple condensate particle growth curves in the $N_{\rm Rb}$–$N_{\rm Cs}$ plane. The regions separated by the dotted black lines have been defined in accordance to the experimental results in [77] where the structure of the density profiles observed depend on condensate particle numbers.

The trajectory taken in each of these simulations is determined by the final chemical

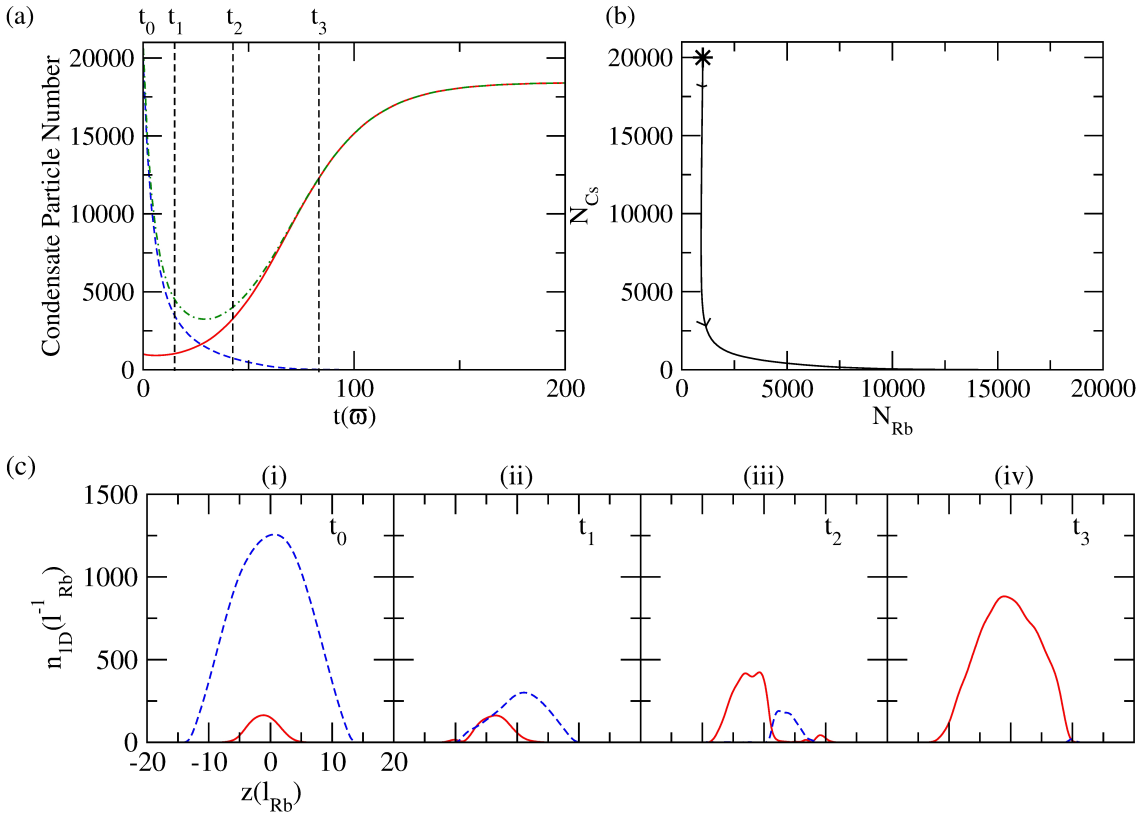

Figure 4.2: (a) Condensate particle numbers against time; Rb ((Solid) red curve), Cs ((Dashed) blue curve) and Total particle number ((Dotted) green curve). (b) Growth curve in the $N_{\rm Rb}$—$N_{\rm Cs}$ plane. (c) Bottom: Density profiles at times t = (i) 0, (ii) 16, (iii) 40, (iv) 80($\bar{\omega}$) for Rb ((Solid) red curve) and Cs ((Dashed) blue curve).

potentials rather than γ_i. For constant values of $\gamma_1 = \gamma_2$, the order of magnitude of γ_i determines solely the timescale over which growth/decay occurs although as this is already a sensitive competing dynamical growth process. Unequal γ_i's for the two species could largely modify the dynamics. In our simulations, we first note that all of the growth curves finish either on the horizontal or vertical axes, i.e. with a one component condensate where the other condensate has vanished from the system. One component is always found to vanish from the system as the growth rates do not change over time as would be the case in an experimental setup: this feature is inherent in our purely dissipative model. Physically, this represents all of the particles being in the thermal cloud for that component (although this is only implicit within our simplified model). Nevertheless, this is still broadly consistent with the experimental findings as there were numerous unpublished results showing images where only one of the species was condensed [238]. The influence of the final chemical potentials on the path taken is clear when comparing the green and orange growth curves in Figure 4.3 respectively labelled by D and E which start from the same steady state initial condition and evolve to different final single species condensates. The nonlinear dynamics and competing processes do not give us a direct handle on the precise trajectories in the N_{Rb}–N_{Cs} plane although extensive simulations have enabled us to probe the most common types of trajectories, as discussed in detail below and shown in Figure 4.3.

A number of our simulations (Figure 4.3, cases A, C and D) do not lead to any structural changes in the integrated density profiles while growth/decay occurs and each species occupies the same overall position until one vanishes (to the thermal cloud) leaving a single species condensate. In case A, the initial density profile is asymmetric with Rb and Cs sitting side–by–side in the axial direction. Once growth/decay begins, Rb vanishes rapidly from the system leaving a condensate with only Cs present. The growth curve for case B has similar initial particle numbers and similar density profile changes during growth. In this case, Rb decays while Cs grows in the centre of the trapping potentials. This growth of Cs splits the Rb into two distinct parts either side of Cs. Over longer time evolutions, Rb vanishes leaving a Cs condensate. For case D, we start with a symmetric density profile and Rb will decay over time. The asymmetric intermediate density profiles in case D are due to the asymmetry present in the initial steady state solution where, as Rb slowly decreases, the right peak of Rb vanishes before the left peak giving a side–by–side density profile. We obtain a Cs only condensate over longer time scales. In case E, we start with the same initial condition as case D but choose different final chemical potentials for each of these simulations resulting in different growth curves. In the intermediate plot for the green growth curve for case E, we observe a spontaneous dark–bright soliton (where a dip in one component is filled by the other and oscillated in the axial direction) which oscillates in the trapping potential until all the Cs bright component no longer exists in

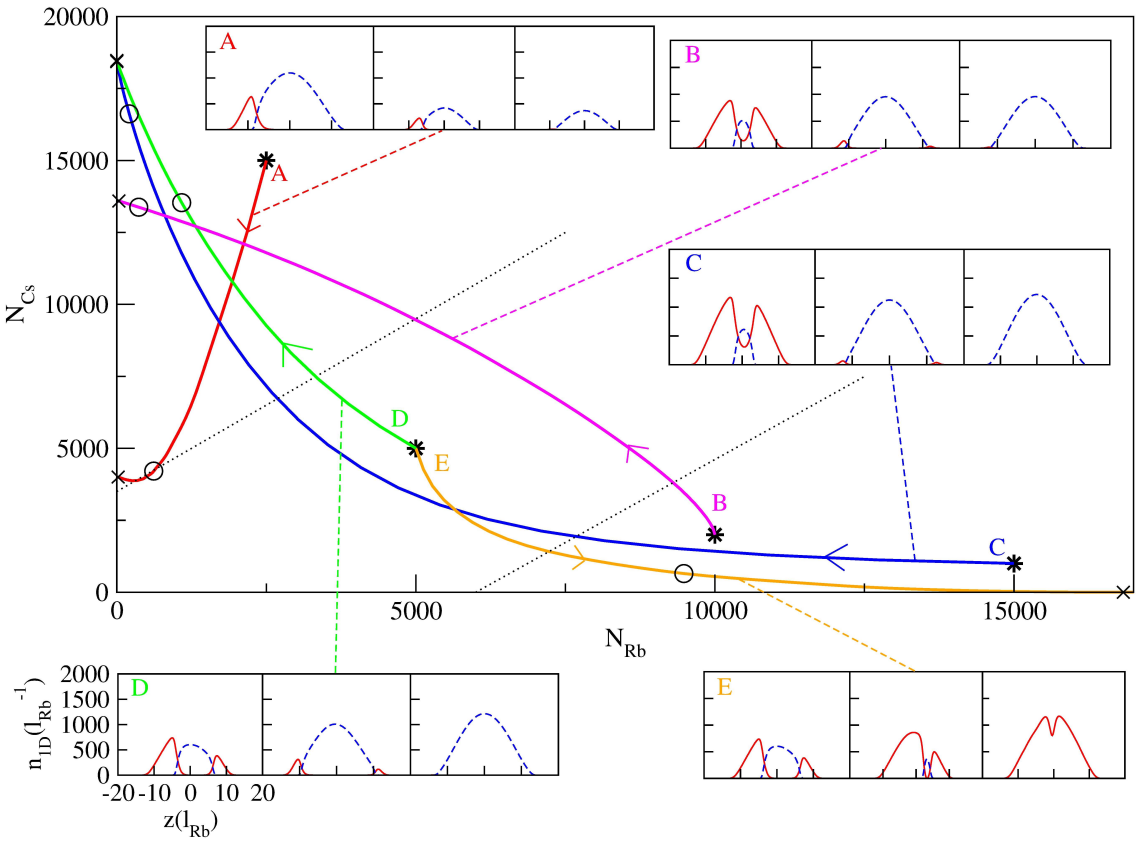

Figure 4.3: Condensate particle growth curves in N_{Cs} (vertical) and N_{Rb} (horizontal) plane. Initial (steady state), intermediate and final density distributions depicted by stars circles and crosses respectively. The intermediate and final plots are not at the same time between A-E. Dotted lines — boundaries of experimental regions. Each set of three density profiles corresponds to initial, intermediate and final 1D integrated density profiles for Rb — (Solid) red curve and Cs — (Dashed) blue curve.

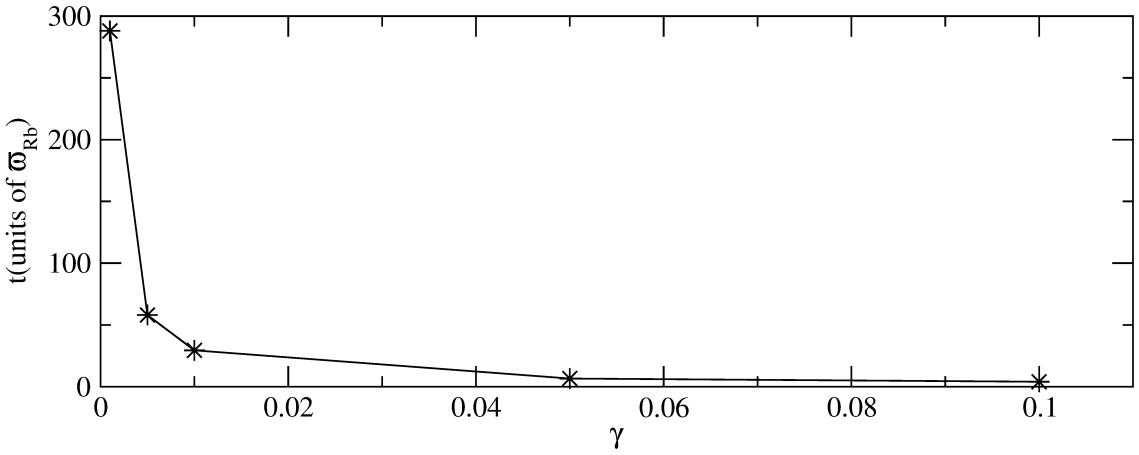

Figure 4.4: Time taken for black growth curve from Figure 4.2 to get to $N_{\rm Rb} = 8000$ and $N_{\rm Cs} = 5400$ against $\gamma = \gamma_{\rm Rb} = \gamma_{\rm Cs}$.

the system. Finally in case B, we observe similar density evolution to case D but over a different growth path in the $N_{\rm Rb}$–$N_{\rm Cs}$ plane.

The time taken for a two–species condensate mixture to grow/decay depends nonlinearly on the value of the phenomenological growth rate chosen. To show this, we follow the same procedure as for growth curve in Figure 4.2 while considering different values of $\gamma = \gamma_{\rm Rb} = \gamma_{\rm Cs}$. The dynamical evolution of the condensate clouds undergo the same changes as in Figure 4.2 but over shorter/longer timescales. Numerical results in Figure 4.4, where the time taken to grow/decay to $N_{\rm Rb} = 8000$ and $N_{\rm Cs} = 5400$ is from an initial configuration of $N_{\rm Rb} = 10000$ and $N_{\rm Cs} = 2000$ plotted against different values of $\gamma_{\rm Rb} = \gamma_{Cs}$, shows the time dependence on $\gamma_{\rm Rb} = \gamma_{\rm Cs}$ is clearly nonlinear.

In this Section, we have looked at growth/decay in a two component system corresponding to the experimental parameters used in [77] and found, in some minority cases, the density profiles evolved through different experimental regions going from a symmetric density profile to a side–by–side one. However, in the majority of cases, we have not found the growth of the condensates to match those seen experimentally. Here, we note the limits of this model such as the inability to start with thermal clouds and quench these in order to form condensates to mimic the experimental protocol in more detail. In the following Section, we will show results obtained by collaborators in Taiwan which directly include the thermal cloud through the use of Coupled SPGPE (CSPGPE). These results form the basis and are the main motivation for our subsequently presented work looking at dark–bright solitons in the context of the CDGPE.

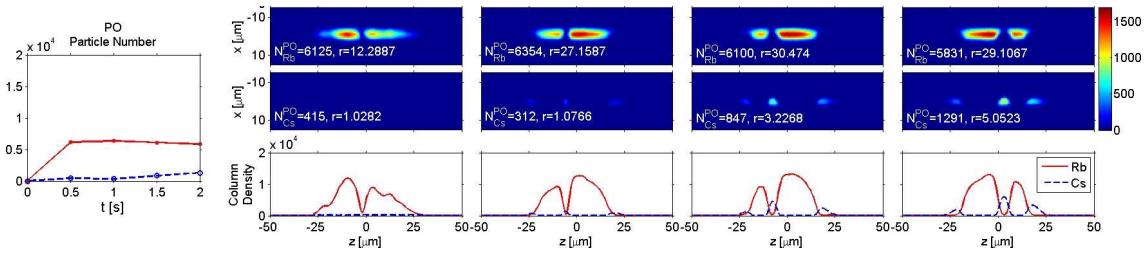

Figure 4.5: Typical CSPGPE simulation. (a) Condensate (Penrose–Onsager) particle numbers. Rb — (Solid) red curve; Cs — (Dashed) blue curve. (b) Two–dimensional surface densities for Rb(top) and Cs(bottom). (c) Integrated column density. Rb — (Solid) red curve; Cs — (Dashed) blue curve. Figure by I. K. Liu.

4.3 Coupled Stochastic Projected Gross–Pitaevskii Equations Results

In this Section, we present a brief overview of the work carried out by our collaborators I. K. Liu and S. C. Gou. These results, which reveal the spontaneous emergence of dark–bright solitons, form the basis for our motivation to investigate the role of such structures during growth in condensate mixtures within our purely dissipative model.

Figure 4.5 shows a typical CSPGPE evolution of the Rb and Cs clouds when a dark–bright soliton spontaneously emerges. In these simulations, additional linear potentials are used in the harmonic traps in accordance with the best match results from mean–field simulations to experiment covered in Chapter 3. Consistent with experimental observations [77], the Rb condensate grows first and sympathetically cools the Cs particles until these also form a condensate. In this simulation, Cs grows in a dark solitonic structure present in the Rb condensate. Oscillations of this now dark–bright soliton structure can be seen in the integrated density profile. Other simulations, where dark–bright solitons spontaneously formed, were carried out for this system. This is broadly consistent with the Kibble–Zurek scenario, whereby defects (here in the form of dark or dark-bright solitons) freeze into the density profile as the system acquires constant phase *locally* [239]. If a dark–bright soliton grows rapidly, the density becomes pinned if the Cs in the dark–bright soliton grows very rapidly, leading to mean–field potential pinning. On the other hand, if the Cs particles do not form a condensate quickly no dark–bright solitons are observed. This is due to the continued growth of N_{Rb} forcing the system into an axial side–by–side structure when Cs forms a condensate over longer time scales. We note here that similarly to results obtained for the CDGPE in Section 4.2, over long evolution times one component vanishes from the system leaving us with a single species condensate.

The remainder of our work in this Chapter is motivated by the scenario when a dark–bright solitonic structure has formed during growth and how the dark–bright soliton(s) affect the growth of the system. We shall investigate this through the CDGPEs, a cleaner

system where no noise is present in order to emphasise the role of a dark–bright soliton on the density profiles. In our simulations such a structure is imprinted in a pure form rather than the less pure stochastically generated structure arising in a real quench. In the following section, we first look at dark–bright solitons at zero–temperature in three dimensions through the CGPEs before introducing growth via CDGPEs in a subsequent section.

4.4 Dark–Bright Solitons at Zero–Temperature

Here, we investigate the dynamical evolution of dark–bright solitons in three–dimensions with the experimental parameters taken once again from [77]. The trapping potentials are elongated in one axial direction ($\omega_\perp \simeq 10\omega_z$), thus our system can be considered to be quasi–1D (see Section 2.10.3 for a discussion on the 1D dark–bright soliton). The best fit additional linear potentials to the harmonic traps between steady state mean–field simulations and experimental results from Chapter 3 are considered. In Figure 4.6, plots of the dynamical evolution for each atomic species are shown with one or two dark–bright solitons. When only one soliton is present at the beginning of the evolution (Figure 4.6 (a)), similar results to the 1D case (Figure 2.5) are observed due to cigar shaped harmonic trap, i.e. suppressed dynamics in the transverse directions due to the quasi-1D configuration. The soliton oscillates at regular intervals in the axial direction. For two initial solitons (Figure 4.6 (b)), the two interact similarly to the 1D system at first (Figure 2.8): the size of the oscillations increases due to the soliton cross overs. However after a few oscillations, the two solitons merge to form one larger dark–bright soliton. This new soliton takes up an asymmetric (non–central) position in the axial direction and has small oscillations. Over long time scales, the oscillations cease due to the phase step no longer being present once the solitons merge.

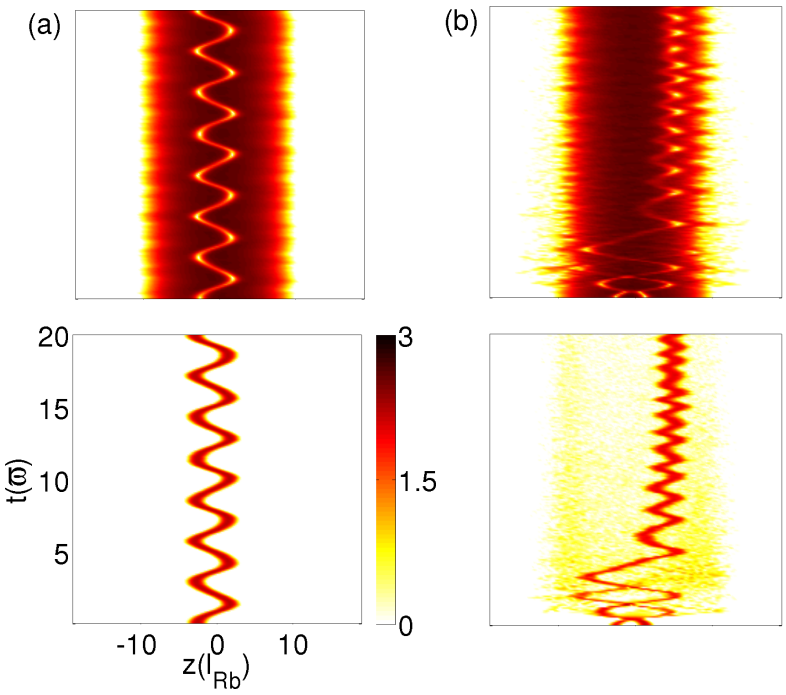

Figure 4.6: Dynamical evolution of Rb (top) and Cs (bottom) with (a) one dark–bright soliton, (b) two dark–bright solitons. Condensate particle numbers $N_{\mathrm{Rb}} = 4000$ and $N_{\mathrm{Cs}} = 200$.

4.5 Dark–Bright Solitons at Finite–Temperature

In this section we investigate the dynamical evolution of a dark–bright soliton in a two–component BEC. Growth/decay is included through the means of phenomenological growth (Equations (4.1)). Initially we consider systems with one dark–bright soliton. Then the same system with multiple solitons, all imprinted numerically through a phase slip, is examined.

4.5.1 One Dark–Bright Soliton

We present our results for different dynamical evolutions of a single dark–bright soliton in the Rb–Cs immiscible condensate mixture and observe the same results as the CSPGPE over long evolution times: one component vanishes leaving us with a one species condensate. We note here that the final chemical potentials for each species used for our simulations are given by the final particle numbers rather than set directly. The initial condition for dynamical evolution is obtained by imprinting the dark component with a π phase step during imaginary time propagation. We now present our simulation and show the effects of varying parameters.

In Figure 4.7 (a), where the final chemical potential μ_{Cs} is large, the oscillations of

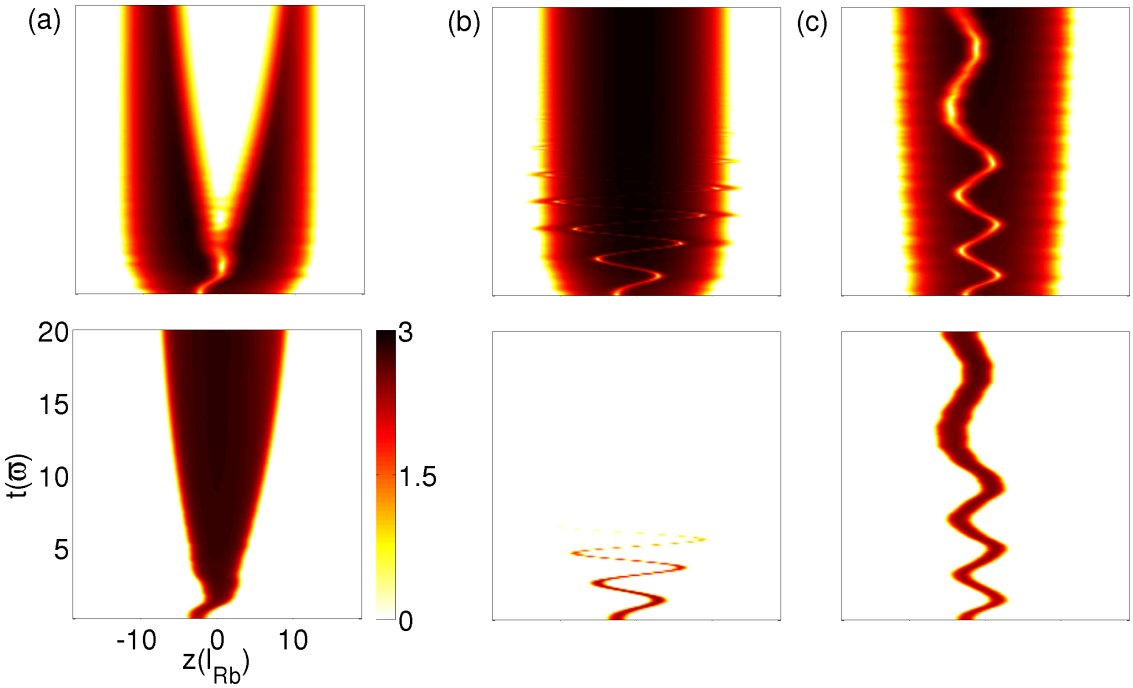

Figure 4.7: Dynamical evolution of Rb (top) and Cs (bottom) with initial dark–bright soliton. (a) $\gamma_i = 0.01$, initial condensate numbers $N_{\mathrm{Rb}} = 4000$ and $N_{\mathrm{Cs}} = 200$, final chemical potentials given by final particle numbers $N_{\mathrm{Rb}} = 15000$ and $N_{\mathrm{Cs}} = 10000$. (b) $\gamma_i = 0.01$, initial condensate numbers $N_{\mathrm{Rb}} = 4000$ and $N_{\mathrm{Cs}} = 200$, final chemical potentials given by final particle numbers $N_{\mathrm{Rb}} = 15000$ and $N_{\mathrm{Cs}} = 5000$. (c) $\gamma_i = 0.001$, initial condensate numbers $N_{\mathrm{Rb}} = 4000$ and $N_{\mathrm{Cs}} = 200$, final chemical potentials given by final particle numbers $N_{\mathrm{Rb}} = 15000$ and $N_{\mathrm{Cs}} = 10000$.

the dark–bright soliton speedily come to a stop once the number of condensed Cs atoms increase beyond a critical threshold, with Cs overwhelming in the centre of the trapping potential. In time, all Rb condensate atoms vanish from the system, resulting in a single species Cs BEC beyond the plotted timescale. Figure 4.7 (b) depicts the inverse scenario where we have small μ_{Cs}. The dark–bright soliton can be seen to oscillate, distorting the Rb cloud until the Cs bright component dies out from the system resulting in a single species Rb BEC. During the studies of this one dark–bright soliton system, we investigated the role of the initial position of the soliton but found this had minimal impact on the dynamical evolution. Similarly, the initial number of Cs particles can be increased (at least three times larger) and has minimal qualitative impact on the dynamical evolution of both condensate clouds. Figure 4.7 (c) shows the dark–bright soliton oscillating a number of times over the plotted timescale. By comparing Figure 4.7 (a) and Figure 4.7 (c) where the growth rate γ_i has been decreased by an order of magnitude, it is clear the solitonic features are prolonged due to the longer time required for the number of Cs particles to reach a critical value. After longer timescales both of these cases reach the same end

result: a single component Cs BEC.

When increasing γ_{Cs} only, shown in Figure 4.8 (a), the bright component increases quicker than previously seen in Figure 4.7 (a) and less dark–bright soliton oscillations are observed. Over longer timescales, all Rb atoms are no longer in the condensate. By decreasing γ_{Cs} only in comparison to Figure 4.7 (a), shown in Figure 4.8 (b),the bright Cs component no longer dominates in the centre of the trapping potential but rather oscillates over a long period of time until it is pushed out to one side due to the trap asymmetries we considered in our model. Eventually, all the Cs condensate cloud will vanish from the system.

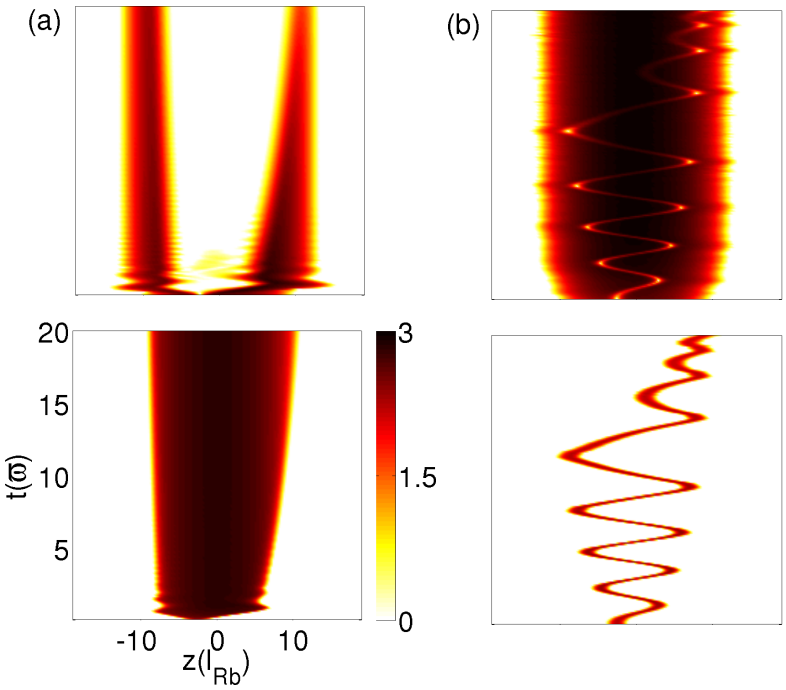

Figure 4.8: Dynamical evolution of Rb (top) and Cs (bottom) with initial dark–bright soliton. Initial condensate numbers $N_{\mathrm{Rb}} = 4000$ and $N_{\mathrm{Cs}} = 200$, final chemical potentials given by final particle numbers $N_{\mathrm{Rb}} = 15000$ and $N_{\mathrm{Cs}} = 5000$. (a) $\gamma_{\mathrm{Rb}} = 0.01$ and $\gamma_{\mathrm{Cs}} = 0.1$, (b) $\gamma_{\mathrm{Rb}} = 0.01$ and $\gamma_{\mathrm{Cs}} = 0.001$.

The difference in the dynamical evolution due to the impact of the additional linear potentials to the harmonic trapping potential may not be extensive but the small changes that these create are still clear as shown in Figure 4.9. The most significant change is the time taken for the condensate clouds to grow/decay: when the trap asymmetries are *not* present the dynamics evolve over a smaller timescale and single species BECs arise sooner. A by product of this feature is the number of visible oscillations from the dark–bright soliton is reduced.

When a single dark–bright soliton is present in the initial density profile and growth

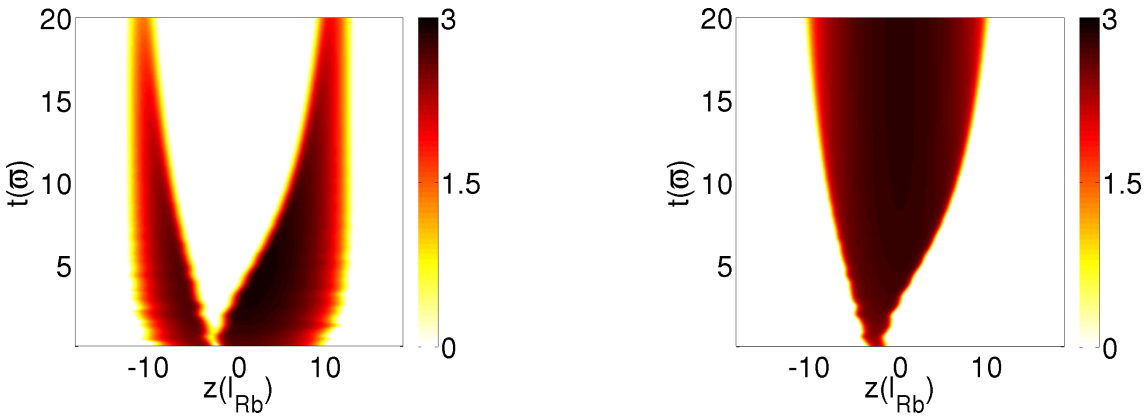

Figure 4.9: Dynamical evolution of Rb (left) and Cs (right) with initial dark–bright soliton with no offset in harmonic trapping potential. $\gamma_i = 0.01$, initial condensate numbers $N_{\mathrm{Rb}} = 4000$ and $N_{\mathrm{Cs}} = 200$, final chemical potentials given by final particle numbers $N_{\mathrm{Rb}} = 15000$ and $N_{\mathrm{Cs}} = 10000$.

is modelled through phenomenological damping, we have seen that even though there are only two possible steady state outcomes (condensates of either Rb or Cs), many different dynamical paths can be taken to reach these final density profiles. Experimentally, growth ceases before time of flight expansion and any density profile during the dynamical evolution can be imaged.

4.5.2 Multiple Dark–Bright solitons

In this section, we present numerical results for the dynamical evolution of a two–component system with two initial dark–bright solitons. Once again, finite–temperature effects are included through phenomenological growth via the CDGPEs.

In Figure 4.10, the results for three simulations are shown where *only* the position of one soliton has been changed. In the axial direction z, the left–hand side soliton has the same initial position ($z(l_{\mathrm{Rb}}) = -2.6$) while the starting position of the right hand soliton is varied. In all three simulations, the Cs condensate will continue to grow while the Rb cloud will decay eventually leaving us with a one component Cs condensate only. This is consistent with Figure 4.7 (a) as the same parameters are used, the sole difference being the additional initial dark-bright soliton. In Figure 4.10 (a), the right hand soliton is close to the centre of the trap in comparison to the left soliton ($z(l_{\mathrm{Rb}}) = 1.2$). When these solitons begin to oscillate, they initially cross paths similarly to dark–bright solitons at zero temperature (Figure 2.8). Once the solitons have interacted, one stabilises at the centre of the trapping potential while the other is pushed to the outskirts of the trapping potential, in accordance with the asymmetries present due to the additional linear potential. Over longer time scales, the growth of the soliton in the centre of the system continues while the other decays giving similar results to Figure 4.7 (a). In Figure 4.10 (b), the right hand side soliton is placed further away from the centre of the trap ($z(l_{\mathrm{Rb}}) = 5.0$). In this case,

when the solitons meet due to their oscillations they merge to form a single dark–bright soliton. After a few small oscillations the soliton is fixed at the centre of the trap resulting in a comparable outcome to Figure 4.7 (a). Finally, Figure 4.10 (c) has initial dark–bright solitons placed symmetrically either side of the trap centre (right hand side soliton at $z(l_{\mathrm{Rb}}) = 2.6$). In this case, we get a mixture of the previous two results. The solitons initially cross paths and then merge into one larger dark–bright soliton.

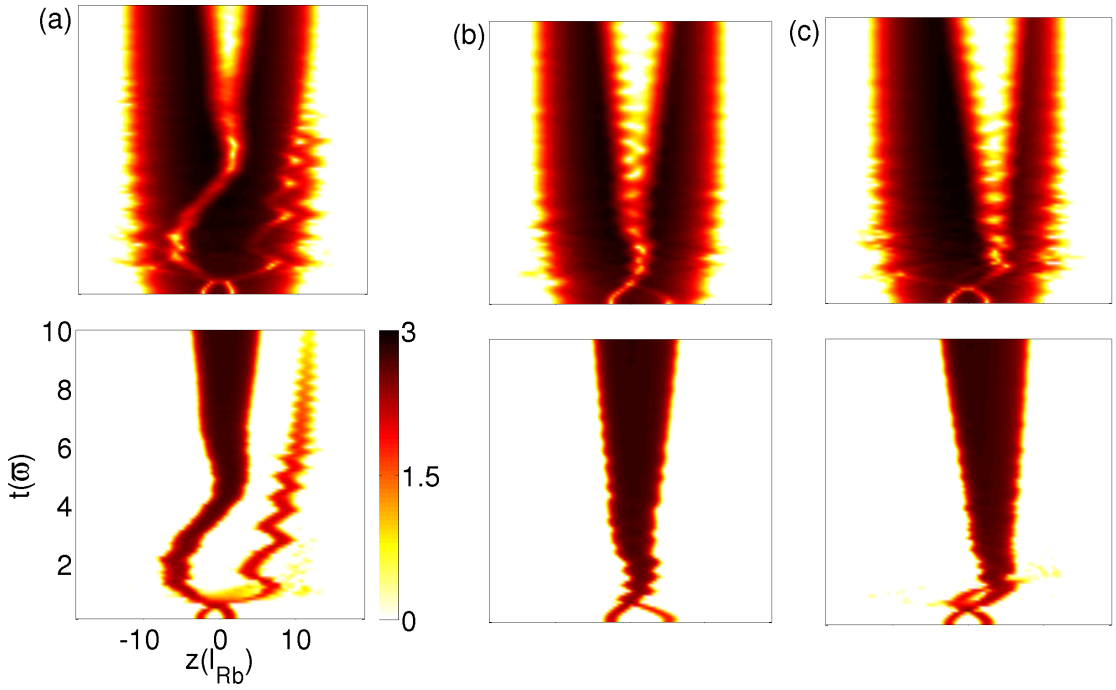

Figure 4.10: Dynamical evolution of Rb (top) and Cs (bottom) with initial dark–bright solitons with $\gamma_i = 0.01$, initial condensate numbers $N_{\mathrm{Rb}} = 4000$ and $N_{\mathrm{Cs}} = 200$, final chemical potentials given by final particle numbers $N_{\mathrm{Rb}} = 15000$ and $N_{\mathrm{Cs}} = 10000$. Initial position ($z(l_{\mathrm{Rb}}) = -2.6$) of left soliton unchanged throughout. Right soliton (a) $z(l_{\mathrm{Rb}}) = 1.2$, (b) $z(l_{\mathrm{Rb}}) = 5.0$ and (c) $z(l_{\mathrm{Rb}}) = 2.6$.

We attempted to add more solitons to the system but two would merge while using imaginary time propagation giving us once again two initial solitons. However, from Figure 4.10, we obtained the same qualitative dynamics once the solitons have merged or one has decayed compared to the same system with one soliton when equivalent parameters are used. This leads us to believe that a system with more solitons would have similar results in which one central Cs condensate cloud would remain at the centre of the trapping potential. Thus the dynamics over long time scales does not appear to depend on the number of initial dark–bright solitons. However, the number of initial dark–bright solitons does lead to a large amount of possible density profiles over short time scales.

4.6 Chapter Summary

In this Chapter we simulated growth in a two–component system through phenomenological growth in the CGPEs. We showed that over long time scales one condensate species would always grow while the other would decay. This growth/decay is dependent on the final chemical potentials used where each chemical potential affects the other species. During the simulations, when the growth curve crossed through experimental regions [77], changes in the density profiles were seen in agreement with experimental results despite these happening in a minority of cases. Our collaborator I. K. Liu examined this system through evolutions of the CSPGPE and observed spontaneous formation of dark–bright solitons which turned out to be rather crucial in the short to intermediate timescales of relevance to experiments. After introducing dark–bright solitons in two–species condensates at zero temperature, we looked at the evolution of solitons when growth/decay is included in the model. This system will also give a clearer picture of the impact of dark–bright solitons only in comparison to the CSPGPE results. The oscillations of dark–bright solitons die out when growth is included, and the time scale is dependent on the magnitude of the growth rate. The deliberate inclusion of multiple dark–bright solitons leads to new possible density profiles over short time scales, however over longer time scales the same dynamical evolution as for one soliton is observed when using equivalent parameters.

Part III

Classical Field Methods for Non Trapped Bose Gases

Chapter 5

Condensate Mixture Dynamics at Non–Zero Temperatures

In this Chapter, we investigate finite temperature effects through strongly nonequilibrium initial conditions as first introduced in Section 2.11.5. After providing a description of our numerical procedure, we present typical results of our simulations obtained by dynamical evolution of the dimensionless GPE. By first studying the evolution of a single species until a thermalised state is reached, we compare miscible and immiscible two component systems with nonequilibrium initial conditions. The coupled evolution is then investigated when the particles from a single thermalised component are split into two components. Finally the impact of quenching the interspecies interactions is studied. We then present the outcome of repeated quenches at regular time intervals, with the intention of determining the extent to which a vortex tangle can be sustained as this could provide a novel route to quantum turbulence.

5.1 Exploring Single Component Results

In this Section, we describe the numerical procedure used to simulate the evolution of single component systems from highly nonequilibrium initial conditions. We then qualitatively reproduce the numerical results from References [224, 232] when exploring the evolution of this system before generalising these findings to two component systems in the following Section.

5.1.1 Numerical Procedure

Our numerical simulations are conducted within a three dimensional periodic box starting with strongly nonequilibrium initial conditions in the GPE. These are

$$\phi\left(\mathbf{r}, t=0\right) = \sum_{\mathbf{k}}^{\mathbf{k}_{max}} a_{\mathbf{k}} \exp\left(i\mathbf{k}\cdot\mathbf{r}\right) \tag{5.1}$$

where the phases of the complex amplitudes $a_{\mathbf{k}}$ are distributed randomly. The initial wavefunction $\phi\left(\mathbf{r}, t=0\right)$ is renormalised to fix the particle and energy densities. The condensed particle and occupation numbers are calculated over time using the Discrete Fourier Transform, detailed in Appendix C. For all the simulations, we use the time step $\mathrm{d}t = 0.01$ with all physical quantities presented in this Chapter expressed in terms of natural units. The initial state is propagated in time using the GPE (2.45) until an equilibrium solution is reached where the condensate fraction n_0/N is constant. To determine the equilibrium properties of the system, we use the ergodic hypothesis such that time averages on our simulations represent ensemble averages. Unlike the Penrose–Onsager criterion for Bose–Einstein condensation where the condensate wavefunction corresponds to the mode of the system which has the largest eigenvalue [119], the number of particles in the condensate is identified here by the occupation number of the zero momentum mode $\mathbf{k} = 0$. In these calculations, an ultraviolet momentum cutoff, $\mathbf{k}_c$, is introduced such that, for $\mathbf{k} > \mathbf{k}_c$, $n_{\mathbf{k}}(t) = 0$. In natural systems, the cutoff manifests itself through viscosity or diffusion effects [232]. In numerical simulations of the GPE equation, this cutoff arises naturally due to spatial discretisation. The effect of varying the cutoff has been considered by repeating simulations with more spatial points in each direction [240]. The results at equilibrium were found to be independent, within statistical error, of the cutoff due to spatial grid discretisation.

5.1.2 Quasicondensate Evolution

Starting with nonequilibrium initial conditions, we performed numerical simulations with varying numbers of computational modes. We show the evolution of the condensate fractions in Figure 5.1 for three numbers of modes (16^3, 32^3, 64^3). The condensate fraction n_0/N increases during dynamical evolution of the system until it converges to some value as the system approaches the some thermodynamic limit. Over long periods of time, the condensate fraction is independent of the number of modes for equal particle and energy densities. In other words, the number of modes only weakly affects the condensate atom number fraction in the thermodynamic limit.

Now, we investigate the effect of increasing the total energy while keeping the particle density N/V fixed. This is equivalent to increasing the kinetic energy in the system.

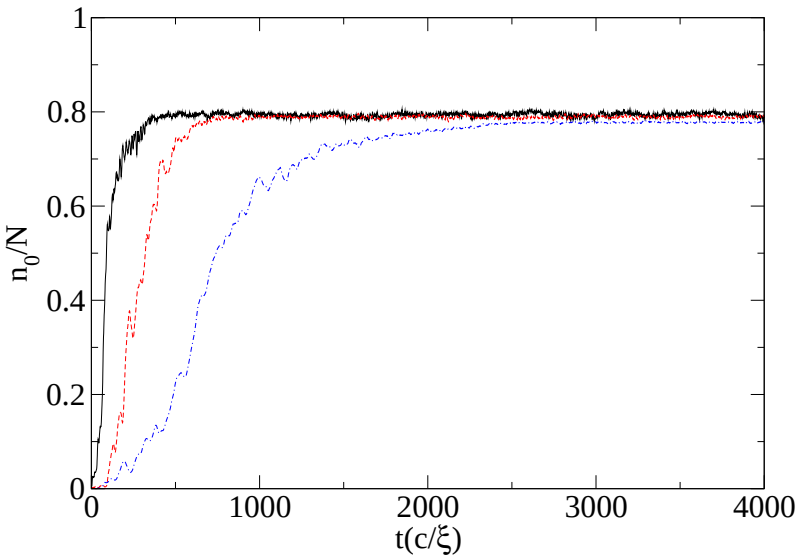

Figure 5.1: Temporal evolution of condensate fraction n_0/N with $\langle E\rangle/V = 1$, $N/V = 1/2$. (Solid) black curve — 16^3 computation modes; (dashed) red curve — 32^3 computation modes; (dot–dashed) blue curve — 64^3 computation modes.

When the total energy is increased, the final condensate fraction in the system is expected to decrease. Figure 5.2 shows the numerical results for simulations with different total energy. The condensate fraction decreases as the total energy is increased. Similarly if the particle density is increased (decreased) for fixed energy, the condensate fraction increases (decreases) due to the energy per particle decreasing (increasing).

Figure 5.3 shows the distribution of particles $N_k = \sum_{k' \leq k} n_{k'}$ where $k = \sqrt{k_x^2 + k_y^2 + k_z^2}$. The occupation of the condensate mode ($k = 0$) increases over time. This is consistent with the increase of the condensate fraction (Figure 5.1). We note the presence of a "shoulder", i.e. sharp change in gradient of the curves, which becomes sharper for longer simulation times as particles are redistributed. By definition of N_k, the number of quasicondensate particles is equal to the height of the shoulder. This evolution of the distribution of particles is in agreement with previous numerical simulations from Reference [224]. In simulations with 64^3 computational modes, the quasicondensate part of the wavefunction arises swiftly. The pronounced shoulder takes longer to appear for a higher number of computational modes. In our units, each momentum mode, i.e. $k = 0, 1, 2...(\sqrt{12}\pi/L)$, where L is the half number of computational modes in each direction, represents one energy level.

It is important to track the topological defects of the long–wavelength part of the complex field ϕ. To achieve this, we follow the approach in References [224, 234, 241] where high–frequency momenta are suppressed by the transformation $a_{\mathbf{k}} \rightarrow a_{\mathbf{k}} * \max\{1 - k^2/k_c^2, 0\}$ for a cutoff wavenumber k_c. In choosing the cutoff wavenumber k_c to plot the evolution

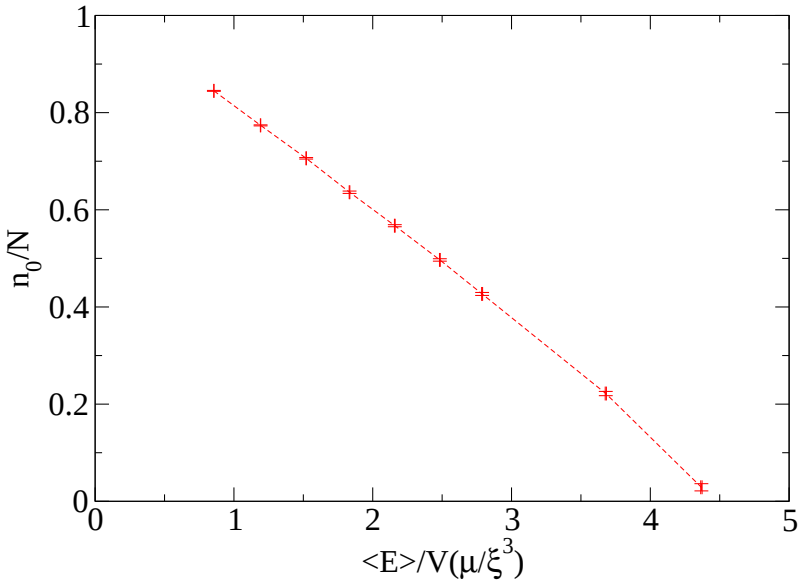

Figure 5.2: Condensate fraction n_0/N against total energy density $\langle E\rangle/V(\mu/\xi^3)$. Each simulation has 64^3 modes with $N/V = 0.5$. Each point and error bars are averaged over 10^3 time units.

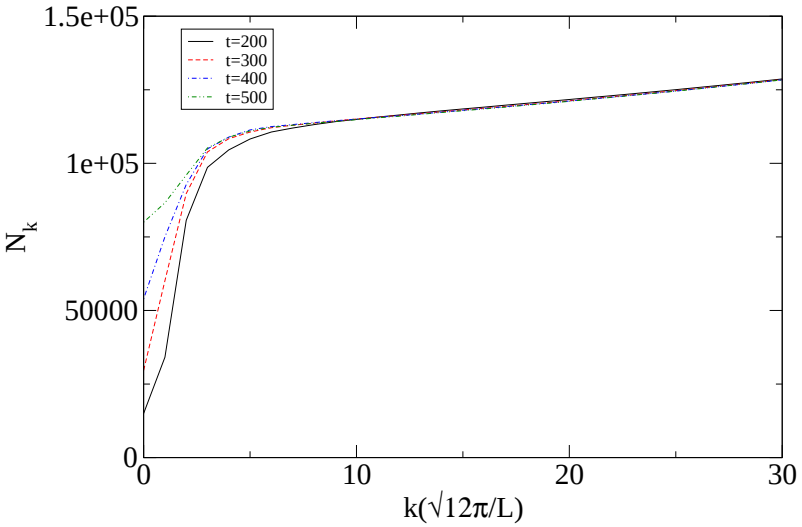

Figure 5.3: Evolution of $N_k = \sum_{k'\leq k} n_{k'}$ for $\langle E\rangle/V = 1$, $N/V = 1/2$ with 64^3 computational modes.

of topological defects, it is natural to take k_c larger than the shoulder (see Figure 5.3) to encompass the entirety of quasicondensate and remove the higher momentum part of the wavefunction.

Figure 5.4 shows the results of visualising topological defects where the cut off wavenumber is given by $k_c = 8(\sqrt{12}\pi/L)$. All of the Figures showing topological defects in this Chapter use the isosurface $\left|\tilde{\phi}\right|^2 = 0.05\langle\left|\tilde{\phi}\right|^2\rangle$ where $\tilde{\phi}$ is the long wavelength part of the field ϕ. With our chosen value for k_c, the eight lowest energy levels are included and it is larger that the shoulder in Figure 5.3, therefore none of the quasicondensate modes are neglected. The initial turbulent quasicondensate decays quickly due to thermalisation and reconnections leading to a vortex tangle. The number of vortices continue to slowly decay until only a few vortex rings are visible. At $t = 1200$, 1400 and $1600(c/\xi)$ we see the last topological defect of the turbulent decay: a single vortex ring. For longer times, the vortex ring decays leaving no topological defects in our numerical box.

In order to encompass the quasicondensate part, we choose $k_c = 8$ for the remainder of this Chapter based on the positioning of the shoulder in Figure 5.3. However, there is no exact cutoff and we found that all the results were largely independent for a range of values. For the evolution shown in Figure 5.4, the results were independent for $6 \leq k_c \leq 14$. In contrast to the phenomenological cutoff used in References [224, 234, 241], a constant cutoff is preferable rather than a time dependent formula due to the nature of the work in the following Sections of this Chapter. All results starting with highly nonequilibrium initial conditions can follow a phenomenological cutoff but this is no longer valid if system parameters are changed over the course of numerical simulations.

The exponential decay of the vortex linelength related to Figure 5.4 is shown in Figure 5.5. The vortex linelength decays faster(slower) for larger(smaller) energy densities. The algorithm to calculate the vortex linelength was written by N. G. Berloff (Department of Applied Mathematics and Theoretical Physics, University of Cambridge, Cambridge, United Kingdom) and updated by A. J. Youd (Joint Quantum Centre Durham-Newcastle, School of Mathematics and Statistics, Newcastle University, Newcastle upon Tyne, NE1 7RU, United Kingdom). After the high–frequency momenta have been suppressed, the algorithm checks for where the wavefunction is zero to find where the cores of the vortices are located. We generalised this method for use with two components in the following Section. One other possible method for calculating vortex linelength is to investigate the location of 2π phase windings in the system. Figure 5.6 shows the location of the vortices located by the algorithm corresponding to the isosurface at $t = 1400(c/\xi)$ in Figure 5.4. To confirm the presence of a vortex ring, we take a slice through the ring in one direction ($x = 20(\xi)$) and plot the phase of the slice in Figure 5.7. A 2π phase winding is observed at the locations where the vortex ring crosses the plane of the view. These wind in opposite directions due to the opposite rotation of the vortices at each point: clockwise and

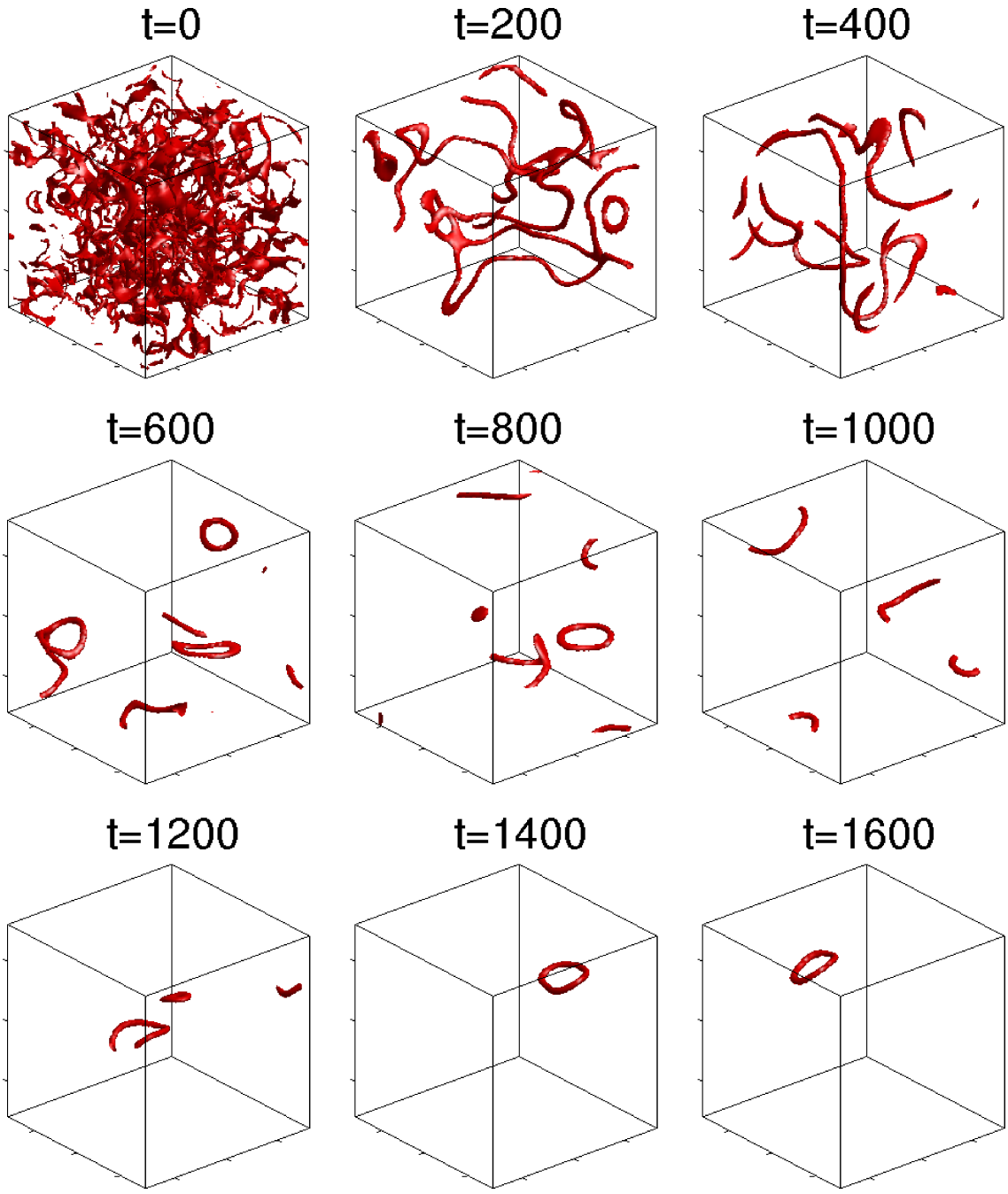

Figure 5.4: Evolution of topological defects given by the isosurfaces $\left|\tilde{\phi}\right|^2 = 0.05\langle\left|\tilde{\phi}\right|^2\rangle$ where $\tilde{\phi}$ is the long wavelength part of the field ϕ. The cutoff number is given by $k_c = 8$ such that high–frequency spatial waves are suppressed by the factor $\max\{1 - k^2/k_c^2, 0\}$.

anticlockwise respectively.

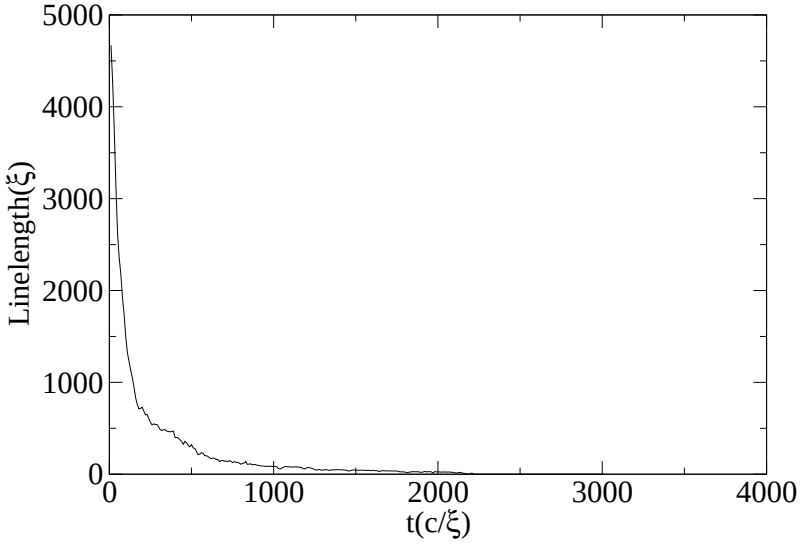

Figure 5.5: The decay of vortex linelength over time corresponding to the evolution in Figure 5.4.

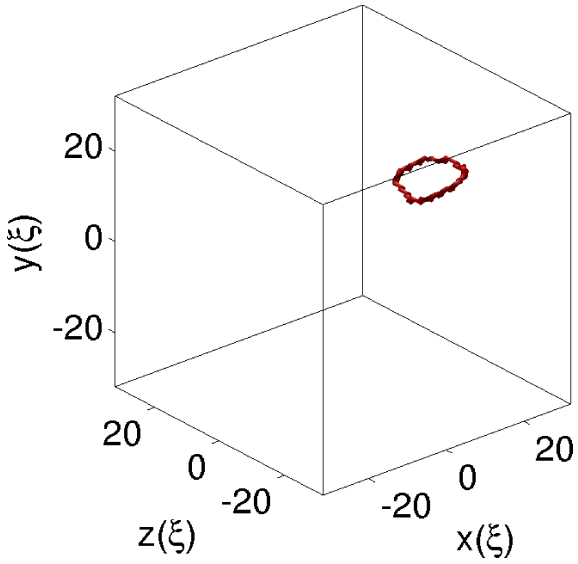

Figure 5.6: Vortex ring located by linelength algorithm corresponding to isosurface plot at $t = 1400$ in Figure 5.4. Axis shown for to clarify location of 2D slice shown in Figure 5.7.

We presented in detail the dynamical quasicondensate evolution for a single component starting with highly non–equilibrated initial conditions. The condensate fraction increases over time until it reaches thermal equilibrium, determined by the particle and energy densities. By visualising the topological defects, the decay of the initially turbulent vortices

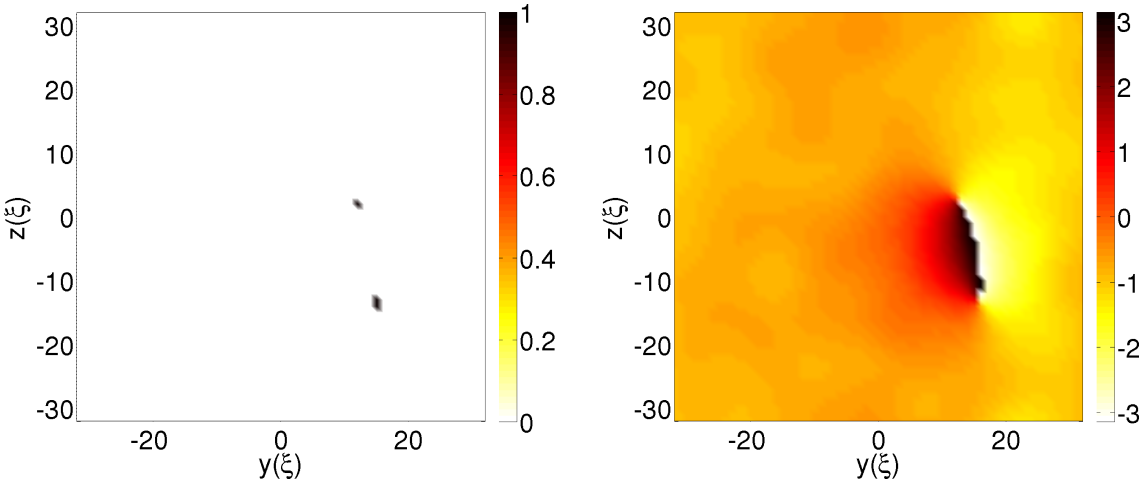

Figure 5.7: (Left) Isosurface slice in $y-z$ plane at $x = 20$ from Figure 5.6. (Right) Phase of filtered wavefunction in $y - z$ plane at $x = 20$.

is visible and confirmed by the exponential decay of the total vortex linelength. In the following Section, we study the role of a second additional component in the system and investigate the importance of the immiscibility criteria.

5.2 Mixtures

Having introduced and tested our numerical scheme and method against existing results, we now tackle the two component problem where the main differences with a single component are caused by the addition of the interspecies interaction strength now present in the model. We first look at two components and initiate both of these with nonequilibrium initial conditions. This has been previously studied in the case of miscible quasicondensates only [234, 241]. Then, starting with an equilibrated single species wavefunction, we split the particles between components and dynamically evolve this new system. This procedure is experimentally relevant when two hyperfine states of the same atom are used as the two components. Finally, we consider the impact of quenching the interspecies interactions strength on the condensate fractions and vortex linelengths. Throughout all of the results presented in this Section, we take $m_1 = m_2$ which is consistent with experiments where two hyperfine states of the same atomic species are considered.

5.2.1 Nonequilibrium Initial Conditions

Similarly to our initial conditions for a single component in Section 5.1.2, we first consider each component to have different highly nonequilibrium initial conditions. Simulations for weak interspecies interactions with nonequal particle and energy densities have been

carried out and our results are in excellent agreement with References [234, 241]. The main aim for these numerical simulations is to investigate the consequences of varying the strength of the interspecies interaction to encompass both miscible and immiscible regimes.

First we investigate miscible condensates for which the evolution of the topological defects are presented in Figure 5.8 where we have used a constant cutoff k_c and equal particle and energy densities. We stress here that a range of cutoffs were once again examined and no changes were observed in the isosurface density plots. The observed vortex decay is similar to that seen in Figure 5.4 where the vortex tangle decreases with time. The first component (shown in red) vanishes first. A single vortex ring is observed at $t = 1400$ and $t = 1600$. The radius of this vortex ring decays over time until vanishing leaving no topological defects.

Figure 5.9 shows the topological defects for an immiscible system. Contrary to the miscible case, the initial vortex tangle does not decay. We now observe the boundaries of the phase segregated domains. The components quickly separate into two domains: one for each quasicondensate. The filtered isosurfaces no longer depicts the vortices in the system but the interface between the components, i.e. the boundary of each quasicondensate. Unlike miscible quasicondensates, these topological defects never vanish from the system as the condensates constantly interact with each other. For an immiscible system, a measure of vortex linelengths is required to determine the dynamics inside each of the spatially separated domains.

The evolution of the condensate fractions starting from highly nonequilibrium initial conditions for a range of values for g_{12} are shown in Figure 5.10. Due to each component starting with the same particles and energy densities the thermalised condensate fraction values are the same for each component. As the interspecies interaction strength is increased, we see the condensate fraction decreases due to the additional energy present in the system from the stronger interspecies interaction terms in each of the CGPEs. This feature is enhanced when the immiscibility criteria is satisfied.

The vortex linelengths corresponding to the condensate fractions of Figure 5.10 are shown in Figure 5.11. For the miscible condensates, the vortex linelengths decay in a similar manner as seen for a single component. We note that, even though the condensates are miscible in both cases (blue and green curves), the larger the interspecies interaction strength the quicker they decay. We have seen complimentary results in a single component to correlate this finding: by increasing the intraspecies interactions, the decay of the vortex linelength occurs more quickly. For immiscible condensates, the vortex linelength does not drop to zero but rather decreases to a steady limit. A typical example of the vortices counted by the linelength algorithm are shown in Figure 5.12 showing the presence of vortices in each of the spatially separated quasicondensate domains. By taking a slice at

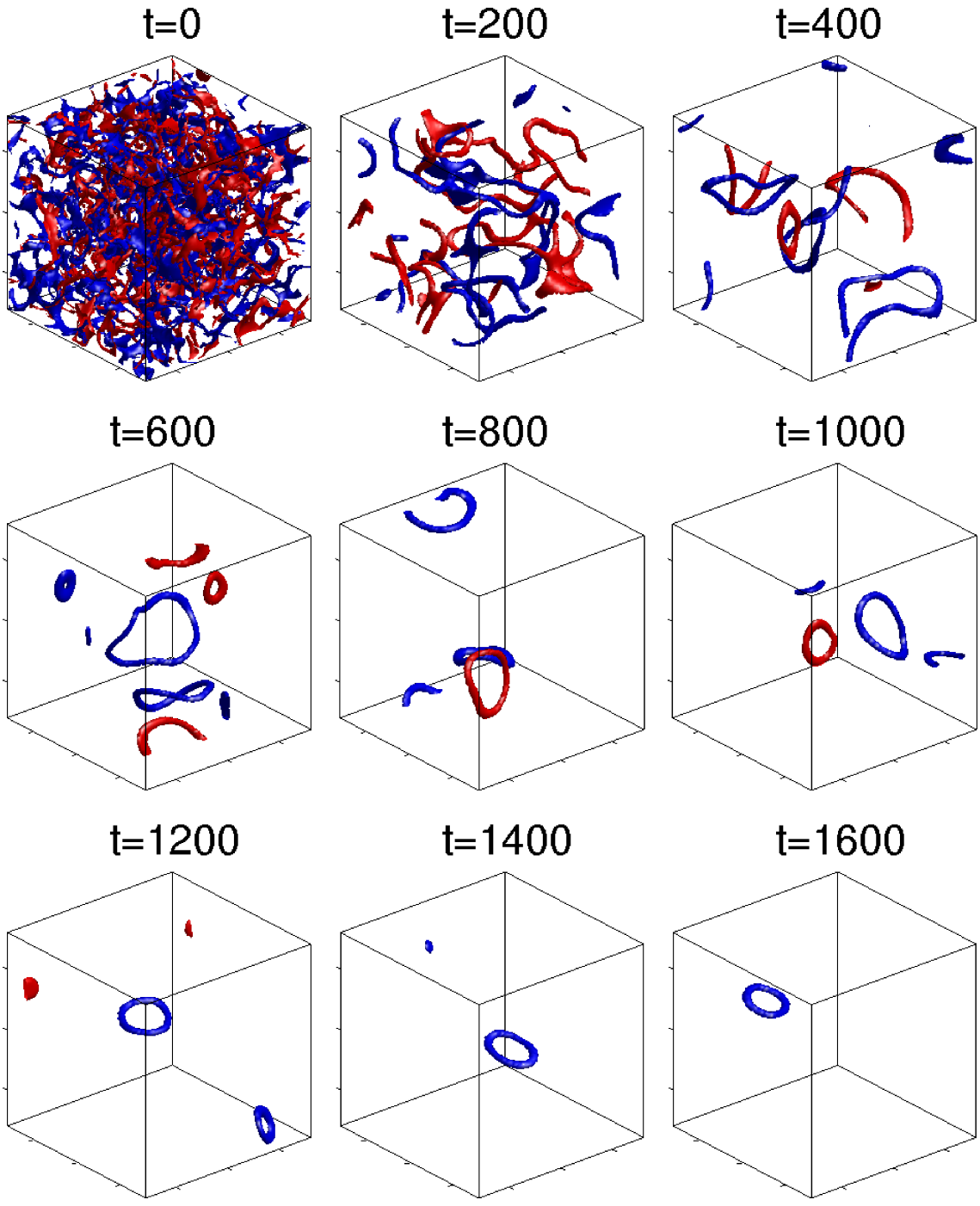

Figure 5.8: As in Figure 5.4, evolution of topological defects of two components with $g_{11} = g_{22} = 1.0$ and $g_{12} = 0.5$ (miscible). Both wavefunctions share the same initial energy and particle densities for nonequilibrium initial conditions. First component — red; Second component — blue.

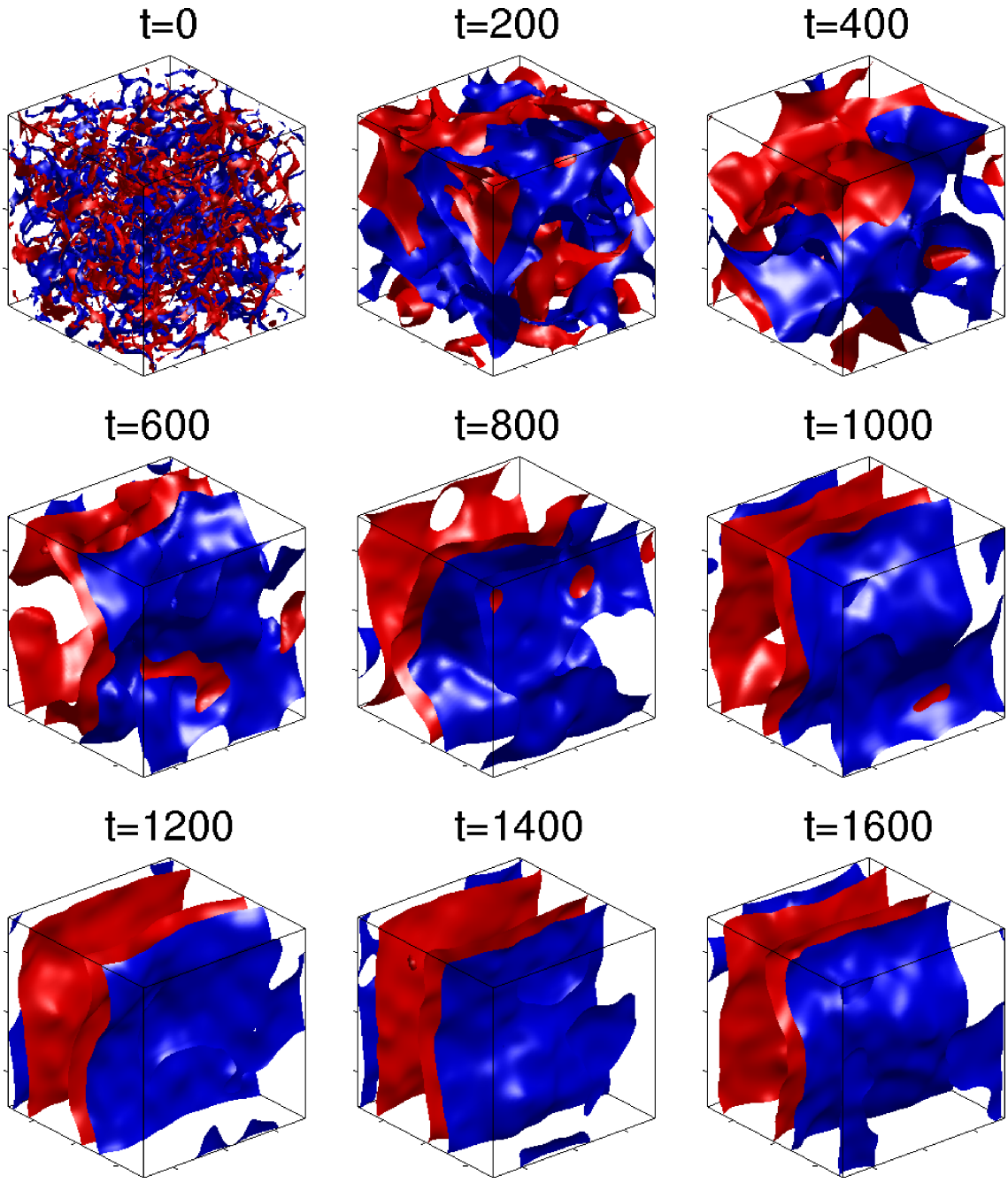

Figure 5.9: As in Figure 5.8 but with $g_{11} = g_{22} = 1.0$ and $g_{12} = 1.5$ (immiscible). First component — red; Second component — blue.

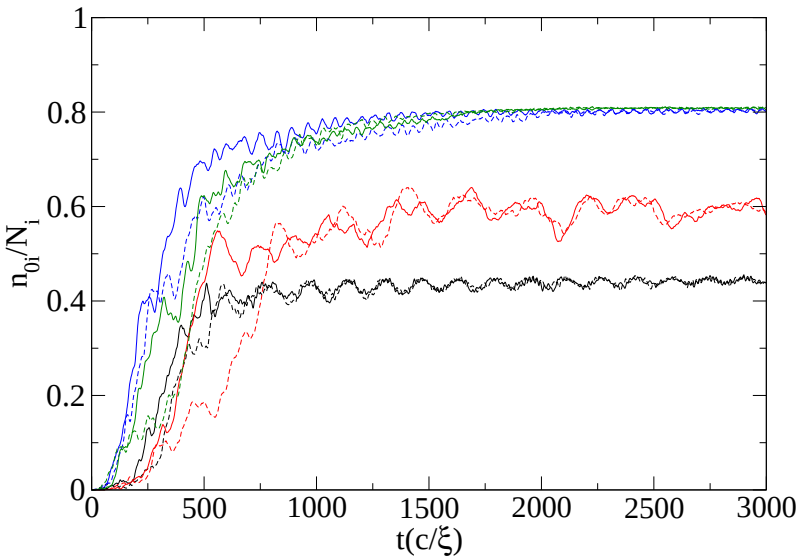

Figure 5.10: Condensate fraction n_{0i}/N_i evolution for two components starting from nonequilibrium initial conditions with same energy and particle densities with $g_{12} = 1.5$ (black curves), $g_{12} = 1.05$ (red curves), $g_{12} = 0.5$ (blue curves) and $g_{12} = 0.1$ (green curves). In all curves $g_{11} = g_{22} = 1.0$. First component — solid curves; Second component — dashed curves.

$x = 0$ for each component (see Figures 5.13 and 5.14) and plotting their corresponding phase portraits, 2π phase windings confirm the presence of vortices. Higher numbers of vortices are present in each domain for larger *immiscible* interspecies interactions.

Different thermalised condensate fractions are obtained depending on the initial kinetic energy and number of particles in each component. Figure 5.15 shows the evolution of the condensate fractions for three simulations with equal particle and kinetic energies in each component. The additional total energy is due solely to the increase in interspecies interaction strength. For miscible condensates, the condensate fraction of one component increases while the other decreases in comparison to zero interspecies interactions. This is due to both components equilibrating to the same temperature. The added energy for immiscible components decreases the condensate fraction for both components.

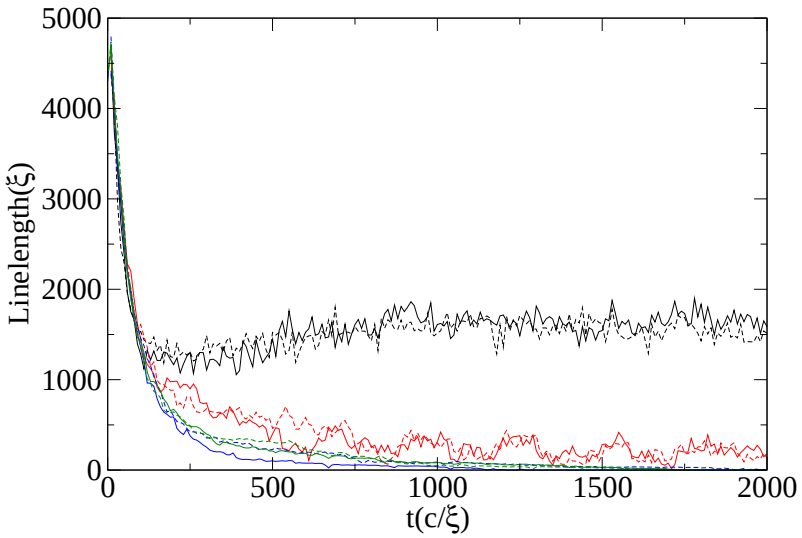

Figure 5.11: Vortex linelengths over time with $g_{11} = g_{22} = 1.0$ for $g_{12} = 1.5$ (black curves), $g_{12} = 1.05$ (red curves), $g_{12} = 0.5$ (blue curves) and $g_{12} = 0.1$ (green curves). First component — solid curve; Second component — dashed curve.

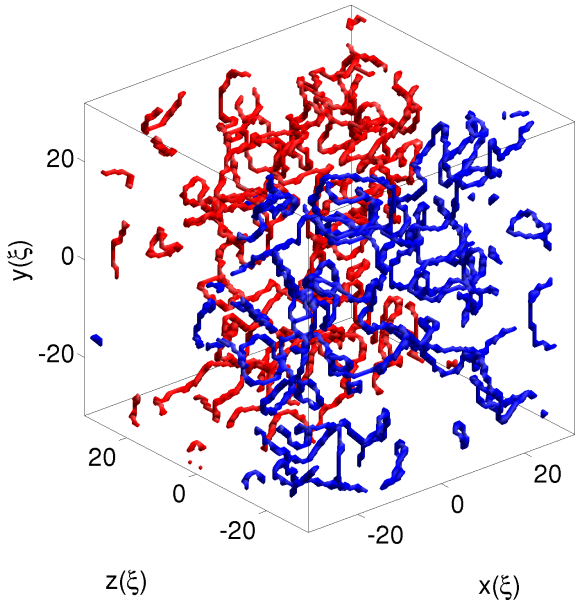

Figure 5.12: Vortices included by linelength algorithm corresponding to isosurface plot at $t = 800$ in Figure 5.9. The cutoff number is given by $k_c = 8$ such that high–frequency spatial waves are suppressed by the factor $\max\{1 - k^2/k_c^2, 0\}$. First component — red; Second component — blue.

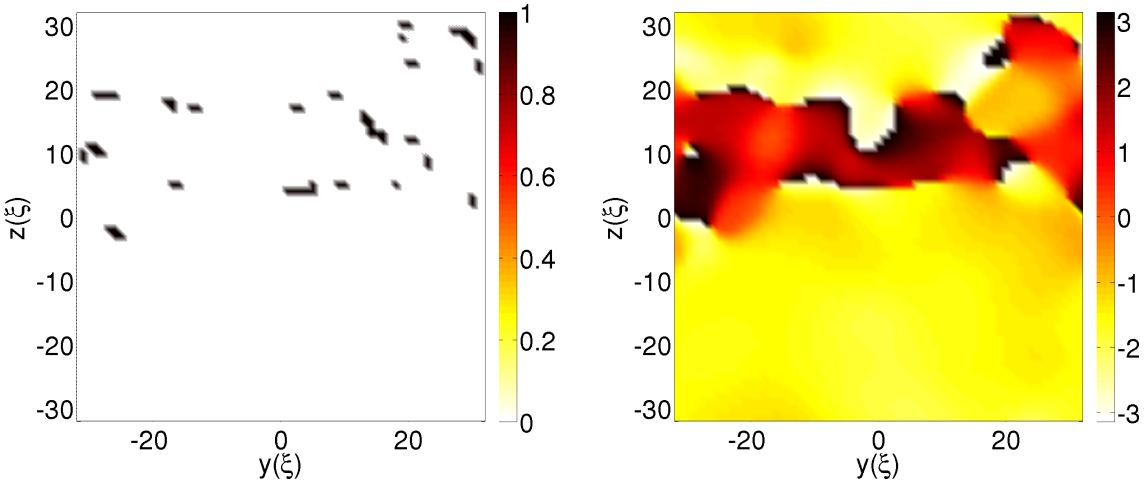

Figure 5.13: (Left) Isosurface slice in $y-z$ plane at $x=0$ of the first component from Figure 5.12. (Right) Phase of filtered wavefunction in $y-z$ plane at $x=0$.

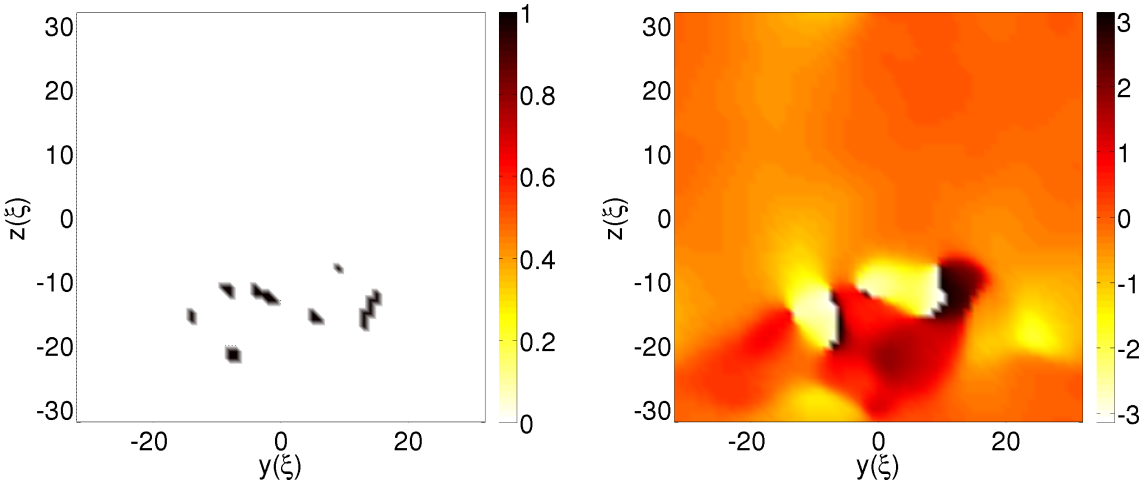

Figure 5.14: (Left) Isosurface Slice in $y-z$ plane at $x=0$ of the second component from Figure 5.12. (Right) Phase of filtered wavefunction in $y-z$ plane at $x=0$.

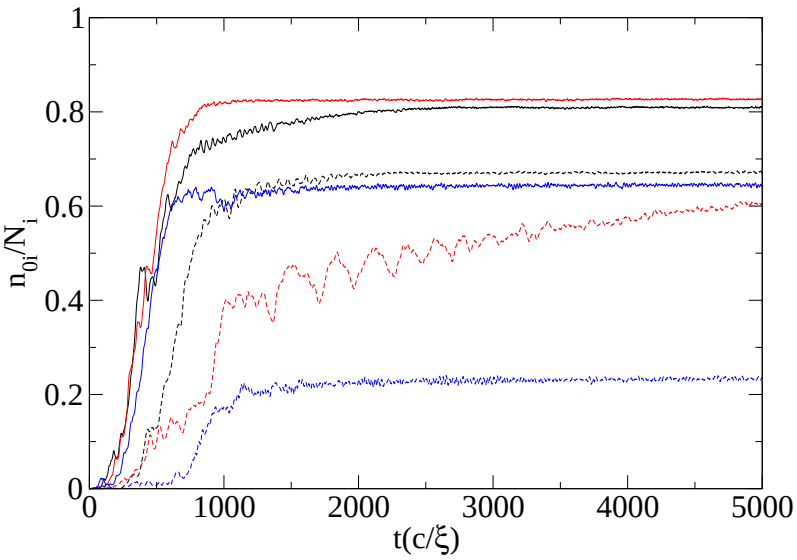

Figure 5.15: Condensate fractions for $g_{11} = g_{22}$, $N_1/V = 0.5$ and $N_2/V = 0.25$. Solid and dashed curve are component one and two respectively. Black curves: $g_{12} = 0$, $\langle E \rangle / V = 0.37$; Red curves: $g_{12} = 0.5$, $\langle E \rangle / V = 0.42$; Blue curves: $g_{12} = 1.5$, $\langle E \rangle / V = 0.57$.

5.2.2 Splitting from One to Two Components

We now examine the dynamics of taking a thermalised single species condensate, where no topological defects are visible, and splitting it into two components. Experimentally this is equivalent to flipping a number of the particles into a second *new* hyperfine state of the same atomic species where both hyperfine states now interact together. When performing this split numerically we set

$$\begin{aligned} \phi_1 &= \sqrt{\frac{100-\alpha}{100}}\phi_{\text{old}} \\ \phi_2 &= \sqrt{\frac{\alpha}{100}}\phi_{\text{old}} \end{aligned} \tag{5.2}$$

where ϕ_{old} is the thermalised single component wavefunction and α the percentage of atoms flipped into the second component. This split conserves the total number of particles in the system. In addition, some small extra noise (maximum $\pm 5\%$ particles) is added to each wavefunction once the split is performed taking into account experimental uncertainty and such that when $\alpha = 50$, both components are not exactly equal ($\phi_1 \neq \phi_2$). The condensate fraction of the single species used in this Section is ≈ 0.8.

Figures 5.16 and 5.17 show the thermalised condensate fractions of each component relative to splitting percentages and strength of the interspecies interactions for both equal and unequal intraspecies interactions. We first observe that for $g_{12} = 0$, the condensate fractions of each component are close (but not equal due to the noise) to that of the initial

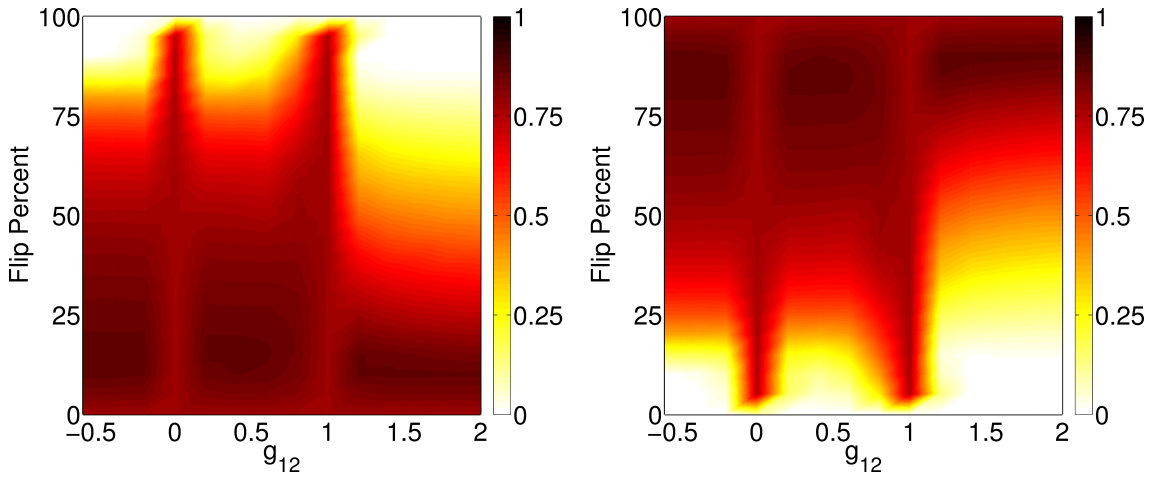

Figure 5.16: Thermalised condensate fractions for the first (left) and second (right) component for a range of flip percentages, i.e. the percentage of the single species wavefunction in the second component, and interspecies interactions with equal intraspecies interactions $g_{11} = g_{22} = 1.0$. Each condensate fraction is averaged over 10^3 time units.

one component wavefunction. For miscible (attractive or repulsive g_{12}) the condensate fractions remain high until the majority ($> 85\%$) of the particles are in one component at which point the smaller component no longer forms a condensate. At the barrier between miscibility and immiscibility ($g_{12} = 1$ in Figure 5.16), the condensate fraction is once again high for $\alpha \neq 0$ and $\alpha \neq 100$. For immiscible condensates, the additional energy from domain boundaries plays an important role with one component often overpowering for nonequal splits. In Figure 5.17 where the intraspecies interactions are not equal, the onset of immiscibility is no longer abrupt and a new miscible regime arises: $g_{11} < g_{12} < g_{22}$. This has a small impact on ϕ_1 only and the condensate fraction is reduced in places. The second component is unaffected.

When splitting to a miscible mixture, no topological defects arise in the system, i.e. no vortices form. In the case of immiscible condensates, the evolution of topological defects is shown in Figure 5.18. The method used for determining the initial wavefunctions for each component leads to initially overlapping densities. As these separate quickly due to the strong interspecies interactions, domains form. These are seen throughout in the isosurface plots. Similarly to the numerical results in Figure 5.9 for longer evolution times, each component forms one well defined domain. Unlike previous results, the vortex linelength does not decay during this dynamical evolution but rather increases from its initially zero value to a maximum around which it thermalises. The final outcome is very similar to that in the previous Section for the linelength of immiscible condensates. The increase in linelength observed here demonstrates that vortices are formed in this two component system due to the immiscibility criteria being satisfied. The vortex linelength for miscible components, once split, remains zero throughout.

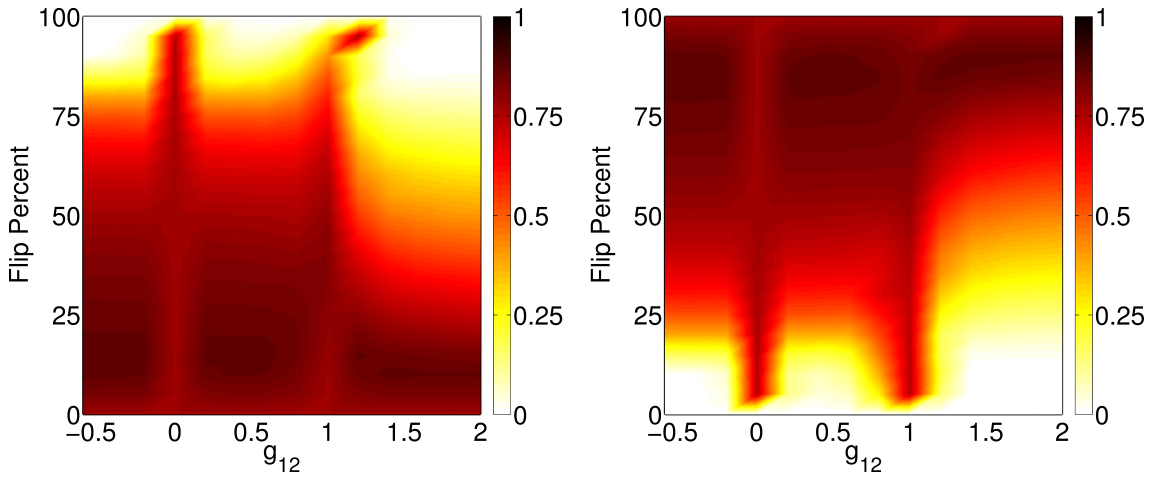

Figure 5.17: Thermalised condensate fractions for the first (left) and second (right) component for a range of flip percentages, i.e. the percentage of the single species wavefunction in the second component, and interspecies interactions with non–equal intraspecies interactions $g_{11} = 1.0 \neq g_{22} = 1.2$. Each condensate fraction is averaged over 10^3 time units.

We have studied the experimentally relevant splitting of one component into two and seen the effects on the quasicondensate fractions depending on how each component is populated and the strength of the interspecies interactions. When splitting into an immiscible mixture, vortices are formed in each domain due to the kinetic energy driven into the components by the repulsive dynamics following the split.

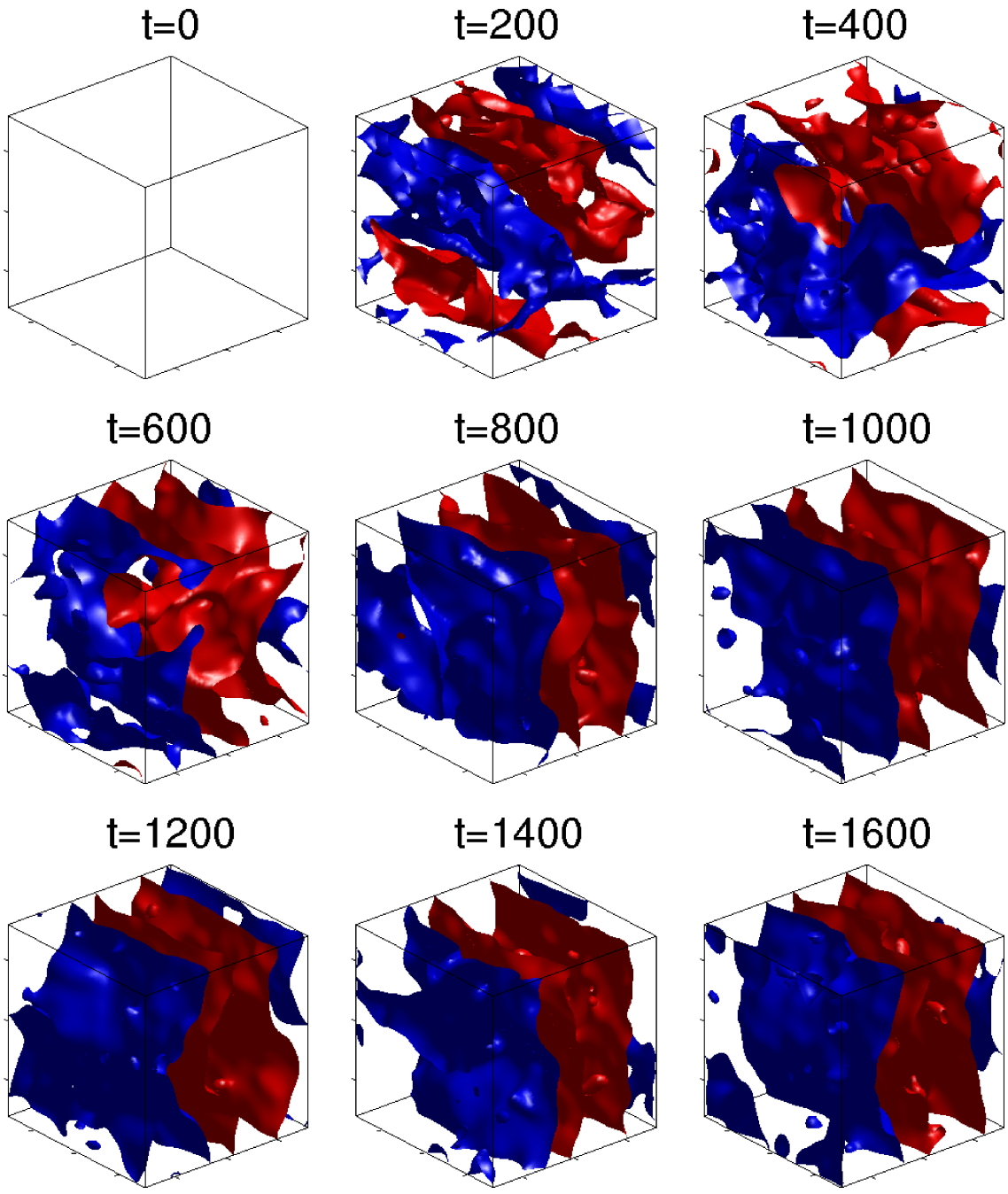

Figure 5.18: As in Figure 5.8 with $g_{11} = g_{22} = 1.0$ and $g_{12} = 1.5$ (immiscible). At $t = 0$, single species thermalised wavefunction is split (50%) into two components. First component — red; Second component — blue.

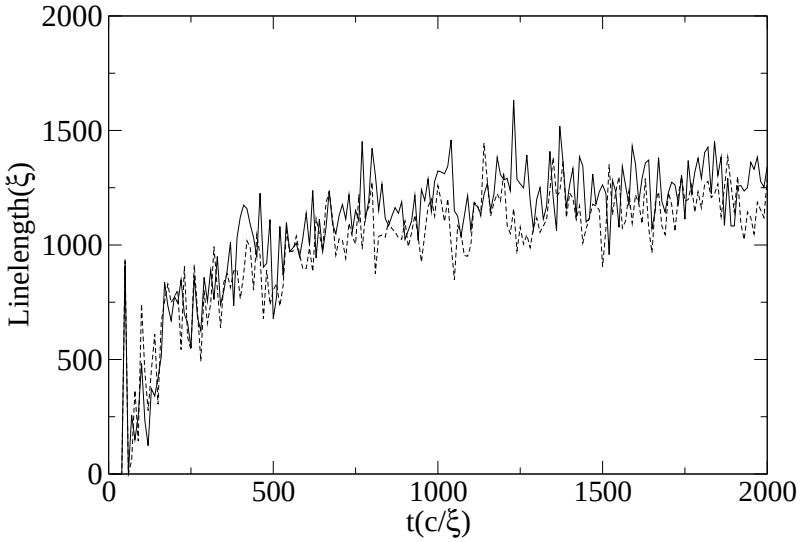

Figure 5.19: Vortex linelength over time corresponding to the evolution in Figure 5.18 where at $t = 0$ single species thermalised wavefunction flipped (50%) into second species where $g_{11} = g_{22} = 1.0$ and $g_{12} = 1.5$ (immiscible). First component — solid curve; Second component — dashed curve.

5.2.3 Quenching the Interspecies Interaction Strength

Here, instead of starting with one component, we initially start with two miscible or immiscible thermalised quasicondensates and quench the interspecies interaction strength in order to investigate the possible generation of topological defects. We also stress the importance of the immiscibility criteria in vortex formation. For a quench from miscible to immiscible, we expect similar results to those observed in the previous Section where one component is split into an immiscible mixture. However when quenching from immiscible to miscible, decay of vortex linelength is anticipated.

Figure 5.20 shows the topological defects when quenching the strength of the interspecies interactions such that the components go from immiscible to miscible. After a very short period of time, the domains vanish and a vortex tangle can be seen. The contrast between miscible and immiscible quasicondensates is clearly observed. The number of vortices in the system then decays over time until all of these vanish. As vortices are present in each domain, this quench leads to a mixing of the components and the vortex tangles mix. The quench from miscible to immiscible is comparable to that seen in Figure 5.18 where the domains are quickly formed. The impact of quenching on the condensate fractions is shown in Figure 5.21. Quenching from miscible to immiscible leads to a decrease in the condensate fractions due to the additional energy from the strength of the interspecies interactions. The decrease takes place rapidly due to the immiscibility criteria driving the system. The quench from immiscible to miscible increases the condensate fractions. The thermalisation of this process takes longer due to the components only slowly mixing, a

process which is not forced. The thermalised condensate fraction is marginally lower due to a surplus of energy remaining from the large interspecies interactions in comparison to a system which is not quenched. Finally in Figure 5.22 we show the evolution of the vortex linelengths when quenching the system. When quenching from immiscible to miscible the linelength quickly decreases then slowly decays until no vortices remain. Quenching from miscible to immiscible increases the total vortex linelength until a maximum value is reached.

In this Section we investigated the consequence of suddenly changing the strength of the interspecies interactions such that the system is driven through the miscibility/immiscibility barrier. Similarities were seen with results from the previous Section where the system was flipped from one to two components, specifically when quenching from miscible to immiscible. However when quenching from immiscible to miscible, the mixing of the two condensates leads to a decay of vortices. If the system was not quenched through the miscibility/immiscibility barrier the transition would not drive the system. Quenching between two miscible interaction strengths does not qualitatively change the system. The only effects are a modified condensate fraction: no vortices are driven into the system. When quenching between two immiscible interaction strengths, the total vortex linelength decreases (increases) when the interspecies interactions are decreased (increased).

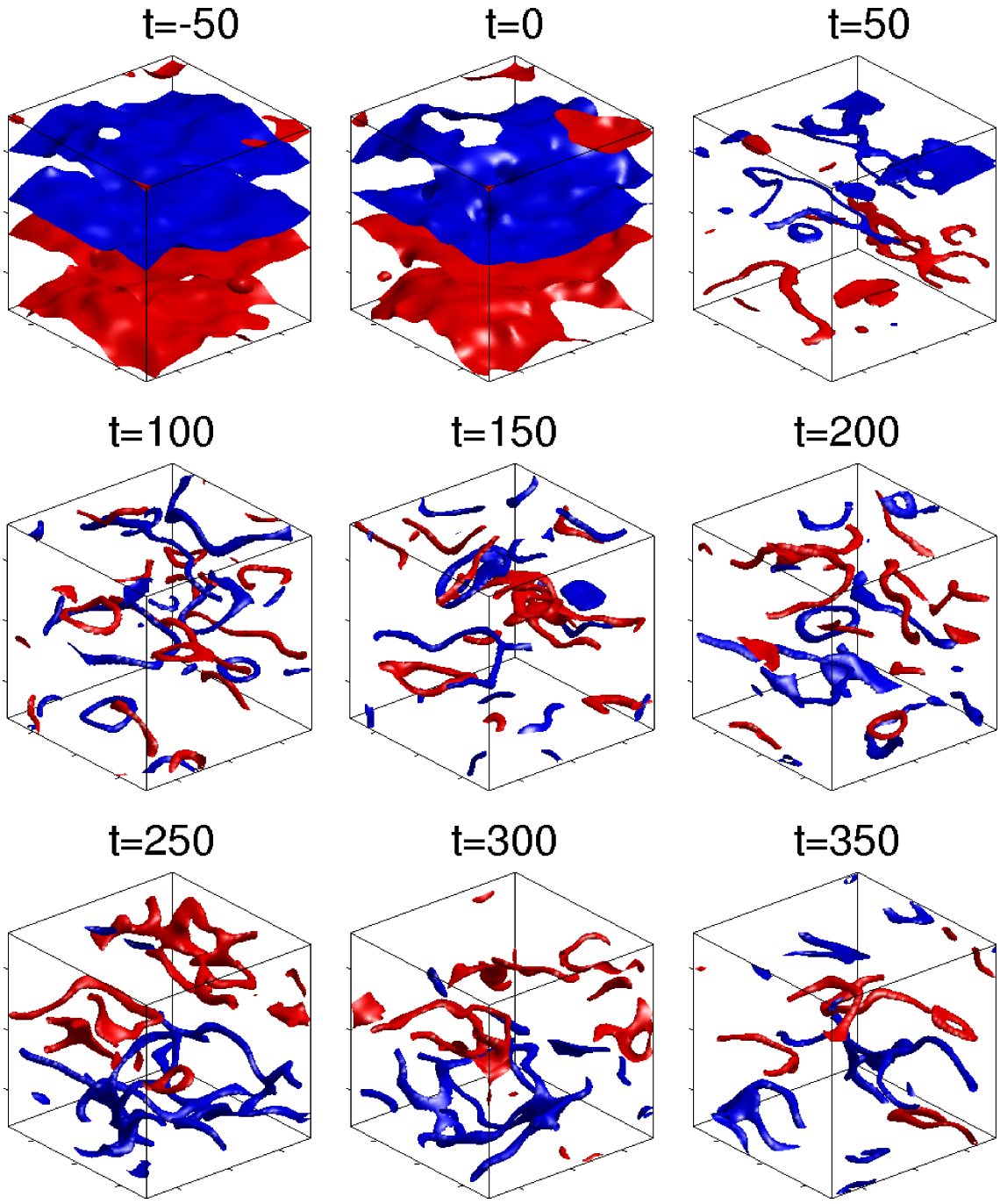

Figure 5.20: As in Figure 5.8 with $g_{11} = g_{22} = 1.0$. At $t = 0$, interspecies interactions strength quenched from $g_{12} = 1,5$ (immiscible) to $g_{12} = 0,5$ (miscible). First component — red; Second component — blue.

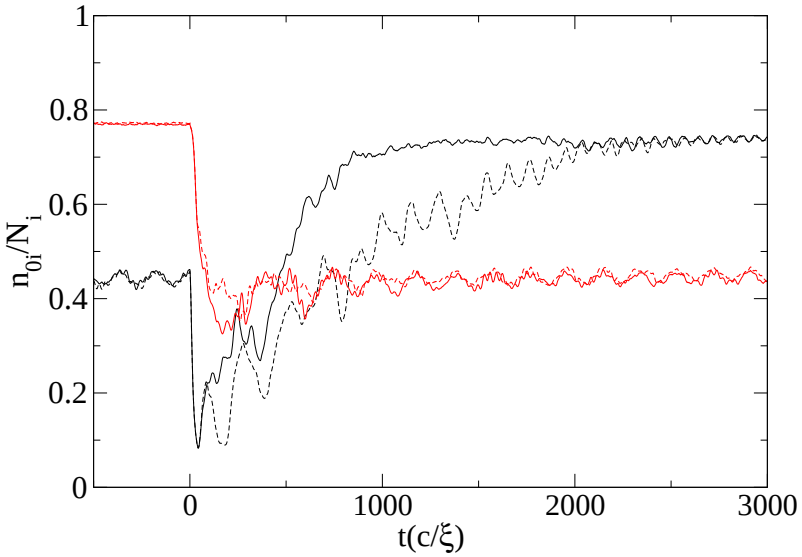

Figure 5.21: Condensate fraction n_{0i}/N_i evolution for two components with interspecies interactions quench from immiscible ($g_{12} = 1.5$) to miscible ($g_{12} = 0.5$)(black curves) and miscible ($g_{12} = 0.5$) to immiscible ($g_{12} = 1.5$) (red curves) at $t = 0$. $g_{11} = g_{22} = 1.0$. First component — solid curves; Second component — dashed curves.

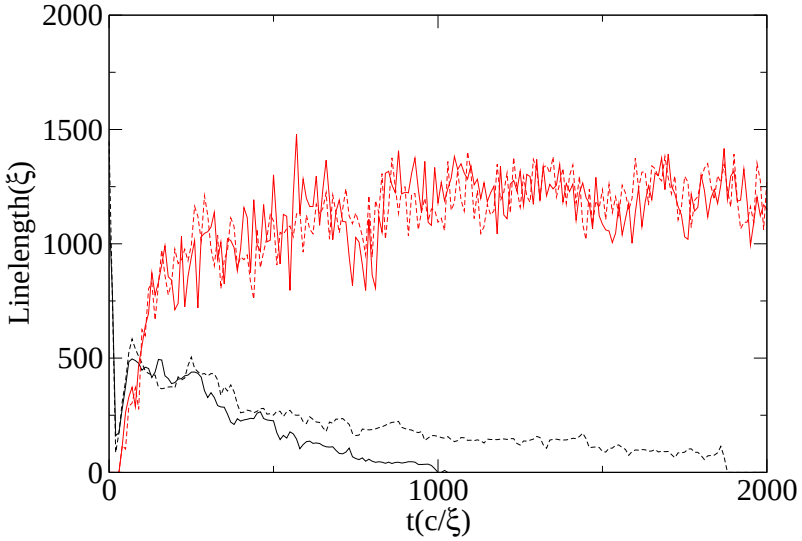

Figure 5.22: Vortex linelength for two components with interspecies interactions quench from immiscible ($g_{12} = 1.5$) to miscible ($g_{12} = 0.5$)(black curves) and miscible ($g_{12} = 0.5$) to immiscible ($g_{12} = 1.5$) (red curves) at $t = 0$. $g_{11} = g_{22} = 1.0$. First component — solid curves; Second component — dashed curves.

5.2.4 Repeated Interspecies Interactions Strength Quenches

In this Section we investigate the impact of continually quenching the system through the miscibility/immiscibility criteria to drive the vortex tangle, with the intention of exploring where this could provide a novel route to the generation of quantum turbulence. Quantum turbulence was introduced in Section 1.5 and recent developments in this area for binary mixtures were discussed.

In Figure 5.23, the system is quenched every 250 time units. The initial state before the first quench at $t = 0$ is immiscible. The topological defects swap from mixed vortex tangles to segregated domains, i.e. phase segregated vortex tangles after each quench. Some vortex decay occurs during the miscible phase but the vortices are always present when the next quench is performed. If the system is not quenched through the miscibility/immiscibility barrier the mixed vortex tangles are not driven into the system. The condensate fractions (see Figure 5.24) do not reach a thermodynamic equilibrium. These never reach zero and condensates are always present. The vortex linelengths (see Figure 5.25) interchange between a maximum and lower values for an immiscible and a miscible system respectively.

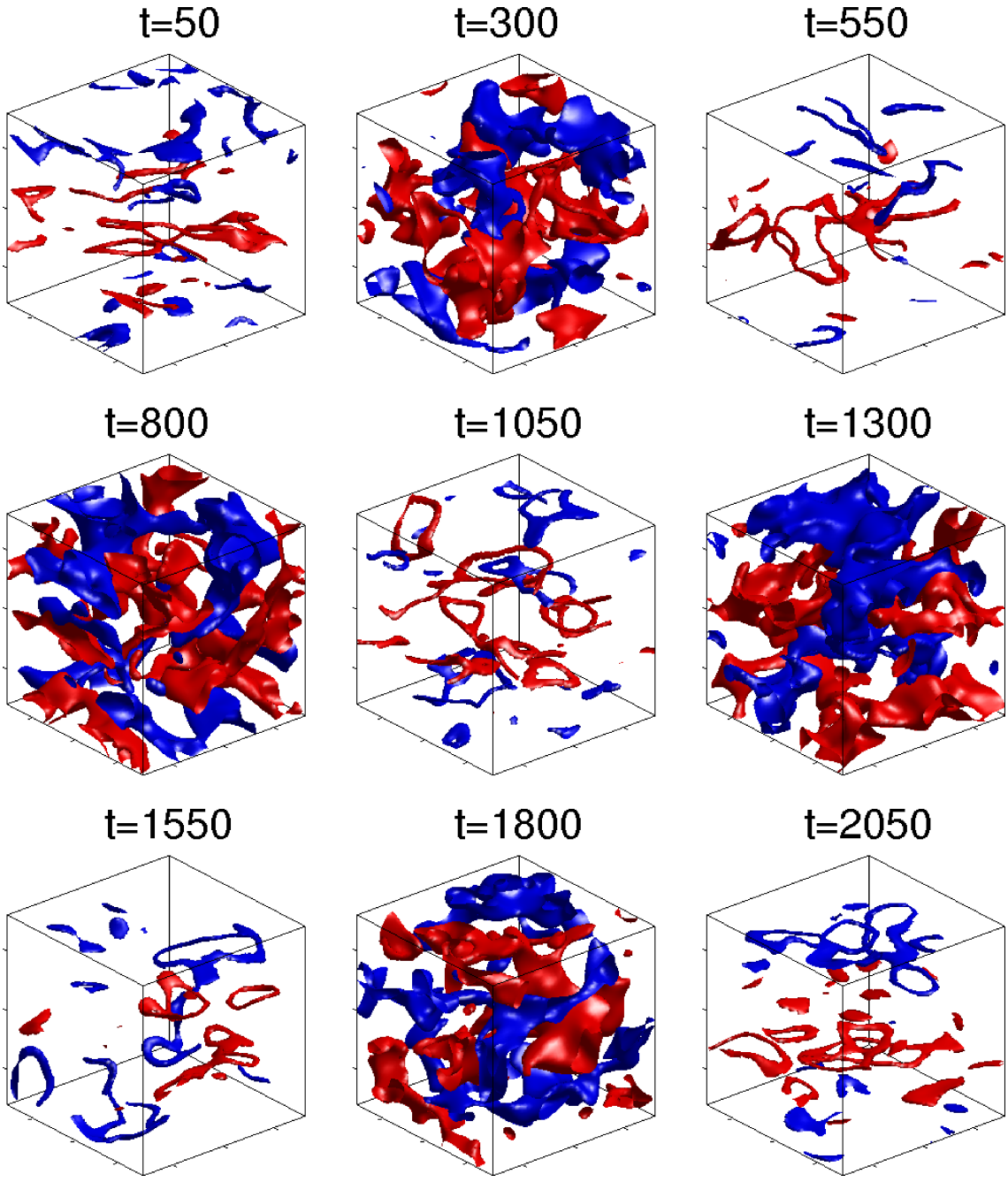

Figure 5.23: As in Figure 5.8 with $g_{11} = g_{22} = 1.0$. Interspecies interactions strength quenched between $g_{12} = 1, 5$ (immiscible) and $g_{12} = 0, 5$ (miscible) every 250 time units. At $t = 0$ the system is miscible after the initial flip (50%)from one equilibrated component. First component — red; Second component — blue.

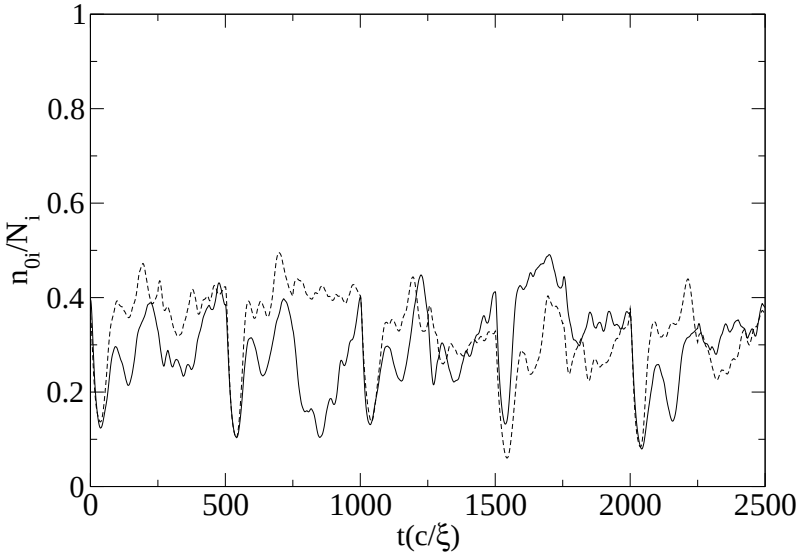

Figure 5.24: Condensate fraction n_{0i}/N_i evolution for two components for interspecies interactions quenched between immiscible ($g_{12} = 1.5$) to miscible ($g_{12} = 0.5$) every 250 time units. At $t = 0$ the system is miscible and single species thermalised wavefunction flipped (50%) into second species. $g_{11} = g_{22}$. First component — solid curve; Second component — dashed curve.

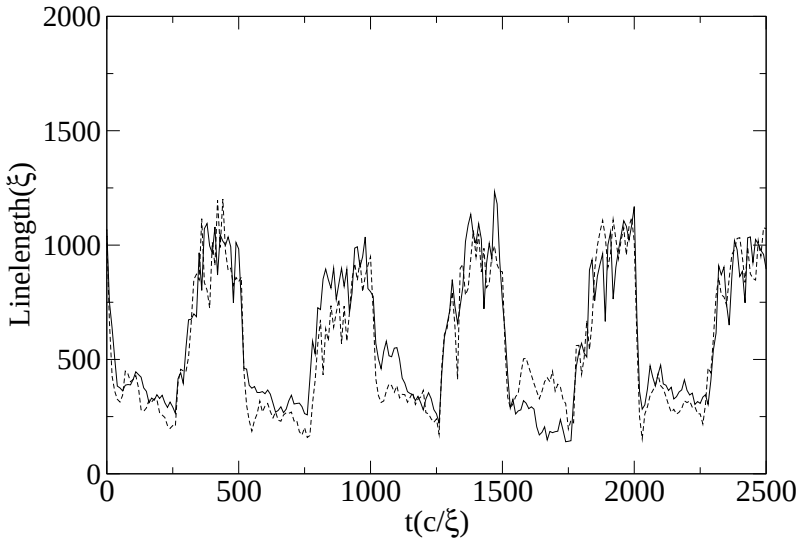

Figure 5.25: Vortex linelength over time corresponding to the evolution in Figure 5.23 where at $t = 0$ single species thermalised wavefunction split (50%) into two components where $g_{11} = g_{22} = 1.0$ and $g_{12} = 0.5$ (miscible). Interspecies interactions quench between immiscible ($g_{12} = 1.5$) and miscible ($g_{12} = 0.5$) every 250 time units. First component — solid curve; Second component — dashed curve.

5.3 Chapter Summary

In this Chapter, we have numerically simulated quasicondensates in periodic boxes. By first considering a single component system starting with highly nonequilibrium initial conditions, the turbulent state decays as the number of vortices decay due to rethermalisation of the particles and reconnections of the topological defects. All vortices eventually vanish from the system while the condensate fraction reaches a thermodynamic limit. The final condensate fraction depends on the initial particle and energy densities.

When a two component system from initial nonequilibrium conditions is considered, two distinct evolutions arise. For miscible components, the vortex tangle decays similarly to the one component system. Phase segregated domains form when immiscibility between components is satisfied. Vortices are present in each domain. Thus we have a phase segregated vortex tangle. We then considered a system where the two components are formed by splitting a thermalised single species system. No novel features were seen for miscible quasicondensates. For immiscible components, domains form once again and the vortex linelength increases. Condensate fraction decreases due to the additional energy from the strong interspecies interactions.

Finally we considered quenching the interspecies interactions in thermalised two components. If the quench does not drive the system through the miscibility/immiscibility barrier, no major changes were seen. When quenching from miscible to immiscible, domains form and the vortex linelength increases. The condensate fraction decreases due to this quench. Isotropic vortex tangles emerge for quenching from immiscible to miscible due to the vortices from each domain mixing. The vortices subsequently decay. The condensate fraction increases to a steady equilibrium. When repeating a quench at regular intervals, vortices never vanish and the system is driven between mixed and phase segregated vortex tangles. As such, this method provides a potential novel route to the generation of quantum turbulence.

Chapter 6

Conclusions and Possible Future Work

In this final Chapter, we summarise the main results of this Thesis followed by possibilities for future investigations.

6.1 Conclusions

In this Thesis, we have explored two–species mixtures of Bose gases. More specifically, we have studied a Rb–Cs condensate mixture in relation to a recent experiment [77]. Initially investigating steady–states of this system at zero–temperature with the simplest mean–field model, we were able to qualitatively reproduce the three particle–dependent density profiles observed experimentally. Then, through the addition of phenomenological growth/decay and dark–bright solitons, different density profiles were seen during the dynamical growth of the coupled condensates. We then moved on to consider the evolution of Bose gases using the so–called classical–field methods in periodic boxes with no trapping potentials, studying how the miscibility/immiscibility of the system changed the thermal dynamics and equilibrium state.

6.1.1 Two–Species Condensates at Zero Temperature

Condensate mixtures have been a topic of intense research since the first experimental realisations of BEC. From the coupled Gross–Pitaevskii equations, we obtained the ground state (lowest energy) density profiles of trapped condensate mixtures, firstly with Rb–Na reproducing the results obtained in [80]. This not only demonstrated that our numerical methods were accurate but that by simply varying condensate particle numbers and interspecies interaction strengths a wealth of density distributions are found.

In 1D, by varying the width of the initial conditions used for imaginary time propagation, the number of interfaces between each species can vary greatly depending on interaction strengths and particles numbers. This showed the sensitivity of the steady state solutions on the initial conditions used. As the width of the initial condition is increased, the number of interfaces is reduced. The distribution with the lowest possible number of interfaces had the lowest total energy and is therefore the true ground state. In 3D the solutions obtained are sensitive to initial conditions although considerably less than in 1D.

The main target of the work on ground state solutions at zero temperature was focused on qualitatively reproducing the experimental results of Reference [77] by means of the simplest possible zero–temperature mean–field theory consisting of two CGPEs. The three different condensate mixture density profiles achieved experimentally depend on the number of condensed Rb and Cs atoms respectively. In perfectly symmetric traps, where the centres of both trapping potential have the same spatial positions, the density profiles obtained were found not to match the experimental results. After a more thorough analysis of the experiment, we offset the trap centres for the two species to account for anticipated experimental offsets (of around 1 μm) via the addition of weak linear potentials in the axial and one transverse direction. We stressed that the asymmetries caused by harmonic trap offsets between the two trap centres in the axial and transverse directions are small relative to the size of the condensate clouds. This explains why asymmetric density profiles can be observed in two–species experiments with different atomic species as two magnetic traps are required which are extremely hard to align perfectly. Dramatic differences in the density profiles arose with the addition of weak linear potentials. Importantly, this allowed us to obtain the observed asymmetric profiles. We found a qualitative match between the structural regimes seen experimentally and our simulations by tailoring the gradients of linear potentials. Note that our match was limited to the qualitative structure of the profiles only and disregarded the thermal tails in the experimental profiles (which are not included in the zero temperature model).

Although good qualitative agreement with the experimentally reported profiles was obtained by changing the initial conditions of the simulations, for example one of the components being more tightly localised in the centre, we found that this could affect the final equilibrated profiles. Numerous metastable states (of comparable, but not identical, energies) exist for each configuration. In the early stages of coupled growth under the same parameter regimes, such a situation could arise. The analysis presented in this work was based on equilibrium density profiles. In the experiments, as the two species were sympathetically cooled, the initial number of condensate atoms within each species (or the sequence by which growth proceeded) was not accurately known. Moreover, the density profiles were typically measured after a variable hold time, without necessarily

guaranteeing that the structures observed were indeed true equilibrium states (as opposed to some long-lived metastable steady-states).

6.1.2 Dynamical Studies of Two–Component Mixtures at Finite Temperature

We investigated the role of growth in a two component immiscible system modelled via phenomenologically damped CGPEs. Starting with a range of steady state density distributions, the addition of a non–zero damping term can be used to simulate growth. Perturbing the chemical potential of each condensate induces competing dynamical evolution between the species which eventually causes one of the species to vanish entirely, thus leaving only a single species condensate. In a few cases, we have seen the density profiles change from a symmetric density profile to an asymmetric one during growth provided additional linear potentials are present (which enables the condensates to shift relative to each other in a transverse direction).

By looking at the simulations performed by our collaborators I. K. Liu *et al.* with the CSPGPEs using the parameters from [77], spontaneous dark–bright solitons emerged. This prompted the investigation into dynamical evolution of dark–bright solitons with and without phenomenological growth. At zero temperature, single solitons oscillate back and forth in the axial direction while two solitons merge after a short period of time. With some finite temperature effects included phenomenologically, the extra damping factor plays an important role on the dynamics. Similarly to a system with no solitons, one condensate always vanishes entirely. Soliton oscillations can always be seen in the dynamics before damping overwhelms the condensate evolution. By varying the magnitude of the growth rate, we were able to identify many variations in the number of oscillations by the dark–bright soliton(s). In addition, the impact of the small offsets due to the additional linear potentials to the trap was clear. The offsets gave rise to more soliton oscillations before the growth/decay of the condensates took over. When two dark–bright solitons were present, three cases were recognised: a passing of the solitons with full segregation, immediate merging on first contact and merging after few oscillations.

Our work showed a large number of distinct density profiles are possible during the coupled condensates dynamics. When comparing to a recent two–species experiment [77] on which our parameters are based, we observed some qualitative agreement between condensate density profiles while considering growth. However not only is the model used here a toy model with static growth, as there is no explicit consideration of the thermal cloud dynamics. Moreover the coupled experimental results available did not analyse the nonequilibrium structures in detail to be able to investigate a more detailed comparison.

6.1.3 Classical Field Methods

We first considered the evolution of a single component starting with strongly nonequilibrated initial conditions. By considering the quasicondensate part of the wavefunction, we observed the presence of a turbulent state of vortices in the early stages of the evolution. This state decayed due to vortex reconnections, with the total vortex linelength decreasing over time. The system rethermalised as particles enter lower momentum modes and the condensate fraction (ratio of particles in the condensate to the total number of particles) increased. A vortex ring is the final observable defect. A fully thermalised state is obtained when the vortex ring vanished and the condensate fraction reached the thermodynamic limit. The effect of considering varying numbers of computational modes was shown not to change the final thermalised state but simply to change the time taken to reach this state for the same particle and energy densities. The final condensate fraction was determined solely by the initial particle and energy densities.

A system with two components was then considered, both of these starting from nonequilibrated initial conditions. The differences between choosing miscible or immiscible interaction strength was clear. The miscible quasicondensates thermalised similarly to a single component system. The vortex tangle decayed until no topological defects were present and the condensate fractions increased to a thermodynamic limit. However for strong interspecies interactions, the components quickly phase segregated and the domains were seen in the topological defects. The total vortex linelength did not decay to zero but rather reached a minimum value: the stronger the interspecies interactions the more vortices remain. By viewing the phase, we showed that vortex tangles were present in each domain. In addition, immiscible condensates had lower condensate fractions due to the additional energy from the large interspecies interactions. Changing the initial particle and energy densities for each component separately influenced the final condensate fractions.

Using a fully thermalised single component (constant condensate fraction and zero vortex linelength), we investigated splitting this state into two components for different intra and interspecies interaction strengths and number of particles in each component. A clear difference can be seen not only between miscible and immiscible quasicondensates but also high and low percentages of total particle numbers in each component. Furthermore, strong interspecies interactions lead to phase segregated vortex tangles due to the formation of domains.

Finally, we investigated the impact of suddenly quenching the strength of the interspecies interactions. If the quench did not drive the system through the miscibility/immiscibility barrier, no qualitative changes occurred to the presence of the topological defects. Quenching in miscible systems did not lead to the generation of vortices and for immiscible systems the vortex linelength changed in relation to the strength of the in-

terspecies interactions. Quenching from miscible to immiscible gave rise to similar results as splitting one component into two immiscible components: domains formed with phase segregated vortex tangles and condensate fractions decrease. Quenching the interactions from immiscible to miscible lead to an isotropic vortex tangle as the components slowly mix and subsequently decay. Repeating the quench at regular intervals drove the vortex tangle thereby providing a possible novel route to the generation of quantum turbulence.

6.2 Further Work

6.2.1 Two Species In Harmonic Traps

A number of other more accurate models for finite–temperature nonequilibrium Bose gases exist [242]. I. K. Liu *et al.* are currently continuing collaborative simulations using the SPGPE in 3D with the parameters from Reference [77] and the best match trap asymmetries obtained in Chapter 3 of this Thesis. Other efforts for modelling multicomponent condensates with the ZNG formalism are being undertaken [243].

Correlated to the work done in periodic boxes, we wish to investigate if macroscopic excitations arise when quenching the interspecies interactions in harmonic traps. For counterflow in two trapped immiscible condensates spontaneous solitons appeared due to the quasi–1D nature of the system [244]. Solitons and vortices may appear depending on the dimensionality of the system. It would be interesting to investigate these features both at zero–temperature and at finite temperature with the PGPE. The projector is recommended in harmonic trapping potentials in order to explicitly impose an energy cutoff.

6.2.2 Object Motion Through Non Trapped Quasicondensates

The critical velocity has been shown to depend on the condensate fraction [240] when moving a penetrable sphere through a thermalised system. We have conducted preliminary studies to investigate a system with a moving impenetrable cylinder.

In a homogeneous system, vortex nucleation due to a cylinder has been observed and studied in great detail for classical viscous fluids [245, 246] and quantum fluids [192, 247, 248]. For our simulations, we solve the GPE in the moving frame with speed v along the x direction. To avoid transient excitations associated with suddenly moving the cylinder, its speed is increased according to

$$v = \nu \tanh(0.1t) \tag{6.1}$$

where ν is the amplitude of the velocity. The potential is chosen to be zero everywhere

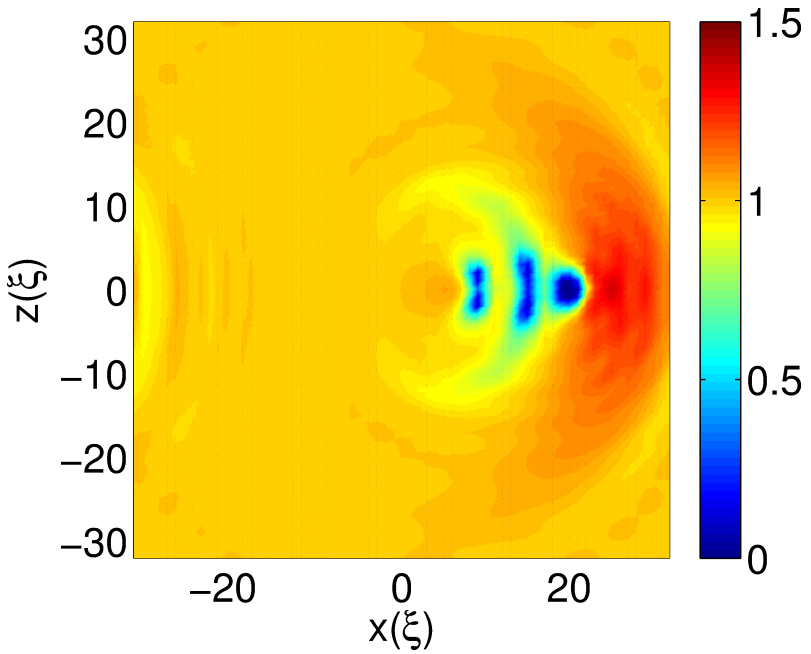

Figure 6.1: Slice of flow past a cylinder from right to left with initial uniform density.

apart from a localised repulsive cylinder which represents the obstacle

$$V(x,z) = V_{max} \exp\left((x-x_0)^2 + z^2\right) \tag{6.2}$$

where V_{max} is the potential associated with the cylinder and x_0 the position in the x direction in the moving frame. In our simulations we take $V_{max} = 10$ and $x_0 = 20$. Figure 6.1 shows a typical vortex nucleation due to a moving impenetrable cylinder with uniform density.

When considering a thermalised wavefunction, taking a slice in the y direction does not lead to direct observation of vortices due to the ambient random fluctuations. One expects that the vortex lines produced by the cylinder will tend to align in the direction of the cylinder (y). Visualisation of the vortex lines is then aided by averaging the density along the direction of the cylinder. In these averaged 2D density plots (see Figure 6.2), regions of low density downstream of the cylinder indicate the positions of the vortices. Note that the averaged vortex density does not decrease to zero since the vortex lines will actually be curved and sinuous in the averaged direction (due to Kelvin waves and the effect of the excited background condensate). Starting from a thermalised state with $n_0/N \approx 0.77$, vortex nucleation is evidenced when the vortex linelength measured by the system becomes non–zero and occurs for velocities above the critical speed $v_c = 0.31$. The evolution of the condensate fraction for velocities above and below the critical velocity is shown in Figure 6.3. For small v, the condensate fraction remains fixed. When this critical speed

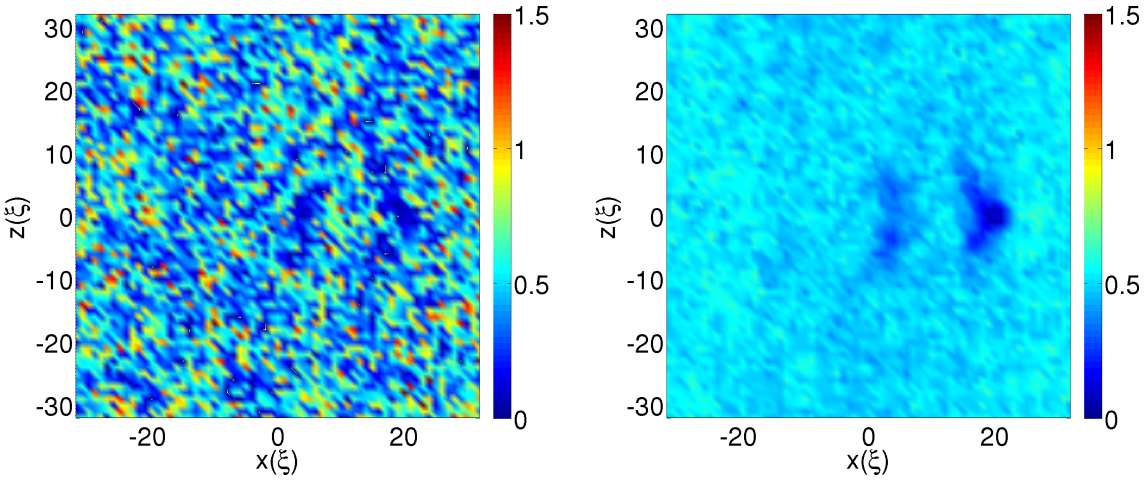

Figure 6.2: (Left) Slice of flow past a cylinder from right to left with initial thermalised state. (Right) Average over all slices in y direction of flow past a cylinder from right to left with initial thermalised state.

is exceeded, the condensate fraction decreases until reaching zero. Once the condensate fraction reaches zero, no more vortices are created. By plotting the topological defects in Figure 6.4 the creation of paired vortex lines at the cylinder can be seen. Immediately after forming, these vortex lines become curved and reconnect at several points along y. These reconnections then lead to the formation of vortex rings.

Having confirmed the nucleation of vortices by the flow of a thermalised state past a impenetrable cylinder, we wish to investigate the dependence of the critical velocity on the initial condensate fraction and width of the cylinder. The length of the cylinder shall also be altered. This is not believed to cause significant changes to the dynamical evolution. Due to the size of our numerical grid and periodic boundary conditions, the vortices quickly pass through the bounds of our box and interfere with any future dynamics. To avoid this, we intend on repeating these simulations with more computational modes to investigate the longer term evolution of vortices. Finally, we shall extend this work to miscible two component condensates.

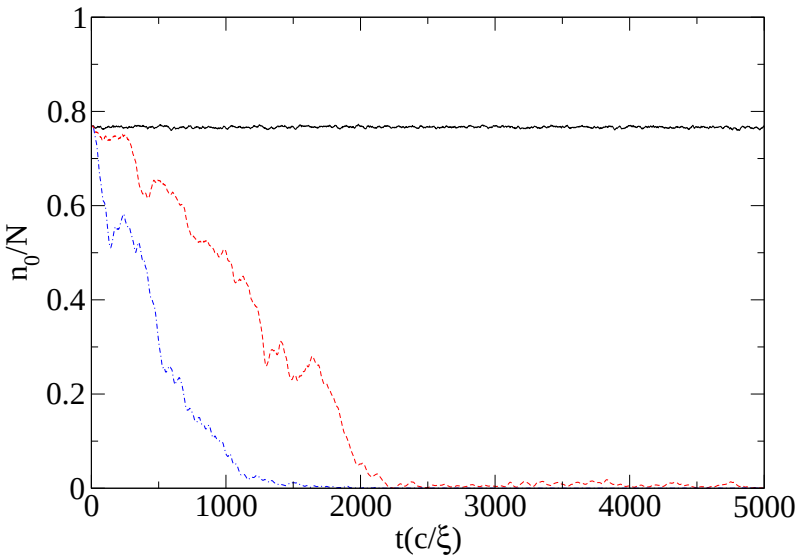

Figure 6.3: Condensate fractions against time for $v = 0.2$ (black — solid), $v = 0.31$ (red — dashed) and $v = 0.4$ (blue — dot–dashed).

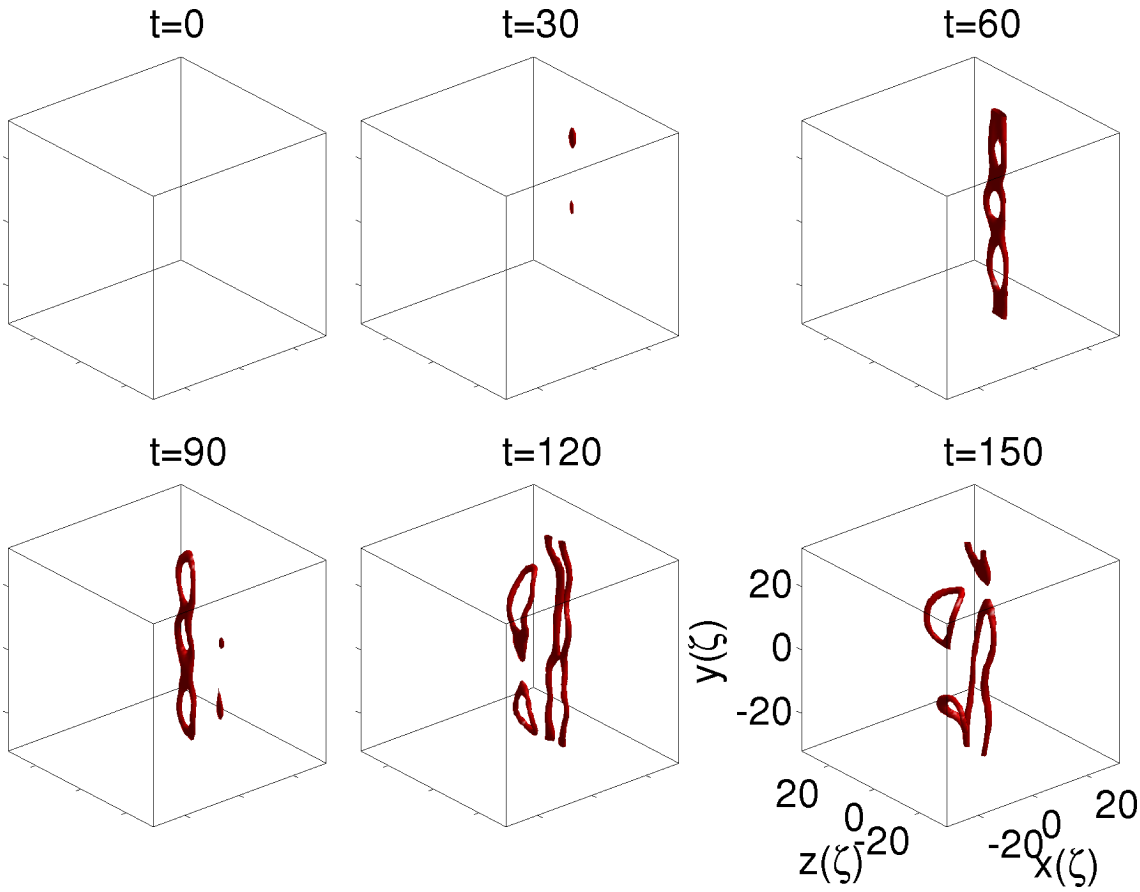

Figure 6.4: Evolution of topological defects given by the isosurfaces $\left|\tilde{\phi}\right|^2 = 0.05\langle\left|\tilde{\phi}\right|^2\rangle$ where $\tilde{\phi}$ is the long wavelength part of the field ϕ. The cutoff number is given by $k_c = 8$ such that high–frequency spatial waves are suppressed by the factor $\max\{1 - k^2/k_c^2, 0\}$. Flow is in the x direction.

Appendix A

Coupled Gross–Pitaevskii Equations

In this Appendix, we show a detailed derivation of the time–dependent Coupled Gross–Pitaevskii equations. The second order quantized Hamiltonian for condensate mixtures is written in terms of the Bose field operators $\hat{\Psi}_i(\mathbf{r},t)$ ($\hat{\Psi}_i^\dagger(\mathbf{r},t)$) for creation (annihilation) of particle in species i at position $\mathbf{r}$ and time t by [121]

$$\begin{aligned}\hat{H} = &\int \mathrm{d}\mathbf{r}\hat{\Psi}_1^\dagger(\mathbf{r},t)\,\hat{h}_1\hat{\Psi}_1(\mathbf{r},t)\\ &+\frac{1}{2}\int \mathrm{d}\mathbf{r}\int \mathrm{d}\mathbf{r}'\hat{\Psi}_1^\dagger(\mathbf{r}',t)\,\hat{\Psi}_1^\dagger(\mathbf{r},t)\,V_1(\mathbf{r}-\mathbf{r}')\,\hat{\Psi}_1(\mathbf{r},t)\,\hat{\Psi}_1(\mathbf{r}',t)\\ &+\int \mathrm{d}\mathbf{r}\hat{\Psi}_2^\dagger(\mathbf{r},t)\,\hat{h}_2\hat{\Psi}_2(\mathbf{r},t)\\ &+\frac{1}{2}\int \mathrm{d}\mathbf{r}\int \mathrm{d}\mathbf{r}'\hat{\Psi}_2^\dagger(\mathbf{r}',t)\,\hat{\Psi}_2^\dagger(\mathbf{r},t)\,V_2(\mathbf{r}-\mathbf{r}')\,\hat{\Psi}_2(\mathbf{r},t)\,\hat{\Psi}_2(\mathbf{r}',t)\\ &+\frac{1}{2}\int \mathrm{d}\mathbf{r}\int \mathrm{d}\mathbf{r}'\hat{\Psi}_1^\dagger(\mathbf{r}',t)\,\hat{\Psi}_2^\dagger(\mathbf{r},t)\,V_{12}(\mathbf{r}-\mathbf{r}')\,\hat{\Psi}_1(\mathbf{r},t)\,\hat{\Psi}_2(\mathbf{r}',t)\end{aligned} \tag{A.1}$$

where V_1, V_2 and V_{12} are the contact interactions acting between the bosons of species one, species two and between each species respectively. $\hat{h}_i = \left(\hbar^2/2m_i\right)\nabla^2 + V_{exti}(\mathbf{r})$ is the single particle Hamiltonian where m_i is the mass and $V_{ext(i)}(\mathbf{r})$ the external potential acting on each species. As stated in Section 2.1, we can approximate the contact interactions to

$$\begin{aligned}V_1(\mathbf{r}-\mathbf{r}') &= g_{11}\delta(\mathbf{r}-\mathbf{r}')\\ V_2(\mathbf{r}-\mathbf{r}') &= g_{22}\delta(\mathbf{r}-\mathbf{r}')\\ V_{12}(\mathbf{r}-\mathbf{r}') &= g_{12}\delta(\mathbf{r}-\mathbf{r}')\end{aligned} \tag{A.2}$$

where

$$g_{ii} = \frac{4\pi\hbar^2 a_{ii}}{m_i},\ g_{12} = \frac{4\pi\hbar^2 a_{12} m_1 m_2}{(m1 + m_2)}. \tag{A.3}$$

The Bose field operators obey the following commutation relations [121]

$$\begin{aligned}
&\left[\hat{\Psi}_i\left(\mathbf{r},t\right),\hat{\Psi}_i^{\dagger}\left(\mathbf{r}',t\right)\right] = \delta\left(\mathbf{r}-\mathbf{r}'\right),\\
&\left[\hat{\Psi}_i\left(\mathbf{r},t\right),\hat{\Psi}_i\left(\mathbf{r}',t\right)\right] = \left[\hat{\Psi}_i^{\dagger}\left(\mathbf{r},t\right),\hat{\Psi}_i^{\dagger}\left(\mathbf{r}',t\right)\right] = 0,\\
&\left[\hat{\Psi}_i\left(\mathbf{r},t\right),\hat{\Psi}_j^{\dagger}\left(\mathbf{r}',t\right)\right] = \left[\hat{\Psi}_i\left(\mathbf{r},t\right),\hat{\Psi}_j\left(\mathbf{r}',t\right)\right] = \left[\hat{\Psi}_i^{\dagger}\left(\mathbf{r},t\right),\hat{\Psi}_j^{\dagger}\left(\mathbf{r}',t\right)\right] = 0.
\end{aligned} \tag{A.4}$$

Inserting the contact interaction assumption into Equation (A.1) and integrating out the dependence on $\mathbf{r}'$ leads to

$$\begin{aligned}
\hat{H} = &\int \mathrm{d}\mathbf{r}\hat{\Psi}_1^{\dagger}\left(\mathbf{r},t\right)\hat{h}_1\hat{\Psi}_1\left(\mathbf{r},t\right)\\
&+\frac{g_{11}}{2}\int \mathrm{d}\mathbf{r}\hat{\Psi}_1^{\dagger}\left(\mathbf{r},t\right)\hat{\Psi}_1^{\dagger}\left(\mathbf{r},t\right)\hat{\Psi}_1\left(\mathbf{r},t\right)\hat{\Psi}_1\left(\mathbf{r},t\right)\\
&+\int \mathrm{d}\mathbf{r}\hat{\Psi}_2^{\dagger}\left(\mathbf{r},t\right)\hat{h}_2\hat{\Psi}_2\left(\mathbf{r},t\right)\\
&+\frac{g_{22}}{2}\int \mathrm{d}\mathbf{r}\hat{\Psi}_2^{\dagger}\left(\mathbf{r},t\right)\hat{\Psi}_2^{\dagger}\left(\mathbf{r},t\right)\hat{\Psi}_2\left(\mathbf{r},t\right)\hat{\Psi}_2\left(\mathbf{r},t\right)\\
&+\frac{g_{12}}{2}\int \mathrm{d}\mathbf{r}\hat{\Psi}_1^{\dagger}\left(\mathbf{r},t\right)\hat{\Psi}_2^{\dagger}\left(\mathbf{r},t\right)\hat{\Psi}_1\left(\mathbf{r},t\right)\hat{\Psi}_2\left(\mathbf{r},t\right).
\end{aligned} \tag{A.5}$$

The Heisenberg equation of motion for species 1 becomes

$$
\begin{aligned}
\mathrm{i}\hbar\frac{\partial\hat{\Psi}_1\left(\mathbf{r}',t\right)}{\partial t} &= \left[\hat{\Psi}_1\left(\mathbf{r}',t\right),\hat{H}\right] \\
&= \hat{\Psi}_1\left(\mathbf{r}',t\right)\Bigg[\int \mathrm{d}\mathbf{r}\hat{\Psi}_1^\dagger\left(\mathbf{r},t\right)\hat{h}_1\hat{\Psi}_1\left(\mathbf{r},t\right) \\
&\qquad \text{(A)} \\
&\quad + \frac{g_{11}}{2}\int \mathrm{d}\mathbf{r}\hat{\Psi}_1^\dagger\left(\mathbf{r},t\right)\hat{\Psi}_1^\dagger\left(\mathbf{r},t\right)\hat{\Psi}_1\left(\mathbf{r},t\right)\hat{\Psi}_1\left(\mathbf{r},t\right) \\
&\qquad \text{(C)} \\
&\quad + \int \mathrm{d}\mathbf{r}\hat{\Psi}_2^\dagger\left(\mathbf{r},t\right)\hat{h}_2\hat{\Psi}_2\left(\mathbf{r},t\right) \\
&\qquad \text{(B)} \\
&\quad + \frac{g_{22}}{2}\int \mathrm{d}\mathbf{r}\hat{\Psi}_2^\dagger\left(\mathbf{r},t\right)\hat{\Psi}_2^\dagger\left(\mathbf{r},t\right)\hat{\Psi}_2\left(\mathbf{r},t\right)\hat{\Psi}_2\left(\mathbf{r},t\right) \\
&\qquad \text{(D)} \\
&\quad + \frac{g_{12}}{2}\int \mathrm{d}\mathbf{r}\hat{\Psi}_1^\dagger\left(\mathbf{r},t\right)\hat{\Psi}_2^\dagger\left(\mathbf{r},t\right)\hat{\Psi}_1\left(\mathbf{r},t\right)\hat{\Psi}_2\left(\mathbf{r},t\right)\Bigg] \\
&\qquad \text{(E)} \\
&\quad - \Bigg[\int \mathrm{d}\mathbf{r}\hat{\Psi}_1^\dagger\left(\mathbf{r},t\right)\hat{h}_1\hat{\Psi}_1\left(\mathbf{r},t\right) \\
&\qquad \text{(A)} \\
&\quad + \frac{g_{11}}{2}\int \mathrm{d}\mathbf{r}\hat{\Psi}_1^\dagger\left(\mathbf{r},t\right)\hat{\Psi}_1^\dagger\left(\mathbf{r},t\right)\hat{\Psi}_1\left(\mathbf{r},t\right)\hat{\Psi}_1\left(\mathbf{r},t\right) \\
&\qquad \text{(C)} \\
&\quad + \int \mathrm{d}\mathbf{r}\hat{\Psi}_2^\dagger\left(\mathbf{r},t\right)\hat{h}_2\hat{\Psi}_2\left(\mathbf{r},t\right) \\
&\qquad \text{(B)} \\
&\quad + \frac{g_{22}}{2}\int \mathrm{d}\mathbf{r}\hat{\Psi}_2^\dagger\left(\mathbf{r},t\right)\hat{\Psi}_2^\dagger\left(\mathbf{r},t\right)\hat{\Psi}_2\left(\mathbf{r},t\right)\hat{\Psi}_2\left(\mathbf{r},t\right) \\
&\qquad \text{(D)} \\
&\quad + \frac{g_{12}}{2}\int \mathrm{d}\mathbf{r}\hat{\Psi}_1^\dagger\left(\mathbf{r},t\right)\hat{\Psi}_2^\dagger\left(\mathbf{r},t\right)\hat{\Psi}_1\left(\mathbf{r},t\right)\hat{\Psi}_2\left(\mathbf{r},t\right)\Bigg]\hat{\Psi}_1\left(\mathbf{r}',t\right)
\end{aligned}
\tag{A.6}
$$

Taking the terms labelled by an A in Equation (A.6) gives

$$\begin{aligned}
&\int \mathrm{d}\mathbf{r}\left(\hat{\Psi}_1\left(\mathbf{r}',t\right)\hat{\Psi}_1^{\dagger}\left(\mathbf{r},t\right)\hat{h}_1\hat{\Psi}_1\left(\mathbf{r},t\right)-\hat{\Psi}_1^{\dagger}\left(\mathbf{r},t\right)\hat{h}_1\hat{\Psi}_1\left(\mathbf{r},t\right)\hat{\Psi}_1\left(\mathbf{r}',t\right)\right)\\
&=\int \mathrm{d}\mathbf{r}\left(\hat{\Psi}_1\left(\mathbf{r}',t\right)\hat{\Psi}_1^{\dagger}\left(\mathbf{r},t\right)\hat{h}_1\hat{\Psi}_1\left(\mathbf{r},t\right)-\hat{\Psi}_1^{\dagger}\left(\mathbf{r},t\right)\hat{h}_1\hat{\Psi}_1\left(\mathbf{r}',t\right)\hat{\Psi}_1\left(\mathbf{r},t\right)\right)\\
&=\int \mathrm{d}\mathbf{r}\left(\hat{\Psi}_1\left(\mathbf{r}',t\right)\hat{\Psi}_1^{\dagger}\left(\mathbf{r},t\right)\hat{h}_1\hat{\Psi}_1\left(\mathbf{r},t\right)-\hat{\Psi}_1^{\dagger}\left(\mathbf{r},t\right)\hat{\Psi}_1\left(\mathbf{r}',t\right)\hat{h}_1\hat{\Psi}_1\left(\mathbf{r},t\right)\right)\\
&=\int \mathrm{d}\mathbf{r}\left(\hat{\Psi}_1\left(\mathbf{r}',t\right)\hat{\Psi}_1^{\dagger}\left(\mathbf{r},t\right)-\hat{\Psi}_1^{\dagger}\left(\mathbf{r},t\right)\hat{\Psi}_1\left(\mathbf{r}',t\right)\right)\hat{h}_1\hat{\Psi}_1\left(\mathbf{r},t\right)\\
&=\int \mathrm{d}\mathbf{r}\delta\left(\mathbf{r}'-\mathbf{r}\right)\hat{h}_1\hat{\Psi}_1\left(\mathbf{r},t\right)\\
&=\int \mathrm{d}\mathbf{r}\hat{h}_1\hat{\Psi}_1\left(\mathbf{r}',t\right)\\
&=\hat{h}_1\hat{\Psi}_1\left(\mathbf{r}',t\right)
\end{aligned} \tag{A.7}$$

as $\hat{\Psi}_1^{\dagger}\left(\mathbf{r}',t\right)\hat{\Psi}_1\left(\mathbf{r},t\right)=\hat{\Psi}_1\left(\mathbf{r},t\right)\hat{\Psi}_1^{\dagger}\left(\mathbf{r}',t\right)$ from $\left[\hat{\Psi}_1\left(\mathbf{r},t\right),\hat{\Psi}_1\left(\mathbf{r}',t\right)\right]=0$, the fields are the operators and the potential and kinetic energy are complex coefficients and $\left[\hat{\Psi}_1\left(\mathbf{r}',t\right),\hat{\Psi}_1^{\dagger}\left(\mathbf{r},t\right)\right]=\delta\left(\mathbf{r}'-\mathbf{r}\right)$.

Similarly taking the terms labelled by a B in Equation (A.6)

$$\begin{aligned}
&\int \mathrm{d}\mathbf{r}\left(\hat{\Psi}_1\left(\mathbf{r}',t\right)\hat{\Psi}_2^{\dagger}\left(\mathbf{r},t\right)-\hat{\Psi}_2^{\dagger}\left(\mathbf{r},t\right)\hat{\Psi}_1\left(\mathbf{r}',t\right)\right)\hat{h}_2\hat{\Psi}_2\left(\mathbf{r},t\right)\\
&=0
\end{aligned} \tag{A.8}$$

as $\left[\hat{\Psi}_1\left(\mathbf{r}',t\right),\hat{\Psi}_2^{\dagger}\left(\mathbf{r},t\right)\right]=0$.

Taking the terms labelled by C in 2.7

$$\begin{aligned}
&\frac{g_{11}}{2}\int \mathrm{d}\mathbf{r}\hat{\Psi}_1\left(\mathbf{r}',t\right)\hat{\Psi}_1^{\dagger}\left(\mathbf{r},t\right)\hat{\Psi}_1^{\dagger}\left(\mathbf{r},t\right)\hat{\Psi}_1\left(\mathbf{r},t\right)\hat{\Psi}_1\left(\mathbf{r},t\right)\\
&-\frac{g_{11}}{2}\int \mathrm{d}\mathbf{r}\hat{\Psi}_1^{\dagger}\left(\mathbf{r},t\right)\hat{\Psi}_1^{\dagger}\left(\mathbf{r},t\right)\hat{\Psi}_1\left(\mathbf{r},t\right)\hat{\Psi}_1\left(\mathbf{r},t\right)\hat{\Psi}_1\left(\mathbf{r}',t\right)\\
&=\frac{g_{11}}{2}\left[\int \mathrm{d}\mathbf{r}\hat{\Psi}_1\left(\mathbf{r}',t\right)\hat{\Psi}_1^{\dagger}\left(\mathbf{r},t\right)\hat{\Psi}_1^{\dagger}\left(\mathbf{r},t\right)\hat{\Psi}_1\left(\mathbf{r},t\right)\hat{\Psi}_1\left(\mathbf{r},t\right)\right.\\
&\left.-\int \mathrm{d}\mathbf{r}\hat{\Psi}_1^{\dagger}\left(\mathbf{r},t\right)\hat{\Psi}_1^{\dagger}\left(\mathbf{r},t\right)\hat{\Psi}_1\left(\mathbf{r}',t\right)\hat{\Psi}_1\left(\mathbf{r},t\right)\hat{\Psi}_1\left(\mathbf{r},t\right)\right]\\
&=\frac{g_{11}}{2}\int \mathrm{d}\mathbf{r}\left(\hat{\Psi}_1\left(\mathbf{r}',t\right)\hat{\Psi}_1^{\dagger}\left(\mathbf{r},t\right)\hat{\Psi}_1^{\dagger}\left(\mathbf{r},t\right)-\hat{\Psi}_1^{\dagger}\left(\mathbf{r},t\right)\hat{\Psi}_1^{\dagger}\left(\mathbf{r},t\right)\hat{\Psi}_1\left(\mathbf{r}',t\right)\right)\hat{\Psi}_1\left(\mathbf{r},t\right)\hat{\Psi}_1\left(\mathbf{r},t\right)\\
&=g_{11}\int \mathrm{d}\mathbf{r}\hat{\Psi}_1^{\dagger}\left(\mathbf{r}',t\right)\hat{\Psi}_1\left(\mathbf{r}',t\right)\hat{\Psi}_1\left(\mathbf{r}',t\right)\\
&=g_{11}\hat{\Psi}_1^{\dagger}\left(\mathbf{r}',t\right)\hat{\Psi}_1\left(\mathbf{r}',t\right)\hat{\Psi}_1\left(\mathbf{r}',t\right)
\end{aligned}\tag{A.9}$$

as $\left[\hat{\Psi}_1\left(\mathbf{r},t\right),\hat{\Psi}_1\left(\mathbf{r}',t\right)\right]=0$ and

$$\begin{aligned}
\left[\hat{\Psi}_1\left(\mathbf{r}',t\right),\hat{\Psi}_1^{\dagger}\left(\mathbf{r},t\right)\hat{\Psi}_1^{\dagger}\left(\mathbf{r},t\right)\right]&=\left[\hat{\Psi}_1\left(\mathbf{r}',t\right),\hat{\Psi}_1^{\dagger}\left(\mathbf{r},t\right)\right]\hat{\Psi}_1^{\dagger}\left(\mathbf{r},t\right)+\hat{\Psi}_1^{\dagger}\left(\mathbf{r},t\right)\left[[\hat{\Psi}_1\left(\mathbf{r}',t\right),\hat{\Psi}_1^{\dagger}\left(\mathbf{r},t\right)\right]\\
&=\delta\left(\mathbf{r}'-\mathbf{r}\right)\hat{\Psi}_1^{\dagger}\left(\mathbf{r},t\right)+\hat{\Psi}_1^{\dagger}\left(\mathbf{r},t\right)\delta\left(\mathbf{r}'-\mathbf{r}\right)\\
&=2\delta\left(\mathbf{r}'-\mathbf{r}\right)\hat{\Psi}_1^{\dagger}\left(\mathbf{r},t\right).
\end{aligned}\tag{A.10}$$

Similarly terms labelled by D in Equation (A.6) give

$$\begin{aligned}
&\frac{g_{22}}{2}\int \mathrm{d}\mathbf{r}\left[\hat{\Psi}_1\left(\mathbf{r}',t\right),\hat{\Psi}_2^{\dagger}\left(\mathbf{r},t\right)\hat{\Psi}_2^{\dagger}\left(\mathbf{r},t\right)\right]\hat{\Psi}_2\left(\mathbf{r},t\right)\hat{\Psi}_2\left(\mathbf{r},t\right)\\
&=0
\end{aligned}\tag{A.11}$$

as

$$\left[\hat{\Psi}_1\left(\mathbf{r}',t\right),\hat{\Psi}_2^{\dagger}\left(\mathbf{r},t\right)\hat{\Psi}_2^{\dagger}\left(\mathbf{r},t\right)\right]=0\tag{A.12}$$

The final terms labelled E in Equation (A.6) give

$$\begin{aligned}
&\frac{g_{12}}{2}\left[\int \mathrm{d}\mathbf{r}\hat{\Psi}_1\left(\mathbf{r}',t\right)\hat{\Psi}_1^\dagger\left(\mathbf{r},t\right)\hat{\Psi}_2^\dagger\left(\mathbf{r},t\right)\hat{\Psi}_1\left(\mathbf{r},t\right)\hat{\Psi}_2\left(\mathbf{r},t\right)\right.\\
&\left.-\int \mathrm{d}\mathbf{r}\hat{\Psi}_1^\dagger\left(\mathbf{r},t\right)\hat{\Psi}_2^\dagger\left(\mathbf{r},t\right)\hat{\Psi}_1\left(\mathbf{r},t\right)\hat{\Psi}_2\left(\mathbf{r},t\right)\hat{\Psi}_1\left(\mathbf{r}',t\right)\right]\\
&=\frac{g_{12}}{2}\left[\int \mathrm{d}\mathbf{r}\hat{\Psi}_1\left(\mathbf{r}',t\right)\hat{\Psi}_1^\dagger\left(\mathbf{r},t\right)\hat{\Psi}_2^\dagger\left(\mathbf{r},t\right)\hat{\Psi}_1\left(\mathbf{r},t\right)\hat{\Psi}_2\left(\mathbf{r},t\right)\right.\\
&\left.-\int \mathrm{d}\mathbf{r}\hat{\Psi}_1^\dagger\left(\mathbf{r},t\right)\hat{\Psi}_2^\dagger\left(\mathbf{r},t\right)\hat{\Psi}_1\left(\mathbf{r}',t\right)\hat{\Psi}_1\left(\mathbf{r},t\right)\hat{\Psi}_2\left(\mathbf{r},t\right)\right]\\
&=\frac{g_{12}}{2}\int \mathrm{d}\mathbf{r}\left(\hat{\Psi}_1\left(\mathbf{r}',t\right)\hat{\Psi}_1^\dagger\left(\mathbf{r},t\right)\hat{\Psi}_2^\dagger\left(\mathbf{r},t\right)-\hat{\Psi}_1^\dagger\left(\mathbf{r},t\right)\hat{\Psi}_2^\dagger\left(\mathbf{r},t\right)\hat{\Psi}_1\left(\mathbf{r}',t\right)\right)\hat{\Psi}_1\left(\mathbf{r},t\right)\hat{\Psi}_2\left(\mathbf{r},t\right)\\
&=\frac{g_{12}}{2}\int \mathrm{d}\mathbf{r}\left[\hat{\Psi}_1\left(\mathbf{r}',t\right),\hat{\Psi}_1^\dagger\left(\mathbf{r},t\right)\hat{\Psi}_2^\dagger\left(\mathbf{r},t\right)\right]\hat{\Psi}_1\left(\mathbf{r},t\right)\hat{\Psi}_2\left(\mathbf{r},t\right)\\
&=\frac{g_{12}}{2}\int \mathrm{d}\mathbf{r}\delta\left(\mathbf{r}'-\mathbf{r}\right)\hat{\Psi}_2^\dagger\left(\mathbf{r},t\right)\hat{\Psi}_1\left(\mathbf{r},t\right)\hat{\Psi}_2\left(\mathbf{r},t\right)\\
&=\frac{g_{12}}{2}\int \mathrm{d}\mathbf{r}\hat{\Psi}_2^\dagger\left(\mathbf{r}',t\right)\hat{\Psi}_2\left(\mathbf{r}',t\right)\hat{\Psi}_1\left(\mathbf{r}',t\right)\\
&=\frac{g_{12}}{2}\hat{\Psi}_2^\dagger\left(\mathbf{r}',t\right)\hat{\Psi}_2\left(\mathbf{r}',t\right)\hat{\Psi}_1\left(\mathbf{r}',t\right)
\end{aligned} \tag{A.13}$$

as

$$\begin{aligned}
\left[\hat{\Psi}_1\left(\mathbf{r}',t\right),\hat{\Psi}_1^\dagger\left(\mathbf{r},t\right)\hat{\Psi}_2^\dagger\left(\mathbf{r},t\right)\right]&=\left[\hat{\Psi}_1\left(\mathbf{r}',t\right),\hat{\Psi}_1^\dagger\left(\mathbf{r},t\right)\right]\hat{\Psi}_2^\dagger\left(\mathbf{r},t\right)+\hat{\Psi}_1^\dagger\left(\mathbf{r},t\right)\left[\hat{\Psi}_1\left(\mathbf{r}',t\right),\hat{\Psi}_2^\dagger\left(\mathbf{r},t\right)\right]\\
&=\delta\left(\mathbf{r}'-\mathbf{r}\right)\hat{\Psi}_2^\dagger\left(\mathbf{r},t\right)
\end{aligned} \tag{A.14}$$

Combining these leads to

$$\mathrm{i}\hbar\frac{\partial\hat{\Psi}_1\left(\mathbf{r},t\right)}{\partial t}=\hat{h}_1\hat{\Psi}_1\left(\mathbf{r},t\right)+g_{11}\hat{\Psi}_1^\dagger\left(\mathbf{r},t\right)\hat{\Psi}_1\left(\mathbf{r},t\right)\hat{\Psi}_1\left(\mathbf{r},t\right)+\frac{g_{12}}{2}\hat{\Psi}_2^\dagger\left(\mathbf{r},t\right)\hat{\Psi}_2\left(\mathbf{r},t\right)\hat{\Psi}_1\left(\mathbf{r},t\right) \tag{A.15}$$

Similarly, it can be shown for species 2 that

$$\mathrm{i}\hbar\frac{\partial\hat{\Psi}_2\left(\mathbf{r},t\right)}{\partial t}=\hat{h}_2\hat{\Psi}_2\left(\mathbf{r},t\right)+g_{22}\hat{\Psi}_2^\dagger\left(\mathbf{r},t\right)\hat{\Psi}_2\left(\mathbf{r},t\right)\hat{\Psi}_2\left(\mathbf{r},t\right)+\frac{g_{12}}{2}\hat{\Psi}_1^\dagger\left(\mathbf{r},t\right)\hat{\Psi}_1\left(\mathbf{r},t\right)\hat{\Psi}_2\left(\mathbf{r},t\right) \tag{A.16}$$

We now decompose the Bose field operator $\hat{\Psi}_i\left(\mathbf{r},t\right)$ in terms of a macroscopically–

populated mean field term $\phi_i(\mathbf{r},t) = \langle\hat{\Psi}_i(\mathbf{r},t)\rangle$ and a fluctuation term $\hat{\psi}_i(\mathbf{r},t)$ and get

$$\begin{aligned}\hat{H} = &\int \mathrm{d}\mathbf{r}\left(\phi_1^* + \hat{\psi}_1^\dagger\right)\hat{h}_1\left(\phi_1 + \hat{\psi}_1\right)\\ &+ \frac{g_{11}}{2}\int \mathrm{d}\mathbf{r}\left(\phi_1^* + \hat{\psi}_1^\dagger\right)\left(\phi_1^* + \hat{\psi}_1^\dagger\right)\left(\phi_1 + \hat{\psi}_1\right)\left(\phi_1 + \hat{\psi}_1\right)\\ &+ \int \mathrm{d}\mathbf{r}\left(\phi_2^* + \hat{\psi}_2^\dagger\right)\hat{h}_2\left(\phi_2 + \hat{\psi}_2\right)\\ &+ \frac{g_{22}}{2}\int \mathrm{d}\mathbf{r}\left(\phi_2^* + \hat{\psi}_2^\dagger\right)\left(\phi_2^* + \hat{\psi}_2^\dagger\right)\left(\phi_2 + \hat{\psi}_2\right)\left(\phi_2 + \hat{\psi}_2\right)\\ &+ \frac{g_{12}}{2}\int \mathrm{d}\mathbf{r}\left(\phi_1^* + \hat{\psi}_1^\dagger\right)\left(\phi_2^* + \hat{\psi}_2^\dagger\right)\left(\phi_1 + \hat{\psi}_1\right)\left(\phi_2 + \hat{\psi}_2\right)\end{aligned} \tag{A.17}$$

Rearranging leads to

$$\begin{aligned}\hat{H} = &\int \mathrm{d}\mathbf{r}\phi_1^*\hat{h}_1\phi_1 + \phi_1^*\hat{h}_1\hat{\psi}_1 + \hat{\psi}_1^\dagger\hat{h}_1\phi_1 + \hat{\psi}_1^\dagger\hat{h}_1\hat{\psi}_1\\ &+ \frac{g_{11}}{2}\int \mathrm{d}\mathbf{r}\left(\phi_1^*\phi_1^* + 2\phi_1^*\hat{\psi}_1^\dagger + \hat{\psi}_1^\dagger\hat{\psi}_1^\dagger\right)\left(\phi_1^2 + 2\phi_1\hat{\psi}_1 + \hat{\psi}_1\hat{\psi}_1\right)\\ &+ \int \mathrm{d}\mathbf{r}\phi_2^*\hat{h}_2\phi_2 + \phi_2^*\hat{h}_2\hat{\psi}_2 + \hat{\psi}_2^\dagger\hat{h}_2\phi_2 + \hat{\psi}_2^\dagger\hat{h}_2\hat{\psi}_2\\ &+ \frac{g_{22}}{2}\int \mathrm{d}\mathbf{r}\left(\phi_2^*\phi_2^* + 2\phi_2^*\hat{\psi}_2^\dagger + \hat{\psi}_2^\dagger\hat{\psi}_2^\dagger\right)\left(\phi_2^2 + 2\phi_2\hat{\psi}_2 + \hat{\psi}_2\hat{\psi}_2\right)\\ &+ \frac{g_{12}}{2}\int \mathrm{d}\mathbf{r}\left(\phi_1^*\phi_2^* + \phi_2^*\hat{\psi}_1^\dagger + \phi_1^*\hat{\psi}_2^\dagger + \hat{\psi}_1^\dagger\hat{\psi}_2^\dagger\right)\left(\phi_1\phi_2 + \phi_2\hat{\psi}_1 + \phi_1\hat{\psi}_2 + \hat{\psi}_1\hat{\psi}_2\right)\end{aligned} \tag{A.18}$$

The Hamiltonian is separated into parts according to the dependence on $\hat{\psi}_i$, $\hat{H} = \hat{H}_0 + \hat{H}_1 + \hat{H}_2 + \hat{H}_3 + \hat{H}_4$ where the contributions are

$$\hat{H}_0 = \int \mathrm{d}\mathbf{r}\phi_1^*\hat{h}_1\phi_1 + \frac{g_{11}}{2}|\phi_1|^4 + \phi_2^*\hat{h}_2\phi_2 + \frac{g_{22}}{2}|\phi_2|^4 + \frac{g_{12}}{2}|\phi_1|^2|\phi_2|^2 \tag{A.19}$$

$$\begin{aligned}\hat{H}_1 = &\int \mathrm{d}\mathbf{r}\phi_1^*\hat{h}_1\hat{\psi}_1 + \hat{\psi}_1^\dagger\hat{h}_1\phi_1 + g11\phi_1^*|\phi_1|^2\hat{\psi}_1 + g11\phi_1|\phi_1|^2\hat{\psi}_1^\dagger\\ &+ \int \mathrm{d}\mathbf{r}\phi_2^*\hat{h}_2\hat{\psi}_2 + \hat{\psi}_2^\dagger\hat{h}_2\phi_2 + g22\phi_2^*|\phi_2|^2\hat{\psi}_2 + g22\phi_2|\phi_2|^2\hat{\psi}_2^\dagger\\ &+ \frac{g_{12}}{2}\int \mathrm{d}\mathbf{r}\phi_1^*|\phi_2|^2\hat{\psi}_1 + \phi_2^*|\phi_1|^2\hat{\psi}_2 + \phi_1|\phi_2|^2\hat{\psi}_1^\dagger + \phi_2|\phi_1|^2\hat{\psi}_2^\dagger\end{aligned} \tag{A.20}$$

$$\begin{aligned}\hat{H}_2 = &\int \mathrm{d}\mathbf{r}\hat{\psi}_1^\dagger\hat{h}_1\hat{\psi}_1 + \frac{g_{11}}{2}\left((\phi_1^*)^2\hat{\psi}_1\hat{\psi}_1 + \phi_1^2\hat{\psi}_1^\dagger\hat{\psi}_1^\dagger\right) + 2g_{11}|\phi_1|^2\hat{\psi}_1^\dagger\hat{\psi}_1\\ &+ \int \mathrm{d}\mathbf{r}\hat{\psi}_2^\dagger\hat{h}_2\hat{\psi}_2 + \frac{g_{22}}{2}\left((\phi_2^*)^2\hat{\psi}_2\hat{\psi}_2 + \phi_2^2\hat{\psi}_2^\dagger\hat{\psi}_2^\dagger\right) + 2g_{22}|\phi_2|^2\hat{\psi}_2^\dagger\hat{\psi}_2\\ &+ \frac{g_{12}}{2}\int \mathrm{d}\mathbf{r}\phi_1^*\phi_2^*\hat{\psi}_1\hat{\psi}_2 + \phi_1\phi_2\hat{\psi}_1^\dagger\hat{\psi}_2^\dagger + |\phi_2|^2\hat{\psi}_1^\dagger\hat{\psi}_1 + \phi_1\phi_2^*\hat{\psi}_1^\dagger\hat{\psi}_2 + |\phi_1|^2\hat{\psi}_2^\dagger\hat{\psi}_2 + \phi_1^*\phi_2\hat{\psi}_2^\dagger\hat{\psi}_1\end{aligned} \tag{A.21}$$

$$\begin{aligned}\hat{H}_3 =& g_{11}\int \mathrm{d}\mathbf{r}\phi_1\hat{\psi}_1^\dagger\hat{\psi}_1^\dagger\hat{\psi}_1 + \phi_1^*\hat{\psi}_1^\dagger\hat{\psi}_1\hat{\psi}_1 \\ &+ g_{22}\int \mathrm{d}\mathbf{r}\phi_2\hat{\psi}_2^\dagger\hat{\psi}_2^\dagger\hat{\psi}_2 + \phi_2^*\hat{\psi}_2^\dagger\hat{\psi}_2\hat{\psi}_2 \\ &+ g_{12}\int \mathrm{d}\mathbf{r}\phi_2^*\hat{\psi}_1^\dagger\hat{\psi}_1\hat{\psi}_2 + \phi_1^*\hat{\psi}_2^\dagger\hat{\psi}_1\hat{\psi}_2 + \phi_2\hat{\psi}_1^\dagger\hat{\psi}_2^\dagger\hat{\psi}_1 + \phi_1\hat{\psi}_1^\dagger\hat{\psi}_2^\dagger\hat{\psi}_2\end{aligned} \tag{A.22}$$

$$\hat{H}_4 = \int \mathrm{d}\mathbf{r}\frac{g_{11}}{2}\hat{\psi}_1^\dagger\hat{\psi}_1^\dagger\hat{\psi}_1\hat{\psi}_1 + \frac{g_{22}}{2}\hat{\psi}_2^\dagger\hat{\psi}_2^\dagger\hat{\psi}_2\hat{\psi}_2 + \frac{g_{12}}{2}\hat{\psi}_1^\dagger\hat{\psi}_2^\dagger\hat{\psi}_1\hat{\psi}_2 \tag{A.23}$$

All the atoms are assumed to be in the condensate $\hat{\psi}_i = 0$ and the Hamiltonian is then given solely by $\hat{H}_0$. When substituted into the Heisenberg equation of motion (A.6), Equations (A.15) and (A.16) result in the CGPEs which accurately describes systems at zero temperature

$$\begin{aligned}\mathrm{i}\hbar\frac{\partial\phi_1(\mathbf{r},t)}{\partial t} &= \left[\frac{\hbar^2}{2m_1}\nabla^2 + V_1 + g_{11}\left|\phi_1(\mathbf{r},t)\right|^2 + g_{12}\left|\phi_2(\mathbf{r},t)\right|^2\right]\phi_1(\mathbf{r},t) \\ \mathrm{i}\hbar\frac{\partial\phi_2(\mathbf{r},t)}{\partial t} &= \left[\frac{\hbar^2}{2m_2}\nabla^2 + V_2 + g_{22}\left|\phi_1(\mathbf{r},t)\right|^2 + g_{12}\left|\phi_1(\mathbf{r},t)\right|^2\right]\phi_2(\mathbf{r},t)\end{aligned} \tag{A.24}$$

A.1 Dimensionless Analysis

We show how the CGPEs can be reduced to a dimensionless form. This analysis was done in collaboration with S. A. Gardiner (Joint Quantum Centre (JQC) Durham–Newcastle, Department of Physics, Durham University) Here we outline this reduction and highlight some key features that emerge. We start from the CGPEs (2.52), where the trap is provided by cylindrically symmetric harmonic trapping potentials with common minima i.e.

$$V_i = \frac{m_i}{2}\left[\omega_{(i)\perp}^2\left(x^2+y^2\right) + \omega_{(i)z}^2 z^2\right]. \tag{A.25}$$

Let $\lambda_i = \omega_{(i)\perp}^2/\omega_{(i)z}^2$ be the trap aspect ratios of component 1 and 2 respectively. The coupled GPEs can then be rewritten as

$$\begin{aligned}\mathrm{i}\hbar\frac{\partial\phi_1}{\partial t} &= \left[-\frac{\hbar^2}{2m_1}\nabla^2 + \frac{m_1\omega_{(1)z}}{2}\left[\lambda_1\left(x^2+y^2\right)+z^2\right] + g_{11}\left|\phi_1\right|^2 + g_{12}\left|\phi_2\right|^2\right]\phi_1 \\ \mathrm{i}\hbar\frac{\partial\phi_2}{\partial t} &= \left[-\frac{\hbar^2}{2m_2}\nabla^2 + \frac{m_2\omega_{(2)z}}{2}\left[\lambda_2\left(x^2+y^2\right)+z^2\right] + g_{22}\left|\phi_2\right|^2 + g_{12}\left|\phi_1\right|^2\right]\phi_2\end{aligned} \tag{A.26}$$

where g_{ii} and g_{12} are given in Section 2.10. We choose a set of symmetrized harmonic units, codified as $\hbar = \sqrt{m_1 m_2} = \sqrt{\omega_{(1)z}\omega_{(2)z}} = 1$. This means we have time, length, and

energy units of

$$\tau = \frac{1}{\sqrt{\omega_{(1)z}\omega_{(2)z}}}, \tag{A.27}$$

$$\ell = \frac{\sqrt{\hbar}}{\left(m_1 m_2 \omega_{(1)z}\omega_{(2)z}\right)^{1/4}}, \tag{A.28}$$

$$\epsilon = \hbar\sqrt{\omega_{(1)z}\omega_{(2)z}}. \tag{A.29}$$

Rescaled renderings of the coupled GPEs (where we also normalize the wavefunctions ψ_1 and ψ_2 to 1, in order to make the dependence on the particle numbers N_1 and N_2 of the two species more explicit), expressed in terms of a minimal number of parameters, are then

$$\begin{aligned} \mathrm{i}\frac{\partial\phi_1}{\partial t} &= \left[-\frac{\gamma}{2}\nabla^2 + \frac{1}{2\kappa\gamma}\left[\lambda_1\left(x^2+y^2\right)+z^2\right] + \gamma\alpha_{11}\left|\phi_1\right|^2 + \left(\frac{\gamma^2+1}{2\gamma}\right)\eta\alpha_{12}\left|\phi_2\right|^2\right]\phi_1 \\ \mathrm{i}\frac{\partial\phi_2}{\partial t} &= \left[-\frac{1}{2\gamma}\nabla^2 + \frac{\kappa\gamma}{2}\left[\lambda_2\left(x^2+y^2\right)+z^2\right] + \left(\frac{\gamma^2+1}{2\gamma}\right)\frac{\alpha_{22}}{\eta}\left|\phi_2\right|^2 + \frac{\alpha_{12}}{\gamma}\left|\phi_1\right|^2\right]\phi_2 \end{aligned} \tag{A.30}$$

where

$$\gamma = \sqrt{\frac{m_2}{m_1}}, \tag{A.31}$$

$$\kappa = \frac{\omega_2}{\omega_1}, \tag{A.32}$$

$$\eta = \sqrt{\frac{N_2}{N_1}}, \tag{A.33}$$

$$\alpha_{ij} = 4\pi\left(\frac{a_{ij}}{\ell}\right)\sqrt{N_i N_j}. \tag{A.34}$$

Using the total particle number $N = N_1 + N_2$, the interaction coefficients can alternatively be phrased as

$$\alpha_{11} = 4\pi\left(\frac{a_{11}}{\ell}\right)\frac{N}{\eta^2+1}, \tag{A.35}$$

$$\alpha_{12} = 4\pi\left(\frac{a_{12}}{\ell}\right)\frac{\eta N}{\eta^2+1}, \tag{A.36}$$

$$\alpha_{22} = 4\pi\left(\frac{a_{22}}{\ell}\right)\frac{\eta^2 N}{\eta^2+1}, \tag{A.37}$$

which is a particularly natural description if the two species are simply different internal states of the same atom (in which case $\gamma = 1$, simplifying the system of equations further). We therefore have eight independent dimensionless parameters (including λ_1 and λ_2). In 1D, there are six independent parameters as $\lambda_1 = \lambda_2 = 1$.

Appendix B

Numerical Methods

The work presented in this thesis is based on numerical simulations of the dimensionless CGPEs using fourth–order Runge–Kutta in time and second or fourth–order finite order finite difference discretisation in space [249]. These numerical methods are outlined in Sections B.1 and B.2, derived using Taylor series expansions obtained by expanding an n–times differentiable function $f(x)$

$$f\left(x+h\right)=f\left(x\right)+hf^{'}\left(x\right)+\frac{h^{2}}{2!}f^{''}\left(x\right)+...+\frac{h^{n}}{n!}f^{n}\left(x\right)+... \tag{B.1}$$

where h is a small step. Additionally, we present how ground state density profiles are obtained through use of imaginary time propagation.

B.1 Runge–Kutta Method

For some function $u(t)$, consider the differential equation

$$\frac{\mathrm{d}u}{\mathrm{d}t}=u^{'}=g(t,u). \tag{B.2}$$

We take $t_n = n\Delta t$ where Δt is the small time step and $u_n = u(t_n)$ be the function $u(t)$ after n iterations. The sought out solution is $u_{n+1} = u(t_n + \Delta t)$. The formula for Euler's method is

$$u_{n+1}=u_{n}+\Delta tg\left(t_{n},u_{n}\right)+O\left(\Delta t^{2}\right) \tag{B.3}$$

which advances u_n to u_{n+1} and is derived from Equation (B.1) by neglecting terms with second order or higher derivatives. For practical use, this method is not recommended due to the lack of accuracy compare to other methods and it is not very stable. In addition, the formula is unsymmetrical: it uses derivative information at the beginning of the interval only.

We now consider the taylor expansion of u with the second order derivative term

$$u_{n+1} = u_n = \Delta t u_n^{'} + \frac{\Delta t^2}{2} u_n^{''} + O\left(\Delta t^3\right) \tag{B.4}$$

where $u_n^{''}$ is obtained from Equation (B.2) such that

$$u_n^{''} = \frac{\partial g\left(t_n, u_n\right)}{\partial t} + \frac{\partial g\left(t_n, u_n\right)}{\partial u} g\left(t_n, u_n\right) = g_t\left(t_n, u_n\right) + g_u\left(t_n, u_n\right) g\left(t_n, u_n\right). \tag{B.5}$$

By substitution we obtain

$$\begin{aligned} u_{n+1} &= u_n + \Delta t g\left(t_n, u_n\right) + \frac{\Delta t^2}{2} g_t\left(t_n, u_n\right) + g_u\left(t_n, u_n\right) g\left(t_n, u_n\right) + O\left(\Delta t^3\right) \\ &= u_n + \frac{\Delta t}{2} g\left(t_n, u_n\right) + \frac{\Delta t}{2}\left[g\left(t_n, u_n\right) + \Delta t\left(g_t\left(t_n, u_n\right) + g_u\left(t_n, u_n\right) g\left(t_n, u_n\right)\right)\right] + O\left(\Delta t^3\right). \end{aligned} \tag{B.6}$$

Now consider the Taylor expansion for $g\left(t, u\right)$

$$g\left(t + h, u + k\right) = g\left(t, u\right) + h g_t\left(t, u\right) + k g_u\left(t, u\right) + ... \tag{B.7}$$

Taking $h = \Delta t$ and $k = \Delta t g$ gives

$$g\left(t + \Delta t, u + \Delta t g\right) = g\left(t, u\right) + \Delta t g_t\left(t, u\right) + \Delta t g\left(t, u\right) g_u\left(t, u\right) + ... \tag{B.8}$$

Substitute into Equation (B.6) to give

$$u_{n+1} = u_n + \frac{\Delta t}{2} g + \frac{\Delta t}{2} g\left(t + \Delta t, u + \Delta t g\right) + O\left(\Delta t^3\right). \tag{B.9}$$

This is known as the midpoint method or second–order Runge–Kutta method and is more commonly written as

$$\begin{aligned} k_1 &= g\left(t_n, u_n\right) \\ k_2 &= g\left(t_n + \Delta t, u_n + \Delta t k_1\right) \\ u_{n+1} &= u_n + \frac{\Delta t}{2}\left(k_1 + k_2\right) + O\left(\Delta t^3\right). \end{aligned} \tag{B.10}$$

Unlike Euler's method, a step at the midpoint of the interval is used to calculate the step across the whole interval. It also has a higher order error. In fact, higher order methods often give better accuracy, even though this is not always the case. Such a derivation can be generalized to obtain the fourth–order Runge-Kutta method, used to obtain the

numerical results presented in this Thesis, and is given by

$$u^{n+1} = u^n + \Delta t \left[\frac{1}{6}k_1 + \frac{1}{3}k_2 + \frac{1}{3}k_3 + \frac{1}{6}k_4\right] + O\left(\Delta t^5\right) \tag{B.11}$$

where

$$\begin{aligned} k_1 &= f\left(t_n, u_n\right) \\ k_2 &= f\left(t_n + \frac{\Delta t}{2}, u_n + \frac{1}{2}\Delta t k_1\right) \\ k_3 &= f\left(t_n + \frac{\Delta t}{2}, u_n + \frac{1}{2}\Delta t k_2\right) \\ k_4 &= f\left(t_n + \Delta t, u_n + \Delta t k_3\right). \end{aligned} \tag{B.12}$$

Similarly to the second–order method, three intermediate points are now used to calculate the step across the whole interval.

B.2 Discretisation of Spatial Derivatives

In order to numerically solve the GPE equation, we must calculate the Hamiltonian using finite difference where the wavefunction is discretised on a spatial grid with spacing Δx. In this Section, we introduce the finite difference schemes for a function $u(x)$ in one and two dimensions.

One–Dimensional System

In one dimension, our function $u(x)$ is discretised on a linear grid with $u_i = u(x_i)$ where $i = 0, 1, ..., L$. To derive the central difference schemes, we first write down the Taylor series for u_{i-1} and u_{i+1}

$$u_{i-1} = u_i - \Delta x u_i^{'} + \frac{\Delta x^2}{2} u_i^{''} + O\left(\Delta x^2\right) \tag{B.13}$$

$$u_{i+1} = u_i + \Delta x u_i^{'} + \frac{\Delta x^2}{2} u_i^{''} + O\left(\Delta x^2\right). \tag{B.14}$$

To obtain the first order derivative, we look at $-u_{i-1} + u_{i+1}$

$$-u_{i-1} + u_{i+1} = 2\Delta x u_i^{'} + O\left(\Delta x^2\right) \tag{B.15}$$

and rearrange to obtain

$$\frac{\mathrm{d}u_i}{\mathrm{d}x} = \frac{-u_{i-1} + u_{i+1}}{2\Delta x} + O\left(\Delta x^2\right). \tag{B.16}$$

Similarly to obtain the second order derivative we look at $u_{i-1}-2u_i+u_{i+1}$ and rearranging gives

$$\frac{\mathrm{d}^2 u_i}{\mathrm{d}x^2} = \frac{u_{i-1} - 2u_i + u_{i+1}}{2\Delta x^2} + O\left(\Delta x^2\right). \tag{B.17}$$

Equations (B.16) and (B.17) are the second order central difference approximations. In a similar fashion, the fourth order approximations which are used in this Thesis can be derived and are given by

$$\frac{\mathrm{d}u_i}{\mathrm{d}x} = \frac{u_{i-2} - 8u_{i-1} + 8u_{i+1} - uj + 2}{12\Delta x} + O\left(\Delta x^4\right) \tag{B.18}$$

$$\frac{\mathrm{d}^2 u_i}{\mathrm{d}x^2} = \frac{-u_{i-2} + 16u_{i-1} - 30u_i + 16u_{i+1} - ui + 2}{12\Delta x^2} + O\left(\Delta x^4\right) \tag{B.19}$$

which have superior precision to the second order approximations.

Two–Dimensional System

We now consider the two–dimensional function $u(x, y)$. It is discretised in a box in the x and y directions with spatial separation Δx and Δy respectively where $u_{i,j} = u(x_i, y_j)$. The second order central finite difference approximations for x derivatives, derived in the same manner as for one dimension, are given by

$$\frac{\mathrm{d}u_{i,j}}{\mathrm{d}x} = \frac{-u_{i-1,j} + u_{i+1,j}}{2\Delta x} + O\left(\Delta x^2\right) \tag{B.20}$$

$$\frac{\mathrm{d}^2 u_{i,j}}{\mathrm{d}x^2} = \frac{u_{i-1,j} - 2u_{i,j} + u_{i+1,j}}{2\Delta x^2} + O\left(\Delta x^2\right). \tag{B.21}$$

Similarly derivatives in the y direction can be found. We can now write down the expression for the two–dimensional Laplacian

$$\frac{\mathrm{d}^2 u_{i,j}}{\mathrm{d}x^2} + \frac{\mathrm{d}^2 u_{i,j}}{\mathrm{d}x^2} = \frac{u_{i-1,j} - 2u_{i,j} + u_{i+1,j}}{2\Delta x^2} + O\left(\Delta x^2\right) + \frac{u_{i,j-1} - 2u_{i,j} + u_{i,j+1}}{2\Delta y^2} + O\left(\Delta y^2\right). \tag{B.22}$$

Extension to three–dimensions is straight forward.

B.2.1 Boundary Conditions

In this Thesis, two different boundary conditions are used: hard wall and periodic. For hard wall boundary conditions, the point(s) at the extremities of the spatial grid are set to zero after every time–step. Simulating the GPE in a homogeneous system with this condition gives rise to density profiles as shown in Figure 2.3 at the edge of the grid. These boundary conditions are used for all simulations in Part II of this Thesis. Periodic

boundary conditions are applied by setting (in a one–dimensional case)

$$u_0 = u_{L-1} \text{ and } u_L = u_1 \tag{B.23}$$

such that when the wavefunction passes through one boundary it reappears on the opposite face. Extra boundary points need to be used when considering fourth order or higher finite difference schemes. Periodic boundaries are used in Part III.

B.3 Imaginary Time Propagation

Propagating in imaginary time is an easily implemented method to obtain a ground state of a system. This is implemented by making the substitution $\mathrm{d}t \to -\mathrm{i}\mathrm{d}\tau$. By starting with a rough trial wavefunction, ideally close to the exact solution, and by renormalising to a fixed norm and/or chemical potential during imaginary time propagation, the wavefunction decays towards the ground state of the system. For imaginary time propagation to work, obtaining a fully converged solution is necessary as, if not, the equilibrium state of the system is unknown or incorrect.

Appendix C

Discrete Fourier Transforms

In this appendix, we show the derivation for going from a continuous Fourier transform to a discrete Fourier transform.

Consider $f(x)$, a continuous function of position and its Fourier transform is given by

$$\tilde{f}(k) = \mathcal{F}[f(x)] = \int_{-\infty}^{\infty} f(x)\, e^{-\mathrm{i}kx} \mathrm{d}x. \tag{C.1}$$

Now take $f(x)$ with a discrete representation with spacing Δ_x on a spatial grid $x = [0, L]$ and denote each point by j

$$f(x) \to f(x_j) = f_j, x = j\Delta_x \tag{C.2}$$

where j exists in the range $[0, N_x]$. Now that $f(x)$ has a discrete representation, the Fourier transform acts only at the grid points. It is thus possible to replace the integral with a summation of trapezia of height f_j and width Δ_x

$$\begin{aligned}
\tilde{f}(k) &= \int_{0}^{N_x} f(x)\, e^{-\mathrm{i}kx} \mathrm{d}x \\
&= \left\{ f_0 e^0 + f_1 e^{-\mathrm{i}k\Delta_x} + ... + f_j e^{-j\mathrm{i}k\Delta_x} + ... + f_{N_x} e^{(N_x)\mathrm{i}k\Delta_x} \right\} \Delta_x \\
&= \Delta_x \sum_{j=0}^{j=N_x} f_j e^{-j\mathrm{i}k\Delta_x}.
\end{aligned} \tag{C.3}$$

A spatial grid of length $L = N_x\Delta_x$ and with interval Δ_x corresponds to a momentum grid with length $2\pi/\Delta_x$ and momentum interval $\Delta_k = 2\pi/L = 2\pi/N_x\Delta_x$. Thus the possible momentum values can be $m\Delta_k$ where m exists over the range $[0, N_x]$. The momentum

variable in Equation (C.3) by $k \to k_m = m\Delta_k = 2\pi m/N_x\Delta_x$ giving

$$\tilde{f}\left(k_m\right) = \Delta_x \sum_{j=0}^{j=N_x} f_j e^{-2\pi \mathrm{i} jm/N_x} \tag{C.4}$$

This gives the standard definition of the discrete Fourier transform of the sequence f_j

$$\mathrm{DFT}\left[f_j\right]\left(k_m\right) = \sum_{j=0}^{j=N_x} f_j e^{-2\pi \mathrm{i} jm/N_x}. \tag{C.5}$$

In this definition, the spacing is taken to be unity hence to relate the continuous Fourier transform we have

$$\tilde{f}\left(k_m\right) = \Delta_x \mathrm{DFT}\left[f_j\right]\left(k_m\right). \tag{C.6}$$

This result is valid for 1D. The equivalent 3D discrete Fourier transform is

$$\tilde{f}\left(k_x, k_y, k_z\right) = \Delta_x\Delta_y\Delta_z \mathrm{DFT}\left[f_j\right]\left(k_{m,x}, k_{m,y}, k_{m,z}\right). \tag{C.7}$$

Bibliography

[1] S. N. Bose Z. Phys **26**, 178 (1924).

[2] A. Einstein Nature **141**, 643 (1938).

[3] F. London Sitzber. Kgl. Preuss. Akad. Wiss. **23**, 3 (1925).

[4] F. London Phys. Rev. **54**, 947 (1938).

[5] M. H. Anderson, J. R. Ensher, M. R. Matthews, C. E. Wieman, and E. A. Cornell, *Observation of Bose-Einstein Condensation in a Dilute Atomic Vapor* Science **269**, 198 (1995).

[6] K. B. Davis, M.-O. Mewes, M. R. Andrews, N. J. van Druten, D. S. Durfee, D. M. Kurn, and W. Ketterle, *Bose-Einstein Condensation in a Gas of Sodium Atoms* Phys. Rev. Lett **75**, 3969 (1995).

[7] C. C. Bradley, C. A. Sackett, J. J. Tollett, and R. G. Hulet, *Evidence of Bose-Einstein Condensation in an Atomic Gas with Attractive Interactions* Phys. Rev. Lett **75**, 1687 (1995).

[8] C. C. Bradley, C. A. Sackett, and R. G. Hulet, *Bose-Einstein Condensation of Lithium: Observation of Limited Condensate Number* Phys. Rev. Lett **78**, 985 (1997).

[9] S. Chu, *Nobel Lecture: The manipulation of neutral particles* Rev. Mod. Phys. **70**, 685 (1998).

[10] W. D. Phillips, *Nobel Lecture: Laser cooling and trapping of neutral atoms* Rev. Mod. Phys. **70**, 721 (1998).

[11] C. N. Cohen-Tannoudji, *Nobel Lecture: Manipulating atoms with photons* Rev. Mod. Phys. **70**, 707 (1998).

[12] E. A. Cornell and C. E. Wieman, *Nobel Lecture: Bose - Einstein condensation in a dilute gas, the first 70 years and some recent experiments* Rev. Mod. Phys. **74**, 875 (2002).

[13] W. Ketterle, *Nobel lecture: When atoms behave as waves: Bose-Einstein condensation and the atom laser* Rev. Mod. Phys. **74**, 1131 (2002).

[14] P. Kapitza Nature **141**, 74 (1938).

[15] J. F. Allen and A. D. Misener Nature **141**, 75 (1938).

[16] L. D. Landau J. Phys. (USSR) **5**, 71 (1941).

[17] W. Ketterle, D. Durfee, and D. Stamper-Kurn, *Making, probing and understanding Bose-Einstein condensates* Proceedings of the International School of Physics "Enrico Fermi" p. 67 (1999).

[18] C. Pethick and H. Smith, *Bose-Einstein condensation in dilute gases* (Cambridge University Press, 2002).

[19] C. E. Hecht Physica **25**, 1159 (1959).

[20] *The Nobel Prize in Physics 2001* Nobelprize.org (The Royal Swedish Academy of Sciences, 2001).

[21] D. G. Fried, T. C. Killian, L. Willmann, D. Landhuis, S. C. Moss, D. Kleppner, and T. J. Greytak, *Bose-Einstein Condensation of Atomic Hydrogen* Phys. Rev. Lett **81**, 3811 (1998).

[22] S. L. Cornish, N. R. Claussen, J. L. Roberts, E. A. Cornell, and C. E. Wieman, *Stable ^{85}Rb Bose-Einstein Condensates with Widely Tunable Interactions* Phys. Rev. Lett **85**, 1795 (2000).

[23] G. Modugno, G. Ferrari, G. Roati, R. J. Brecha, A. Simoni, and M. Inguscio, *Bose-Einstein Condensation of Potassium Atoms by Sympathetic Cooling* Science **294**, 1320 (2001).

[24] A. Robert, O. Sirjean, A. Browaeys, J. Poupard, S. Nowak, D. Boiron, C. I. Westbrook, and A. Aspect, *A Bose-Einstein Condensate of Metastable Atoms* Science **292**, 461 (2001).

[25] Y. Takasu, K. Maki, K. Komori, T. Takano, K. Honda, M. Kumakura, T. Yabuzaki, and Y. Takahashi, *Spin-Singlet Bose-Einstein Condensation of Two-Electron Atoms* Phys. Rev. Lett **91**, 040404 (2003).

[26] T. Weber, J. Herbig, M. Mark, H.-C. Nägerl, and R. Grimm, *Bose-Einstein Condensation of Cesium* Science **299**, 232 (2003).

[27] A. Griesmaier, J. Werner, S. Hensler, J. Stuhler, and T. Pfau, *Bose-Einstein Condensation of Chromium* Phys. Rev. Lett **94**, 160401 (2005).

[28] S. Stellmer, M. K. Tey, B. Huang, R. Grimm, and F. Schreck, *Bose-Einstein Condensation of Strontium* Phys. Rev. Lett **103**, 200401 (2009).

[29] Y. N. M. de Escobar, P. G. Mickelson, M. Yan, B. J. DeSalvo, S. B. Nagel, and T. C. Killian, *Bose-Einstein Condensation of Sr^{84}* Phys. Rev. Lett **103**, 200402 (2009).

[30] S. Stellmer, M. K. Tey, R. Grimm, and F. Schreck, *Bose-Einstein condensation of Sr^{86}* Phys. Rev. A **82**, 041602 (2010).

[31] P. G. Mickelson, Y. N. M. de Escobar, M. Yan, B. J. DeSalvo, and T. C. Killian, *Bose-Einstein condensation of Sr^{88} through sympathetic cooling with Sr^{87}* Phys. Rev. A **81**, 051601 (2010).

[32] S. Kraft, F. Vogt, O. Appel, F. Riehle, and U. Sterr, *Bose-Einstein Condensation of Alkaline Earth Atoms: Ca^{40}* Phys. Rev. Lett **103**, 130401 (2009).

[33] M. Lu, N. Q. Burdick, S. H. Youn, and B. L. Lev, *Strongly Dipolar Bose-Einstein Condensate of Dysprosium* Phys. Rev. Lett **107**, 190401 (2011).

[34] T. W. Neely, E. C. Samson, A. S. Bradley, M. J. Davis, and B. P. Anderson, *Observation of Vortex Dipoles in an Oblate Bose-Einstein Condensate* Phys. Rev. Lett. **104**, 160401 (2010).

[35] D. V. Freilich, D. M. Bianchi, A. M. Kaufman, T. K. Langin, and D. S. Hall, *Real-Time Dynamics of Single Vortex Lines and Vortex Dipoles in a Bose-Einstein Condensate* Science **329**, 1182 (2010).

[36] K. Henderson, C. Ryu, C. MacCormick, and M. G. Boshier, *Experimental demonstration of painting arbitrary and dynamic potentials for BoseEinstein condensates* New Journal of Physics **11**, 043030 (2009).

[37] J. A. Sauer, M. D. Barrett, and M. S. Chapman, *Storage Ring for Neutral Atoms* Phys. Rev. Lett. **87**, 270401 (2001).

[38] A. S. Arnold, C. S. Garvie, and E. Riis, *Large magnetic storage ring for Bose-Einstein condensates* Phys. Rev. A **73**, 041606 (2006).

[39] C. Ryu, M. F. Andersen, P. Cladé, V. Natarajan, K. Helmerson, and W. D. Phillips, *Observation of Persistent Flow of a Bose-Einstein Condensate in a Toroidal Trap* Phys. Rev. Lett. **99**, 260401 (2007).

[40] A. Ramanathan, K. C. Wright, S. R. Muniz, M. Zelan, W. T. Hill, C. J. Lobb, K. Helmerson, W. D. Phillips, and G. K. Campbell, *Superflow in a Toroidal Bose-Einstein Condensate: An Atom Circuit with a Tunable Weak Link* Phys. Rev. Lett. **106**, 130401 (2011).

[41] M. Ben Dahan, E. Peik, J. Reichel, Y. Castin, and C. Salomon, *Bloch Oscillations of Atoms in an Optical Potential* Phys. Rev. Lett. **76**, 4508 (1996).

[42] O. Morsch, J. H. Müller, M. Cristiani, D. Ciampini, and E. Arimondo, *Bloch Oscillations and Mean-Field Effects of Bose-Einstein Condensates in 1D Optical Lattices* Phys. Rev. Lett. **87**, 140402 (2001).

[43] H. T. C. Stoof, *Bose-Einstein condensation: Breaking up a superfluid* Nature **415**, 25 (2002).

[44] M. Greiner, O. Mandel, T. Esslinger, T. W. Hansch, and I. Bloch, *Quantum phase transition from a superfluid to a Mott insulator in a gas of ultracold atoms* Nature **415**, 39 (2002).

[45] T. G. Tiecke, M. Kemmann, C. Buggle, I. Shvarchuck, W. von Klitzing, and J. T. M. Walraven, *BoseEinstein condensation in a magnetic double-well potential* Journal of Optics B: Quantum and Semiclassical Optics **5**, S119 (2003).

[46] M. Albiez, R. Gati, J. Fölling, S. Hunsmann, M. Cristiani, and M. K. Oberthaler, *Direct Observation of Tunneling and Nonlinear Self-Trapping in a Single Bosonic Josephson Junction* Phys. Rev. Lett. **95**, 010402 (2005).

[47] A. L. Gaunt, T. F. Schmidutz, I. Gotlibovych, R. P. Smith, and Z. Hadzibabic, *Bose-Einstein Condensation of Atoms in a Uniform Potential* Phys. Rev. Lett. **110**, 200406 (2013).

[48] F. Dalfovo, S. Giorgini, L. P. Pitaevskii, and S. Stringari, *Theory of Bose-Einstein condensation in trapped gases* Rev. Mod. Phys. **71**, 463 (1999).

[49] S. Burger, K. Bongs, S. Dettmer, W. Ertmer, K. Sengstock, A. Sanpera, G. V. Shlyapnikov, and M. Lewenstein, *Dark Solitons in Bose-Einstein Condensates* Phys. Rev. Lett. **83**, 5198 (1999).

[50] J. Denschlag, J. E. Simsarian, D. L. Feder, C. W. Clark, L. A. Collins, J. Cubizolles, L. Deng, E. W. Hagley, K. Helmerson, W. P. Reinhardt, et al., *Generating Solitons by Phase Engineering of a Bose-Einstein Condensate* Science **287**, 97 (2000).

[51] B. P. Anderson, P. C. Haljan, C. A. Regal, D. L. Feder, L. A. Collins, C. W. Clark, and E. A. Cornell, *Watching Dark Solitons Decay into Vortex Rings in a Bose-Einstein Condensate* Phys. Rev. Lett. **86**, 2926 (2001).

[52] Z. Dutton, M. Budde, C. Slowe, and L. V. Hau, *Observation of Quantum Shock Waves Created with Ultra- Compressed Slow Light Pulses in a Bose-Einstein Condensate* Science **293**, 663 (2001).

[53] K. E. Strecker, G. B. Partridge, A. G. Truscott, and R. G. Hulet, *Formation and propagation of matter-wave soliton trains* Nature **417**, 150 (2002).

[54] L. Khaykovich, F. Schreck, G. Ferrari, T. Bourdel, J. Cubizolles, L. D. Carr, Y. Castin, and C. Salomon, *Formation of a Matter-Wave Bright Soliton* Science **296**, 1290 (2002).

[55] U. A. Khawaja, H. T. C. Stoof, R. G. Hulet, K. E. Strecker, and G. B. Partridge, *Bright Soliton Trains of Trapped Bose-Einstein Condensates* Phys. Rev. Lett. **89**, 200404 (2002).

[56] L. Salasnich, A. Parola, and L. Reatto, *Condensate bright solitons under transverse confinement* Phys. Rev. A **66**, 043603 (2002).

[57] L. Salasnich, A. Parola, and L. Reatto, *Modulational Instability and Complex Dynamics of Confined Matter-Wave Solitons* Phys. Rev. Lett. **91**, 080405 (2003).

[58] L. D. Carr and J. Brand, *Spontaneous Soliton Formation and Modulational Instability in Bose-Einstein Condensates* Phys. Rev. Lett. **92**, 040401 (2004).

[59] A. L. Fetter and A. A. Svidzinsky, *Vortices in a trapped dilute Bose-Einstein condensate* Journal of Physics: Condensed Matter **13**, R135 (2001).

[60] C. Lobo, A. Sinatra, and Y. Castin, *Vortex Lattice Formation in Bose-Einstein Condensates* Phys. Rev. Lett. **92**, 020403 (2004).

[61] B. P. Anderson, P. C. Haljan, C. E. Wieman, and E. A. Cornell, *Vortex Precession in Bose-Einstein Condensates: Observations with Filled and Empty Cores* Phys. Rev. Lett. **85**, 2857 (2000).

[62] C. J. Myatt, E. A. Burt, R. W. Ghrist, E. A. Cornell, and C. E. Wieman, *Production of Two Overlapping Bose-Einstein Condensates by Sympathetic Cooling* Phys. Rev. Lett. **78**, 586 (1997).

[63] D. S. Hall, M. R. Matthews, J. R. Ensher, C. E. Wieman, and E. A. Cornell, *Dynamics of Component Separation in a Binary Mixture of Bose-Einstein Condensates* Phys. Rev. Lett. **81**, 1539 (1998).

[64] M. R. Matthews, B. P. Anderson, P. C. Haljan, D. S. Hall, C. E. Wieman, and E. A. Cornell, *Vortices in a Bose-Einstein Condensate* Phys. Rev. Lett. **83**, 2498 (1999).

[65] P. Maddaloni, M. Modugno, C. Fort, F. Minardi, and M. Inguscio, *Collective Oscillations of Two Colliding Bose-Einstein Condensates* Phys. Rev. Lett. **85**, 2413 (2000).

[66] G. Delannoy, S. G. Murdoch, V. Boyer, V. Josse, P. Bouyer, and A. Aspect, *Understanding the production of dual Bose-Einstein condensation with sympathetic cooling* Phys. Rev. A **63**, 051602 (2001).

[67] V. Schweikhard, I. Coddington, P. Engels, S. Tung, and E. A. Cornell, *Vortex-Lattice Dynamics in Rotating Spinor Bose-Einstein Condensates* Phys. Rev. Lett. **93**, 210403 (2004).

[68] K. M. Mertes, J. W. Merrill, R. Carretero-González, D. J. Frantzeskakis, P. G. Kevrekidis, and D. S. Hall, *Nonequilibrium Dynamics and Superfluid Ring Excitations in Binary Bose-Einstein Condensates* Phys. Rev. Lett. **99**, 190402 (2007).

[69] R. P. Anderson, C. Ticknor, A. I. Sidorov, and B. V. Hall, *Spatially inhomogeneous phase evolution of a two-component Bose-Einstein condensate* Phys. Rev. A **80**, 023603 (2009).

[70] S. Tojo, Y. Taguchi, Y. Masuyama, T. Hayashi, H. Saito, and T. Hirano, *Controlling phase separation of binary Bose-Einstein condensates via mixed-spin-channel Feshbach resonance* Phys. Rev. A **82**, 033609 (2010).

[71] T. Busch, J. I. Cirac, V. M. Pérez-García, and P. Zoller, *Stability and collective excitations of a two-component Bose-Einstein condensed gas: A moment approach* Phys. Rev. A **56**, 2978 (1997).

[72] H.-J. Miesner, D. M. Stamper-Kurn, J. Stenger, S. Inouye, A. P. Chikkatur, and W. Ketterle, *Observation of Metastable States in Spinor Bose-Einstein Condensates* Phys. Rev. Lett. **82**, 2228 (1999).

[73] S. B. Papp, J. M. Pino, and C. E. Wieman, *Tunable Miscibility in a Dual-Species Bose-Einstein Condensate* Phys. Rev. Lett. **101**, 040402 (2008).

[74] G. Ferrari, M. Inguscio, W. Jastrzebski, G. Modugno, G. Roati, and A. Simoni, *Collisional Properties of Ultracold K-Rb Mixtures* Phys. Rev. Lett. **89**, 053202 (2002).

[75] G. Modugno, M. Modugno, F. Riboli, G. Roati, and M. Inguscio, *Two Atomic Species Superfluid* Phys. Rev. Lett. **89**, 190404 (2002).

[76] G. Thalhammer, G. Barontini, L. De Sarlo, J. Catani, F. Minardi, and M. Inguscio, *Double Species Bose-Einstein Condensate with Tunable Interspecies Interactions* Phys. Rev. Lett. **100**, 210402 (2008).

[77] D. J. McCarron, H. W. Cho, D. L. Jenkin, M. P. Köppinger, and S. L. Cornish, *Dual-species Bose-Einstein condensate of* ^{87}Rb *and* ^{133}Cs Phys. Rev. A **84**, 011603 (2011).

[78] T.-L. Ho and V. B. Shenoy, *Binary Mixtures of Bose Condensates of Alkali Atoms* Phys. Rev. Lett. **77**, 3276 (1996).

[79] E. P. Bashkin and A. V. Vagov, *Instability and stratification of a two-component Bose-Einstein condensate in a trapped ultracold gas* Phys. Rev. B **56**, 6207 (1997).

[80] H. Pu and N. P. Bigelow, *Properties of Two-Species Bose Condensates* Phys. Rev. Lett. **80**, 1130 (1998).

[81] M. Trippenbach, K. Gral, K. Rzazewski, B. Malomed, and Y. B. Band, *Structure of binary Bose-Einstein condensates* Journal of Physics B: Atomic, Molecular and Optical Physics **33**, 4017 (2000).

[82] B. Tanatar and K. Erkan, *Strongly interacting one-dimensional Bose-Einstein condensates in harmonic traps* Phys. Rev. A **62**, 053601 (2000).

[83] R. A. Barankov, *Boundary of two mixed Bose-Einstein condensates* Phys. Rev. A **66**, 013612 (2002).

[84] H. Pu and N. P. Bigelow, *Collective Excitations, Metastability, and Nonlinear Response of a Trapped Two-Species Bose-Einstein Condensate* Phys. Rev. Lett. **80**, 1134 (1998).

[85] P. Ao and S. T. Chui, *Binary Bose-Einstein condensate mixtures in weakly and strongly segregated phases* Phys. Rev. A **58**, 4836 (1998).

[86] S. T. Chui and A. P, *Broken cylindrical symmetry in binary mixtures of Bose-Einstein condensates* Phys. Rev. A **59**, 1473 (1999).

[87] J. G. Kim and E. K. Lee, *Characteristic features of symmetry breaking in two-component Bose-Einstein condensates* Phys. Rev. E **65**, 066201 (2002).

[88] A. A. Svidzinsky and S. T. Chui, *Symmetric-asymmetric transition in mixtures of Bose-Einstein condensates* Phys. Rev. A **67**, 053608 (2003).

[89] A. A. Svidzinsky and S. T. Chui, *Normal modes and stability of phase-separated trapped Bose-Einstein condensates* Phys. Rev. A **68**, 013612 (2003).

[90] B. D. Esry, *Impact of spontaneous spatial symmetry breaking on the critical atom number for two-component Bose-Einstein condensates* Phys. Rev. A **58**, R3399 (1998).

[91] S. Gautam and D. Angom, *Ground state geometry of binary condensates in axisymmetric traps* Journal of Physics B: Atomic, Molecular and Optical Physics **43**, 095302 (2010).

[92] P. Mason and A. Aftalion, *Classification of the ground states and topological defects in a rotating two-component Bose-Einstein condensate* Phys. Rev. A **84**, 033611 (2011).

[93] J. Jin, S. Zhang, and W. Han, *Spin domain wall in rotating two-component BoseEinstein condensates* Journal of Physics B: Atomic, Molecular and Optical Physics **44**, 165302 (2011).

[94] D. Gordon and C. M. Savage, *Excitation spectrum and instability of a two-species Bose-Einstein condensate* Phys. Rev. A **58**, 1440 (1998).

[95] B. D. Esry and C. H. Greene, *Low-lying excitations of double Bose-Einstein condensates* Phys. Rev. A **57**, 1265 (1998).

[96] F. Riboli and M. Modugno, *Topology of the ground state of two interacting Bose-Einstein condensates* Phys. Rev. A **65**, 063614 (2002).

[97] C. K. Law, H. Pu, N. P. Bigelow, and J. H. Eberly, *"Stability Signature" in Two-Species Dilute Bose-Einstein Condensates* Phys. Rev. Lett. **79**, 3105 (1997).

[98] P. Öhberg, *Stability properties of the two-component Bose-Einstein condensate* Phys. Rev. A **59**, 634 (1999).

[99] S. K. Adhikari, *Coupled Bose-Einstein condensate: Collapse for attractive interaction* Phys. Rev. A **63**, 043611 (2001).

[100] M. A. Cazalilla and A. F. Ho, *Instabilities in Binary Mixtures of One-Dimensional Quantum Degenerate Gases* Phys. Rev. Lett. **91**, 150403 (2003).

[101] T. Kadokura, T. Aioi, K. Sasaki, T. Kishimoto, and H. Saito, *Rayleigh-Taylor instability in a two-component Bose-Einstein condensate with rotational symmetry* Phys. Rev. A **85**, 013602 (2012).

[102] P. K. Shukla, L. Sten, and R. Fedele, *Modulational Instability of Two Colliding Bose - Einstein Condensates* Physica **553**, 6 (2001).

[103] I. Kourakis, P. K. Shukla, M. Marklund, and L. Stenflo, *Modulational instability criteria for two-component BoseEinstein condensates* European Physical Journal B **46**, 381 (2005).

[104] K. Kasamatsu and M. Tsubota, *Multiple Domain Formation Induced by Modulation Instability in Two-Component Bose-Einstein Condensates* Phys. Rev. Lett. **93**, 100402 (2004).

[105] K. Kasamatsu and M. Tsubota, *Modulation instability and pattern formation in two-component Bose-Einstein condensates* Journal of Low Temperature Physics **138**, 669 (2005).

[106] K. Kasamatsu and M. Tsubota, *Modulation instability and solitary-wave formation in two-component Bose-Einstein condensates* Phys. Rev. A **74**, 013617 (2006).

[107] T. S. Raju, P. K. Panigrahi, and K. Porsezian, *Modulational instability of two-component Bose-Einstein condensates in a quasi-one-dimensional geometry* Phys. Rev. A **71**, 035601 (2005).

[108] T. Busch and J. R. Anglin, *Dark-Bright Solitons in Inhomogeneous Bose-Einstein Condensates* Phys. Rev. Lett. **87**, 010401 (2001).

[109] J. J. Garcia-Ripoll and V. M. Perez-Garcia, *Stable and Unstable Vortices in Multi-component Bose-Einstein Condensates* Phys. Rev. Lett. **84**, 4264 (2000).

[110] S. T. Chui, V. N. Ryzhov, and E. E. Tareyeva, *Vortex states in a binary mixture of Bose-Einstein condensates* Phys. Rev. A **63**, 023605 (2001).

[111] D. M. Jezek, P. Capuzzi, and H. M. Cataldo, *Structure of vortices in two-component Bose-Einstein condensates* Phys. Rev. A **64**, 023605 (2001).

[112] P. Öhberg and L. Santos, *Vortex-vortex interaction in two-component Bose-Einstein condensates* Phys. Rev. A **66**, 013616 (2002).

[113] Q.-H. Park and J. H. Eberly, *Nontopological vortex in a two-component Bose-Einstein condensate* Phys. Rev. A **70**, 021602 (2004).

[114] S. J. Woo, S. Choi, L. O. Baksmaty, and N. P. Bigelow, *Dynamics of vortex matter in rotating two-species Bose-Einstein condensates* Phys. Rev. A **75**, 031604 (2007).

[115] K. Kasamatsu and M. Tsubota, *Vortex sheet in rotating two-component Bose-Einstein condensates* Phys. Rev. A **79**, 023606 (2009).

[116] G. Catelani and E. A. Yuzbashyan, *Coreless vorticity in multicomponent Bose and Fermi superfluids* Phys. Rev. A **81**, 033629 (2010).

[117] K. J. H. Law, P. G. Kevrekidis, and L. S. Tuckerman, *Stable Vortex˘Bright-Soliton Structures in Two-Component Bose-Einstein Condensates* Phys. Rev. Lett. **105**, 160405 (2010).

[118] P. Kuopanportti, J. A. M. Huhtamäki, and M. Möttönen, *Exotic vortex lattices in two-species Bose-Einstein condensates* Phys. Rev. A **85**, 043613 (2012).

[119] N. P. Proukakis and B. Jackson, *Finite-temperature models of BoseEinstein condensation* Journal of Physics B: Atomic, Molecular and Optical Physics **41**, 203002 (2008).

[120] B. D. Esry, C. H. Greene, J. P. Burke, Jr., and J. L. Bohn, *Hartree-Fock Theory for Double Condensates* Phys. Rev. Lett. **78**, 3594 (1997).

[121] P. Öhberg and S. Stenholm, *Hartree-Fock treatment of the two-component Bose-Einstein condensate* Phys. Rev. A **57**, 1272 (1998).

[122] B. D. Esry and C. H. Greene, *Spontaneous spatial symmetry breaking in two-component Bose-Einstein condensates* Phys. Rev. A **59**, 1457 (1999).

[123] C.-H. Zhang and H. A. Fertig, *Collective excitations of a two-component Bose-Einstein condensate at finite temperature* Phys. Rev. A **75**, 013601 (2007).

[124] A. Griffin, *Conserving and gapless approximations for an inhomogeneous Bose gas at finite temperatures* Phys. Rev. B **53**, 9341 (1996).

[125] P. Öhberg, *Two-component condensates: The role of temperature* Phys. Rev. A **61**, 013601 (1999).

[126] H. Ma and T. Pang, *Condensate-profile asymmetry of a boson mixture in a disk-shaped harmonic trap* Phys. Rev. A **70**, 063606 (2004).

[127] D. C. Roberts and M. Ueda, *Stability analysis for n-component Bose-Einstein condensate* Phys. Rev. A **73**, 053611 (2006).

[128] S. Ronen, J. L. Bohn, L. E. Halmo, and M. Edwards, *Dynamical pattern formation during growth of a dual-species Bose-Einstein condensate* Phys. Rev. A **78**, 053613 (2008).

[129] A. Smerzi, S. Fantoni, S. Giovanazzi, and S. R. Shenoy, *Quantum Coherent Atomic Tunneling between Two Trapped Bose-Einstein Condensates* Phys. Rev. Lett. **79**, 4950 (1997).

[130] G.-H. Chen and Y.-S. Wu, *Quantum phase transition in a multicomponent Bose-Einstein condensate in optical lattices* Phys. Rev. A **67**, 013606 (2003).

[131] J. Smyrnakis, S. Bargi, G. M. Kavoulakis, M. Magiropoulos, K. Kärkkäinen, and S. M. Reimann, *Mixtures of Bose Gases Confined in a Ring Potential* Phys. Rev. Lett. **103**, 100404 (2009).

[132] D. M. Stamper-Kurn and M. Ueda, *Spinor Bose gases: Explorations of symmetries, magnetism and quantum dynamics* arΞiv (2012).

[133] E. Timmermans, K. Furuya, P. W. Milonni, and A. K. Kerman, *Prospect of creating a composite Fermi Bose superfluid* Physics Letters A **285**, 228 (2001).

[134] Z. Hadzibabic, C. Stan, K. Dieckmann, S. Gupta, M. Zwierlein, a. Görlitz, and W. Ketterle, *Two-Species Mixture of Quantum Degenerate Bose and Fermi Gases* Physical Review Letters **88**, 1 (2002).

[135] G. Roati, F. Riboli, G. Modugno, and M. Inguscio, *Fermi-Bose Quantum Degenerate K40-R87b Mixture with Attractive Interaction* Physical Review Letters **89**, 87 (2002).

[136] C. Silber, S. Günther, C. Marzok, B. Deh, P. Courteille, and C. Zimmermann, *Quantum-Degenerate Mixture of Fermionic Lithium and Bosonic Rubidium Gases* Physical Review Letters **95**, 1 (2005).

[137] M. Tey, S. Stellmer, R. Grimm, and F. Schreck, *Double-degenerate Bose-Fermi mixture of strontium* Physical Review A **82**, 82 (2010).

[138] W. Geist, L. You, and T. A. B. Kennedy, *Sympathetic cooling of an atomic Bose-Fermi gas mixture* Physical Review A **59**, 1500 (1999).

[139] N. Nygaard and K. Mo, *Component separation in harmonically trapped boson-fermion mixtures* Physical Review A **59**, 2974 (1999).

[140] L. Viverit, C. J. Pethick, and H. Smith, *Zero-temperature phase diagram of binary boson-fermion mixtures 1* Physical Review **61**, 1 (2000).

[141] X. Yi and C. Sun, *Phase separation of a trapped Bose-Fermi gas mixture: Beyond the Thomas-Fermi approximation* Physical Review A **64**, 1 (2001).

[142] R. Roth, *Structure and stability of trapped atomic boson-fermion mixtures* Physical Review A **66**, 1 (2002).

[143] a. Albus, S. Gardiner, F. Illuminati, and M. Wilkens, *Quantum field theory of dilute homogeneous Bose-Fermi mixtures at zero temperature: General formalism and beyond mean-field corrections* Physical Review A **65**, 1 (2002).

[144] K. Das, *Bose-Fermi Mixtures in One Dimension* Physical Review Letters **90**, 1 (2003).

[145] M. Rizzi and A. Imambekov, *Pairing of one-dimensional Bose-Fermi mixtures with unequal masses* Physical Review A **77**, 1 (2008).

[146] S. Akhanjee, *Quasiparticle excitations in Bose-Fermi mixtures* Physical Review B **82**, 1 (2010).

[147] Y.-J. Hao, *Ground State Density Distribution of Bose-Fermi Mixture in a One-Dimensional Harmonic Trap* Chinese Physics Letters **28**, 010302 (2011).

[148] P. G. Kevrekidis, D. J. Frantzeskakis, and R. Carretero-Gonzlez, *Emergent Nonlinear Phenomena in Bose-Einstein Condensates* (Springer, 2008).

[149] R. K. Dodd, J. Eilbeck, J. Gibbon, and H. Morris, *Solitons and Nonlinear Wave Equations* (Academic, London, 1982).

[150] L. D. Carr, C. W. Clark, and W. P. Reinhardt, *Stationary solutions of the one-dimensional nonlinear Schrödinger equation. I. Case of repulsive nonlinearity* Phys. Rev. A **62**, 063610 (2000).

[151] P. Emplit, J. P. Hamaide, F. Reynaud, G. Froehly, and A. Barthelemy Opt. Commun. **62**, 374 (1987).

[152] J. Denschlag, J. E. Simsarian, D. L. Feder, C. W. Clark, L. A. Collins, J. Cubizolles, L. Deng, E. W. Hagley, K. Helmerson, W. P. Reinhardt, et al., *Generating Solitons by Phase Engineering of a Bose-Einstein Condensate* Science **287**, 97 (2000).

[153] S. Stellmer, P. Soltan-Panahi, S. Dorscher, M. Baumert, E.-M. Richter, J. Kronjager, K. Bongs, and K. Sengstock, *Oscillations and interactions of dark and dark-bright solitons in Bose-Einstein condensates* Nat. Phys. **4**, 496 (2008).

[154] A. Weller, J. P. Ronzheimer, C. Gross, J. Esteve, M. K. Oberthaler, D. J. Frantzeskakis, G. Theocharis, and P. G. Kevrekidis, *Experimental Observation of Oscillating and Interacting Matter Wave Dark Solitons* Phys. Rev. Lett. **101**, 130401 (2008).

[155] S. Stellmer, C. Becker, P. Soltan-Panahi, E.-M. Richter, S. Dörscher, M. Baumert, J. Kronjäger, K. Bongs, and K. Sengstock, *Collisions of Dark Solitons in Elongated Bose-Einstein Condensates* Phys. Rev. Lett. **101**, 120406 (2008).

[156] Z. Dutton, M. Budde, C. Slowe, and L. V. Hau, *Observation of Quantum Shock Waves Created with Ultra- Compressed Slow Light Pulses in a Bose-Einstein Condensate* Science **293**, 663 (2001).

[157] P. Engels and C. Atherton, *Stationary and Nonstationary Fluid Flow of a Bose-Einstein Condensate Through a Penetrable Barrier* Phys. Rev. Lett. **99**, 160405 (2007).

[158] G.-B. Jo, J.-H. Choi, C. A. Christensen, Y.-R. Lee, T. A. Pasquini, W. Ketterle, and D. E. Pritchard, *Matter-Wave Interferometry with Phase Fluctuating Bose-Einstein Condensates* Phys. Rev. Lett. **99**, 240406 (2007).

[159] B. Damski and W. H. Zurek, *Soliton Creation During a Bose-Einstein Condensation* Phys. Rev. Lett. **104**, 160404 (2010).

[160] D. J. Frantzeskakis, *Dark solitons in atomic BoseEinstein condensates: from theory to experiments* Journal of Physics A: Mathematical and Theoretical **43**, 213001 (2010).

[161] C. Hamner, J. J. Chang, P. Engels, and M. A. Hoefer, *Generation of Dark-Bright Soliton Trains in Superfluid-Superfluid Counterflow* Phys. Rev. Lett. **106**, 065302 (2011).

[162] S. Middelkamp, J. Chang, C. Hamner, R. Carretero-Gonzlez, P. Kevrekidis, V. Achilleos, D. Frantzeskakis, P. Schmelcher, and P. Engels, *Dynamics of dark-bright solitons in cigar-shaped BoseEinstein condensates* Physics Letters A **375**, 642 (2011).

[163] M. A. Hoefer, J. J. Chang, C. Hamner, and P. Engels, *Dark-dark solitons and modulational instability in miscible two-component Bose-Einstein condensates* Phys. Rev. A **84**, 041605 (2011).

[164] C. Becker, S. Stellmer, P. Soltan-Panahi, S. Dörscher, M. Baumert, E. M. Richter, J. Kronjäger, K. Bongs, and K. Sengstock, *Oscillations and interactions of dark and dark-bright solitons in Bose-Einstein condensates* Nature Physics **4**, 9 (2008).

[165] H. E. Nistazakis, D. J. Frantzeskakis, P. G. Kevrekidis, B. A. Malomed, and R. Carretero-González, *Bright-dark soliton complexes in spinor Bose-Einstein condensates* Phys. Rev. A **77**, 033612 (2008).

[166] M. Vijayajayanthi, T. Kanna, and M. Lakshmanan, *Bright-dark solitons and their collisions in mixed N-coupled nonlinear Schrödinger equations* Phys. Rev. A **77**, 013820 (2008).

[167] H. Li, D. Wang, and Y. Cheng, *Dynamics of darkbright vector solitons in a two-component BoseEinstein condensate* Chaos, Solitons and Fractals **39**, 1988 (2009).

[168] D. Yan, J. J. Chang, C. Hamner, P. G. Kevrekidis, P. Engels, V. Achilleos, D. J. Frantzeskakis, R. Carretero-González, and P. Schmelcher, *Multiple dark-bright solitons in atomic Bose-Einstein condensates* Phys. Rev. A **84**, 053630 (2011).

[169] S. Rajendran, P. Muruganandam, and M. Lakshmanan, *Interaction of darkbright solitons in two-component BoseEinstein condensates* Journal of Physics B: Atomic, Molecular and Optical Physics **42**, 145307 (2009).

[170] L. Qiu-Yan, L. Zai-Dong, Y. Shu-Fang, L. Lu, and F. Guang-Sheng, *Formation of combined solitons in two-component BoseEinstein condensates* Chinese Physics B **19**, 080501 (2010).

[171] V. Achilleos, P. G. Kevrekidis, V. M. Rothos, and D. J. Frantzeskakis, *Statics and dynamics of atomic dark-bright solitons in the presence of impurities* Phys. Rev. A **84**, 053626 (2011).

[172] J. Stockhofe, P. G. Kevrekidis, D. J. Frantzeskakis, and P. Schmelcher, *Darkbright ring solitons in BoseEinstein condensates* Journal of Physics B: Atomic, Molecular and Optical Physics **44**, 191003 (2011).

[173] A. Álvarez, J. Cuevas, F. Romero, and P. Kevrekidis, *Darkbright discrete solitons: A numerical study of existence, stability and dynamics* Physica D: Nonlinear Phenomena **240**, 767 (2011).

[174] V. A. Brazhnyi and V. M. Prez-Garca, *Stable multidimensional soliton stripes in two-component BoseEinstein condensates* Chaos, Solitons and Fractals **44**, 381 (2011).

[175] X. Liu, H. Pu, B. Xiong, W. M. Liu, and J. Gong, *Formation and transformation of vector solitons in two-species Bose-Einstein condensates with a tunable interaction* Phys. Rev. A **79**, 013423 (2009).

[176] D. Schumayer and B. Apagyi, *Stability of static solitonic excitations of two-component Bose-Einstein condensates in finite range of interspecies scattering length* a_{12} Phys. Rev. A **69**, 043620 (2004).

[177] V. Achilleos, D. Yan, P. G. Kevrekidis, and D. J. Frantzeskakis, *Dark-bright solitons in BoseEinstein condensates at finite temperatures* New Journal of Physics **14**, 055006 (2012).

[178] M. Tsubota, *Quantum turbulencefrom superfluid helium to atomic BoseEinstein condensates* Journal of Physics: Condensed Matter **21**, 164207 (2009).

[179] A. J. Allen, N. G. Parker, N. P. Proukakis, and C. F. Barenghi, *Quantum turbulence in atomic Bose-Einstein condensates* arXiv (2013).

[180] H. Takeuchi, S. Ishino, and M. Tsubota, *Binary Quantum Turbulence Arising from Countersuperflow Instability in Two-Component Bose-Einstein Condensates* Phys. Rev. Lett. **105**, 205301 (2010).

[181] D. Kobyakov, A. Bezett, E. Lundh, M. Marklund, and V. Bychkov, *Turbulence in binary Bose-Einstein condensates generated by highly nonlinear Rayleigh-Taylor and Kelvin-Helmholtz instabilities* Phys. Rev. A **89**, 013631 (2014).

[182] K. Fujimoto and M. Tsubota, *Counterflow instability and turbulence in a spin-1 spinor Bose-Einstein condensate* Phys. Rev. A **85**, 033642 (2012).

[183] K. Fujimoto and M. Tsubota, *Spin turbulence in a trapped spin-1 spinor Bose-Einstein condensate* Phys. Rev. A **85**, 053641 (2012).

[184] B. Villaseor, R. Zamora-Zamora, D. Bernal, and V. Romero-Rochn, *Quantum turbulence by vortex stirring in a spinor Bose-Einstein condensate* arXiv (2013).

[185] E. P. Gross Phys. Rev. **106**, 161 (1957).

[186] E. P. Gross, *Structure of Quantized Vortex in Boson Systems* Il Nuovo Cimento **20**, 454 (1961).

[187] E. P. Gross, *Structure of Quantized Vortex in Boson Systems* Journal of Mathematical Physics **4**, 195 (1963).

[188] V. L. Ginzburg and L. P. Pitaevskii Sov. Phys. JETP **7**, 858 (1958).

[189] L. P. Pitaevskii, *Vortex lines in an imperfect Bose gas* Sov. Phys. JETP **13**, 451 (1961).

[190] G. Baym and C. J. Pethick, *Ground-State Properties of Magnetically Trapped Bose-Condensed Rubidium Gas* Phys. Rev. Lett. **76**, 6 (1996).

[191] E. Madlung Zeit. fur Phys. **40**, 622 (1926).

[192] T. Winiecki, B. Jackson, J. F. McCann, and C. S. Adams, *Vortex shedding and drag in dilute Bose-Einstein condensates* Journal of Physics B: Atomic, Molecular and Optical Physics **33**, 4069 (2000).

[193] L. Onsager Nuovo Cimento **6**, 279 (1949).

[194] R. Feynman, *Chapter II Application of Quantum Mechanics to Liquid Helium*, vol. 1 (Elsevier, 1955).

[195] F. Pereira Dos Santos, J. Léonard, J. Wang, C. J. Barrelet, F. Perales, E. Rasel, C. S. Unnikrishnan, M. Leduc, and C. Cohen-Tannoudji, *Bose-Einstein Condensation of Metastable Helium* Phys. Rev. Lett. **86**, 3459 (2001).

[196] C. Samuelis, E. Tiesinga, T. Laue, M. Elbs, H. Knöckel, and E. Tiemann, *Cold atomic collisions studied by molecular spectroscopy* Phys. Rev. A **63**, 012710 (2000).

[197] G. Modugno, G. Ferrari, G. Roati, R. J. Brecha, A. Simoni, and M. Inguscio, *Bose-Einstein Condensation of Potassium Atoms by Sympathetic Cooling* Science **294**, 1320 (2001).

[198] A. Marte, T. Volz, J. Schuster, S. Dürr, G. Rempe, E. G. M. van Kempen, and B. J. Verhaar, *Feshbach Resonances in Rubidium 87: Precision Measurement and Analysis* Phys. Rev. Lett. **89**, 283202 (2002).

[199] C. Chin, V. Vuletić, A. J. Kerman, S. Chu, E. Tiesinga, P. J. Leo, and C. J. Williams, *Precision Feshbach spectroscopy of ultracold* Cs_2 Phys. Rev. A **70**, 032701 (2004).

[200] M. Olshanii, *Atomic Scattering in the Presence of an External Confinement and a Gas of Impenetrable Bosons* Phys. Rev. Lett. **81**, 938 (1998).

[201] F. Wang, D. Xiong, X. Li, D. Wang, and E. Tiemann, *Observation of Feshbach resonances between ultracold Na and Rb atoms* Phys. Rev. A **87**, 050702 (2013).

[202] T. Takekoshi, M. Debatin, R. Rameshan, F. Ferlaino, R. Grimm, H.-C. Nägerl, C. R. Le Sueur, J. M. Hutson, P. S. Julienne, S. Kotochigova, et al., *Towards the production of ultracold ground-state RbCs molecules: Feshbach resonances, weakly bound states, and the coupled-channel model* Phys. Rev. A **85**, 032506 (2012).

[203] E. Zaremba, T. Nikuni, and A. Griffin, *Dynamics of Trapped Bose Gases at Finite Temperatures* Journal of Low Temperature Physics **116**, 277 (1999).

[204] N. P. Proukakis, K. Burnett, and H. T. C. Stoof, *Microscopic treatment of binary interactions in the nonequilibrium dynamics of partially Bose-condensed trapped gases* Phys. Rev. A **57**, 1230 (1998).

[205] R. Walser, J. Williams, J. Cooper, and M. Holland, *Quantum kinetic theory for a condensed bosonic gas* Phys. Rev. A **59**, 3878 (1999).

[206] A. Griffin, T. Nikuni, and E. Zaremba, *Bose-Condensed Gases at Finite Temperatures* (Cambridge University Press, 2009).

[207] D. Jaksch, C. W. Gardiner, and P. Zoller, *Quantum kinetic theory. II. Simulation of the quantum Boltzmann master equation* Phys. Rev. A **56**, 575 (1997).

[208] M. Holland, J. Williams, and J. Cooper, *Bose-Einstein condensation: Kinetic evolution obtained from simulated trajectories* Phys. Rev. A **55**, 3670 (1997).

[209] H. Stoof, *Coherent Versus Incoherent Dynamics During Bose-Einstein Condensation in Atomic Gases* Journal of Low Temperature Physics **114**, 11 (1999).

[210] H. T. C. Stoof, *Initial Stages of Bose-Einstein Condensation* Phys. Rev. Lett. **78**, 768 (1997).

[211] H. Stoof and M. Bijlsma, *Dynamics of Fluctuating BoseEinstein Condensates* Journal of Low Temperature Physics **124**, 431 (2001), ISSN 0022-2291.

[212] R. A. Duine and H. T. C. Stoof, *Stochastic dynamics of a trapped Bose-Einstein condensate* Phys. Rev. A **65**, 013603 (2001).

[213] P. Blakie, A. Bradley, M. Davis, R. Ballagh, and C. Gardiner, *Dynamics and statistical mechanics of ultra-cold Bose gases using c-field techniques* Advances in Physics **57**, 363 (2008).

[214] C. W. Gardiner and M. J. Davis, *The stochastic GrossPitaevskii equation: II* Journal of Physics B: Atomic, Molecular and Optical Physics **36**, 4731 (2003).

[215] S. Choi, S. A. Morgan, and K. Burnett, *Phenomenological damping in trapped atomic Bose-Einstein condensates* Phys. Rev. A **57**, 4057 (1998).

[216] P. L. P. Zh. Eksp. Teor. Fiz. **35**, 408 (1958).

[217] P. L. P. Sov. Phys.—JETP **35**, 282 (1959).

[218] A. A. Penckwitt, R. J. Ballagh, and C. W. Gardiner, *Nucleation, Growth, and Stabilization of Bose-Einstein Condensate Vortex Lattices* Phys. Rev. Lett. **89**, 260402 (2002).

[219] M. Tsubota, K. Kasamatsu, and M. Ueda, *Vortex lattice formation in a rotating Bose-Einstein condensate* Phys. Rev. A **65**, 023603 (2002).

[220] K. Kasamatsu, M. Tsubota, and M. Ueda, *Nonlinear dynamics of vortex lattice formation in a rotating Bose-Einstein condensate* Phys. Rev. A **67**, 033610 (2003).

[221] N. P. Proukakis, N. G. Parker, C. F. Barenghi, and C. S. Adams, *Parametric Driving of Dark Solitons in Atomic Bose-Einstein Condensates* Phys. Rev. Lett. **93**, 130408 (2004), URL `http://link.aps.org/doi/10.1103/PhysRevLett.93.130408`.

[222] J. A. Seman, E. A. L. Henn, R. F. Shiozaki, G. Roati, F. J. Poveda-Cuevas, K. M. F. Magalhes, V. I. Yukalov, M. Tsubota, M. Kobayashi, K. Kasamatsu, et al., *Route*

to turbulence in a trapped Bose-Einstein condensate Laser Physics Letters **8**, 691 (2011).

[223] M. Brewczyk, M. Gajda, and K. Rzaewski, *Classical fields approximation for bosons at nonzero temperatures* Journal of Physics B: Atomic, Molecular and Optical Physics **40**, R1 (2007).

[224] N. G. Berloff and B. V. Svistunov, *Scenario of strongly nonequilibrated Bose-Einstein condensation* Phys. Rev. A **66**, 013603 (2002).

[225] M. J. Davis, R. J. Ballagh, and K. Burnett, *Dynamics of thermal Bose fields in the classical limit* Journal of Physics B: Atomic, Molecular and Optical Physics **34**, 4487 (2001).

[226] M. J. Davis, S. A. Morgan, and K. Burnett, *Simulations of Bose Fields at Finite Temperature* Phys. Rev. Lett. **87**, 160402 (2001).

[227] Y. M. Kagan, B. V. Svistunov, and G. V. Shlyapnikov Sov. Phys. JETP **75**, 387 (1992).

[228] B. V. Svistunov J. Mosc. Phys. Soc. **1**, 373 (1991).

[229] B. V. Svistunov Sov. Phys. JETP **78**, 187 (1994).

[230] V. N. Popov, *Functional Integrals in Quantum Field Theory and Statistical Physics* (Reidel, Dordrecht, 1983).

[231] K. Goral, M. Gajda, and K. Rzazewski, *Multi-mode description of an interacting Bose-Einstein condensate* Opt. Express **8**, 92 (2001).

[232] C. Connaughton, C. Josserand, A. Picozzi, Y. Pomeau, and S. Rica, *Condensation of Classical Nonlinear Waves* Phys. Rev. Lett. **95**, 263901 (2005).

[233] N. G. Berloff and A. J. Youd, *Dissipative Dynamics of Superfluid Vortices at Nonzero Temperatures* Phys. Rev. Lett. **99**, 145301 (2007).

[234] N. Berloff and C. Yin, *Turbulence and Coherent Structures in Two-Component Bose Condensates* Journal of Low Temperature Physics **145**, 187 (2006).

[235] M. Trippenbach, K. Gral, K. Rzazewski, B. Malomed, and Y. B. Band, *Structure of Binary Bose-Einstein Condensates* Journal of Physics B: Atomic, Molecular and Optical Physics **33**, 4017 (2000).

[236] D. Jenkin, D. McCarron, M. Kppinger, H. Cho, S. Hopkins, and S. Cornish, *Bose-Einstein condensation of ^{87}Rb in a levitated crossed dipole trap* The European Physical Journal D - Atomic, Molecular, Optical and Plasma Physics **65**, 11 (2011).

[237] H. Cho, D. McCarron, D. Jenkin, M. Kppinger, and S. Cornish, *A high phase-space density mixture of ^{87}Rb and ^{133}Cs: towards ultracold heteronuclear molecules* The European Physical Journal D - Atomic, Molecular, Optical and Plasma Physics **65**, 125 (2011).

[238] D. J. McCarron, H. W. Cho, D. L. Jenkin, M. P. Köppinger, and S. L. Cornish Private Communication (2012).

[239] W. H. Zurek, *Causality in Condensates: Gray Solitons as Relics of BEC Formation* Phys. Rev. Lett. **102**, 105702 (2009).

[240] M. Leadbeater, T. Winiecki, and C. S. Adams, *Effect of condensate depletion on the critical velocity for vortex nucleation in quantum fluids* Journal of Physics B: Atomic, Molecular and Optical Physics **36**, L143 (2003).

[241] H. Salman and N. G. Berloff, *Condensation of classical nonlinear waves in a two-component system* Physica D: Nonlinear Phenomena **238**, 1482 (2009).

[242] N. P. Proukakis, S. A. G. ans M. Davis, and M. Szymanska, *Quantum Gases: Finite Temperature and Non-Equilibrium Dynamics* (2013).

[243] M. Edmonds Private Communication (2014).

[244] F. Tsitoura, V. Achilleos, B. A. Malomed, D. Yan, P. G. Kevrekidis, and D. J. Frantzeskakis, *Matter-wave solitons in the counterflow of two immiscible superfluids* Phys. Rev. A **87**, 063624 (2013).

[245] S. Taneda J. Phys. Soc. Jpn. **11**, 302 (1956).

[246] S. Taneda J. Phys. Soc. Jpn. **50**, 1398 (1981).

[247] T. Frisch, Y. Pomeau, and S. Rica, *Transition to dissipation in a model of superflow* Phys. Rev. Lett. **69**, 1644 (1992).

[248] T. Winiecki, J. F. McCann, and C. S. Adams, *Pressure Drag in Linear and Nonlinear Quantum Fluids* Phys. Rev. Lett. **82**, 5186 (1999).

[249] W. H. Press, S. A. Teukolsky, A. T. Vetterling, and B. P. Flannery, *Numerical Recipies in Fortran* (Cambridge University Press, 1992), second edition ed.